# Towards Local Property Assessment of Advanced Manufactured Microstructures

—

## A Case Study in Linear Friction Welded Titanium




Christopher Massimo Magazzeni

The Queen's College

University of Oxford

Supervisors: Prof Angus J Wilkinson and Dr Jicheng Gong

A thesis submitted for the degree of

*Doctor of Philosophy*

Hilary 2022

# a. Acknowledgements

I am eternally grateful to the many who have enabled, guided, and supported me in this journey.

To Angus, Jicheng and Dave Rugg, for their guidance and supervision. To Arutyun, on whose shoulders this project stood. To the Oxford Micromechanics team and especially Profs Dave and Ed, Drs Phani, Anna, Bo, Jack, Hazel, John, and Ed, and my close colleagues Keivan, Ed, Shaz, Yi, Inigo, Rob, and Becs for mentoring, teaching, discussing, and ideating. To Rory, for the many enriching, stimulating, and creative hours in collaboration during the pandemic. To my collaborators Chris Gearhart, Phillip, Chi-Toan, Dave, and Abdallah with whom I had the privilege to engage with their expertise, creativity, and contributions in the projects herein. To the EM suite – in particular Gareth and Jenny – for their sustained support in this learning period. To Roger and Tony for their experimental support. To my funding bodies, the Royal Commission for the Exhibition of 1851, the EPSRC, and Rolls-Royce plc, for their enabling role.

To the AerOx team who I had the privilege of learning from – Jiawei, Reece, Yana, Mathilde, Jack & Jack, and Sophie. To the Oxford Space Initiative – Marc, Michele, Lucas, David, Eamonn, and Sally – for inviting me to explore a new field and providing me with perspective.

To my fellow Taberdars, and the broader Oxford family who have accompanied me in this journey throughout my years here – David, Thomas, Gian, George, Tom Davies, Lemuel, Tom & Valeria, Anuraag, Paddy, Leslie, Dom, Nick, Lewis, Jack and Tara. To the musicians and comedians who provided me with joy.

To Jack and Kilian, who made the leap with me from Homerton. To Robin, for accompanying, guiding, encouraging, moralising. To my family, who inspired me to take this journey.

To Léna, for your un-ending patience, love, and kindness from day one.

# Contents


a. Acknowledgements ..... 2
b. Abstract ..... 6
c. Publications ..... 7
c.I. Conferences ..... 8
d. Glossary of Terms ..... 9
I. Introduction ..... 11
I.I. Background ..... 11
I.I.1. Titanium ..... 12
I.I.2. Characterisation Methods ..... 16
I.I.2.1. EBSD ..... 16
I.I.2.2. Micromechanical Testing ..... 17
I.I.3. Linear Friction Welding ..... 20
I.II. Case Study – Ti-64 LFW ..... 22
1. Chapter 1: Static local property assessment through multi-modal mapping ..... 27
1.1. Introduction ..... 27
1.2. Methods ..... 29
1.2.1. Sample Preparation ..... 29
1.2.2. EBSD mapping ..... 30
1.2.3. Nanoindentation mapping ..... 30
1.2.4. Analysis Methodology ..... 32
1.3. Results ..... 34
1.3.1. Dataset 1 – CP Titanium ..... 34
1.3.2. Dataset Two – Linear Friction Weld ..... 41
1.4. Discussion and Limitations ..... 44
1.4.1. Reliability of input information ..... 44

1.4.2. Reliability of analysis ..... 44

1.4.3. Quantitative results ..... 45

1.5. Conclusion ..... 46

2. Chapter 2: Dynamic local property assessment through meso-scale ultrasonic fatigue ..... 48

2.2. Background and Motivation ..... 48

2.2.1. Local Stress States – Microstructural Fatigue ..... 52

2.2.2. Fatigue in advanced manufactured titanium ..... 53

2.2.3. Ultrasonic Fatigue and Meso-scale Fatigue ..... 56

2.2.4. Fatigue Testing Protocols ..... 58

2.3. Context – Previous Small Scale Fatigue Work in the Group ..... 63

2.4. Experimental Methods ..... 70

2.4.1. Process Flow Determination ..... 71

2.4.1.1. Foil Preparation and Damage Layers ..... 72

2.4.1.2. Damage layer removal – mounting and grinding ..... 76

2.4.1.3. Cantilever design ..... 78

2.4.1.4. Design and Results of Foil 1 ..... 82

2.4.1.5. Perfect Coupling ..... 87

2.4.1.6. Foil 1 Perfect Coupling results ..... 91

2.4.1.7. Electropolishing ..... 95

2.4.1.8. Design and Testing of Foil 2 ..... 101

2.4.1.9. Dimensional Variation ..... 105

2.4.1.10. Stiffness Measurement ..... 108

2.4.1.11. Geometrical Analysis ..... 111

2.4.2. Experimental Fatigue Setup ..... 124

2.4.2.1. Specimen Holders ..... 128

2.5. Fatigue Testing Protocols ..... 129

2.5.1. Introduction ..... 130

2.5.2. Computational Framework ..... 131

2.5.3. Applying Bayes Theory to Fatigue Testing ..... 134

2.5.4. Construction of joint posterior for fatigue strength testing ..... 135

2.5.5. Applying Bayesian maximum entropy sampling to fatigue data ..... 138

2.5.6. Discretisation of the Prior ..... 141

2.5.7. Choice of Initial Prior ..... 142

2.5.8. Bayesian Staircase Protocol ..... 143

2.5.9. Bayesian Step Protocol ..... 147

2.5.10. Statistical Model Selection ..... 152

2.5.11. Comparing Protocols and limitations ..... 154

2.5.12. Extension to PSN Curves ..... 157

2.5.12.1. A note about Propagation ..... 168

2.5.13. PSN Single-Stress Protocol ..... 168

2.5.14. PSN Multiple Stress Protocol ..... 171

2.6. Experimental Results ..... 175

2.6.1. Results of Foil 3&4 ..... 175

2.6.2. Results of Foil 7-11 ..... 195

2.7. Discussion ..... 206

2.8. Conclusion ..... 217

3. Project Conclusions ..... 219
4. References ..... 221
5. Appendix ..... 245
5.1. Metallographic Preparation ..... 245
5.2. Nanoindentation Mapping Supplementary Details ..... 246
5.3. Nanoindentation Stiffness Measurement ..... 252
5.4. Fatigue Sample Holder Machining ..... 255

## b. Abstract

Recent developments in manufacturing technology have enabled a wealth of designs to be created and implemented in engineered products. These methods, empowered in part through data-driven approaches to materials processing, have optimised the structure of additive products and refined the processes for complex joining technologies. However, in doing so they radically change the material structure, often introducing strong local heterogeneity either by design or by consequence. A commensurate local understanding of the material and its behaviour at relevant length scales is necessary in order to ensure these parts live up to the stringent requirements in demanding or safety critical applications. Two methods are developed to contribute to this effort, with data-driven approaches to similarly accelerate the development cycles described above.

The effect of microstructure on the mechanical behaviour is investigated with these methods using a Ti-64 linear friction welded (LFW) joint as a case study. The LFW joint contains a highly varied microstructure, from the globular alpha and bimodal structures in the parent material on either side to the Widmänstatten structure found near the weld-line. The weld-line itself is known to be highly crystallographically textured, with a preference for the c axis to align with the transverse direction. The local static and dynamic material properties from the bulk microstructures to the

refined and textured weld-line have been explored through nanoindentation and a novel meso-scale fatigue method.

Local static properties are determined through correlated nano-indentation mapping and Electron Back Scatter Diffraction (EBSD), providing rapid structure property assessments. Local fatigue properties are explored with a Bayesian Optimised data collection protocol and novel meso-scale ultrasonic fatigue test, permitting the efficient sampling of fatigue behaviour of weld-line material. These two methods provide new methods and datasets for assessing the properties of advanced manufactured materials, reflecting established knowledge and novel quantitative comparisons in the case study described.

## c. Publications

The following published and pre-printed articles result from the work done during this project. Those written as first author appear prominently in the text of this thesis.

- P. S. Karamched, Y. Xiong, C.-T. Nguyen, D. M. Collins, C. M. Magazzeni, and A. J. Wilkinson, “Weighted ellipse fitting routine for spotty or incomplete Debye-Scherrer rings on a 2D detector,” *Prepr. J. Appl. Crystallogr. A J. Int. Union Crystallogr.*, arXiv 2021.
- CM Magazzeni, R Rose, C Gearhart, J Gong, AJ Wilkinson, ”Bayesian Optimised Collection Strategies for Fatigue Testing: Constant Life Testing”, *Prepr. Fat. & Frac. of Eng. Mat. & Struc.*, arXiv *2021*
- C. M. Magazzeni, “Towards a Local Property Assessment of Materials,” *J. Eng. Integr. Soc.*, no. 51, pp. 34–36, Sep. 2021.
- Y Xiong, P Karamched, CT Nguyen, DM Collins, N Grilli, CM Magazzeni, E Tarleton, AJ Wilkinson, ”An in-situ synchrotron diffraction study of stress relaxation in titanium: Effect of temperature and oxygen on cold dwell fatigue”, *Acta Mater.*, vol. 213, p. 116937, Jul. 2021

- HM Gardner, P Gopon, CM Magazzeni, A Radecka, K Fox, D Rugg, J Wade, DEJ Armstrong, MP Moody, PAJ Bagot, ”Quantifying the effect of oxygen on micro-mechanical properties of a near-alpha titanium alloy”, *J. Mater. Res.*, vol. 36, no. 12, pp. 2529-2544, Jan. 2021
- CM Magazzeni, HM Gardner, I Howe, P Gopon, JC Waite, D Rugg, DEJ Armstrong, AJ Wilkinson, ”Nanoindentation in multi-modal map combinations: A Correlative Approach to Local Mechanical Property Assessment”, *J. Mater. Res.*, vol. 36, no. 11, pp. 2235–2250, Jan. 2021
- NTH Farr, SF Hamad, E Gray, CM Magazzeni, F Longman, DEJ Armstrong, JP Foreman, F Claeyssens, NH Green, C Rodenburg, ”Identifying and mapping chemical bonding within phenolic resin using secondary electron hyperspectral imaging”, *Polym. Chem.*, vol. 12, no. 2, pp. 177–182, Jan. 2021
- Y Xiong, P Karamched, CT Nguyen, DM Collins, CM Magazzeni, E Tarleton, AJ Wilkinson, ”Cold Creep of Titanium: Analysis of stress relaxation using synchrotron diffraction and crystal plasticity simulations”, *Acta Mater.*, vol. 199, pp. 561–577, Oct. 2020
- A Reza, CA Dennett, MP Short, JWaite, Y Zayachuk, CM Magazzeni, S Hills, F Hofmann ”Non-contact, non-destructive mapping of thermal diffusivity and surface acoustic wave speed using transient grating spectroscopy”, *Rev. Sci. Instrum.*, vol. 91, no. 5, May 2020.

## c.I. Conferences

- Engineering Integrity Society - Fatigue 2021
    - Speaker: ”Local Fatigue Property Assessments of Linear Friction Welds”, *March 2021*
- The Welding Institute - East Midlands Branch Meeting

- Invited speaker: ”Local Property Assessments of Linear Friction Welds” *March 2020*

- Nanobruken Nanomechanical Testing International Conference
  - Speaker: ”Multi-dimensional property correlation with Nanoindentation Mapping”, *February 2020*
- Engineering Integrity Society - Additive Manufacturing Workshop
  - Organiser, *June 2019*
- The Materials Society International Conference 2019
  - Speaker: ”Local Property Assessments of Linear Friction Welds”, *March 2019*
- Hexagonal Materials HEXMAT 2018
  - Speaker: ”Local Property Assessments of Ti-64 Linear Friction Welds”, *September 2018*

## d. Glossary of Terms

- Ti-64: Titanium 6 weight % Aluminium 4 weight % Vanadium
- CP: Commercially Pure
- HCP: Hexagonally Close Packed
- CRSS: Critically Resolved Shear Stress
- LFW: Linear Friction Weld(ing)
- HAZ: Heat Affected Zone
- SEM / TEM: Scanning Electron Microscope / Transmission Electron Microscope
- FEG: Field Emission Gun
- EBSD: Electron Back-Scattered Diffraction
- GND: Geometrically Necessary Dislocation
- CSM: Continuous Stiffness Measurements
- MIC: Microscope to Indenter Calibration

- ECC: Enhanced Correlation Coefficient
- EDM: Electro-Discharge Machining
- EP: Electro-Polishing
- IPA: Iso-Propyl Alcohol
- LCF / HCF / VHCF: Low Cycle Fatigue, High Cycle Fatigue, Very High Cycle Fatigue
- SN: Stress and Number of cycles
- PSN: Probabilistic SN
- PCA: Principal Component Analysis
- MAP: Maximum *A Posteriori* Probability
- HPD: High Posterior Density
- BIC: Bayes Information Criterion
- CDF/PDF: Cumulative Distribution Function / Probability Distribution Function
- (CP)-FEM: (Crystal Plasticity)-Finite Element Modelling
- FIP: Fatigue Indicator Parameter
- CAD: Computer Aided Diagram

# I. Introduction

## I.I. Background

*Parts of this section are adapted from the Literature Review submitted earlier as part of this thesis project, as well as from the article titled "Towards Local Property Assessment of Materials" published by the Journal of the Engineering Integrity Society in September 2021* [1].

The past few decades have seen the rapid development of new manufacturing techniques and applications. The rise of this Industry 4.0, or more specifically advanced manufacturing, has enabled new designs and better performing materials for a wide range of applications [2]–[4]. Additive manufacturing has allowed for vastly complex designs ranging from hollow structures for waveguides to structural components with optimised shapes [5]–[8]. Friction welding (Figure 1) or composite materials have enabled materials with improved structural performance coupled with reduced design limitations [9]–[13]. As we incorporate more complex processes, either through improved physical technology or through the incorporation of more advanced analytical methods such as Artificial Intelligence/Machine Learning (AI/ML), our focus becomes ever refined and small-scale.

Two major driving forces can be thought of as pushing us in this direction: the drive for broadening a design space that is inaccessible through subtractive manufacturing and the drive for producing materials with better properties. With more rapid development cycles, we are beginning to see prototypes of materials that have combined both exotic structures and shapes as well as internal material (micro-) structure [14]–[17] – an application of Industry 4.0 on material microstructure itself. Our components and constitutive materials are becoming tailored to the desired designs and properties. Conventional approaches to quality assessment have the opportunity to experience a similar transition. In light of both faster prototyping of new processes, as well as increasing complexity, testing methods can be developed that explore shorter length scales whilst providing scalable insights [18], [19].

Consider a material system used in advanced and high value engineering applications: titanium alloys. As a result of its high strength, low density, and good corrosion resistance, titanium alloys are frequently found in the aerospace industry (for use in aero-engines or structural components), architectural cladding, and the medical and chemical industries [20]. These qualities have motivated their use in the above advanced manufacturing methods.

This thesis will explore methods to determine local property of advanced manufactured titanium, using a case study of a linear friction weld.

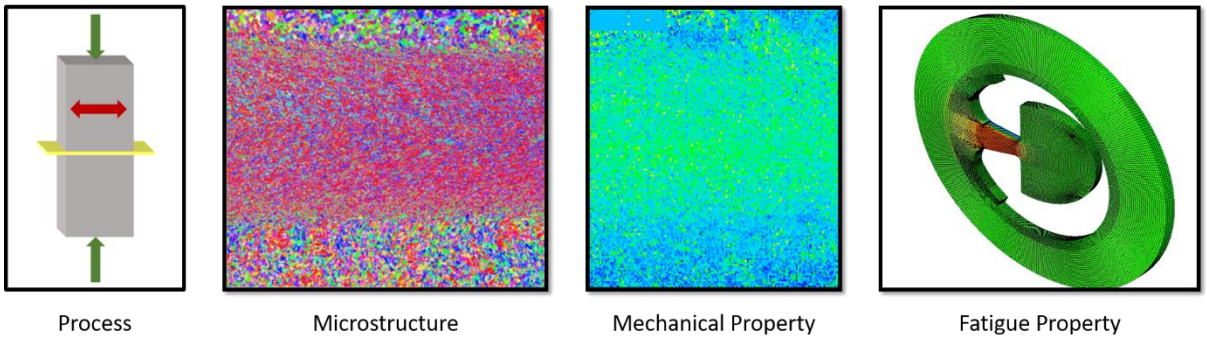



*Figure 1: Visual summary of the works in this thesis. From left to right: first panel: Linear Friction Weld process, visualised as two parent material blocks (grey) under forging pressure (green arrow) and oscillation (red arrow) producing a solid-state flash (yellow). Second panel: EBSD out of plane inverse pole figure map of microstructure of LFW process, showing weld-line in the centre. Third panel: nanoindentation hardness map of the same area. Final panel: simulation of stress induced in laser cut meso-cantilever.*

### I.I.1. Titanium

Prior to discussion on manufacturing and testing methods, the basic materials science of titanium and its alloys will be discussed. The mechanical behaviour of titanium is intimately linked to that of the wider class of Hexagonal Close Packed (HCP) materials. In HCP materials, the $(0001)$ basal, $\{10\bar{1}0\}$ prismatic, and the $\{10\bar{1}1\}$ pyramidal are all active slip systems, with the $\frac{a}{3} < 11\bar{2}0 >$ or <a> directions being close-packed. Due to its crystal symmetry, the elastic and plastic mechanical responses of HCP materials are highly anisotropic: slip directions in the basal plane do not lie at right angles, and <a> type Burgers vectors are different lengths to <c+a> [21]. This affects the energy barrier for the motion of different slip planes, imparting anisotropy in strength and critically resolved shear stress (CRSS).

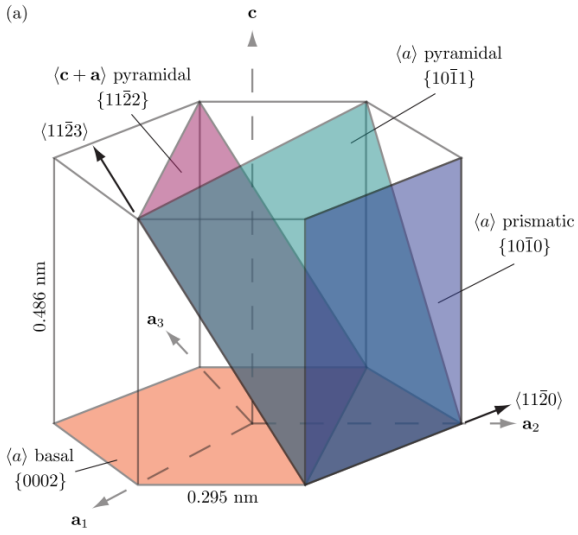



*Figure 2: Available slip systems in a hexagonal unit cell, from the thesis of Dr. Chapman* [22].

In HCP materials, ductility is fulfilled through twinning mechanisms or crystalline slip on the four slip plane families on which the line vector and the Burgers vector can lie, summarised in Table 1.

*Table 1: Table adapted from Lutjering & Williams: "Slip systems in the hexagonal alpha phase"* [20]*, including CRSS values.*

| Slip System Type | Burgers Vector Type | Slip Direction | Slip Plane | Total No. of Slip Systems | | CRSS at RT /MPa |
|---|---|---|---|---|---|---|
| | | | | Total | Independent | |
| 1 Basal | $< a >$ | $< 11\bar{2}0 >$ | $(0002)$ | 3 | 2 | 180 |
| 2 Prismatic | $< a >$ | $< 11\bar{2}0 >$ | $\{10\bar{1}0\}$ | 3 | 2 | 225 |
| 3 Pyramidal | $< a >$ | $< 11\bar{2}0 >$ | $\{10\bar{1}1\}$ | 6 | 4 | - |
| 4 Pyramidal | $< c + a >$ | $< 11\bar{2}3 >$ | $\{11\bar{2}2\}$[1] | 6 | 5 | 800 |

The anisotropy in stiffness of HCP materials can also be seen in experiments showing the relationship of Young's modulus to declination angle (the angle of the stress axis to the c axis), as seen in Figure 3.

[1] The activation of the $\{11\bar{2}2\}$ slip plane is an active question: some experiments show discrepancy in the activation of this plane in tension vs compression, with instead an activation of the first order $\{10\bar{1}1\}$.

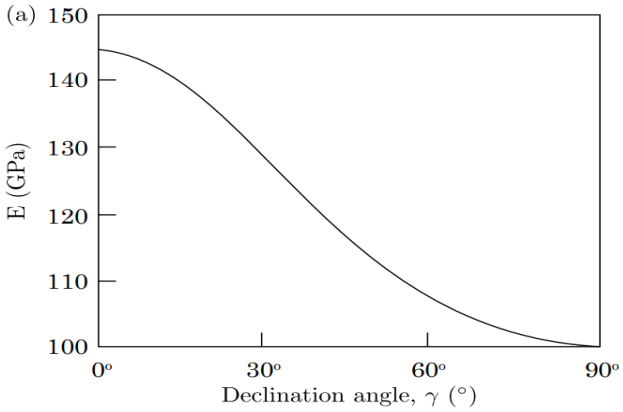



*Figure 3: Graph from Lutjering* [20] *showing the relationship between Young's Modulus and declination angle of the tensile axis and the c axis in alpha titanium.*

The mechanical behaviour is also heavily dependent on alloying. The four classical methods of alloy hardening are: precipitation hardening, dislocation density hardening, solid solution hardening, and boundary hardening. In the case of commercial titanium alloys, precipitation and solid solution hardening are both present regardless of the alloying content [20]. The effect of different alloying on the hardness of titanium alloys can be broadly accounted as the effect of alpha-phase or beta-phase stabilisers present. In the alpha phase, it is "significantly hardened by the interstitial element oxygen" [20]. For example, the yield stress in titanium with 0.18% oxygen and 0.4% oxygen is 170MPa and 480 MPa, respectively [20]. In the case of other alpha stabilising alloying elements such as aluminium, zirconium, and tin, there is also an increase in hardness due to their large size and high solubility [23]. It can also be seen that deformation mechanisms change with alloying content, for example: "Williams *et al* showed that alloying with Al increases the CRSS for <c+a> slip but inhibits twinning more" [21], [24], and as of 6% Al content, twinning is not seen as a deformation mechanisms at all in the literature[2] [22]. As the presence of alpha stabilisers generally produces the same effect, and due to aluminium's importance as a primary

[2] Indications of twinning in Ti-6Al-4V have been observed in the Micromechanics group at Oxford, though this result has not been published.

alloying element, the effect of these alpha stabilisers can be compared through the use of an "equivalent aluminium content", noted by Rosenberg [25]:

The elements which are highly soluble in the beta phase, so-called "beta-stabilisers", are: molybdenum, vanadium, tungsten, niobium, tantalum, chromium, nickel, cobalt, and iron. Often, titanium engineering alloys with a mixed microstructure (so-called "near alpha" or alpha/beta microstructures) can often be split into several categories based on characteristic microstructures: lamellar, bimodal, and globular alpha (though these are often restricted to discussions on alpha/near alpha alloys). Example micrographs of such microstructures are given in Figure 4. Lamellar structures are characterised by high fatigue crack propagation mitigation and fracture toughness [26], though bimodal structures are more resistant to fatigue crack initiation. There is a need for modern analysis on the effect of microstructure on fatigue crack initiation and propagation in globular alpha titanium, a microstructure often found in the fan blades of aero-engines.

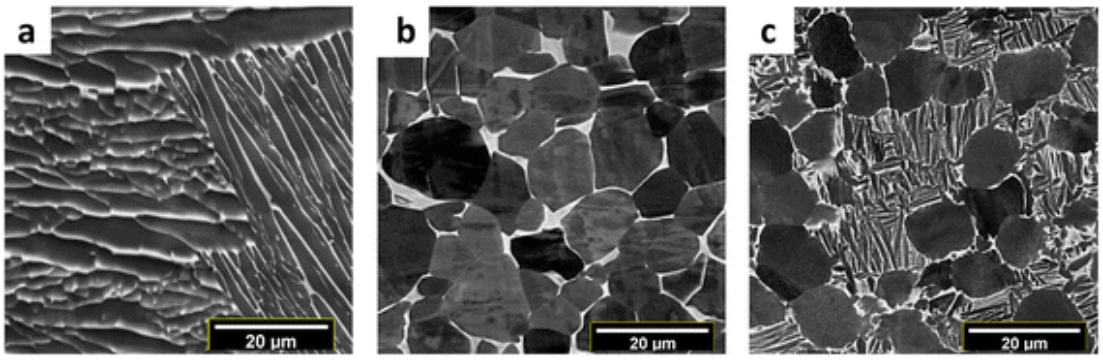



*Figure 4: Example micrographs of titanium microstructures from Salem et al.* [19]*: "a) fully lamellar microstructure, b) fully equiaxed [alpha/near-alpha] microstructure, and c) bi-modal microstructure".*

In the aerospace industry, one of the most commonly used alloys is titanium 6 wt. % Al 4 wt. % V (Ti-64). This alloying content "has an exceptional good balance of strength, ductility, fatigue, and fracture properties" [20]. In the case of aircraft parts, this alloy offers significant weight savings compared to structural steels due to its high strength to weight ratio (up to 40% weight savings from steels [27]), high corrosion resistance due to its protective oxide layer [20], and fatigue properties [27].

## I.I.2. Characterisation Methods

### I.I.2.1. EBSD

In 1928, Japanese physicist Seishi Kikuchi observed diffraction bands in Mica [28], emanating from diffuse scattering of the electron beam on a targeted crystal. Electron beam backscattered diffraction (EBSD) has since been developed to produce orientation maps by Adams *et al* [29], and Krieger-Lassen *et al* [30], whereby a real-space image of a sample is composed of a collection of diffraction patterns containing the orientation information at a given point. The benefit of this technique over TEM-based electron diffraction or x-ray diffraction is the "versatility in mapping orientation, crystal type, and perfection over a wide range of step sizes" [31]. In current setups, this is done in an SEM with a bulk sample tilted to a high angle in order to maximise the number of backscattered electrons leaving the surface of the sample [32].

The patterns produced are gnomonic projects of the Kikuchi bands on the detector screen [33], which can be represented as a subset of a sphere made up of Kikuchi bands, an example shown in Figure 5.

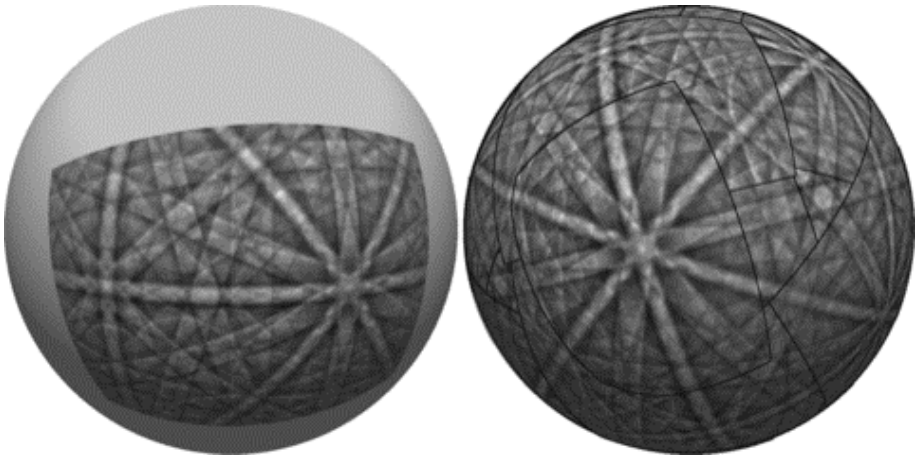


*Figure 5: Figure from A.P. Day* [34] *"showing a single experimental EBSP (electron back-scattered pattern) mapped on to the surface of a sphere (left) and several montaged EBSPs (right) shown with black outlines", showing the sphere of bands emanating from a diffraction point in the centre.*

The orientation can be determined from indexing the bands and their location relative to the pattern centre [33]. It was subsequently shown by Quested *et al.* [35] that within a grain of a given crystallographic orientation, a shift or a rotation in the EBSP corresponds to a strain, or deformation, in the crystal. In a series of papers by Wilkinson, Meaden, and Dingley [36]–[39], this method was greatly improved upon using cross-correlation techniques, allowing for the precise determination of strain tensor elements to $\pm 10^{-4}$ [40]. This was quantified to provide a strain map for the sample, followed by a map of geometrically necessary dislocation (GND) density with developments from Jiang *et al* [41], Calcagnotto *et al* [42], and Pantleon *et al* [43].

At the onset of plastic deformation, "GNDs are generated rapidly and at some point will exceed SSD [statistically stored GND] density and […] dominate work-hardening processes" [44]. It has shown to be related to the past processing history of materials affecting their behaviour, such as in hot-rolled Ti-64 [45], and in understanding complex mechanisms in stress corrosion cracking (SCC) [46]. Determination of GND density is also an important tool for understanding the plastic response of materials from any source of stress [47], [48]. This technique has proven invaluable in the understanding of microstructural features to mechanical properties, through observing the microstructural effects of testing such as fatigue [49], [50], and selecting individual features for nano-indentation or micro-cantilever work [51], [52].

### I.I.2.2. Micromechanical Testing

Since the 1950s it has been observed that the mechanical properties of materials are affected by the scale of testing volumes. It was first observed that as the grain size decreased, the yield strength of bulk test specimens increased, through the relationship in equation (1):

$$\sigma_{LYP} - \sigma' \propto d^{-\frac{1}{2}} \qquad (1)$$

$\sigma_{LYP}$ is the stress of the lower yield point, $\sigma'$ is the yield stress for a single crystal, and $d$ is the grain size [53]–[55]. While it has recently been shown that the data on which the Hall-Petch

equation is based can be fitted with a wide range of power laws [55], the hardening of the material can be explained from the obstruction of dislocation motion due to a higher density of grain boundaries (and hence a higher number of grains per unit volume).

Oliver and Pharr provided the fundamental work describing the size effects and considerations necessary when carrying out nano-indentation tests [56], [57] and further work from Fleck *et al* [58] noted that the hardening of materials also occurred when the extrinsic size of the specimen was reduced. Experiments were carried out where wires of decreasing size were torsionally deformed, resulting in an observed "strain gradient hardening": "a few volume percent of micron scale non-deforming particles dramatically raises the rate of work hardening in metals, those of millimetre [sic] scale do not" [58]. With the advancements in focussed ion beam (FIB) technology, it has been possible to probe mechanical behaviour of isolated materials on the sub-millimetre and sub-micron scale.

Many of these experiments have been enabled by the development of instrumented nanoindenters, which use electro-magnetic coils to apply and measure forces on a diamond (or other) indenter tip [59]. This method is discussed in detail in the Nanoindentation chapter on page 27. When considering any of these micro-mechanical tests, however, it is therefore important to carefully consider the scalability of results, relating them to bulk values. This effect in micro-scale mechanical testing was observed by Uchic [60], wherein various sized micro-pillars were tested in micro-compression tests showing a marked influence of pillar width on the yield strength and the slip behaviour. A figure from this paper is shown in Figure 6.

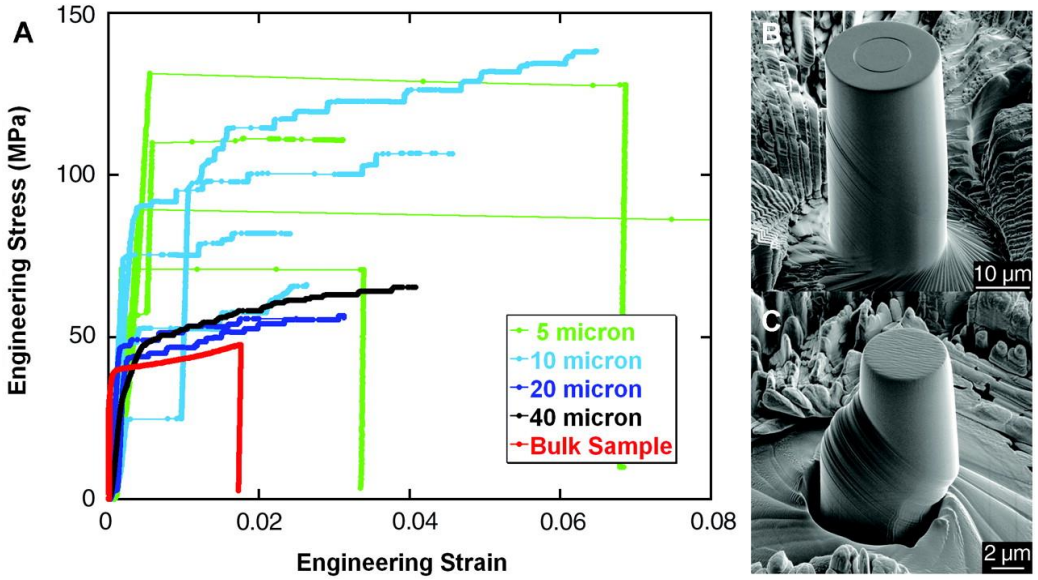



*Figure 6: Figure from* [60]*, showing the relationship of pillar size with the behaviour in a stress strain curve in single crystal nickel. Two examples of pillars are shown on the right hand side, with a wider 10um pillar (top right) showing minimal slip banding, and the smaller 2um (lower right) showing a high degree of slip.*

This effect has even been investigated *in situ* with a nano-scale compression test viewed in a TEM to directly observe the "one-to-one relationship between the mechanical data and the microstructure evolution" [61].

Micromechanical testing has provided understanding of phenomena occurring in a material on small length-scales, but also strongly affects bulk properties. For example, the diffusion of oxygen and nitrogen in titanium causes so-called “alpha-case”: a more brittle outer layer of material causing the component to be prone to crack initiation. In a comprehensive report by Rugg *et al.*, micromechanical testing methods such as nano-indentation, micro-cantilevers, and atom probe tomography were used in order to quantify the extent of alpha case in heat treated Ti-64 in engineering components [62].

In order to better understand these effects, a crystal plasticity finite element modelling (CPFEM) method was developed by Roters *et al* [63], seeking to model these systems through phenomenologically derived laws using computational methods. This has led to a series of papers by Dr. J Gong, where a combination of experimental micro-cantilever work and CPFEM has provided data for the CRSS of individual slip systems in single crystal alpha-titanium [64]–[67]. Of

particular interest and relevance to this project is Dr. Gong's work on micromechanical fatigue specimens: using milled microcantilevers to carry out either repeated indentation [65], or high-cycle acoustically induced fatigue [68].

The above work would not have been possible on bulk samples due to the scale of local features (in some cases microstructure, in others, chemical composition). Methods such as these micro-experiments and CPFEM, as well as the comparison of results to bulk-obtainable data are key in enabling this scalable local understanding, as demonstrated in the above work.

### I.I.3. Linear Friction Welding

Recent developments in manufacturing technology have allowed for the joining of non-axisymmetric parts through linear friction welding (LFW). This technique is a solid state joining process where two parts are rapidly fretted in a linear reciprocating motion, generating frictional heat and plastic deformation. A force is applied normal to the interface throughout the process, forcing some material out, described as "flash", removing oxides and impurities, and the two plasticised surfaces are welded together [69]. A basic diagram depicting this process is found in Figure 7. In the context of aircraft manufacturing, this allows the fan blades to join to the fan disk, removing the need for a bulky mechanical lock. This causes significant weight savings (up to 30% in some components [70]), and removes fretting damage which can lead to fretting fatigue failure [71]. In addition, this process has many benefits over conventional welding methods such as: the ability to weld dissimilar metals, the lack of molten pools causing "solidification defects (e.g. hot cracking, porosity, segregation, etc)" [72], [73], the self-removal of surface oxides and contaminants, and the high reliability of the process route [73].

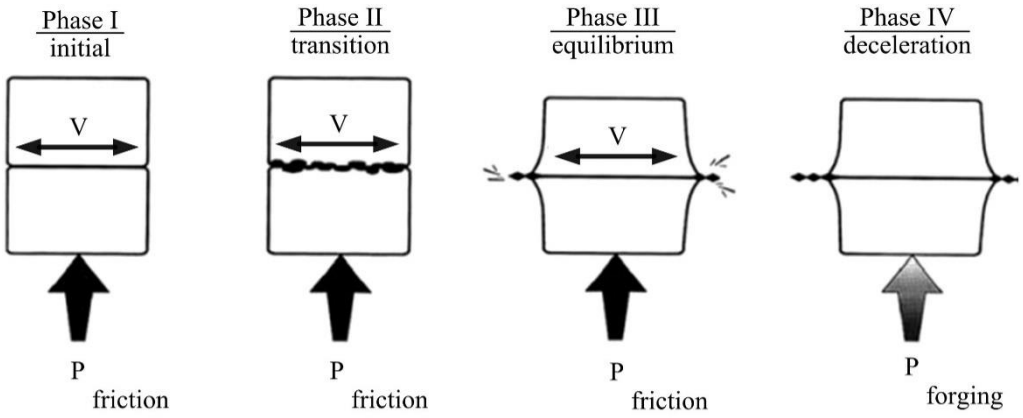



*Figure 7: Diagram from* [74] *showing the basic process of linear friction welding divided into four phases.*

As a result, LFW technology has been closely studied and modelled in order to best optimise the process for highly durable components [70], [75]–[79]. Efforts have been made in order to remove voids and remnant oxides trapped within the weld [80]. Various studies on the fatigue properties of friction welded Ti-64 have been performed, showing higher fatigue strength in weld regions [79], with many observing failures in parent material [81], inclusions and foreign bodies, or surface defects [82]. There is a need to investigate more closely the fatigue properties of LFW welds through the isolation of individual features (the weld zone against the parent material): the microstructure of linear friction welds have high local variation on a scale of several tens of microns, as seen in Figure 8.

Following the improvement of the LFW process to remove process-driven defects and inclusions, the limiting factor to fatigue life may arise from the microstructure: these regions need to be studied individually in a micromechanical context in order to determine the behaviour of the microstructures themselves.

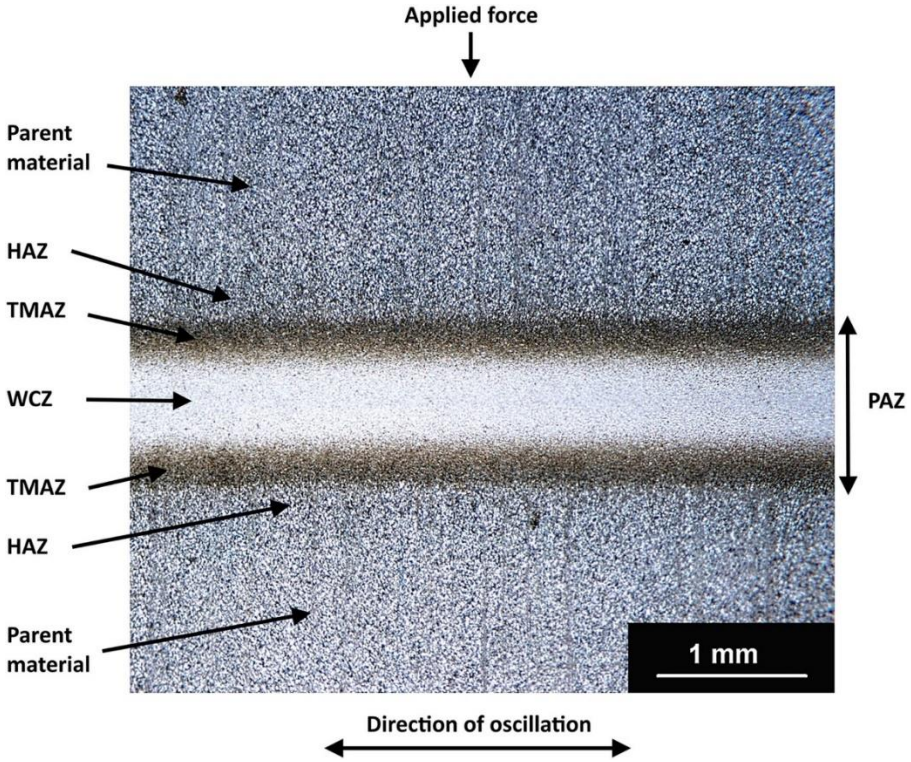



*Figure 8: Microstructure of a Ti-64 LFW weld from [83], showing a highly refined microstructure in the middle of the weld, a deformed region, and the unaffected parent material. The distance between the middle of the weld and the parent material is roughly 0.5 mm.*

## I.II. Case Study – Ti-64 LFW

The material of study is a Ti-64 linear friction weld sourced from Rolls-Royce plc. Two rectangular sections of material of dimensions 4.2 x 20 x 2 cm each are welded the narrow and long axis, with each parent material similar to that of blade and disk material in a jet engine's compressor section. While both are Ti-64, the microstructure differs: the blade-similar material is alpha/globular, while the disk-similar material is bimodal. Figure 9 shows a photograph of the material, while Figure 10 shows micrographs of the relevant microstructures.

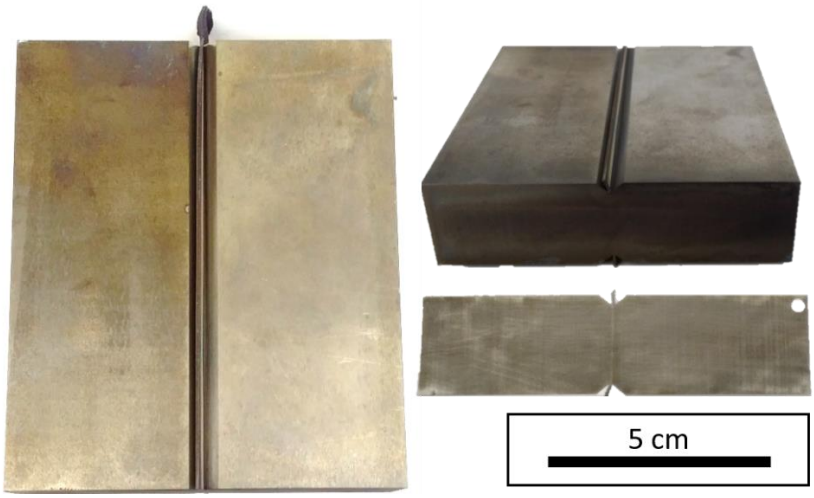



*Figure 9: Photographs showing half the Ti-64 LFW block from the top (Left), angled, (Top Right), and side-on (Bottom-Right).*

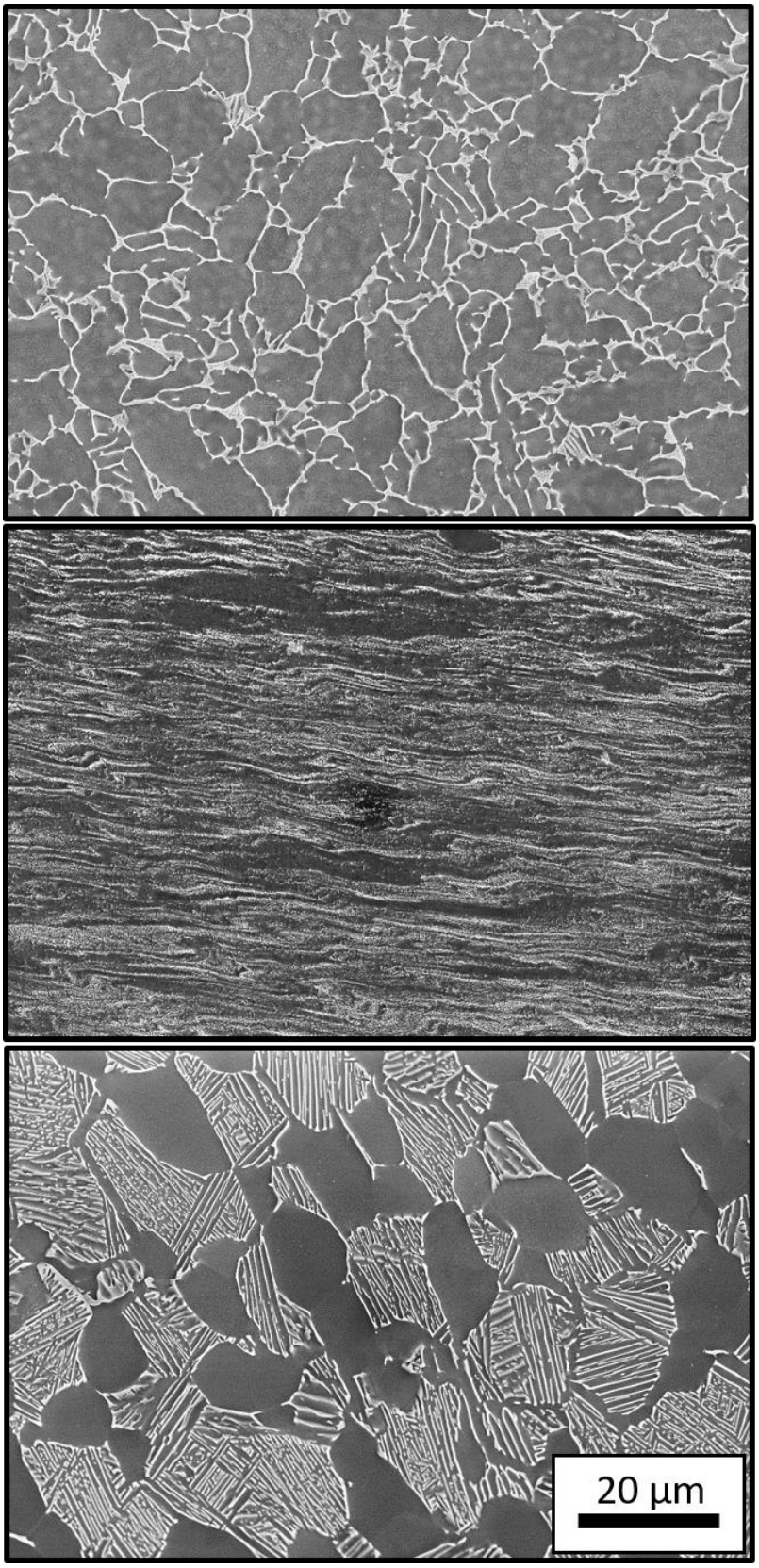



*Figure 10: Micrographs of the linear friction weld specimen, showing the blade-representative material (Top), the centre weld-line (Middle), and the disk-representative material (Bottom). Micrographs collected on the Zeiss Merlin FEG-SEM at 1000x magnification, and 30 kV. The light-coloured phase is the beta phase, while the dark coloured phase is the alpha. Sample was electropolished using routine detailed in XXX.*

The parameters of the weld are proprietary and are not the subject of this investigation. However, the project's motivation stems from the use of similar welds used in the Intermediate Compressor section of Trent XWB engines, enabling significant weight savings.

In addition to the strong grain refinement, the weld-line is also highly textured – EBSD data shown in Figure 11 of the same region as in Figure 10 shows an out of plane inverse pole figure (IPFZ), with pole figures for weld and parent material showing the strong texture element.

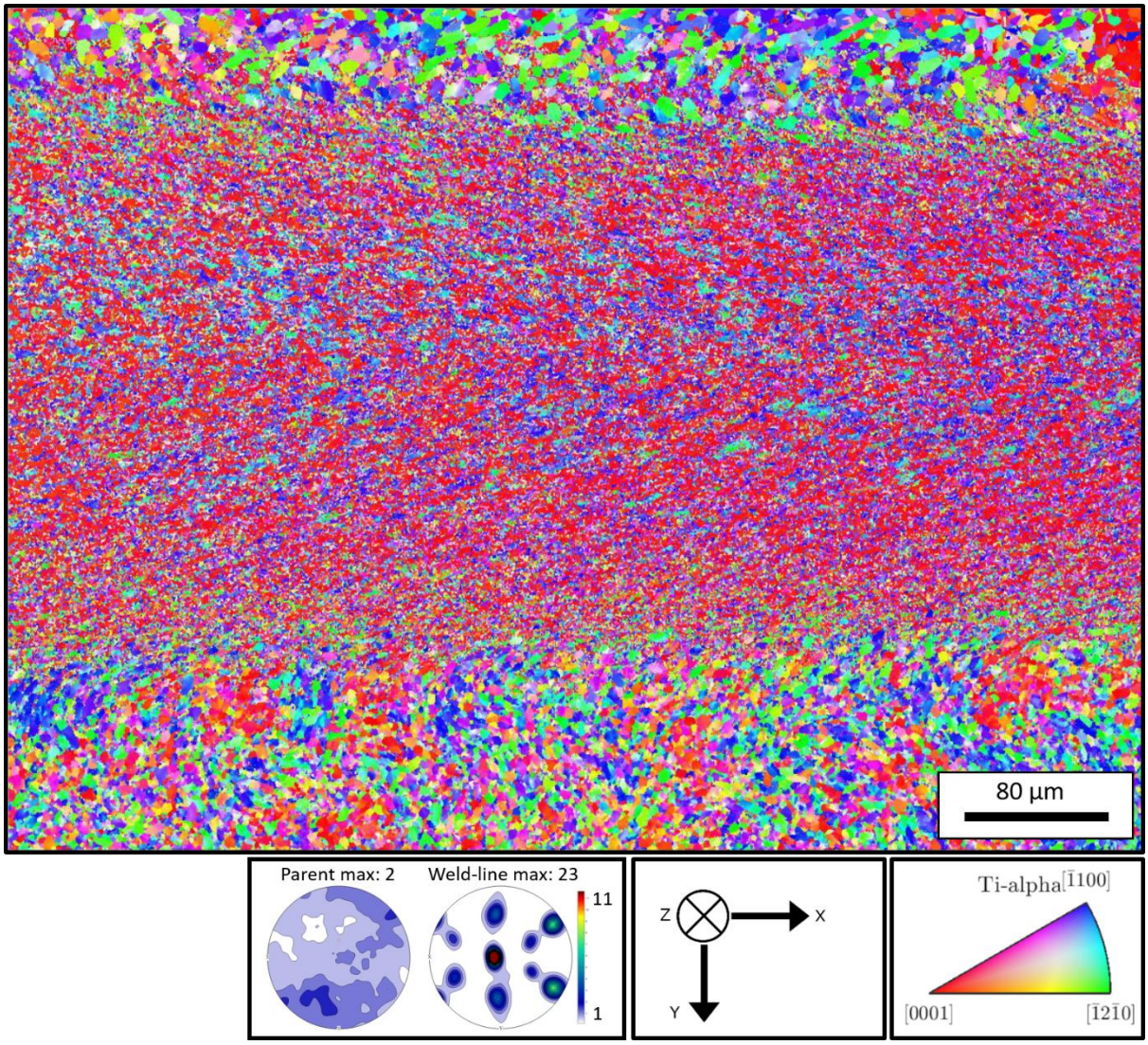



*Figure 11: EBSD IPFZ figure of the Ti-64 LFW sample weld-line collected on the Zeiss Merlin FEG-SEM, showing the refined grain structure and strong texture component in the centre. Bottom row shows (left to right): Pole figure for parent and weld-line, with a maximum value of 2 and 23 respectively, axes directions, and pole key for alpha phase. Beta phase omitted due to low number of sample points.*

The mechanical property can also be evaluated both through conventional micro-indentation hardness tests, with early results by the author seen in Figure 12 showing strong local property variation. This material description, alongside those in the section above and in the chapters, provide the basis for the results discussed in each chapter.

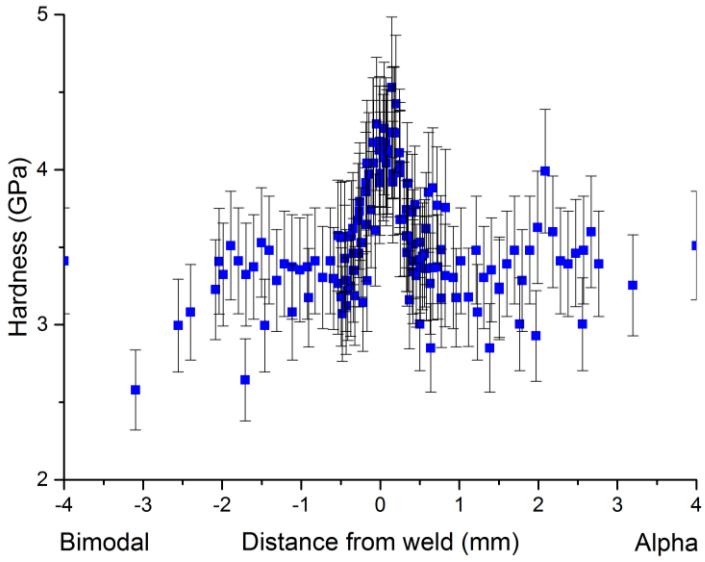



*Figure 12: Vickers micro-indentation tests to investigate the hardness across the Ti-64 weld-line.*

The thesis will subsequently be divided into the following chapters:

- Nanoindentation Chapter: development and results of a method to correlate multi-modal static property data at microstructurally relevant length scales.
- Fatigue Chapter: development and results of both an experimental method for obtaining meso-scale fatigue data of weld-line material and a novel protocol for its efficient collection.

# 1. Chapter 1: Static local property assessment through multi-modal mapping

*This chapter is adapted from a publication in the Journal of Materials Research under the title of "Nanoindentation in multi-modal map combinations: A Correlative Approach to Local Mechanical Property Assessment"* [84]*, with amendments to apply this technique to the advanced manufactured Ti-64 LFW.*

## 1.1. Introduction

Over the past decades, significant advances have been made in techniques used to determine material properties on an ever finer length scale, allowing for a better understanding of basic material property-microstructure relationships [52], [56], [64]. These developments have provided crucial insight into fundamental materials science, facilitating more accurate multi-scale modelling [85]–[91], as well as the necessary property assessment for modern manufacturing processes with small features [15], [79], [92]–[95].

Researchers have used crystallographic techniques [33], [52], [96]–[98], composition measurements [31], [62], [99]–[101], and nanoindentation [62], [102], [103] amongst a variety of other techniques to determine local properties. As microstructural feature sizes become smaller, and systems more complex, there is a need for a distributed approach to understanding how multiple factors may affect one another, and in turn affect the viability of parts in complex service environments [62], [104].

Recent developments in nanoindentation instrumentation have enabled a wide range of experimental procedures, including more complex loading and sensing regimes such as strain-rate experiments to measure the effect of indentation rate [105]–[107], and more complex specimen preparation techniques such as micro-pillar compression to isolate microstructural features [108]–[112]. A recent addition to the tools available for local mechanical property assessment has been the development of rapid nanoindentation mapping: mechanical property maps of

hardness and modulus can be obtained that resolve micron-scale microstructural features [113]–[115], and create, at an unprecedented rate, large datasets for statistical analysis [116].

Work carried out using this technique has shown developments in distinguishing between phases in cement [116], [117], or dissimilar material coatings [114] through indentation alone and has enabled the collection of statistically significant datasets [114], [117]–[122]. Statistical clustering methods are available to classify data points and extract characteristic properties from a finite set of discrete phases. However, in microstructures where changes in local property are continuous, or are within a few tens of percent, alternative approaches requiring additional source signals need to be developed in order to de-convolute more nuanced structure-property relationships. There is scope to collect multi-dimensional datasets from microstructurally-rich materials that combine chemical, crystallographic, and mechanical data at high resolution. However, the challenge remains to correctly collect, correct, align, and correlate these very different properties.

Nanoindentation mapping contains an inherent trade-off between resolution and accuracy, manifested as the trade-off between indent spacing and depth. Deeper indents generally provide higher accuracy data of material bulk properties [123] though care must be taken when spacing indents close to one another as the plastic zone of one indent can affect the result of the second. This depth to spacing ratio has been discussed by Sudharshan Phani *et al.* [113], where a ratio of depth to spacing of 1:10 is recommended in nanoindentation maps. This directive on depth to spacing ratios alone does not imply any resolution limit in nanoindentation mapping. However, in combination with the above statement on shallow indent accuracy, the trade-off is: the smaller the indentation spacing, the larger the error in the data. This is either due to depth to spacing ratios approaching or lying below the above recommendation, or due to surface effects at shallow depths affecting bulk material hardness measurement [123]. Some experiments indicate that for nanoindents approximately 100 nm in depth, this error for each indent is larger than the

error from decreasing the depth to spacing ratio, justifying the use of a 1:7 ratio for certain experiments where high spatial resolution is desired.

In this chapter, a method is presented for directly correlating crystallographic data from Electron BackScatter Diffraction (EBSD), and mechanical properties data from nanoindentation. From this, multiple underlying factors of mechanical variation can be directly correlated, including variations in mechanical response as a function of crystal orientation or grain boundary effects.

The method and analysis is presented on two titanium test specimens: an equiaxed and weakly-textured commercially pure titanium system to show initial results, and the Ti-64 LFW system to highlight the capabilities of this system in rapidly obtaining structure property relations from complex systems at high resolution. Further datasets on oxygen diffusion profiles in titanium using chemical data from Wavelength Dispersive Spectroscopy of X-rays can be found in the publications linked to this method [84], [124].

## 1.2. Methods

### 1.2.1. Sample Preparation

Some preliminary measurements (dataset 0) were obtained from a fused silica sample, often used as a calibration material system for nanoindentation. The sample had been supplied by Goodfellow Ltd. and was used as polished, with results shown in the Appendix on page 246.

The first dataset was collected on grade 1 commercially pure titanium, supplied by Timet UK Ltd with an approximate size of 5x5x10 mm. The chemical composition, in weight percent, was: 0.07 oxygen, 0.035 iron, 0.012 carbon, 0.0035 nitrogen, and the remainder titanium [66]. The second dataset was collected on the supplied Ti-64 linear friction weld, cut with the face perpendicular to both the forging and welding direction.

Both specimens were metallographically polished until clear grain contrast became visible under a polarized light microscope. The method of preparing titanium samples embedded into Bakelite is described in the Appendix under Metallographic Preparation on page 245.

In dataset 1, a region of good quality polish towards the centre of the specimen was analysed, and in dataset 2, a region spanning the globular alpha parent material to the vicinity of the weld-line was studied. Each region of interest was demarcated by nano-indents or otherwise recognisable features and an EBSD map followed by a nanoindentation map were taken of the same approximate region. This sequence was chosen to minimise the effect of one measurement method onto the other: nanoindentation mapping as the most surface-destructive was performed last. The carbon contamination deposited via electron beam has been shown in preliminary experiments not to significantly affect nanoindentation readings performed at a depth of at least 100 nm.

### 1.2.2. EBSD mapping

EBSD data was collected on a Zeiss Merlin FEG-SEM at a beam energy of 15 & 20 keV for specimen 1 and 2 respectively, with a probe current of 10 nA. A Bruker e-Flash HR EBSD detector operated by Esprit 2.0 software was used to acquire the EBSD maps with patterns collected and saved at a resolution of 150 x 150 pixels. For specimen 1 the mapped area was 460 µm by 620 µm at a step size of 0.8 µm, while for specimen 2 a 420 µm by 1470 µm region was mapped at 1 µm spacing. The resolution and sampling density of EBSD is sufficiently high to identify relevant features such as grain morphology, and these are collected such that they are higher resolution than the nanoindentation maps. A discussion of this will follow in the Analysis Methodology section on page 32.

### 1.2.3. Nanoindentation mapping

An Agilent Technologies (now KLA Tencor) G200 nano-indenter system was used to collect nanoindentation maps using the Express Test option. This instrument can perform 1 indent approximately every 3.5 seconds allowing for the collection of thousands of indents overnight. These indents are performed in a regular array, creating a map where every pixel corresponds to one indent. The collection strategy combines a piezo stage for high-resolution spatial accuracy across small areas, and a stepper motor geared stage to allow for large collection areas, albeit

with relatively lower positional accuracy. As such, the overall array is formed of a collection of sub-arrays, herein named “bundles”, within which the piezo stage controls position. The stepper motor movements are used to locate the centre of each bundle, allowing them to be stitched together. A graphical representation of this map-population strategy is shown in the Appendix under Figure 116 on page 246.

For each indent the output data are values for maximum depth, load, modulus, hardness, and contact stiffness, instead of the conventional load-displacement curves collected in continuous stiffness measurements (CSM) [125], [126]. Though the load-displacement curve is not saved by the software in order to reduce file size, the modulus is calculated “on-the-fly” through the Oliver and Pharr method using a power-law fit on the unloading portion of the load-displacement curve [56]. The hardness is calculated through this stiffness-corrected contact depth using the same method [56]. This is in contrast to the more conventional CSM method used to validate measurements, possibly leading to the variations seen in these results.

Prior to discussions of analysis, the effect of thousands of indents on tip wear and calibration was considered. It is advisable for tip area functions to be re-calibrated regularly, either through direct means via atomic force microscopy measurement, or indirect means via indentation in reference material [127]. In common practice, this would often occur after several hundred indents had been performed at most, a time-scale that could span several months. However, the number of indents in nanoindentation maps can often be orders of magnitude larger, with no opportunity to calibrate during data collection. The persistence of the tip area function was therefore experimentally verified through an indentation map of over 33,000 indents on fused silica reference material, with the results shown in the Appendix on page 246. These results show with confidence that maps of several thousand indents can be performed without systematic errors greater than the random error inherent to this type of data.

Further to the tip calibration persistence test described above, a series of nanoindentation mapping tests were performed at depths of 100, 200 and 500 nm and compared to slower, conventional CSM tests at equivalent depths. The nanoindentation maps in these tests were conducted at a depth to spacing ratio of 1:10. In specimen 1, the nanoindentation map was performed at a fixed load of 3 mN, corresponding to an approximate depth of 200 nm, with an indent spacing of 2 μm. In specimen 2, the nanoindentation map was performed at a fixed load of 2.5 mN, corresponding to an approximate depth of 150 nm, with an indent spacing of 2 μm.

### 1.2.4. Analysis Methodology

The analysis method presented correlates spatially resolved property maps on a pixel-by-pixel basis. An experimental and analytical challenge lies in the correct registration of property maps obtained across a wide variety of means. In particular, aligning EBSD signal maps onto nanoindentation maps presents a challenge due to the marked difference in the method of signal collection. Though tilt correction is applied, EBSD collection is performed with electron beam incidence angle of 70 degrees, and a small angular deviation between the two reference frames on the specimen can lead to significant misalignment across maps [128]. In order to resolve this, geometrical transformations and interpolation are used to map all datasets onto the same grid of coordinates. The method presented takes the X and Y coordinates of the nanoindentation maps to be the most accurate coordinate frame.

The transformations are carried out individually, relating all other property maps to the nanoindentation map. Fiducial markers or easily identifiable features act as reference markers across the maps, and an affine transformation is performed on the property map to be registered. The use of the affine transformation assumes the presence of solely linear distortions in all other property maps, i.e. that all distortions are as a result of geometrical projections from collection angles. This implies that the distortion can be described as the sum of x and y translation, scaling, rotation, and shear alone. It is recognised that other, non-linear sources of distortion may be present. For example, mechanical drift during EBSD mapping could be non-linear. However, we

observe in the Results (discussed later on) that affine transformation accounts for the majority of discrepancy between mapping modalities used here at their current resolutions and collection timings. The best-fit affine transformations required to map the positional EBSD data onto the nanoindent reference axes were established by user identification of multiple corresponding points (at least four) within each dataset.

Following this, all property maps were interpolated in order to be scaled into an array the same size as the nanoindentation map. This often reduces the size of the dataset as nanoindentation mapping is not as high resolution as EBSD, but retains the confidence that information obtained from correlations arises from real indents performed on the local material at that point. A "nearest-neighbour" interpolation was used for EBSD datasets to avoid interpolating grain boundaries as smooth transitions. A discussion of this choice is given in the Discussion and Limitations section on page 44.

The same process can be applied to any further property map taken: the position information is transformed, and the property data interpolated appropriately such that a stack of maps is produced, each pixel containing a vector of property information for a given location. It is then possible to correlate individual property pairs by threading through the stack of maps.

A step-by-step guide is shown in the results of the first dataset. The code used for this analysis was written in MATLAB R2019a ® [129], with the code necessary to reproduce these results uploaded to a GitHub Repository named "XPCorrelate" under an MIT License: https://github.com/cmmagazz/XPCorrelate.

## 1.3. Results

### 1.3.1. Dataset 1 – CP Titanium

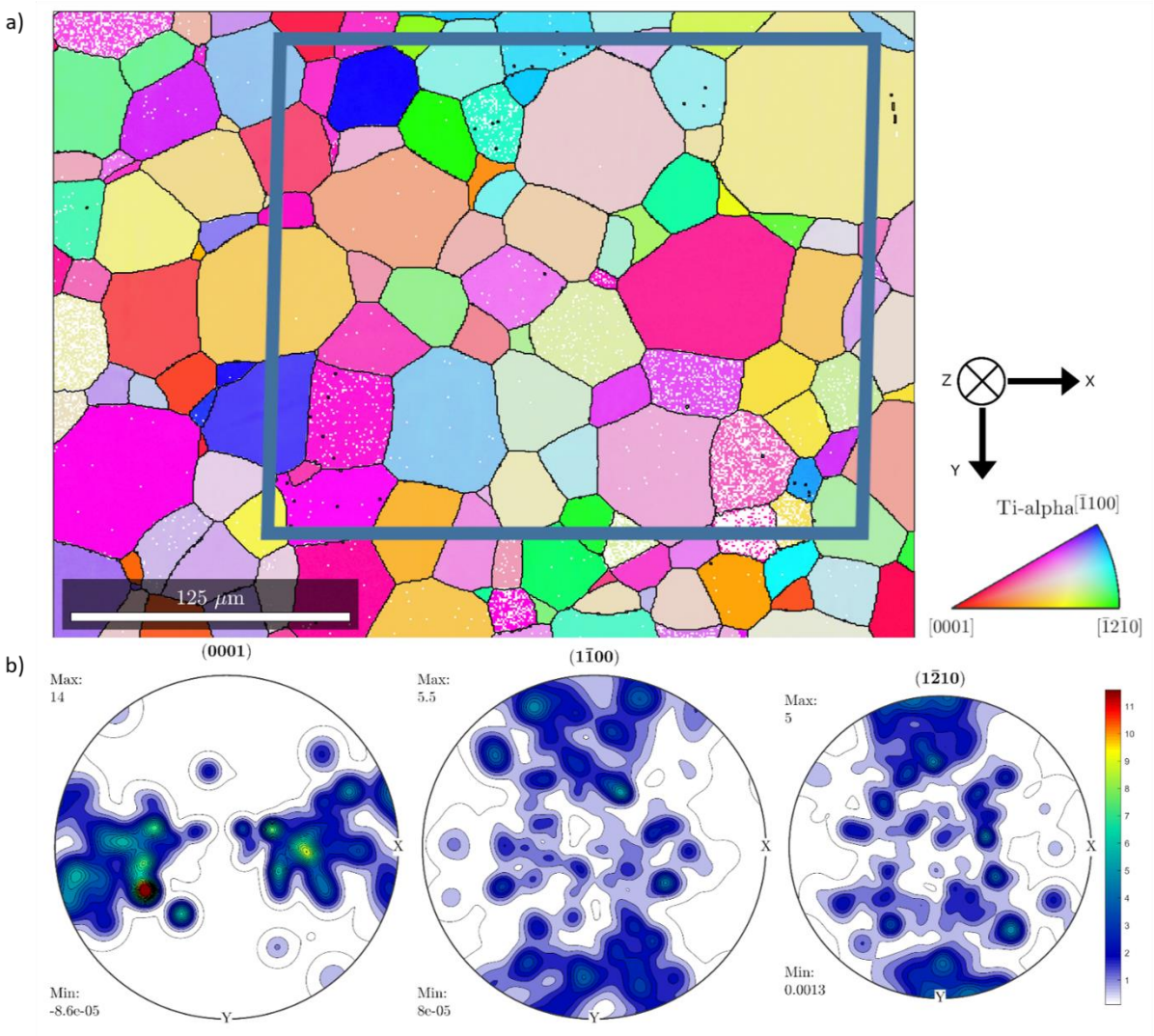



*Figure 13: a) IPFZ EBSD map of the CP titanium specimen with pole key and b) pole figure. Overlay indicates the approximate area to be nanoindented. Details of the mapping parameters are given in Section 1.2.2.*

Figure 13 shows EBSD data obtained from the commercially pure titanium specimen with equiaxed grains with a mean size of approximately 15 µm and weak texture, allowing for a full range of orientations to be probed. A nanoindentation map was then performed on the specimen within the region mapped by EBSD, with results shown in Figure 14.

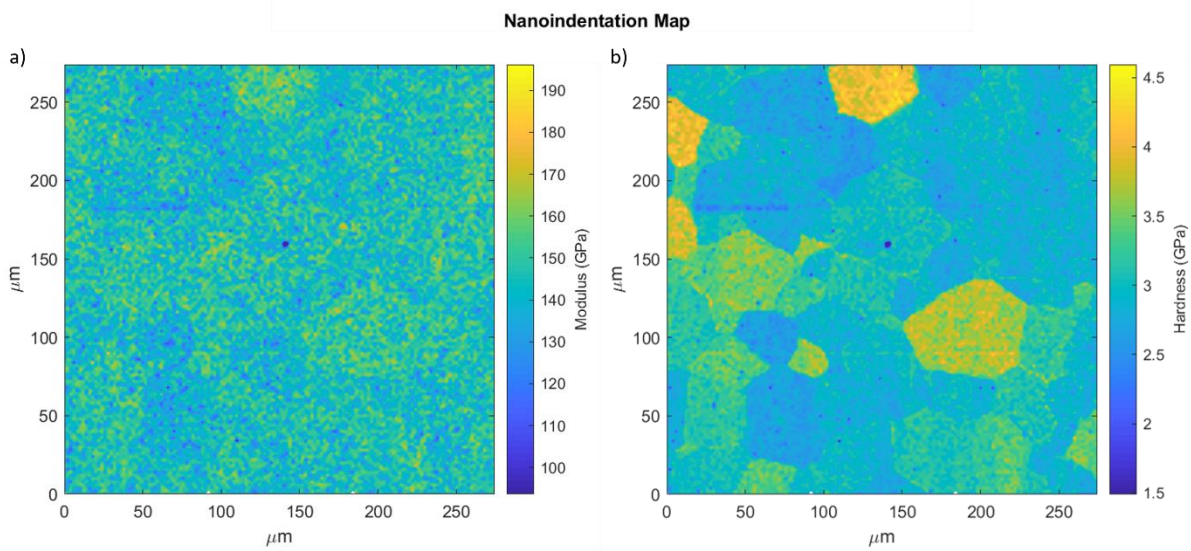



*Figure 14: Nanoindentation map of CP titanium showing a) modulus and b) hardness. The indentation map was performed at a fixed load of 3mN corresponding to an approximate depth of 200nm, and an indent spacing of 2um. The map is 138x138 pixels or indents in size, corresponding to 19044 data points.*

The hardness map in Figure 14 reveals significant contrast between grains, whereas there is lower grain-to-grain contrast in the modulus map, relative to the noise. Noting the dissimilarity in contrast between the hardness and modulus maps – in contradiction to previous reports of this well-studied material showing correlation between the two [98] – points to a more complex relationship between the two. Therefore, further analysis and discussions only include hardness data in order to remain confident in the trends observed. This difference between the hardness and modulus maps is discussed further in the Discussions and Limitations section on page 44.

An affine transformation was performed to align the EBSD map to the nanoindentation map using a set of eight triple junction points in these maps, with the points shown in the Appendix under Figure 119 on page 246. Once aligned, the two maps can be interpolated to the same size, so that correlations between various property fields can be undertaken easily. For consistency, the same colour scheme is used for EBSD as for nanoindentation maps.

As commercially pure titanium crystals are well understood to have high crystal anisotropy due to changes in the declination angle [21], [98], [130], the crystal orientation data is readily simplified to display maps of the declination angle between the basal plane normal (i.e. the c-axis) and the surface normal (i.e. indentation direction). Figure 15 shows the aligned map of declination angle

with nanoindentation, allowing direct comparison between the two arrays of values. These arrays can now be used to create scatter plots relating pixel-by-pixel the declination angle of the c-axis to the measured hardness, shown in Figure 15 c).

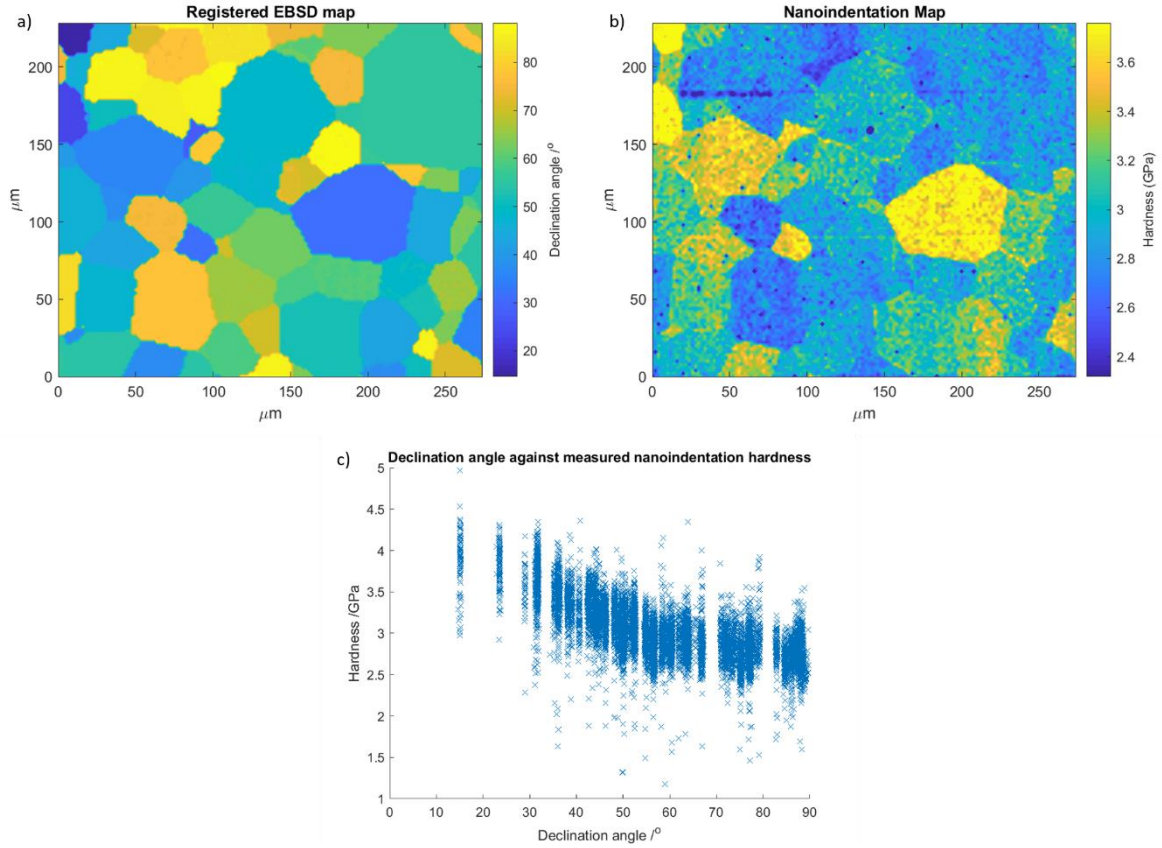



*Figure 15: a) registered EBSD declination angle map, b) nanoindentation obtained hardness map, and c) a scatter plot of declination angle, measured through EBSD, against nanoindentation measured hardness using all 15594 data points.*

This curve closely resembles that reported in previous experiments, notably by Britton et al [98]: the anisotropic effect of declination angle on measured nanoindentation hardness is clearly evident, and the range of hardness (~1GPa) can be used to validate these results. The benefit of this technique lies beyond the immediately visible: a very large quantity of data (>10,000 data points) has been collected in a relatively short time, while retaining all spatial and property information.

The data can be seen to comprise primarily of vertically spread populations at fixed declination angles. Each column of data points in the plot in Figure 15 c) relates to points with the same orientation, often referring to a singular grain but occasionally multiple grains with the same

shared orientation. Within these grains, there is then a spread of hardness data, arising from other contributing factors to hardness, as well as measurement noise.

There are two primary contributions to the noise in this dataset: the misattribution of pixels between maps, and the physical influence of grain boundaries on nanoindentation hardness. The first is a result of the error in transforming the EBSD data and aligning it onto the hardness map, which will be discussed further in Discussion and Limitations. This error will occur in points lying close to grain boundaries: when overlaid, some pixels may contain the hardness data of one grain but the EBSD data of the adjacent grain due to misalignment. The second is due to the real effect that indents close to grain boundaries respond differently to indents performed in the centre of grains. Plastic zones that impinge upon grain boundaries can cause dislocation pile-up and slip transmission, or the grain boundary might act as a dislocation source/sink itself, strongly affecting measured hardness [131]–[137]. In order to avoid the influence of grain boundary associated variation, and capitalising on the wealth of data available, points can be isolated based on spatial location relative to the microstructure. The EBSD data contains information on grain boundary location, and this can be used to calculate the distance of every indent to its nearest grain boundary, shown in Figure 16.

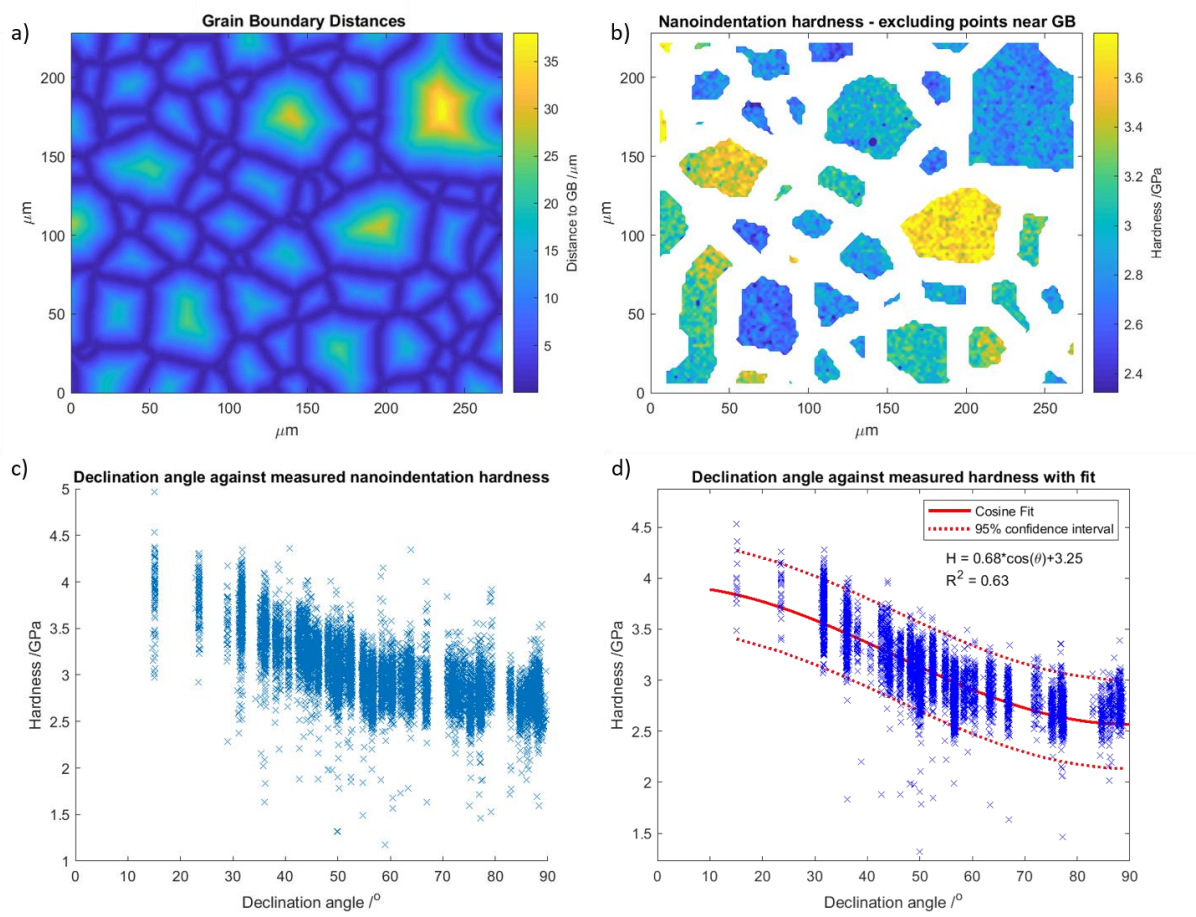



*Figure 16: a) Distances to grain boundaries obtained through the EBSD map, b) the nanoindentation obtained hardness map excluding points in (a) with a value below 7 µm, c) the scatter plot of declination angle, measured through EBSD, plotted against hardness measured through nanoindentation mapping as seen in Figure 15, and d) the scatter plot of c), excluding all points that lie within 7um of a grain boundary as determined by EBSD with an arbitrary simple function fitted. 6246 data points are shown in d). A 95% confidence interval is shown in the plot.*

The above scatter relationship can then be plotted excluding all points that lie within an arbitrarily chosen distance of 7 µm from a grain boundary. This ensures that points are only plotted if they can confidently be assigned their orientation, and are unlikely to be impacted by the nearby grain boundary, and the wealth of data ensures that a strong trend can remain visible.

A simple, arbitrary functional form that fits the boundary conditions of the data has been selected and used to fit the data in Figure 16 d) and is found to give a reasonable representation of the trend. It can be reasonably said that much of the remaining scatter within the data is largely a consequence of measurement noise in nanoindentation data at about 10%. This fitted relationship can then be used to improve the spatial alignment of EBSD and nanoindentation datasets. The measured nanoindentation hardness values were used with the fitted relationship

to produce a ‘simulated’ declination angle map. The simulated map does not contain all the crystallographic information within the EBSD data, but abrupt changes in the effective declination angle clearly demark some of the grain boundaries in a similar way to that evident in the EBSD data. A Sobel edge detection filter [138] was applied to the EBSD, and hardness-derived simulated declination angle maps, to produce the maps shown in Figure 120 (supplementary information).

These were used within an enhanced correlation coefficient (ECC) cross-correlative image alignment procedure [139], [140] to determine a further – specifically homographic – correction, allowing for two more degrees of freedom and capturing a greater range of distortions [141]. This further correction to the transformation from the spatial frames of the EBSD to nanoindentation data is now based on the extent of over-lapped fields, rather than a small number of discrete user-defined control points. The scatter plot and best fit relationship through the hardness and EBSD measured declination angle shows only very minor changes for points remote from the grain boundaries after this correction to the spatial alignment. From this, the same structure-property scatter plot can be obtained with more confidence in the assigned orientation for each point.

Following this correction to the spatial alignment, the behaviour near grain boundaries can be explored with more confidence. The EBSD-measured declination angle at each pixel is used within the fitted relationship to determine the hardness expected for a grain in this orientation. The measured hardness map and the expected hardness calculated from crystal orientation are compared in Figure 17 a) and b). This expected hardness is based on a fit to data obtained well away from grain boundaries, and benefits from lower noise due to the smoothing/averaging inherent in the data fitting process.

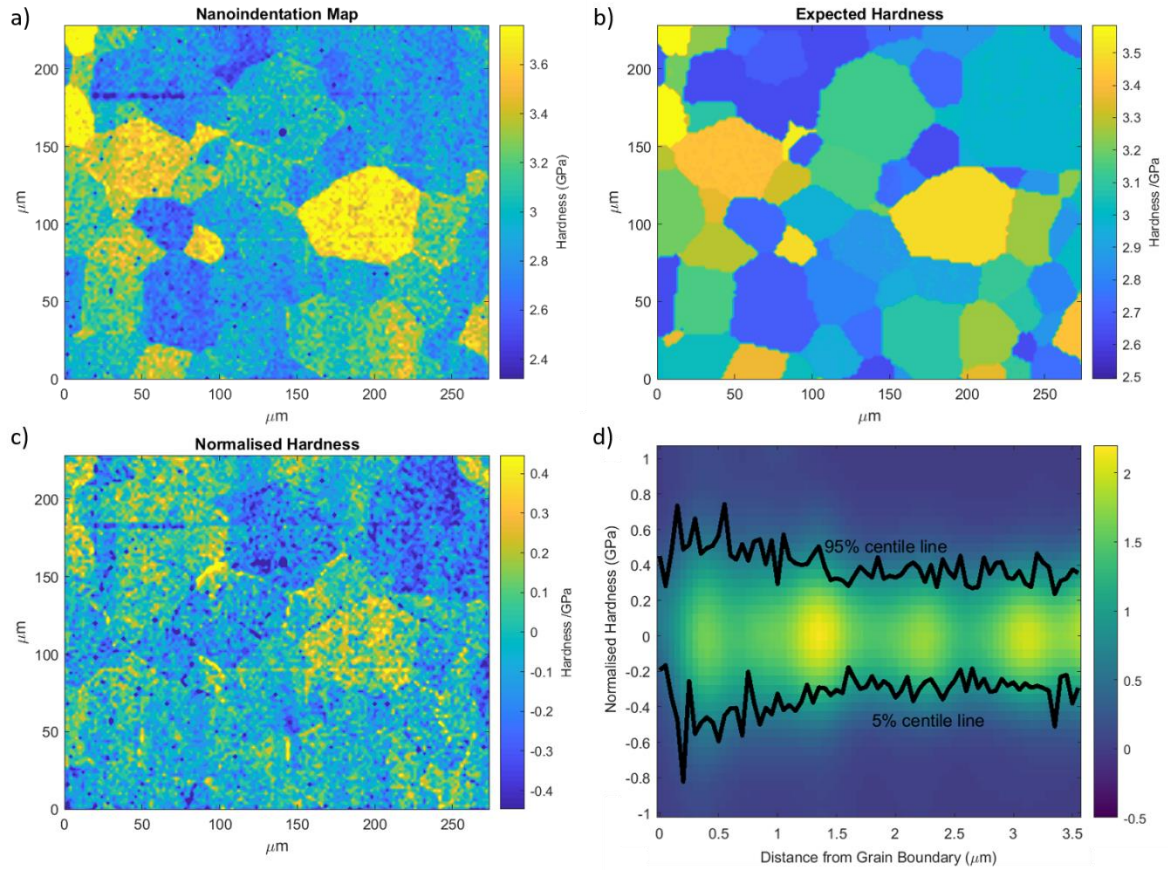



*Figure 17: a) nanoindentation measured hardness, b) expected hardness through the registered EBSD dataset and obtained relationship, c) normalised hardness through subtraction of a) and b), d) normalised hardness as a function of distance to the grain boundary. The colour scale in d) indicates log(1+N) where N is the number of indents at each combination of normalised hardness and distance from a grain boundary, while the lines show the 5$^{th}$ and 95$^{th}$ percentile values from normalised hardness distributions for indents at different distances from grain boundaries.*

Variations in measured hardness across the microstructure can be made more apparent by subtracting the expected hardness from the measured hardness to give what will be referred to as the normalised hardness. This removes the quite marked (>1 GPa) grain-to-grain hardness variation caused by orientation (Figure 17 a) and b)), leaving more subtle small variations visible in the normalised hardness map (Figure 17 c)). In this case, we expect only secondary signals: noise, grain boundary effects, and possible chemical heterogeneities (though these have not been shown to be of concern in CP titanium).

Grain boundaries are clearly highlighted in the normalised hardness map (Figure 17 c)). There are clear effects from noise, as well as from small deviations in nanoindentation positioning: horizontal stripes can be seen, resulting from overlapping indents and their resulting plastic zones due to stage misalignment. Some grains also show higher average measured nanoindentation

hardness, while others show lower values, for which possible explanations include the approximate form of the assumed fitting function, as well as physical mechanisms, such as interactions with close sub-surface grain boundaries, or grains that may have high residual stresses due to cooling [104]. It is clear however, that a primary source of variation in the normalised hardness is due to grain boundary effects. This can be visualised, as shown in Figure 17 d), as normalised hardness as a function of the distance to the grain boundary, showing an increased divergence in normalised hardness in the vicinity of the grain boundary.

A further dataset obtained on CP titanium can be combined to observe variations from chemical composition in tandem to the crystallographic and mechanical variations, shown in the published article linked to this method [84].

### 1.3.2. Dataset Two – Linear Friction Weld

This same method can be used to study the linear friction weld investigated in this study. Figure 18 shows the registered EBSD and nanoindentation maps from the globular alpha parent material to the vicinity of the weld-line, where a refined grain structure and elevated hardness can be seen.

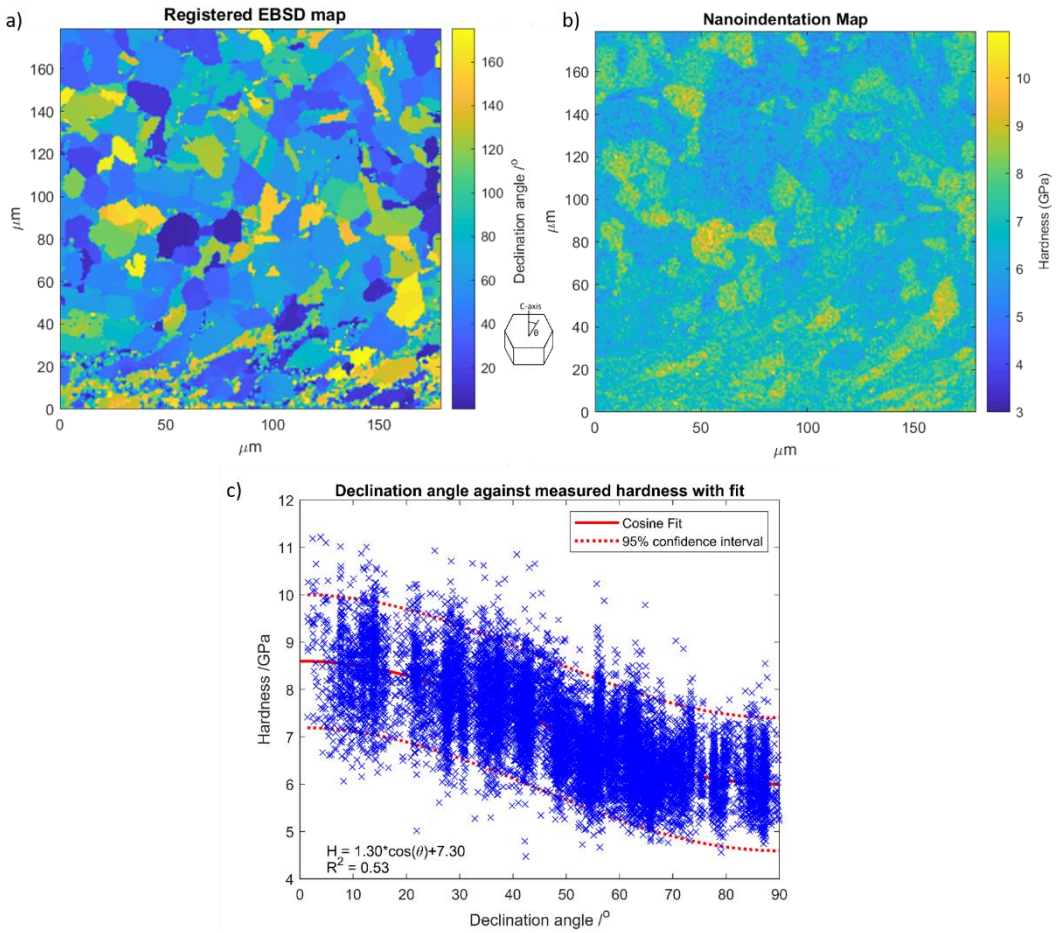



*Figure 18: Nanoindentation correlation mapping of Ti-64 LFW near the weld-line. a) Registered EBSD map of declination angle, b) nanoindentation map of the same area, c) scatter plot of declination angle against nanoindentation hardness with an arbitrary fitting function. All points further than 1 μm from a grain boundary are shown, displaying 12827 points.*

A similar trend-line on the relationship of hardness with declination angle can be seen, however with a greater degree of scatter due to the other effects on mechanical property. These effects can be further decomposed by using the information gathered from the EBSD data to construct a grain area map, and calculate an effective grain radius. This is shown in Figure 19, where the well-studied effect of grain size on mechanical property is seen clearly. This analysis shows that the effective grain radius can be used to describe the additional trend in mechanical property seen in the data with a relationship closely resembling that of early work by Hall and Petch [53], [142].

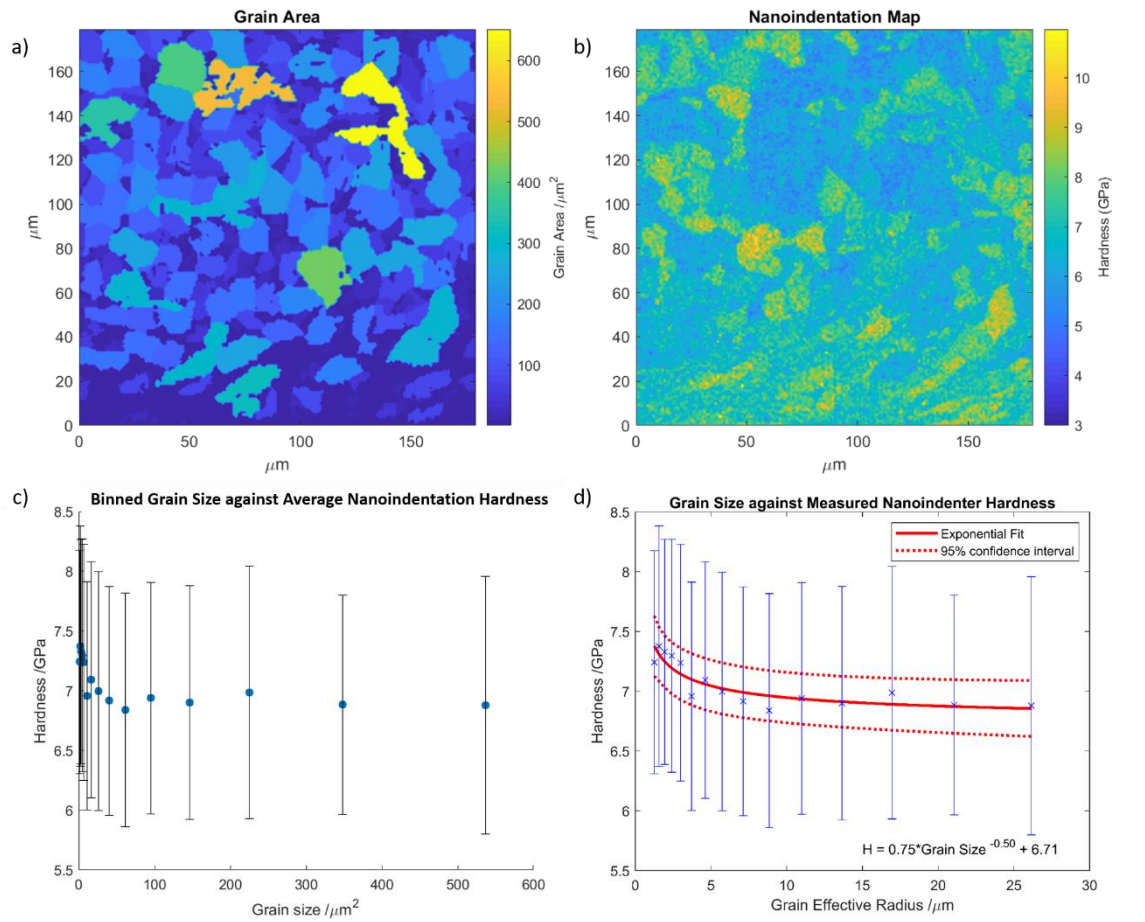



*Figure 19: Further deconstruction of Ti-64 LFW property mapping. a) grain area reconstruction from corrected EBSD map, b) original nanoindentation map as in Figure 18 for comparison, c) grain size, grouped into logarithmic-linear spaced bins, against average nanoindentation hardness with error bars equal to the standard deviation within the bin. Scatter plot in d) shows the effective radii in the bins of c) against nanoindentation hardness with free exponential function fit with an $R^2$ of 0.79.*

These results show the insight that can be gained into the material behaviour by combining these multiple mapping techniques: with only the consideration of grain orientation and size on nanoindentation hardness, structure-property relationships can be obtained. This analysis could be brought further by using additional techniques to characterise advanced manufactured material with similar spatial resolution, such as chemical composition, or residual stress mapping, *etc*.

Analysis on the effect of grain boundaries has been carried out, but further work is required to understand these effects in a scalable and accurate manner.

## 1.4. Discussion and Limitations

### 1.4.1. Reliability of input information

The rapid testing (3.5 sec/indent) used for the nanoindentation mapping generates some limitations to the data generated. The most significant of these is the current limitation to analysis of hardness data. This decision was taken in part due to some further testing required to understand the details of the modulus calculations, as well as the lack of modulus contrast in a material that is known to produce these variations. Hardness data from nanoindentation mapping also contains a significant noise level with variations of 10% of the average value obtained, likely due to the rapid nature in which it is collected.

The spatial alignment of nanoindentation mapping must also be considered. It can be seen from the resulting maps that rows of indents near the edge of a bundle occasionally overlap with neighbouring bundles, as a result of small stage misalignment. This is particularly noticeable in high spatial-resolution nanoindentation mapping, and can adversely affect data quality. Along these rows of indents, there can be significant changes in depth-spacing ratios, and in extreme cases include indents overlapping entirely, with an example shown in Figure 121 (supplementary information). These effects are typically seen when the indent spacing approaches the accuracy limit of the stepper motor used to drive the larger movements of the sample between bundles. Where the stepper motor makes slightly larger spacing between bundles, this does not influence the hardness values but will cause a slight dis-registry with spatial locations in the other maps.

A discussion of the details and limitations of the other input methods used in this paper can be found in previous publications related to those methods in particular [33], [143]–[147].

### 1.4.2. Reliability of analysis

The limitations of the analysis can also be split into two categories: alignment and interpolation. The first is an issue of error arising from the user input of reference points. A small change of a few pixels in one of the reference points can lead to significant changes to the affine transformation, particularly at the corners of the map and when maps have a high aspect ratio.

This could lead to the misattribution of data points as being in the wrong grain. In an attempt to quantify the extent of such issues, the EBSD and nanoindentation maps of dataset 1 were registered multiple times using freshly input control points marked by the same observer. On average 4.3 ± 1.0 % of pixels were assigned different grains when pairs of registered datasets were compared. When the additional full field ECC alignment was used then 3.9 ± 0.5 % of pixels were assigned to different grains.

The second is the question of interpolation. Datasets with discrete boundaries, such as in EBSD, must be interpolated with "nearest-neighbour" methods in order to avoid the fabrication of non-existent orientation data: grain boundaries are discrete, and a point interpolated as any average of points across the boundary is unphysical. However, this discrete nature of the grain assignment often causes stepped or serrated grain boundaries, and amplifies the errors in alignment discussed above.

Despite these limitations, the method presented provides a large quantity of data which can confidently be said to be well assigned, showing trends with high fidelity and data quantity.

### 1.4.3. Quantitative results

The structure-property relationships obtained show strong agreement with those collected and discussed in the literature before. Britton *et al.* [98] have reported the extent of anisotropic response of nanoindentation in CP titanium, with largely similar results in hardness data. However, as mentioned, the values of hardness and modulus collected via nanoindentation mapping have yet to be robustly compared to conventional CSM data, which may justify the relative difference in hardness values as well as our lack of modulus data.

Secondary effects such as grain boundary hardening can also be seen, much in agreement with experiments in the literature, showing variation in nanoindentation hardness in the vicinity of grain boundaries up to several microns in distance [133], [135], as well as the sensitivity of this

variation to the crystal orientation of both grains [136], [137], [148], [149]. Further insights on the underlying grain boundary effects can be explored to provide validation for existing models [150].

Size effects due to both the material grain size and of the testing volume can also be compared. The grain hardening effect seen in Figure 19 can be seen to follow a Hall Petch relationship with an exponent of 0.5 as in the seminal work. The Hall Petch coefficient of $0.75$ GPa $\sqrt{m}$ is on the order of earlier quoted values for titanium, though there remains valid concerns over the variability in fitting parameter forms [55]. Furthermore, care is needed when considering such data with multiply varying signals: the earlier effect of orientation is not included in the Hall Petch fit, and when included these values change to 0.16 and -2 for coefficient and exponent, respectively. While these remain within reasonable bounds, further study is necessary. Finally, the size effect of the testing method itself requires further study, with methods to account for these discussed before. This is particularly notable when comparing the microindentation data in the Case Study section on page 22 to these nanoindentation data.

## 1.5. Conclusion

Nanoindentation mapping has recently become an available tool for the collection of indent arrays with a large number of indents in a short time (e.g. dataset 1 - 15870 points in 15 hours), and is modified in this method to cover large spatial areas (mm length scale) at high resolution (µm resolution) through chained arrays. This has allowed for large datasets of spatially resolved maps displaying mechanical properties at microstructurally relevant length scales.

The analytical method presented enables the combination of such datasets with other source signals – including but not limited to EBSD – and correctly registering them such that direct correlation can be made. In this way, analysis of materials with mechanical property that is more modestly varying, more spatially confined, and correlated with other features can be made, further to existing capabilities in the literature.

This correlative approach permits the analysis of continuous variables, such as crystal orientation, and enables the rapid collection of structure property relationships such as crystal anisotropy in complex microstructures.

It is further possible to deconvolve the effect of multiple varying structural properties on the mechanical response to nanoindentation, such as grain size hardening, and clearly observe secondary effects such as grain boundary hardening.

These insights can be gained in a dramatically shorter amount of time, permitting the close study of novel microstructures at high resolution and at pace, with the possibilities to incorporate such a method in accelerating process development for advanced manufacturing.

This chapter presents the method, as well as highlighting the current limitations of nanoindentation mapping, in the context of results obtainable on a reference material and the LFW case study. Further work can explore the more subtle variations observed, such as grain boundary hardening, to develop robust frameworks for understanding slip transmission with statistically relevant datasets.

The static local property having been explored with this new method, attention is turned to a dynamic local property: fatigue.

# 2. Chapter 2: Dynamic local property assessment through meso-scale ultrasonic fatigue

*Parts of this chapter are adapted from a collaborative publication submitted under the title of "Bayesian Optimised Collection Strategies for Fatigue Testing – Constant Life Testing"* [151].

*Further details are given in the Protocols section on page 129.*

## 2.2. Background and Motivation

Following work by Wilhelm Albert [152], [153] and Wohler in the 19th century [154], [155] the stress amplitude against life curve, named the SN curve, became the most fundamental fatigue result used to characterise materials for use in engineering applications. This curve is used to "life" components, predicting the service lifetime of a component and thereby determining the time interval between maintenance checks or component replacement. A schematic of the SN curve is shown in Figure 20, showing the crucial result that a specimen may fracture below the macroscopic yield stress after sufficient number of cycles. The shape of individual SN curves are influenced by many factors, including material choice, material processing, and loading pattern (the combination of thermal and mechanical stresses). [156].

Early work to characterise this curve by Wohler and subsequently Basquin showed that fatigue behaviour followed a monotonically decreasing curve, with the life of specimens increasing rapidly with decreasing stress, in Basquin's case extending into infinity below some "endurance" stress [157], [158]. The equation determined by Wöhler in 1870 predicted that the log of cycles to failure $N_f$ of railway axles is linearly related to the stress amplitude $\sigma_a$ in a fully reversed fatigue test by equation (2):

$$\log N_f = a - b\sigma_a \tag{2}$$

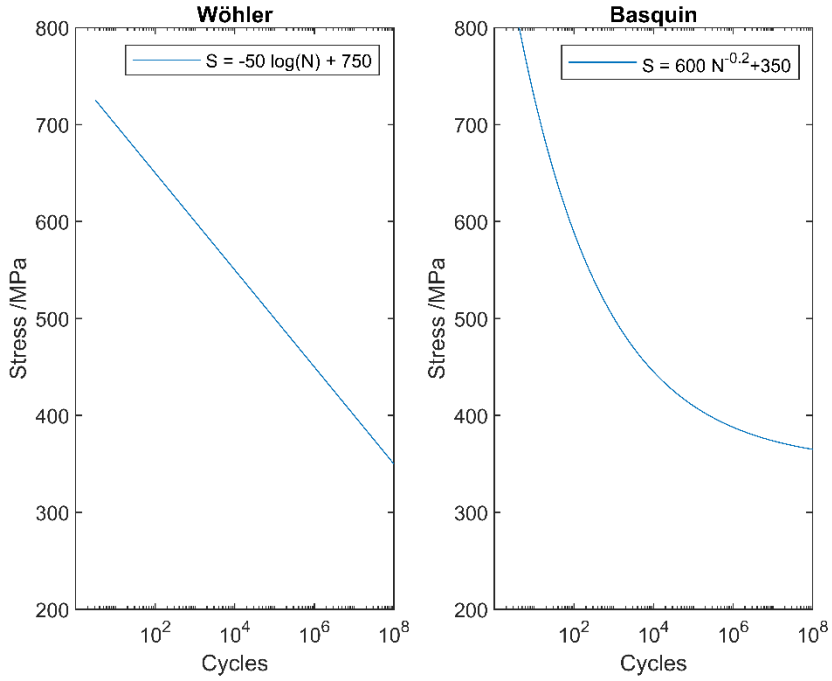



*Figure 20: Two example SN curves, showing the Wöhler curve (left) and the Basquin curve (right) with arbitrary example parameters. These functions describe "the variation of the stress amplitude for fully reversed fatigue loading of nominally smooth specimens as a function of the number of cycles to failure for ferrous and nonferrous alloys"* [156, p. 222]*, between a range of $10^1$ and $10^8$ cycles.*

For non-ferrous materials, a plateau on the SN curve is not observed, and the “endurance limit” is often quoted as the stress for failure at $10^7$ cycles. In all cases, however, the fatigue life was noted to dramatically increase in after approximately $10^6$ – $10^7$ cycles, a term that has been called the “knee point” or “elbow” in the SN curve [159]–[161]. Fatigue failure prior to this point is often described as “Low Cycle Fatigue” (LCF), and after as “High Cycle Fatigue” (HCF) or “Very High Cycle Fatigue” (VHCF).

The importance of fatigue failure cannot be understated: sources estimate that “at least half of all mechanical failures are due to fatigue” [162], representing a significant cost to the world economy [163]. Therefore, understanding the underlying mechanisms behind fatigue failure is key to reliability, sustainability, and safety, particularly in aerospace contexts.

Following the developments of Wöhler, scientists sought out the root cause of fatigue failures. Ewing and Humfrey [164] discovered the presence of “slip-bands”, surface bands that persisted and broadened with increasing cycle number, and caused cracks. In 1956, Thompson, Wadsworth, and Louat labelled these as “persistent slip bands” [165]. These features caused a roughening of the surface, increasing the stress intensity factor locally, and initiating cracks. It had also been observed that in a cyclic stress-strain curve, a plateau would form indicating some mechanism by which damage was absorbed. This was accounted for in 1965 by Helgeland who showed that slip bands were formed in the stress plateau of the stress-strain curve and were softer than the bulk material [156], [166]. Once initiated, the process of fatigue crack propagation can be summarised into three stages:

- Stage I: For small crack lengths, where the plastic zone surrounding the crack tip encompasses one, or a few grains, crack propagation is primarily through single shear, activating the primary slip system. This stage was named Stage I by Forsyth *et al* [167], where zig-zagged crack paths were observed following the directions of nearby visible slip bands.
- Stage II: For larger crack lengths, where the stress intensity factor $\Delta K$ is larger, and multiple slip systems are activated, resulting in a planar crack path normal to the tensile direction. In a model proposed by Laird [168], this results in a crack path that is blunted during loading, as activated slip causes plastic deformation, and then is re-sharpened during compression. This causes a repeated topographical variation from the blunting and sharpening, leading to the characteristic feature of fatigue failures: striations.
- Stage III: Rupture: when the crack has reached a certain size, the part fails as a result of the effective stress exceeding the strength of the material, and ductile or brittle fracture occurs.

The three stages can be seen when plotting crack growth rate against log of ΔK, shown in Figure 21.

This curve shows a sharp increase in growth rate with increasing ΔK at the beginning and end regimes of fatigue crack growth, and a linear segment in which crack growth is stable. This regime is described empirically by the Paris law [169], given as equation (3):

$$\frac{da}{dN} = C\Delta K^m \qquad (3)$$

Where $\frac{da}{dN}$ is the rate of crack growth with cycle number, C is a constant, $\Delta K$ is the range of stress intensity factors, and $m$ is the Paris constant, ranging between 2 and 40 [170]. Further work observed mean stress effects, defining the R ratio as the ratio between the minimum stress and the maximum stress experienced during a cycle, and showing the deleterious effect on fatigue strength of an increased R ratio, or mean stress [156], [171], [172].

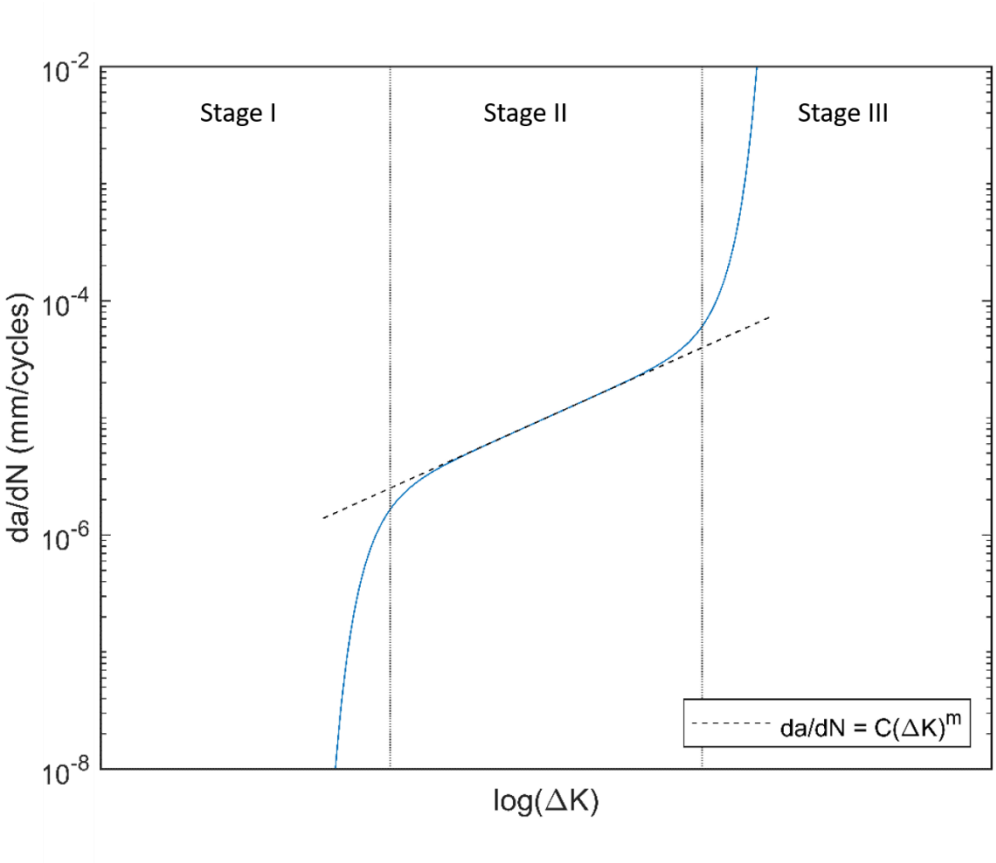



*Figure 21: Representation of crack growth rate ($\frac{da}{dN}$) against the range of stress intensity factors ($log(\Delta K)$). The central region (Stage II) follows the power law relationship of the Paris Law.*

These observations and relationships described the general fatigue behaviour, but further work was needed to characterise mechanisms relating the underlying material structure to the variety of fatigue responses observed in different compositions, regimes, and microstructures.

### 2.2.1. Local Stress States – Microstructural Fatigue

Efforts to understand these mechanisms ranged from exploring distinctions between SN regime (LCF vs HCF), crack growth stage (stages I [173], [174], and II [82], [175]–[178]), and loading effects (including mean stress effects, service history comparisons, or random loading [179]–[185]). These led to the developments of frameworks and models to describe crack initiation, growth, and final fracture such as phase-field methods [170], [186]–[188], Fatigue Indicator Parameters (FIPs), crystal plasticity models, and more. The common thread under all of these studies is the recognition of the importance of local stress state, and local material response.

Work carried out ascertained the differences in mechanisms underpinning the LCF and HCF regimes, outlining that fracture at very high cycle fatigue from relatively low macroscopic stress was due to heterogeneity of plasticity resulting from localised microstructural features, in turn causing higher local stresses leading to inhomogeneous slip activation [161], [189]. Later work developed this into a variety of descriptors used to predict fatigue life, such as "Fatigue Indicator Parameters" (FIPs), within crystal plasticity simulations at the grain level [20], [190]–[194].

These gradually incorporated further details, including state-of-the-art crystal plasticity methods to describe grain pair interactions, or multiple-grain interactions. One such example are so-called "hard-soft" grain pairs, where one grain is favourably oriented for slip and a neighbouring grain is not resulting in dislocation pile-up and high stress concentration [47], [49], [88], [195]–[199].

Part of this body of work can lead towards models to predict fatigue life, often incorporated with cumulative damage rules when considering a variety of loading regimes such as in-service or random loading [160], [200]–[205]. However, these studies underscore the emphasis on understanding material and microstructure-specific behaviour, and there remains significant work required to predict the fatigue behaviour of a well characterised material, if not novel ones.

### 2.2.2. Fatigue in advanced manufactured titanium

Within the work on titanium alloys, significant inroads have been made in characterising the fatigue response, particularly in the context of the varied microstructures found in this material system. However, it is clear that existing frameworks do not fully describe the material behaviour at all regimes. Indeed, Muth *et al.* explores this within the framework of FIPs, noting, "Fatigue crack formation in the VHCF regime is dominated by localized plastic deformation in α-grains regardless of microstructure or mechanical loading conditions, or FIP type" [194]. Dunne *et al.* describes mechanisms of faceted nucleation in Ti at HCF, outlining both the requirement for representative volumes to ensure presence microstructural features of study [206]. Furthermore, as part of a broader class of materials with an HCP crystal structure, load-shedding from the local

anisotropic response was necessary to describe the discrepancy in fatigue life between following complex load regimes with load-holds or dwells [47], [104], [207], [208].

More generally, it is clear that the microstructure influences all stages of fatigue failure: from initiation to final fracture [174], [209]–[211]. In a comprehensive study by Nalla *et al* [210], it was shown that lamellar microstructures "displayed better mode I fatigue-crack-propagation properties than bimodal microstructure in the presence of large (>4 mm) cracks" [210]. Fatigue initiation is also affected by the dislocation mobility after formation, and it has been shown that grain size and in particular alpha colony size affects dislocation motion [20]. This links the HCF properties to thermal processing history as the cooling rate will affect grain size: fine-structured martensitic microstructure, formed by cooling rates approaching 1000 K/min, exhibit increased HCF life [26].

These factors show the dependence of fatigue behaviour, particularly in HCF, on the microstructure of materials. This form of microstructural analysis is required to understand the benefits of various microstructures, and further analysis on the exact dynamics of crack paths are required to form a more general preparedness to fatigue failures.

Examples of this work are shown particularly clearly in material systems with complex microstructures. In advanced manufactured materials, through friction welding, additive manufacturing, or otherwise, microstructures are often highly heterogeneous. These systems provide complex structures where material behaviour may exhibit anisotropy [21], [212]–[214], unique interfacial behaviour [215], or biasing owing to statistically challenging volumes [82], [216], [217].

This can again be described in terms of local stress states, due either to macroscopic morphology and extrinsic factors, or microstructure and intrinsic factors. The first has been discussed in both the context of early fatigue work [156], as well as later work on additive manufacturing [218], [219], [228], [229], [220]–[227]: factors such as porosity, inclusions, and other such factors create

local stress concentrations, initiating fatigue cracks. This has also been explored in the cases of impact damage and foreign object damage (FOD) [176], [183], [230]–[232]. However, recent advances in the process control of such methods as well as in post-processing such as Hot Isostatic Pressing (HIP) have significantly reduced the incidence of failure due to such features [227], [233]–[235]. The reduction of this failure mode exposes the more nuanced behaviour of materials with different microstructures, with these later studies highlighting the effect of such intrinsic effects on fatigue life [79], [92], [241], [194], [211], [216], [236]–[240].

Duval-Chaneac *et al.* [215] discusses this with the case of multi-material layered additively manufactured IN718/316L steel, which experimentally observed the crack growth rate across layers of dissimilar material, comparing the Stage II Paris law crack growth across layers. In addition to observing detailed effects of shielding when transitioning from a softer layer to a harder layer, they more broadly concluded that there is a "clear effect of the microstructure, and varying mechanical properties […] on the fatigue behaviour of layered specimens" [215]. Residual stress effects have also long been studied as factors affecting the local stresses and behaviour of material [242]–[244], especially in the context of surface treatments such as shock peening [231], [243], [245]–[249]. Further experiments show the improved fatigue performance of textured titanium in the certain loading directions [239], [250]–[252], often based on the alignment of the loading direction to favourably induce slip in the basal plane.

This study examines the case of a linear friction weld in Ti-64 material with slightly dissimilar parent microstructures. Studies have reported fatigue results of linear friction welds, with all describing– bar in the case of extrinsic defects such as pores or due to issues resolved by heat treatment – the fatigue strength of weld material as higher than the parent [69], [79], [257]–[259], [81], [82], [216], [217], [253]–[256]. In light of the discussions above, this is not surprising: the reports cited earlier discuss the fatigue benefits in material comparable to that of a linear friction weld-line. From the refined grain structure, heat treatment to alleviate residual stresses,

and a favourable texture component (when the loading direction is parallel to the forging direction, and therefore perpendicular to the Basal and Prismatic plane, the Schmid factor is 0), these results can be used to explain why the linear friction weld does not fracture during bulk fatigue tests.

However, despite the construction of frameworks above, Castellucio *et al.* report that, "nevertheless, the limitation of such approaches assures the continued need for experimental work to determine which mechanisms dominate fatigue damage" [260]. Crucially, in most of these studies, little is determined in the fatigue behaviour of the weld material itself, owing to the rarity of failures in such a small portion of the specimen. This motivates the work in small-scale fatigue testing, in order to probe the fatigue behaviour of individual microstructural features. More broadly – as the length scales in the most advanced processing routes leads to finer-structured material, as must the testing capability scale in order to characterise these materials.

### 2.2.3. Ultrasonic Fatigue and Meso-scale Fatigue

This study follows in the footsteps of colleagues introducing ultrasonic meso-scale (ca ~100µm) fatigue testing. This novel form of testing permits the rapid characterisation of fatigue response in small-scale coupons of ~100 µm in every direction. Prior to reporting on the specific set up used, it is worth briefly describing the existing literature on both small-scale fatigue tests and ultrasonic fatigue test.

Whether for the characterisation of Micro/Nano Electro-Mechanical Systems, miniature robotics, or *in-situ* experiments, small-scale fatigue tests have been used with increased regularity [261]–[264]. However, these tests bring with them a separate suite of concerns, stemming from the small volume of material under consideration. These range from statistical biasing from the limited number of microstructural features [206], [265] to differing material mechanisms such as the Hall-Petch effect or others [53], [142], [175], [266]–[269]. However, many of these effects are restricted particularly to settings where there are fewer than 10 grains across the area of study,

which will be shown not to be the case. Furthermore, these results are compatible with the necessity to measure small-scale properties: indeed, when the microstructure to be studied does not extend beyond a small scale, it is necessary to measure properties in this way and appropriately caveat results.

Since Wöhler's earliest experiments, fatigue tests are often limited in practice to $10^7$ cycles, with such values quoted as the endurance limit, or strength at an infinite number of cycles [156, p. 222]. However, modern engineering components often see stress cycles in the giga-cycle ($10^9$) region, revealing a large gap in experimental data. This is often due to a limit in testing time: many fatigue testers operate at 20 Hz, requiring almost 20 months of continuous testing to reach the $10^9$ cycle mark. In recent decades however, there have been developments in using ultrasonic frequencies to carry out fatigue tests, with various groups obtaining fatigue data at 20 kHz [185], [270]–[272]. Bathias has produced a significant body of work in this domain, developing test methods and collecting and interpreting data in the context of prior fatigue work [273]–[281]. In these circumstances, the gigacycle mark can be reached in just under 14 hours.

Crucially, they show that the concept of an infinite fatigue life, or endurance limit after $10^7$ cycles is misguided [280], and that there is no such infinite fatigue life, or life beyond which a sample will not fail. This was reflected in recent tests by others [282], including tests in Ti-64 [283] with an example shown in Figure 22 [284].

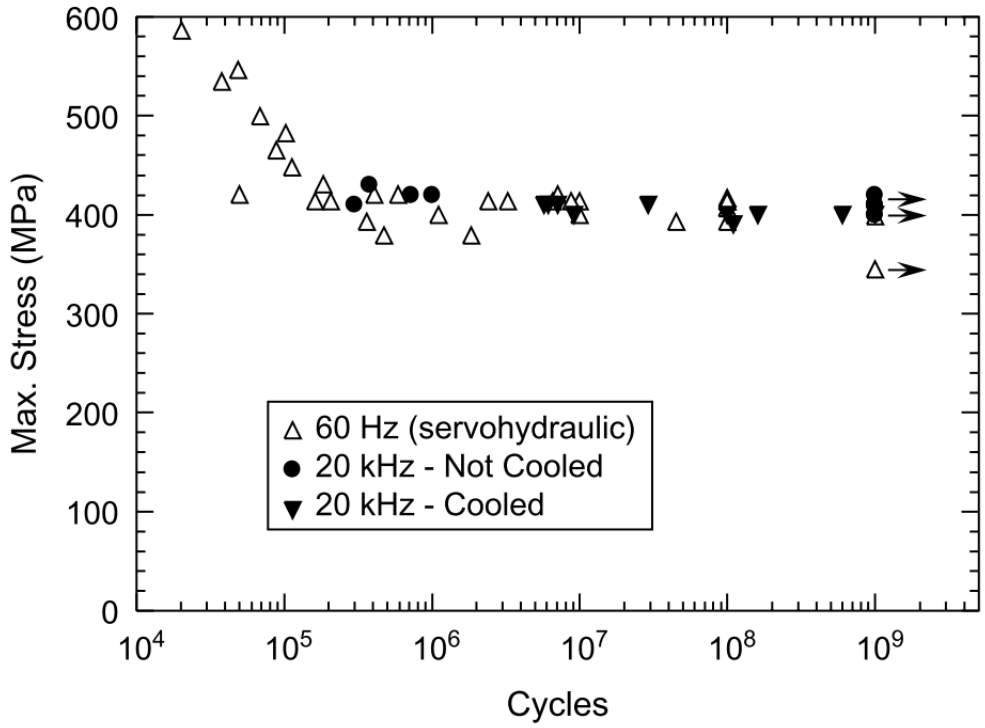



*Figure 22: SN curve from Morrissey et al.* [284]*, showing Ti-64 fatigue data up to $10^9$ cycles. With it are data points from samples tested at 60 Hz showing little to no effect from testing frequency.*

(V)HCF test methods can also be extended to various test frequencies, examining the relationship between these. In addition to the studies above, Morrissey *et al* and others showed that for titanium, consistent results can be seen across orders of magnitude of changes in testing frequency [172], [185], [283]–[286]. Nevertheless, some other studies show results indicating a higher fatigue strength at higher frequencies [287].

This project will employ a similar technology setup in order to test samples at 20 kHz, while examining smaller sample volumes. This project will therefore be able to more closely monitor the consequences of microstructure to fatigue life at high cycle.

### 2.2.4. Fatigue Testing Protocols

Populating the characteristic stress vs life—or SN curve—can be carried out by subjecting test specimens to cyclic loading. Fatigue data is often collected by considering the number of cycles for each sample to fail—or so-called "life testing"—and controlling the applied stress allows even

sampling across this portion of the SN where the SN curve is steep. However, in regions where the curve is shallow, samples generally either fail early during testing, or do not fail within practical testing times (denoted as runout or censored). This makes evaluation of failure likelihood difficult as data from other lives must be projected using parametric SN models, a variety of which are described in the literature [156], [161], [295]–[302], [201], [288]–[294].

These fatigue models allow for interpolation and extrapolation across lives though the debate over their applicability continues: owing to the complex and competing mechanisms driving fatigue failure, these models are often limited to classes of materials or sub-sections of the SN curve, and direct experimental assessment remains necessary in certain cases. The fatigue behaviour at shallow SN regions can remain challenging to sample directly: subtle changes in gradient (e.g. determination of the presence of a fatigue limit or activation of secondary failure mechanisms [303]), or failure distribution—further complicated by variations in failure distribution with life, so-called heteroscedasticity [297], [298], [304]—can be difficult to quantify.

Alternatively, fatigue data can be analysed by considering the condition of a specimen at a certain number of cycles: either failed or survived. As this “constant life” approach fixes the number of cycles to investigate, it does not have the sampling issues associated with the constant stress approach, and can allow for direct statistical interpretation of the fatigue strength at a given life. It allows for a targeted but limited sampling of behaviour at a specific condition.

The preference for either sampling strategy will depend on the fatigue model and regime being studied (shallow vs steep SN curve, parametric or not), the use case of the data (in engineering settings, academic research, or otherwise), and laboratory or material constraints (time sensitivity, cost, number of samples available, concerns about damage, etc.).

When designing fatigue experiments using conventional protocols, international standards advise on the best starting parameters such as test stresses and stress steps [172], [305]–[310]. However, as summarized in Table 2 the ideal testing parameters are a function of the (initially

unknown) mean and spread of the sample set being tested. Consequently, there is scope for improving methods of obtaining results. The staircase and step methods are the most common protocols for obtaining results with single tests, or with multiple tests on an individual sample, respectively.

*Table 2: Outline of conventional constant life fatigue testing protocols*

| Protocol | Description |
|---|---|
| Staircase / Up-down | The first sample is tested at the starting stress. For the next sample, the stress is decreased or increased by a step size if the preceding sample failed or ran out, respectively. The final state (failed or runout) of each sample is recorded. |
| Step | Specimens are initially tested at the starting stress. If the sample runs out, the sample is tested again increasing the stress by the step size until failure. The runout and failure stress is recorded for each sample |

In single-test strategies such as the staircase method, protocol parameters and data analysis are ambiguous, conflicting, or require prior knowledge of the system. As reported by Lin, Lu and Lee [311], there is disagreement within the standards on key protocol parameters for step testing such as sample size, starting stress, and step size as well as the method for analysing test data. The Dixon-Mood [306] method—a common analysis technique used in industry for staircase data—only considers half of the test data (failures or runouts), assumes a normal distribution in failure life, and recommends stress increments approximately equal to the sample set standard deviation which is not initially known. Pollak's investigation [312] on simulated test data showed the effect of sample size and starting stress on the standard deviation and developed correction functions using bootstrapping algorithms to increase the speed of convergence of the mean estimate. Engler-Pinto et al. developed a maximum likelihood-based framework for analysing staircase data which includes the information from all the samples, further incorporating life

testing to generate parametric probabilistic SN curves [313], [314]. These studies all highlight the sensitivity of the protocol parameters in the analysis of single-test results.

Multiple-test methods such as step testing can improve the collection efficiency of data, through a survived stress and a failed stress for each sample. While these tests can raise concerns about the effect of previous tests on the fatigue behaviour – such as damage accumulation lowering the strength, or coaxing raising the strength [205], [305], [315]–[318] – these effects have not been fully characterised, and the testing strategy remains in use across the academic literature [161], [182], [321]–[330], [230], [331]–[334], [232], [248], [249], [292], [293], [319], [320]. To alleviate concerns, stress step methods can be restricted to tests with large step sizes (and thus fewer steps) or in the HCF regime (predominantly elastic response) [305]. However, quantifying this minimal step size is challenging and introduces an experimental trade off: for a larger step size, there is a greater importance on the starting stress level and the sample fatigue strength is less constrained. There is also disagreement in the analysis of these results. The ASTM guide suggests using the mean of the runout and failure stress as the fatigue strength of that sample [307], whereas Lerch *et al* use the runout stresses only [318]. While some analysis methods aiming to account for coaxing or damage effects are commonly used [292], extensive data are required to conclude their applicability and all agree that a larger step size reduces the effect.

While Bayesian methods exist for analysing constant life data and for broader fatigue responses, these are limited to specific parametric models for life testing [308], [335]–[340]. There is therefore scope for:

- Studying the effect of different testing parameters on the estimates of fatigue strength parameters in conventional protocols.
- Optimising testing collection strategies across single and multiple-life tests, involving:
    - Adjusting the stress increment in staircase tests to maximise sample efficiency

    - Investigating the trade-off between step size and accuracy in step-test protocols, and finding optimal starting stress for any step size.
- Comparing between distribution models during analysis.

The notion of optimal test plans for acquiring statistics in experiments has been investigated in many areas of science including fatigue, often optimised via some quantified metric of experimental parameter information such as the Fisher information [341]–[346]. This broad set of methods is applied in a variety of fields, such as geographical sampling [347], robotic path planning [348], or non-destructive testing [349] to name a few.

A subset of such methods is Bayesian Optimised Maximum Entropy Sampling. The method, based on an approach by Lindley [350]–[352], broadly aims to design an experiment that maximises some experimental aim, such as the information gained from each subsequent point. A utility function is created which expresses the utility of testing at any location given the information from the prior. There is much literature on Bayesian optimal experimental design including reviews from DasGupta [353], Chaloner and Verdinelli [354], and more recently by Ryan, Drovandi *et al* [355], [356]. This analytical methodology is adapted in the context of these fatigue experiments, with more detail given in the Fatigue Testing Protocols sub-section of the Methods section on page 129.

These several points outline a motivation to carry out a study in the local fatigue property assessment of advanced microstructures, divided into two primary questions. The first examines the behaviour of a material that intrinsically does not exist in a volume comparable to conventional testing volumes: a smaller scale test methodology is required in order to understand such material, characterise the behaviour of similar microstructures, and validate frameworks for generalised fatigue behaviour prediction. Secondly, the rapid development of advanced manufacturing methodologies exhorts the development of modern testing capabilities.

There is scope for developing a suite of tools for use in the assessment of advanced manufactured materials, from ultrasonic test frequencies in order to rapidly attain (V)HCF regimes, to the development of optimised data collection protocols using computational methods.

## 2.3. Context – Previous Small Scale Fatigue Work in the Group

A methodology for the fatigue testing of volumes with characteristic length scales of ca. 100 µm was developed within the Micro-mechanics group by Dr Gong following an observation of fatigue failure in FIB micro-machined cantilevers during a surface cleaning step in an ultrasonic bath. In the following years, this idea was realised into the existing laboratory setup where a piezo-electric actuator was used to excite weighted cantilevers laser-machined out of rolled thin foils.

The ultrasonic driving system is obtained commercially from Emerson, originally intended for use in plastic welding, inducing vibration at 20 or 30 kHz with an amplitude of ~10s of µm. The setup is comprised of a power supply, actuator, and horn, as seen in Figure 23.

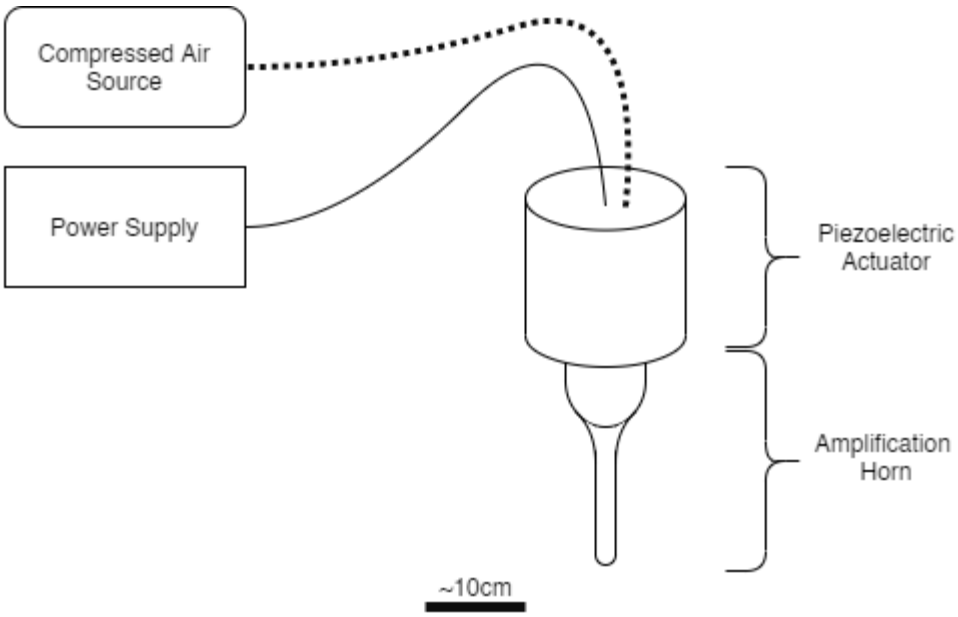



*Figure 23: Diagram of ultrasonic fatigue testing experimental setup. Power supply and compressed air source elements are shown as boxes, feeding into the piezoelectric actuator and amplification horn.*

The amplification horn, attached via grub screw to the piezoelectric actuator, is machined out of commercially pure titanium or nickel. It is designed with a length equal to half a wavelength of the travelling wave in the material, and a gradually reducing cross sectional area such that the driving amplitude is amplified to the tip. In this sense, the horn amplifies the longitudinal standing oscillation down its axis, with the centre undergoing compression and rarefaction, and the nodes on either end undergoing longitudinal movement. The experiments in this thesis employ a variety of horns, described in the experimental results of set Foil7-11 on page 195. However, as discussed later, it is unnecessary to fully characterise the horn response: only that the resonant frequency of the horn is within a few hundred Hz of the actuator (in order to be driven), and that the amplitude response covers a range that is adequate for the specimens to be fatigued.

The specimens are mounted in a modified grub screw assembly, as shown in Figure 24, such that a ring of material is clamped between the lid and the screw. This couples the ring of the specimen to the movement of the horn at the tip: the ring is oscillated in an up-and-down motion. This assembly is screwed axially into the tip of the horn with the location of the sample ca. 3 mm deep, ensuring that the sample is close to the oscillating stress node of the horn whilst also securely held by the grub screw threads.

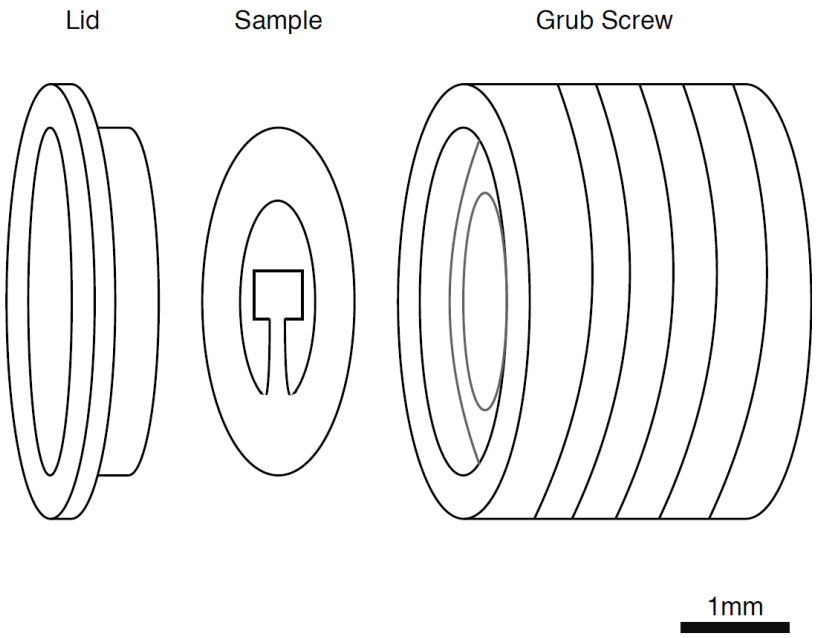



*Figure 24: Diagram of fatigue sample holder assembly. The right section shows an M5 grub screw, with a machine inset for the sample to fit, and a viewing hole to see the sample from the bottom. The left section shows a lid to clamp down on the sample when screwed into the horn. The inner section of this lid must be long enough to make sufficient contact on the ring of the sample. The design of this is detailed in the Appendix under Fatigue Sample Holder Machining on page 255.*

These cantilever-in-ring specimens are designed in Finite Element Software with a counter-weight such that under this oscillatory driving of the ring the hammer oscillates in anti-phase. This relative motion between the hammer and ring induces a bending stress in the neck, allowing for this region of material to be examined under fatigue loading. Through this design, it is possible to probe the fatigue response of material in ~100 µm length scales (limited by this region being surrounded by ca 1.5 mm of material).

The first generation design of these cantilevers consists of a ring, a cantilever neck, and counter-weight, with an early design by Dr Gong shown in Figure 25.

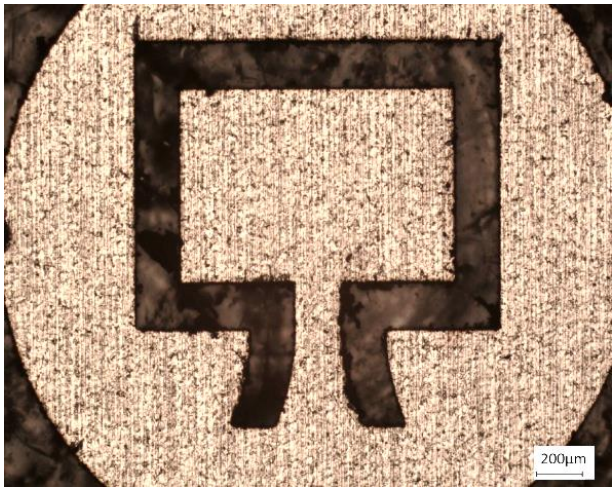



*Figure 25: Optical micrograph of ultrasonic fatigue testing specimen. This example sample, cut from 316L stainless steel, is based on an early generation design with a square paddle (centre) and a straight neck to rounded flared base.*

This design shows a square paddle as the counterweight, with a narrow neck broadening near the base in order to reduce stress concentration. In this particular design, the laser cutting follows the cantilever outline and ~200 µm of clearance. The laser machining of the cantilevers is outsourced to Laser Machining Limited (LML), and in the work of Dr Gong and Dr Arutyunyan [357], many samples can be arranged and cut directly into 100 µm thick rolled sheets of the material to be studied. The cantilever discs are held in place by small tabs that join them to the foil, which are cut out by hand prior to testing.

When inserted into the horn using the holder, the method for controlling the induced stress is via the power transmitted to the piezo-electric actuator. This is controlled via an in-house LabView software, which sends a voltage signal to the power supply. The amplitude of the horn is linearly related to the voltage signal above a lower limit, and can be calibrated via experiments using cameras to observe the blur in the tip position. In this sense, the simplified relationship for the system is:

$$A = bV \tag{4}$$

In equation (4), A is amplitude, V is signal voltage (in this case, proportional to power). However, in addition to being unable to directly observe the amplitude driving the specimen ring, the

primary determinant of stress is the bending angle of the cantilever. This can be measured directly by using a laser. Figure 26 shows a diagram of this laser measurement setup.

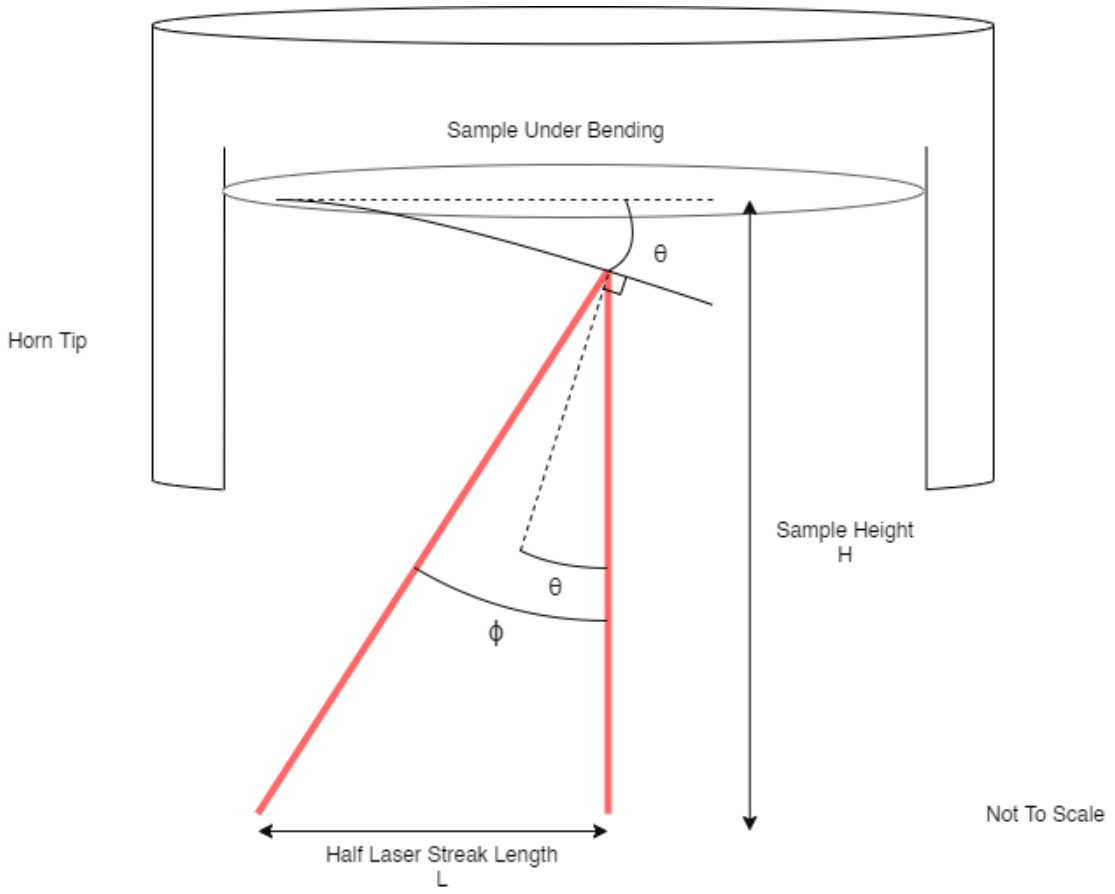



*Figure 26: Diagram of laser calibration setup. Magnified view of the horn tip is shown on the top, with a sample bending to some angular deviation $\theta$. Laser, in red, is shown reflecting off this with some angle $\phi$, causing a streak with length L.*

Here, it can be shown that the cantilever deviation $\theta$, the laser deflection angle $\phi$, and the experimental set up lengths $L$ and $H$ are related by equation (5):

$$\theta = \frac{\phi}{2} = \frac{\tan^{-1}\left(\frac{L}{H}\right)}{2} \tag{5}$$

Thereby providing a method to directly measure the cantilever deflection angle. During testing, it is therefore convenient to find the relationship between input voltage and this deflection angle. Referred to here as the coupling relationship, this allows for defining an input voltage for a desired deflection angle, shown in equation (6).

$$\theta = \kappa V + c \tag{6}$$

Where $\theta$ is the angular deflection of the cantilever, $\kappa$ is the coupling constant, and $V$ is the input signal voltage, which can be equivalently expressed as $P$ for power. As the power supply represents a black box, it has been observed that the relationship between signal voltage and deflection does not pass through the intercept, as shown in Figure 27, and therefore is fitted with a y-intercept. Physically, it is unnecessary to explain this value, nor is it strictly necessary to calibrate the horn to determine the amplitude: it is only necessary to confidently predict what input signal leads to a desired deflection angle.

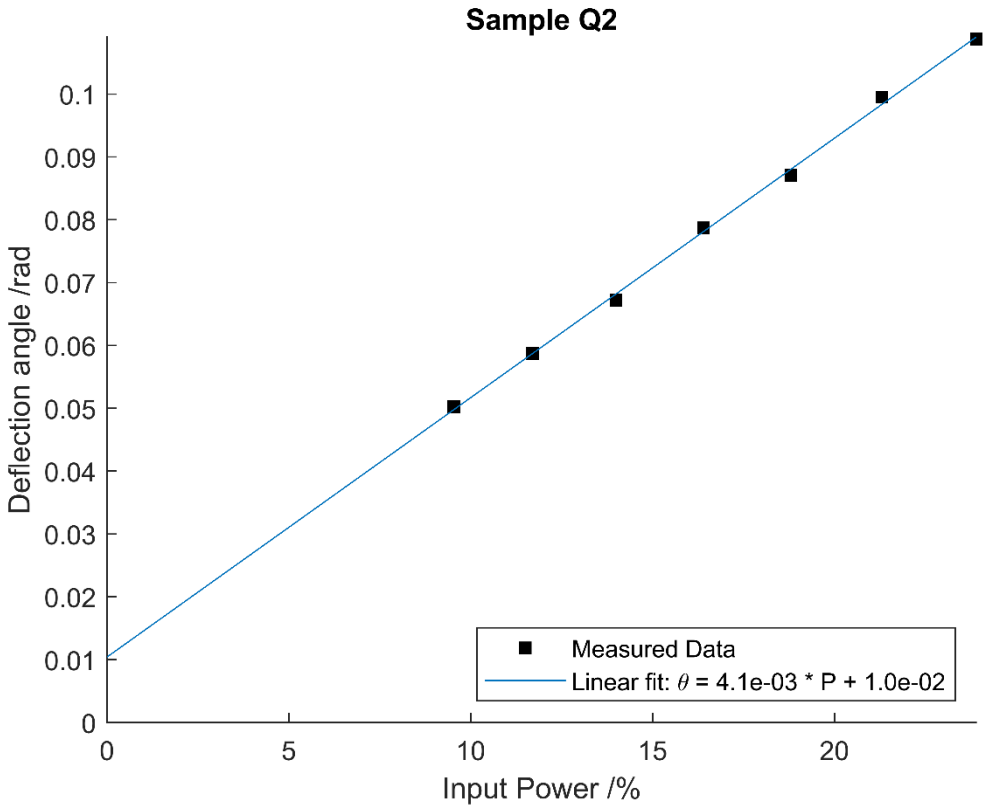



*Figure 27: Example laser calibration curve for sample Q2 in sample set Foil 3&4.*

Each specimen will have a unique coupling constant, resulting from both its individual dynamic response to a driving amplitude, as well as from the variations in how it is pinned in the horn. Furthermore, the uncertainty in measuring the laser streak and the noise from the system leads

to an estimated error in coupling constant of ~10%. A more detailed discussion of this response and variation is given in the Results Section.

Finally, through the ABAQUS modelling, a cantilever design will have a certain induced bending stress per unit angle. For small bending angles, this can be shown to be a linear proportional relationship. As seen in Figure 28, this relationship holds to angular deflections sufficiently large for our experiments, at approximately 0.3 rad, or an angle of 17 degrees. Note: this evaluation simply confirms the use of a proportional relationship between deflection angle and stress, justified through a non-plastic FEM simulation. The aim is to predict the bending stress, via a deflection angle, in turn via an input voltage signal. In summary, this can be expressed as equation (7):

$$\sigma = \rho\theta = \rho * (\kappa V + c) \tag{7}$$

Where $\sigma$ is the stress and $\rho$ is the stress per unit angle. In this way, it is possible to define the testing stress via an experimental laser calibration to determine the coupling constants, and through a simulation to determine the stress per unit angle.

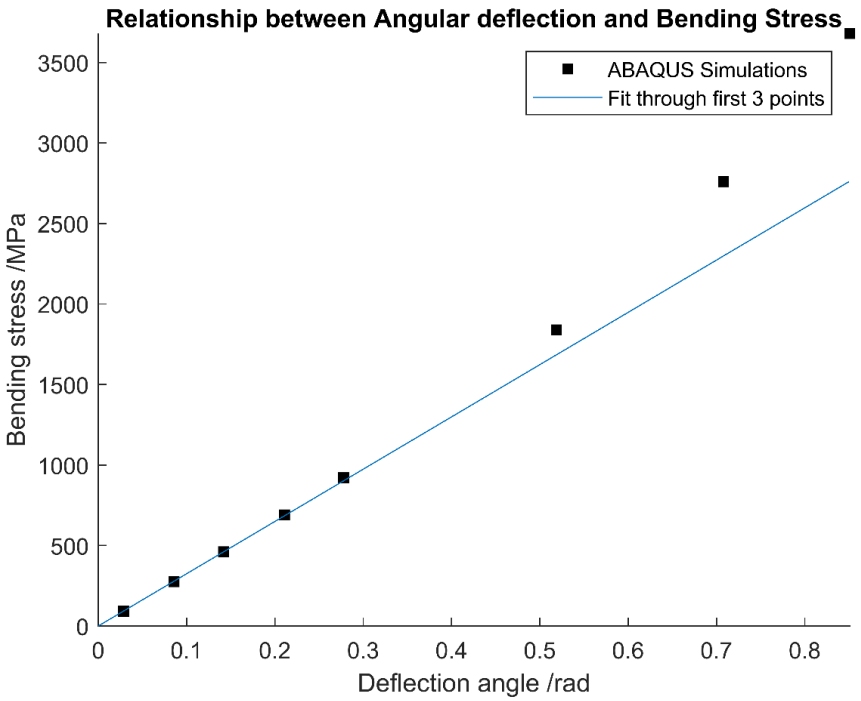



*Figure 28: ABAQUS simulations of stress induced in a cantilever deflected at various angles. The model is based on the Foil 2 sample set design, and does not include any plastic deformation mechanism. As of approximately 0.3 rad, it can be seen that the ABAQUS simulation begins to show a non-linear bending stress response.*

## 2.4. Experimental Methods

As the primary aim of this project entailed the development of the testing methodology itself, this section is divided into the following sections:

- Overview and initial stages of Sample Preparation Methodology
- Preparation of the first set of specimens and testing
- Perfect Coupling
- Electropolishing methodology
- Preparation of the second set of specimens
- Full process flow for sample preparation
- Fatigue Testing Protocols

With each dataset obtained from each foil, further processes were identified as necessary to improve the reliability of results. Table 3 outlines the sample set nomenclature and a brief description of the use in this report.

*Table 3: Outline of the sample sets with name and use in this report.*

| **Sample Set Name** | **Use** |
|---|---|
| Foil 1 | • Development and validation of preparation method<br>• First set of fatigue data on weld<br>• Validation of software for capturing fatigue response<br>• Life testing for simple SN characterisation |
| Foil 2 | • Trial at electropolishing with Nitric acid<br>• Further process flow optimisation<br>• Life testing for simple SN characterisation |
| Foil 3&4 (5&6 not tested) | • 2 Foils used for EP optimisation, 2 Foils tested following full process<br>• Further process optimisation with dimensional variation<br>• Results at $10^6$ cycles |
| Foil 7-11 | • SN characterisation from $10^5$ – $10^7$.<br>• All 5 foils tested following the full process |

### 2.4.1. Process Flow Determination

The primary deliverable presented in this project is that of preparing the source material to be tested. The work done to date had been carried out on rolled metallic sheets, made to a consistent thickness, based on which a model could then be designed for the known foil thickness. This design is then repeated across the relatively large foil to produce hundreds of

cantilever specimens. However, when targeting existing microstructures in a bulk material, a new approach is required.

From the LFW block described in the Introduction, foils could be cut in order to align with the established process flow. To best replicate the loads observed in an engine – that of the axial load-cycles from take-off and landing – as well as minimise the damage a single cut would produce, it was established that the first foils to be cut be in the plane of the 2 x 8.4 cm face. This would provide a ~2 cm weld-line to probe, with the cantilever bending inducing compressive and tensile stresses along the long axis of the foil.

#### 2.4.1.1. Foil Preparation and Damage Layers

In order to incorporate the established process flow, it was decided to aim for developing a method of producing foils similar to those used in earlier work. This came with the added benefit of being general: though the case study of the Ti-64 LFW is explored, this process ought not to be limited to this material system. Non-trivially, however, this required creating large, thin foils from the starting material without changing the underlying material and microstructure. This section details the rationale, justification, and details of this process flow.

The starting step would be to identify a method for creating foils from a block of material, meeting three specific criteria:

1. The capability to cut across a large surface unimpeded, at least to the extent of the starting LFW block size (20 cm in the longest direction).
2. The capability to cut to a specific thickness consistently, with an accuracy and precision of tens of micron.
3. The method must have a minimal damage layer in order to retain the underlying microstructure.

The first criteria ruled out many rotating cutting methods (such as diamond blade saws) and the third ruled out methods that generate significant quantities of heat or deformation (such as band saws or rolling methods). Electro-Discharge Machining (EDM) was chosen to cut the starting block into foils of a desired thickness. This could cut to a specified thickness with consistency and uniformity as well as with a precision of 10 μm. However, while it preserved the microstructure in the bulk, it did generate a damage layer in the cut surface. This was evident through the optical appearance – that of a dark and rough morphology – and through a slight curve in the foils suggesting residual stress.

This layer was studied through SEM inspection, HR-EBSD, and nanoindentation mapping in order to evaluate and measure the extent of this damage. Cross sections of EDM-cut Ti-64 material were mounted and polished, using the same methods described in Section 5.1. SEM and HR-EBSD were used to determine degree of surface roughness and damage from the EDM section, as well

as the presence of an elevated crystal mis-orientation and thereby dislocation density from the EDM process.

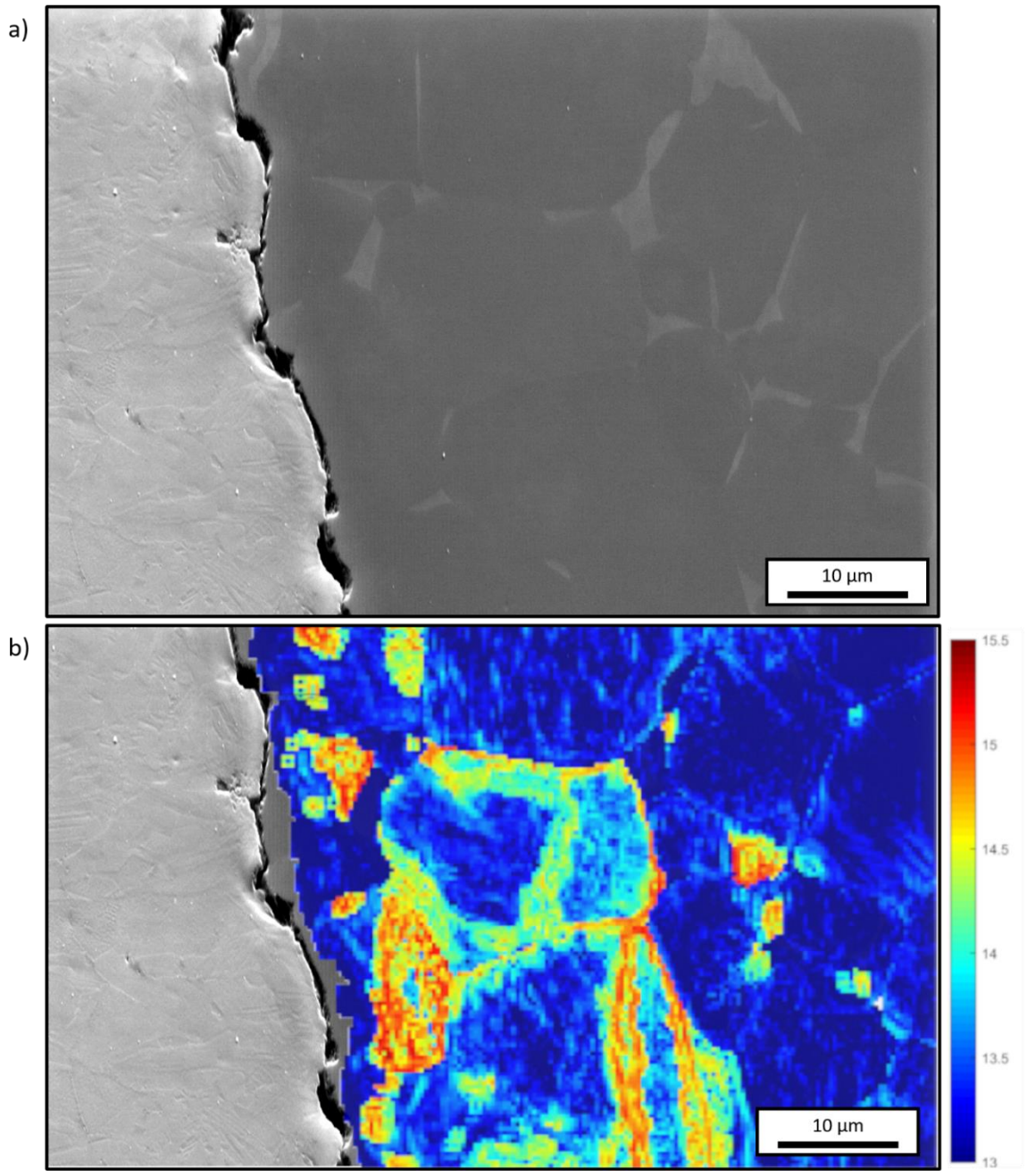



*Figure 29: a) SEM image of Ti-64 alpha microstructure, cross-sectioned to show an EDM-cut edge on the left hand side of the image. On the left hand side, the brighter material is a copper plating used to enhance edge retention during cross-sectional polishing. Panel b) shows the same as a) overlaid with GND density heat map as calculated from xEBSD in units of $log_{10}(GND/m^2)$ [40], [44], [146].*

Figure 29a) shows this experimental setup with the Ti-64 alpha microstructure occupying the right-hand side of the image. The edge runs vertically along the image, in the plane perpendicular to the tilting axis, with the sample rotated into this position in order to maximise signal

measurement from the edge during EBSD pattern collection. On the far left of the image, with a lighter colour and finer grain morphology, a copper plating used to ensure better edge-retention during polishing. It can be seen that the surface roughness extends approximately the same order of magnitude in length to the bimodal microstructure feature length.

Figure 29b) shows this same image overlaid with the Geometrically Necessary Dislocation (GND) density as calculated from the cross-correlation "xEBSD" scripts [40], [44], [146]. It can be seen that the signal is of reasonable quantity up to approximately 1-3 μm from the edge, where the grain size drops dramatically. In the larger grains adjacent, an elevated GND density can be measured, suggesting possible damage from the EDM process up to 20-40 μm in depth. Furthermore, in removing this layer, observations suggest that this damage is in the form of compressive residual stress: samples that have had one layer removed form concave shapes with the remaining damage layer on the inside of the foil curvature.

Finally, nanoindentation mapping was used to observe any significant variation in the mechanical properties from this process. Figure 30 shows this result, demonstrating that any mechanical variation in the base material is limited to approximately 10 μm in depth, assuring that other mechanisms – for example oxygen ingress – have not significantly permeated into the material.

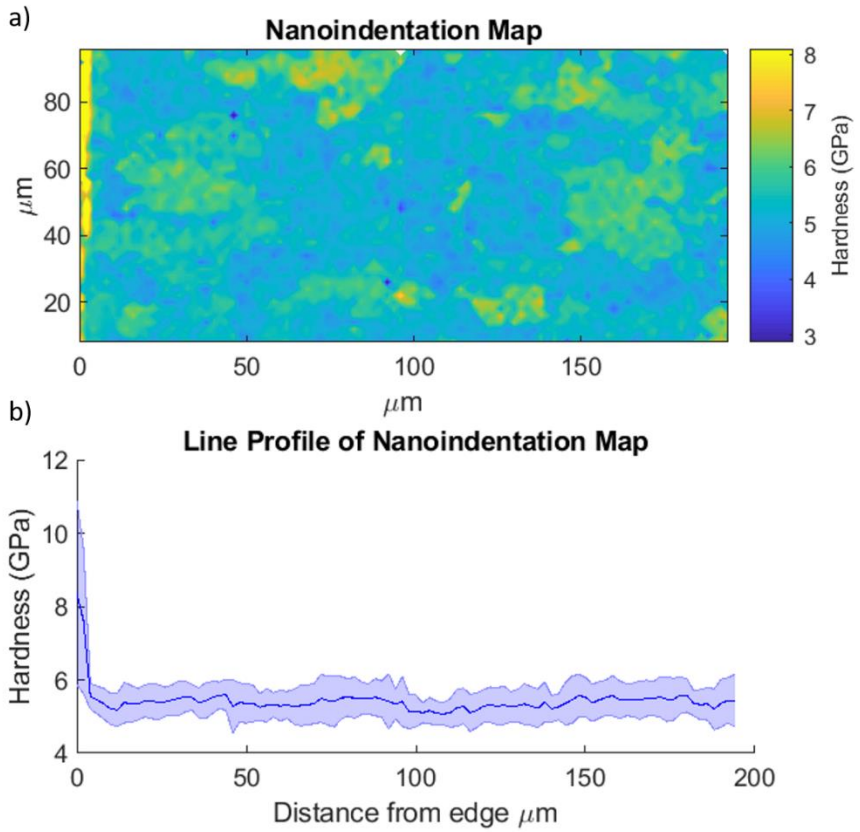



*Figure 30: a) Nanoindentation mapping of Ti-64 material, cross-sectioned to show an EDM cut edge along the left hand side of the image. This map was performed at a load of 5 mN, corresponding to an approximate depth of 200 nm, with a 2 µm separation. 4408 indents are shown. b) Line profile averaging all points along the y-axis, with error bars shown as the standard deviation of this average.*

These results are crucial to determine the quantity of material that must be removed in order to produce a foil with an un-changed microstructure from the bulk. In this case, a minimum of 40 µm must be removed from either side. Therefore, in order to produce a foil of 100 µm target thickness, foils of 180 µm must be cut with EDM.

#### 2.4.1.2. Damage layer removal – mounting and grinding

The next challenge requires developing a process to remove this 40 µm damage layer without introducing significant variations in thickness. This was achieved by modifying the standard metallographic foil mounting mechanism, comprised of a 5 cm diameter threaded core with two

interlocking rings, with a much finer pitch allowing for tighter control of the height of the central core.

It is possible to use a grinding wheel to remove material while keeping a flat surface. However, it was important to ensure that the mount was perfectly planar, and that the samples were as close to co-planar as possible to this in order to avoid undulations or tapers causing thickness variations. In order to achieve this, the following steps were followed:

- The mounting mechanism is ground to 800 grit paper, ensuring that scratches all extend in the same direction across both the core and the ring in contact with the wheel. It is important to ensure that the plane being ground is transverse to the axis of the core, in order to keep the interlocking rings co-planar after rotation.
- The samples are bonded to the core with crystal wax above its melting temperature, covered with aluminium foil, followed by a thick steel plate and this assembly pressed together using office binder clips. When held in this way for several minutes, the wax would flow evenly below the foils, ensuring both that the foil was evenly bonded to the core, and that this bond was as thin as possible.

When cooled this can be disassembled, with the steel plate acting as a flat surface to press the samples down uniformly, and the aluminium foil serving as a flexible and sacrificial layer to avoid this plate from adhering to the wax. This assembly is shown in Figure 31.

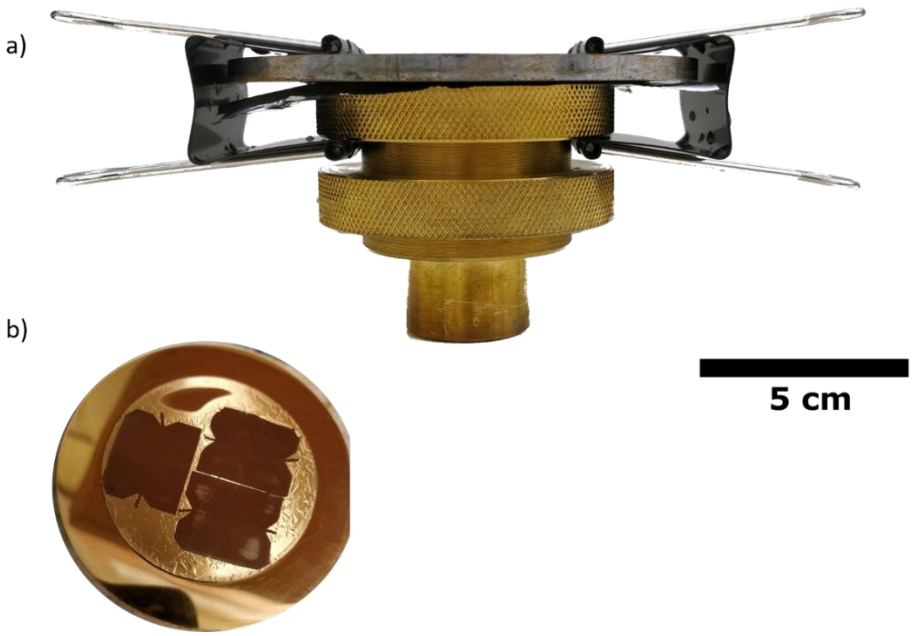



*Figure 31: Mounting system for grinding foils. Side view (top) showing the black binder clamps on either side, pressing the stack together. Starting from the top, the stack consisted of a steel plate, aluminium foil, the specimens, a thin layer of crystal wax, the brass mount. Bottom: a top down view of three foils placed on the mount.*

These were then ground using the standard metallographic preparation technique, progressing from 600 to 4000 grit paper. When measured with a micrometre, the resulting variation would typically be 10%, with a typical thickness reduction of 80 µm, matching the requirement as described above.

From this point on, the foils follow the existing process flow: the thickness is measured, a cantilever model is designed, locations are specified and laser cut.

#### 2.4.1.3. Cantilever design

From the measurement of thickness and the geometry of the foil, a cantilever and layout can be designed. When designing cantilevers for ultrasonic fatigue testing, there are three primary dynamic responses to be optimised:

1. Resonant frequency
2. Stress distribution
3. Maximum stress achieved

The first results from the testing system functioning as a damped harmonic oscillator. The bending of the cantilever hammer is due to an excitation of the outer ring at some frequency and amplitude. The cantilever system must therefore be tuned appropriately, though in this case these are designed to be sub-resonance: cantilevers are designed with a resonant frequency of approximately 25 kHz. Tuning to a frequency slightly above 20 kHz provides two design advantages. Firstly, the amplitude response exactly at resonance is very sensitive to small geometric deviations, and therefore is difficult to control. As seen in Figure 32, a cantilever tuned to a frequency range above resonance can be controlled to a more limited amplitude response range. Secondly, as a crack grows the stiffness reduces, leading to a lower resonant frequency and more rapid fracture. Though this shortens crack growth time significantly, it avoids a limitation in the resonant driving mechanism: the initiation of a crack in a specimen with a resonant frequency below 20 kHz would reduce the resonant frequency further by reducing the stiffness, reducing the driving amplitude. This can cause the crack to be arrested, and the sample to survive indefinitely.

The second results from the aim of the study: to develop a method that may measure the fatigue response of a volume spanning the length of the neck. Avoiding stress concentrations allows for a confidence in the stress level obtained by lowering the sensitivity to the exact geometry of sharp corners. This is measured as the ratio of the stress in plane of the beam to the maximum stress.

The final parameter is optimised by ensuring that the stress induced through oscillation at the available amplitude ranges reaches the stress range desired. In the case of Ti-64, and our experimental setup at 20 kHz with the standard amplification horn, this required reaching approximately 1 GPa from 70 μm of oscillation.

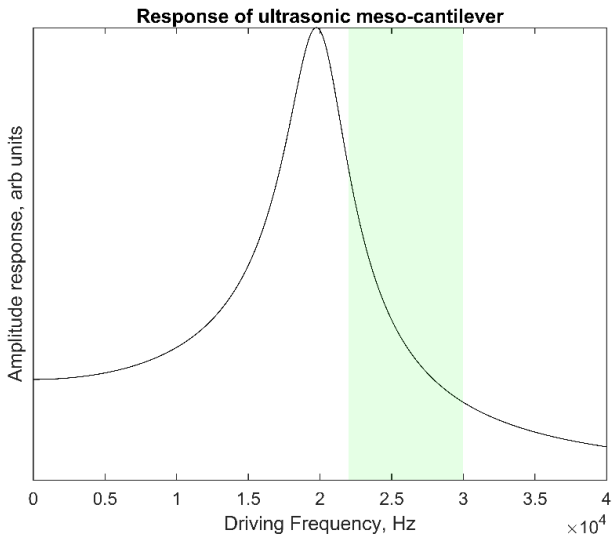



*Figure 32: Amplitude response curve of ultrasonic meso-cantilever. An example curve is shown with arbitrary response function similar to a damped harmonic oscillator, highlighting the targeted region for cantilever resonance frequency in green.*

These cantilevers are designed in ABAQUS Software, using both the eigenvalue frequency solver to determine the resonant frequency of the system, as well as the dynamic steady-state response function to determine stress response to some driving amplitude. It must be noted that for the purposes of these continuum body simulations, the Von Mises stress is measured as an indicator of the body stress. While this is not entirely accurate due to interactions of crystallography at these scales, for simplicity these crystallographic effects are not modelled.

Changes were made to the basic cantilever architecture building from the work of Dr Arutyunyan and Dr Gong in the Context section on page 63. This was necessary due to the high strength to weight ratio of Ti-64 compared to previously tested material, as well as driven by a desire to reduce stress concentrations and more faithfully represent the physics of the system. The first change consisted of modelling the entire ring system, as despite the additional computation time, it was more representative of the experiment with some stress shown to be imparted into the volume pinned by the mounting system (therefore changing resonant frequency).

The final architecture consisted of a linear tapered neck with two fillets on either side. This was found to induce an even stress without concentration (design rule 2), and offer the flexibility to

tune stiffness in order to satisfy design rules 1 and 3. While there are likely algorithms available for the automation and optimisation of such a design process, in practice it was simpler to iterate upon existing design experience due to the complexity in response and likely variation to the ideal in experimental measurements.

The first two generations of cantilevers are shown in Figure 33, with the iteration to the design used in this thesis shown as the third generation. This basic sample architecture is modified for each foil based on the thickness prior to laser cutting and adherence to design rules described above. These designs are then extruded into the plane in order to create the 3D model used for simulations.

The material was modelled as Ti-64 with a characteristic stiffness of 113.8 GPa, and a Poisson's ratio of 0.342 [358]. While this value assumes isotropic behaviour, certainly not applicable to the weld-line, it was shown in literature [82] and in Chapter 2 that the weld-line modulus did not vary significantly for the bending mode employed in this thesis. Care was taken to ensure that mesh density was sufficient to have convergence in measurements: a rough rule of thumb indicated that at least 5-10 elements must be present throughout the thickness of the cantilever to ensure values within 1-5% of the fully converged mesh densities.

This design of each cantilever is then repeated across a CAD diagram of the foil, placing extra care in this case that the centreline of the weld intersects the cantilever necks. In order to create accurate CAD models for the individual foils, these are scanned in regular office printers and image-processing software is used to detect the edges in the high-contrast scans. In later designs, a chord is drawn in the far side from the cantilever, creating an asymmetric view. This is useful for determining by eye the oncoming laser cutting side.

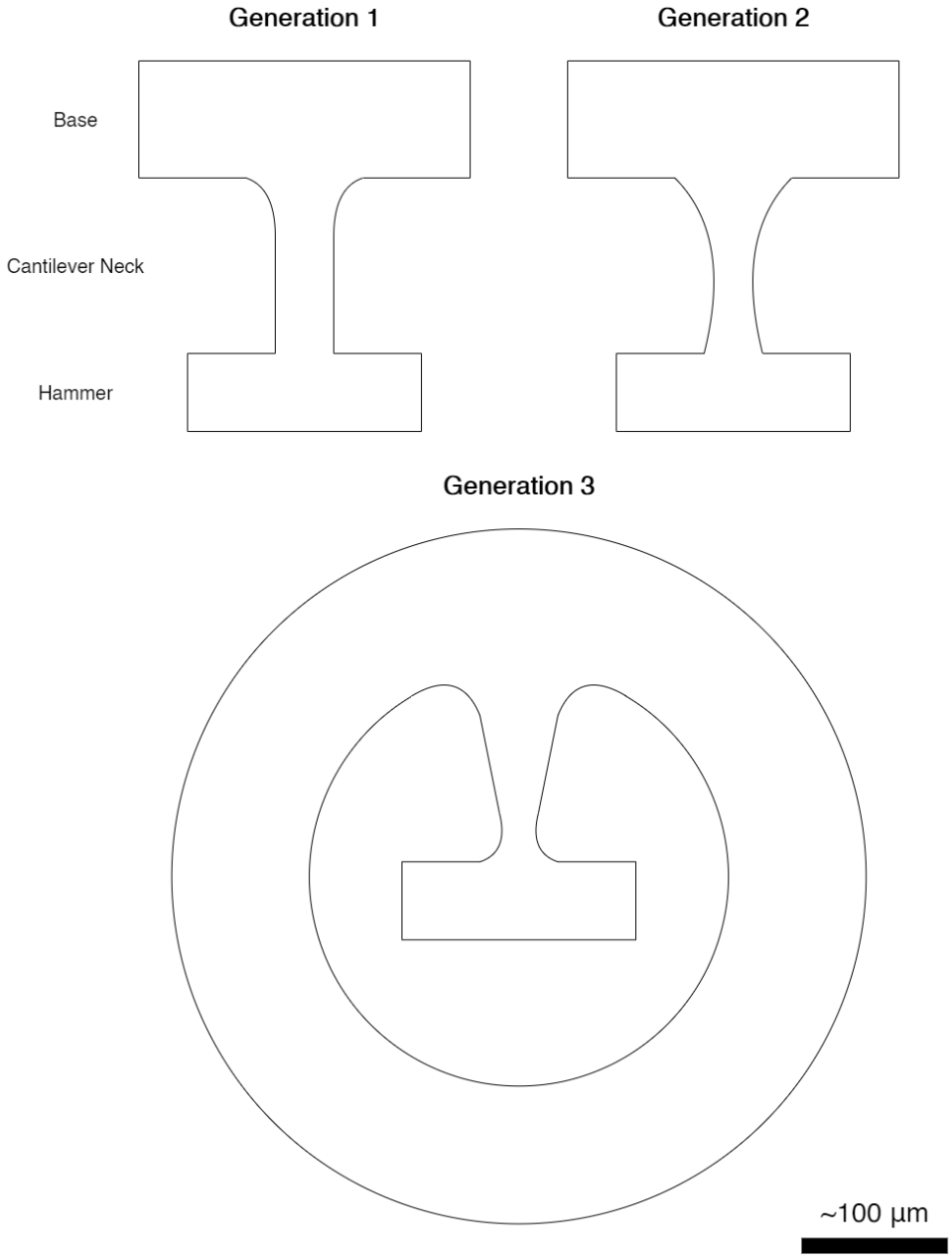



*Figure 33: Iterations of meso-cantilever design. Generation 1 consisted of a base paddle, a fillet with some radius, and a vertical line neck section connected directly to the hammer. Generation 2 consisted of a base paddle and arc section neck to connect to the hammer. Generation 3 consisted of a complete ring, a fillet of some radius connected to a linear tapered neck, a second fillet with some smaller radius, finally connected to the hammer in the centre.*

#### 2.4.1.4. Design and Results of Foil 1

Prior to discussions of further specimen preparation steps, the results of the first specimen set is reported with lessons learnt, motivating the further steps.

The first foil prepared was cut to 250 µm via EDM, followed by the grinding step with a micrometre measured thickness of 145 ± 5 µm , and a square shape of approximately 45 x 22 mm

as seen in Figure 34. A cantilever was designed for this thickness with a resonant frequency of 36 kHz and a stress concentration of ca. 20% unpolished. Following an initial intention to carry out a possible electropolishing step, the design achieved a maximum stress of approximately 1 GPa at 70 µm of vibration, with an estimated final thickness of 120 µm and a resonant frequency of 30 kHz. The thickness reduction from electropolishing was estimated from the previous experience within the group.

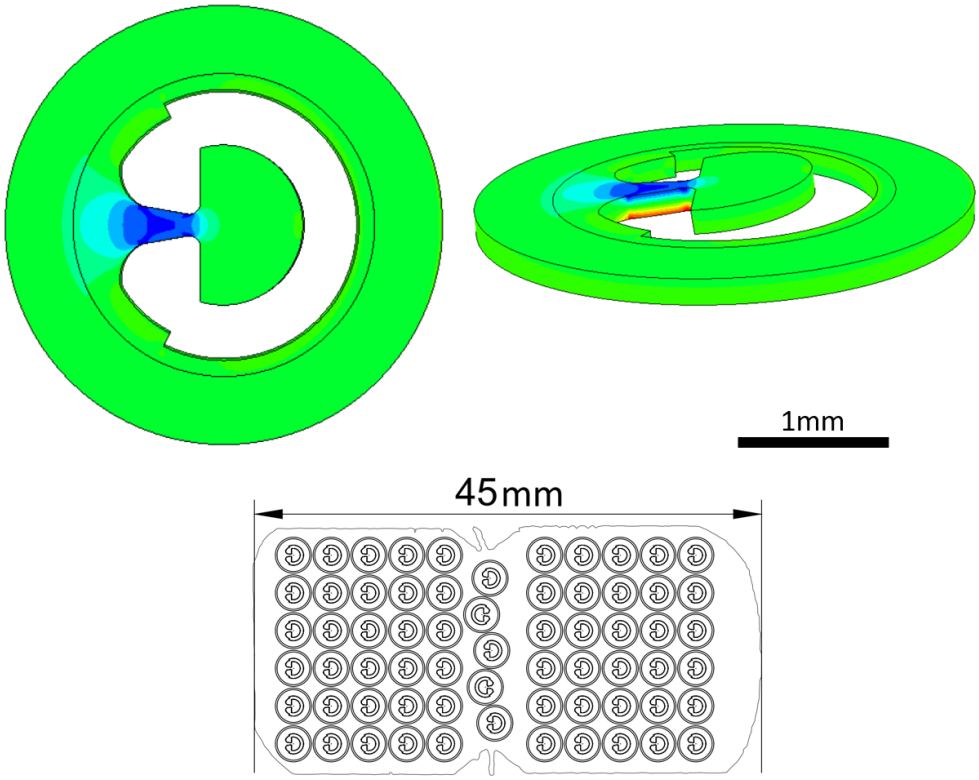



*Figure 34: Cantilever design (Top) and sample layout (Bottom) of Foil 1.*

However, in early electropolishing experiments with conventional recipes the quality of polishing was deemed inadequate: the polishing quality was rarely uniform, often with severe pitting, and the recast layer was not sufficiently removed. The motivation and experimental details of this step are described in the Electropolishing section on page 95. The specimens were therefore tested as received to generate preliminary fatigue results.

To generate these fatigue results, given the low number of specimens, a life-testing protocol was used, changing the stress to find the fatigue life with a focus on the transition to HCF. Figure 35 shows the SN plot of these data.

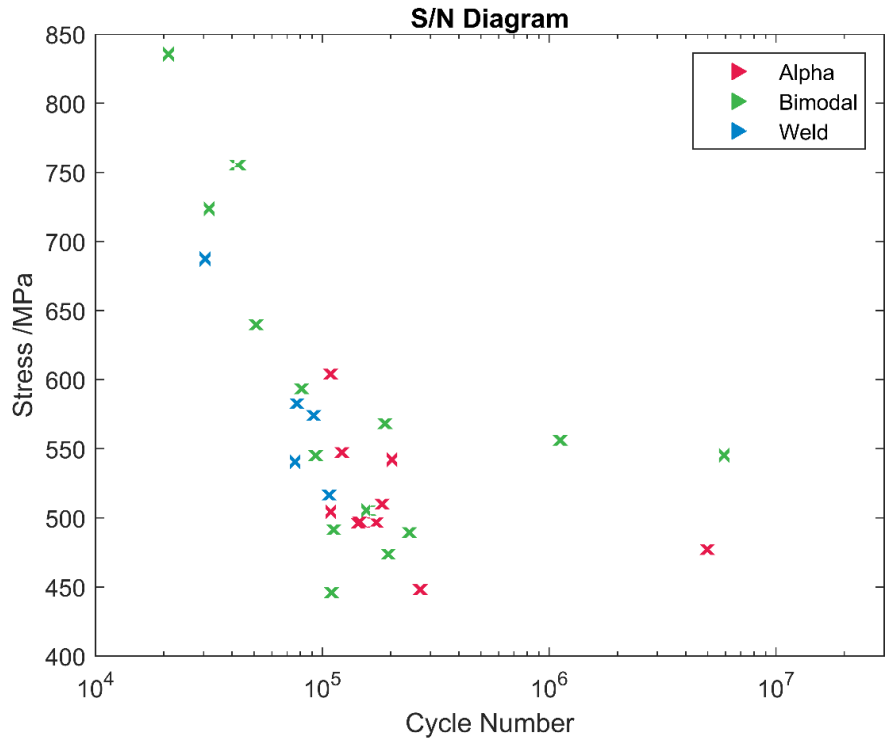



*Figure 35: SN plot of fatigue results from Foil 1, showing the results of 5 weld, 10 alpha, and 14 bimodal samples. The samples were unpolished. Error bars are omitted for clarity, but are approximately 10% in stress and 1000 cycles.*

As these samples were tested as received, the maximum stress achievable was lower, particularly for alpha samples. The results show a typical SN response, with a sharp "elbow" between $10^5$ and $10^6$ cycles at approximately 500MPa ± 60 MPa representing in the context of this study the transition between LCF and HCF. It can be seen that the weld does not have an obviously higher fatigue strength, or life, than the parent material, contrary to the expectation from Section 2.2.

### *Fractography*

The fractography of meso-scale fatigue specimens provides a unique insight into the fracture mechanisms at play given the localised microstructural region they cover. Figure 36 shows the fractography of a bimodal sample failing at ~500 MPa at $10^5$ cycles.

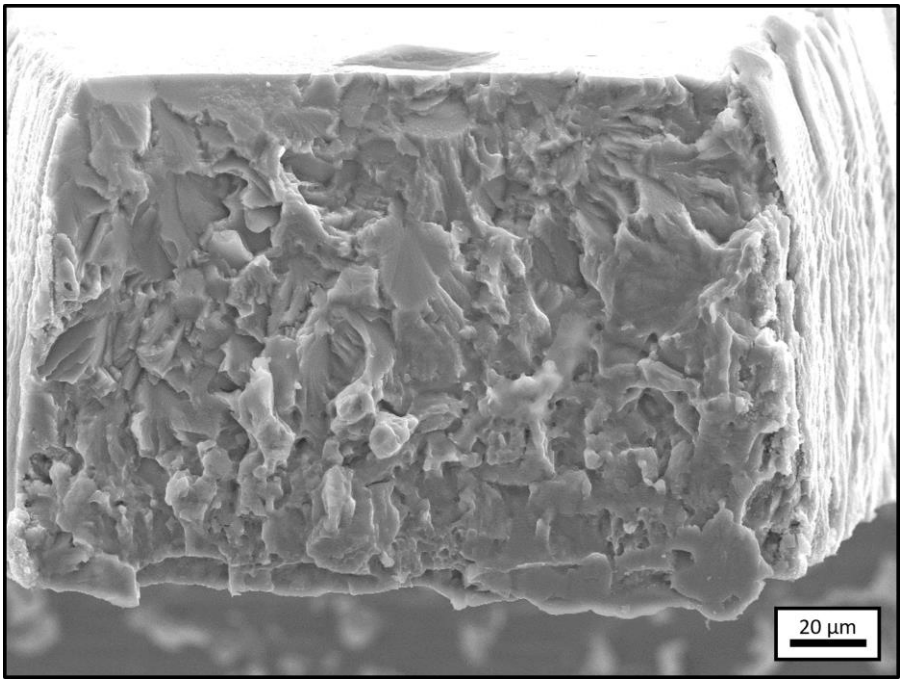



*Figure 36: Fractography of bimodal sample P1 failure, tested to 490 MPa and failing after* $1.12 * 10^5$ *cycles. The fractography may suggest a crack initiated from the top left corner.*

This faceted and low grain-number fracture surface can be contrasted with a weld specimen also tested to ~500 MPa and failing after $10^5$ cycles, shown in Figure 37.

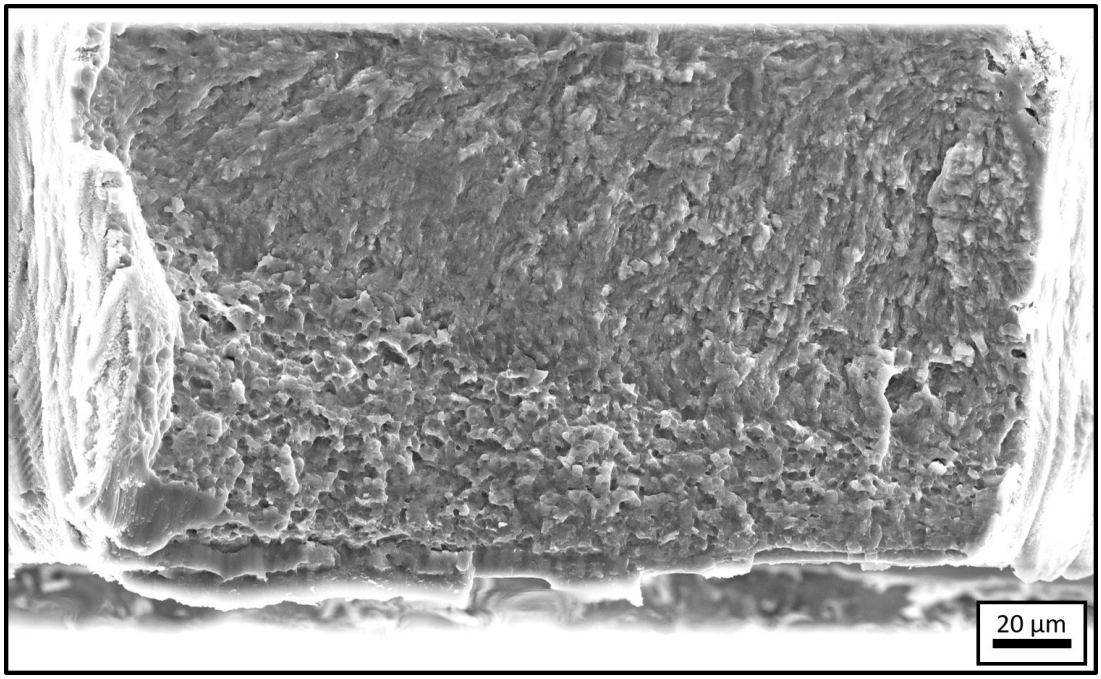



*Figure 37: Fractography of weld sample F2 failure, tested to 520 MPa and failing after* $1.01 * 10^5$ *cycles. The crack initiated from the top right corner, showing finer facets owing to a smaller grain size, followed by final fracture on the bottom left section.*

This shows the benefit of carrying out meso-scale fatigue tests: fracture surfaces are restrained to specific microstructural regions, providing the opportunity to examine the fatigue response and fractography of purely weld material. A further discussion of fractography is given in the Results section on page 175. However, it is equally clear in these micrographs that the recast layer from the laser cutting process plays a significant role in the fatigue response: in the weld fractography, the porosity present from this cutting process is a clear fatigue initiator. The fatigue response therefore cannot be considered that of the base underlying material (including original defects), but a result of the processing route. Further steps are therefore necessary to remove this recast layer, discussed further in the Electropolishing section on page 95.

In carrying out the testing, it was observed that the coupling constant varied significantly between samples, with Figure 38 showing the histogram of coupling constants. Furthermore, the simulated coupling constant for a foil of 145 µm in measured thickness through ABAQUS was 6.5 rad/µm, a value lower than the majority of recorded samples.

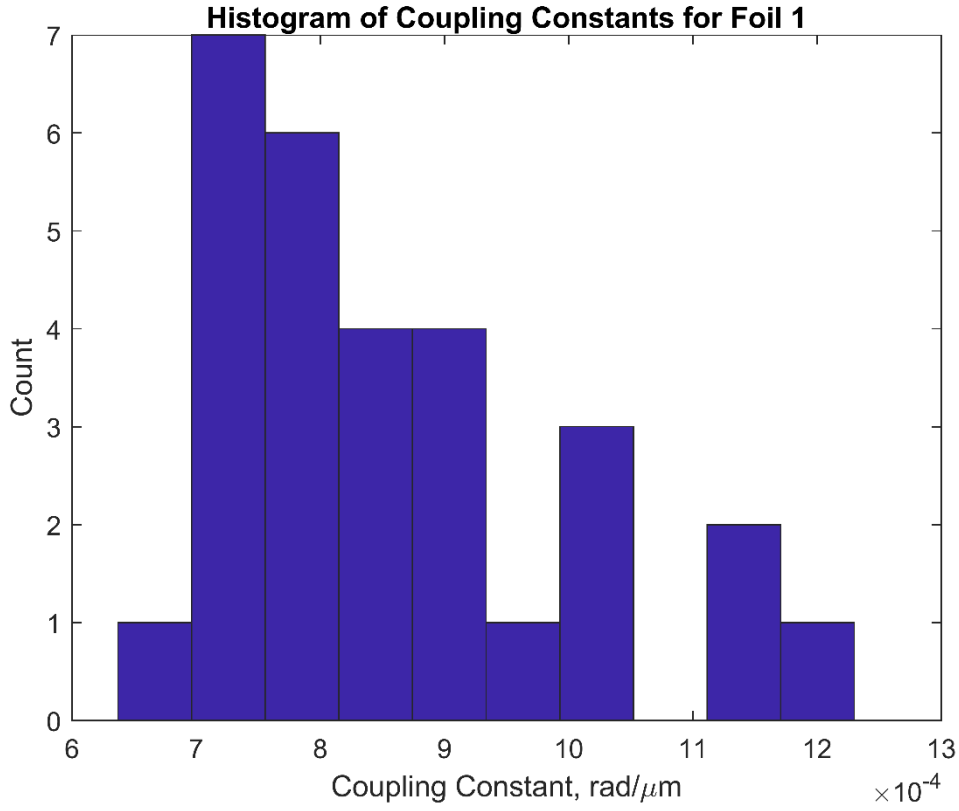



*Figure 38: Experimentally recorded coupling constants for foil 1 specimens. ABAQUS simulations on a foil of 145 µm thickness show a coupling constant of 6.5 rad/µm.*

The combination of an increased observed coupling constant – therefore not indicative of an efficiency loss – and a large spread in its value led to the development of the analysis described in the Perfect Coupling section on page 87.

#### 2.4.1.5. Perfect Coupling

Recall that during fatigue testing the laser calibration provides the coupling constant, or the deflection obtained from some unit of power passed to the tester. If the horn is calibrated using a microscope to determine the relationship between power and vibration amplitude, then it can be estimated that the sample is oscillated to this amplitude as well, or some value below this upper bound. In effect, the vibration amplitude is transferred with some efficiency from the horn tip to the specimen, limited by the inefficiency of the holder through compliance or heat generation. This transfer from horn power to vibration angle is linked by some coupling relationship.

During the ABAQUS modelling, it is possible to replicate this motion: if the full model is designed, as is done in the experiments in this thesis, then the outer ring can be oscillated at 20 kHz to some driving amplitude. The reproduction of this experimental oscillation allows for a simulated coupling constant to be derived via ABAQUS.

Recall equation (7) in the Context section on page 63 relating stress $\sigma$ to some angular deviation $\theta$ with some stress per unit angle ρ, and angular deviation to signal voltage V via some coupling relationship with parameters $\kappa, c$. This can be re-written, if the amplitude of the horn is known, to equation (8):

$$\sigma = \rho\theta = \rho * \mathrm{K} * A \tag{8}$$

$\mathrm{K}$ is the coupling constant in amplitude, linking an amplitude linearly to stress. The coupling constant can be obtained either experimentally via laser calibration or via ABAQUS, where it was initially assumed that by virtue of an efficiency loss, equation (9) holds:

$$Assume: \mathrm{K}_{exp} = \epsilon \mathrm{K}_{\mathrm{ABAQUS}}, 0 < \epsilon < 1 \tag{9}$$

However, during the collection of data for foils 1 and 2, it was noted that the $\mathrm{K}_{\mathrm{exp}}$ was experimentally measured as consistently larger than $\mathrm{K}_{\mathrm{ABAQUS}}$. This could only occur if the amplitude driving the cantilever was higher than what was measured at the tip of the horn, or if the model were incorrect. As the former was experimentally verified through repeated calibrations, the second was considered: the geometry of the cantilever in the model does not correspond to the experimental geometry.

To investigate this, consider that the coupling constant is a function of the cantilevers dynamic response – primarily its resonant frequency. Using the initial cardinal measurements in Figure 48, we can describe the coupling constant as a function of geometry as in equation (10) (assuming material stiffness is known):

$$\mathrm{K}_{\mathrm{ABAQUS}} = f(A, B, C, D, E, t) \tag{10}$$

As these 6 degrees of freedom are too complex to be solved with one measurement of coupling, some simplifications are required. To avoid requiring measurements of all cantilevers, and as these values can be measured with accuracy through SEM or optical microscopy, we set the values of A, B, C, D, and E to the average measurement of all cantilevers. As the thickness of the beam cannot be directly measured easily, it can be left as a free variable in this equation. This is further justified as thickness is known to have a strong effect on dynamic response, in addition to being the least certain and most variable across samples: the laser cutting process has been shown to be consistent between specimens, but the mounting and grinding method will still produce variation in thickness of 10% as described above. Therefore, the simulated coupling constant can be simplified to equation (11):

$$\mathrm{K}_{\mathrm{ABAQUS}} = \mathrm{K}_{\mathrm{ABAQUS}}(t) \tag{11}$$

In this way, we can arrive to equation (12):

$$\theta = \mathrm{K}_{\mathrm{ABAQUS}}(t) * A_{\mathrm{ABAQUS}} = \mathrm{K}_{exp} * A_{exp} \tag{12}$$

Given the assumption that $A_{\mathrm{ABAQUS}} = A_{exp}$. This is the central assumption of this method: that there is a perfect coupling between the horn tip and the sample, or that $\epsilon = 1$ in equation (9).

Thus, the solution to $\mathrm{K}_{\mathrm{ABAQUS}}(t) = \mathrm{K}_{exp}$ implies finding a thickness such that the coupling constants are equal. With this new thickness, a new stress per unit angle can be calculated to correct the stress induced in the beam. The relationships between thickness and the coupling constant and stress per unit angle are shown in Figure 39, computed numerically due to the non-linearity of the system.

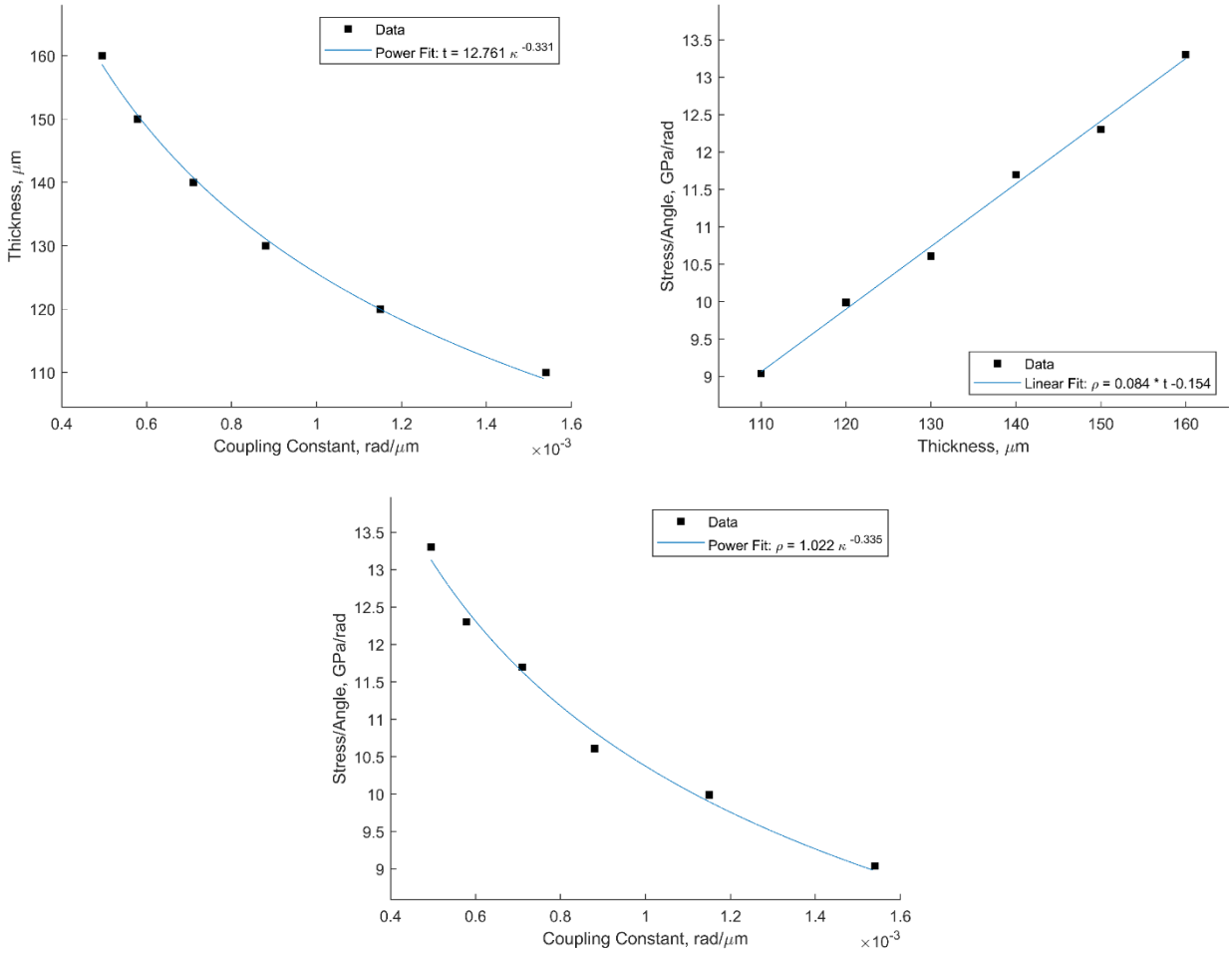



*Figure 39: Perfect Coupling Relationships for design of Foil 1, showing ABAQUS simulations of the dynamic response at 25 μm.*

Substituting into the equation shows this relationship in equations (13) and (14):

$$\sigma = \rho(t)\theta = \rho(t) * \mathrm{K_{exp}} * A \tag{13}$$

$$\sigma = \rho\left(\mathrm{t}\left(\mathrm{K_{exp}}\right)\right) * \mathrm{K_{exp}} * A \tag{14}$$

Where via simulations it is found that thickness is related to the coupling constant via a power law, and stress per unit angle is linearly related to thickness, shown in equations (15) and (16):

$$\mathrm{t}\left(\mathrm{K_{exp}}\right) = \alpha \mathrm{K}_{exp}^{\beta} \tag{15}$$

$$\rho(t) = a * t + b \tag{16}$$

This allows not only for estimating the stress based on an experimentally verified dynamic response – the coupling constant – but also allows for an indirect measurement of thickness (so-called inferred thickness), which can be validated post-fracture.

#### 2.4.1.6. Foil 1 Perfect Coupling results

Using the new Stress/Angle determined through perfect coupling, the stresses in the SN plot can be re-calculated and shown in Figure 40. The samples have changed in stress to a limited degree, with a tightening in the distribution of fatigue strength at a given life. Notably, the samples failing after the $10^6$ cycles align with the elbow.

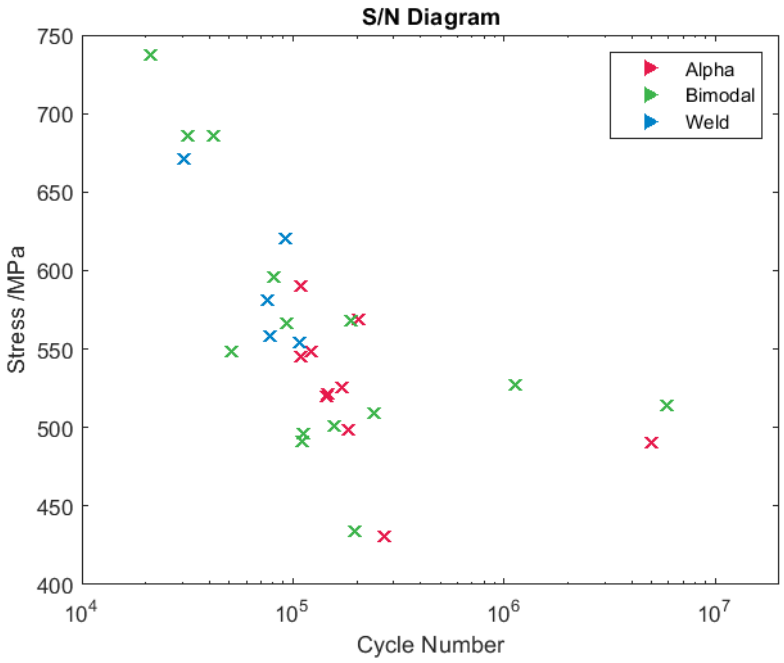



*Figure 40: Perfect Coupling-corrected SN plot of Foil 1 results, cf. Figure 35.*

As the thickness is allowed to vary in order to match the experimental and simulation coupling constant, it is possible to observe the variation in inferred thickness across the foil. This allows for not only a validation of the perfect coupling analysis, but provides an indirect measurement of thickness and its implied variation across the foil.

The plots in Figure 41 show this variation in thickness, indicating a slight taper in the foil towards the bimodal section, where larger variation was observed as well as a reduced average value. When plotting as a surface, it is possible to correlate the inferred thickness of two nearby samples, providing confidence that the variation may not be purely random, and showing sections of the foil that are ground thinner than others during the mounting and polishing step. While this variation is predicted to be approximately 10% or less – confirming that the process step is adequate at producing foils – these results highlight the need to account for thickness variations between samples as they significantly affect the dynamic response.

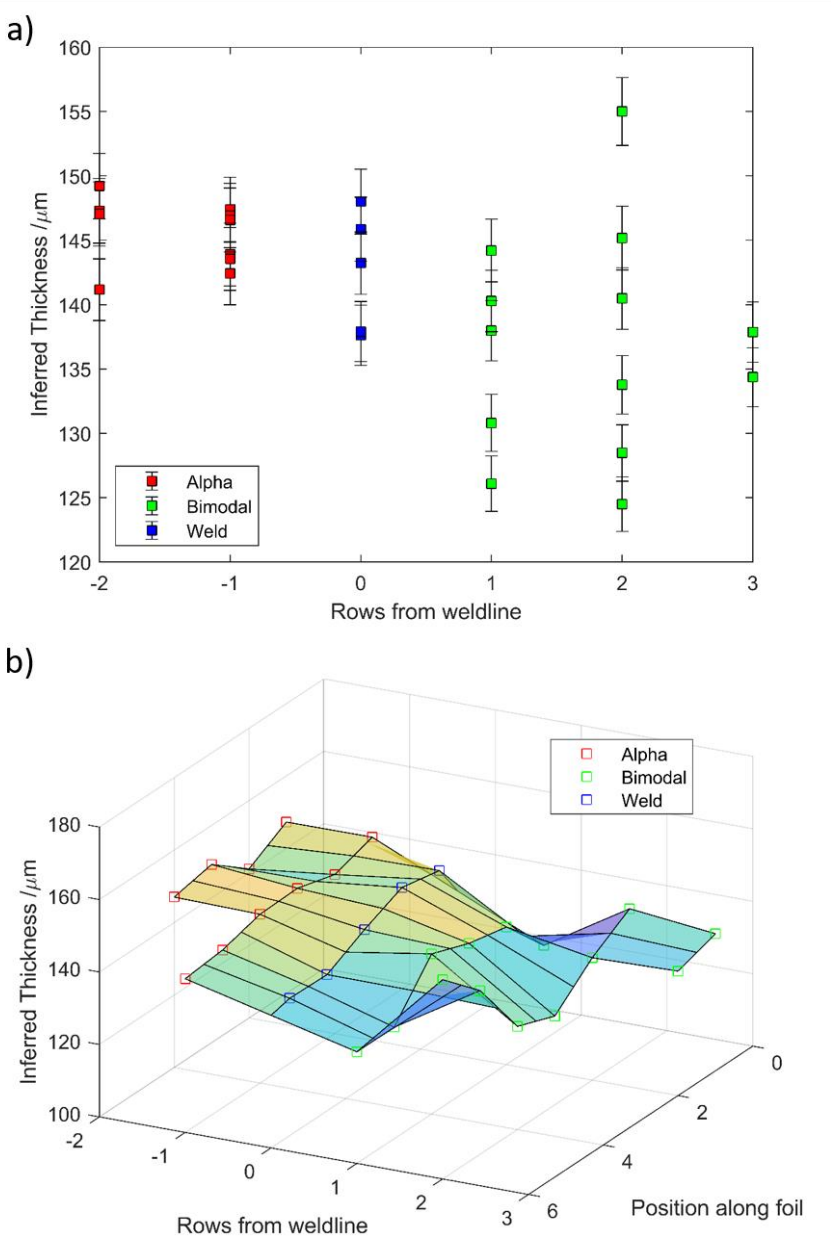



*Figure 41: Perfect coupling inferred thickness in samples of set Foil 1. Panel a) shows the measurements by number of rows to the weld line, while panel b) shows a surface plot of samples by position within the row.*

In order to validate this analysis, the thickness of the sample at the fracture surface was measured of a subset of samples. Figure 42 shows the agreement between the inferred thickness and the measured thickness. Despite the discrepancy, the inferred thickness is often trending in the correct direction from the mean thickness of 145 µm, and the spread roughly agree. However, it is clear that the perfect coupling, which assumes all geometric variations are

accounted by a thickness variation, is insufficient at predicting thickness or variations in dynamic response.

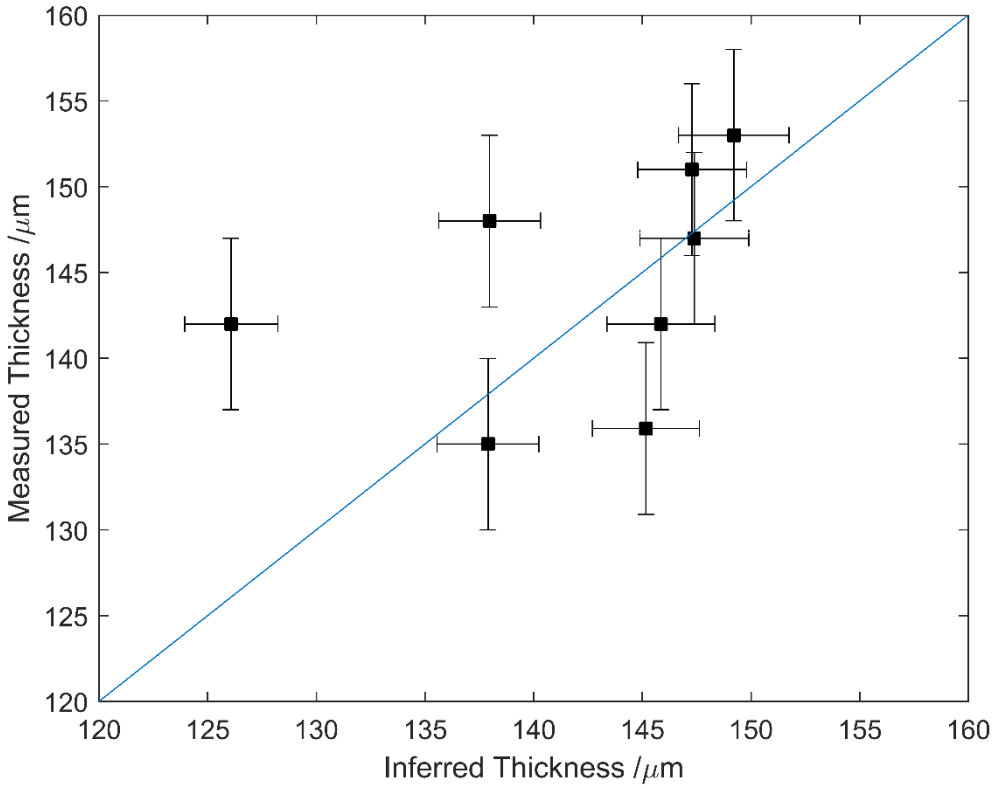



*Figure 42: Perfect Coupling validation through measured and inferred thickness of Foil 1 samples. Black points represent individual samples representative of the set, and the blue line is a guide to the eye for equal measurement.*

The results from this foil show several key points:

- The impact of geometrical variations due to the mounting and grinding step on dynamic response.
- The influence of the laser cutting recast layer in fatigue response, notably that weld specimens have approximately the same fatigue strength.
- The utility of analytical methods such as perfect coupling to use dynamic response to inform the understanding of sample geometry. While geometry ought to be measured post-fracture, a more accurate understanding of sample geometry pre-test can ensure more accurate stress determination during the protocol itself.

#### 2.4.1.7. Electropolishing

The laser-cutting process creates a recast and/or oxide layer at most 5 µm thick. This can be inspected visually, through either SEM imaging of as-received cut specimens, or through cross sections, shown in Figure 43. This layer is not conducive to representative fatigue measurements: in addition to its deviation from microstructures representative of the underlying material, the surface is very rough and introduces significant stress concentrators. This material will need to be removed, though this is not possible through mechanical means, as it plates the surfaces perpendicular to the foil surface.

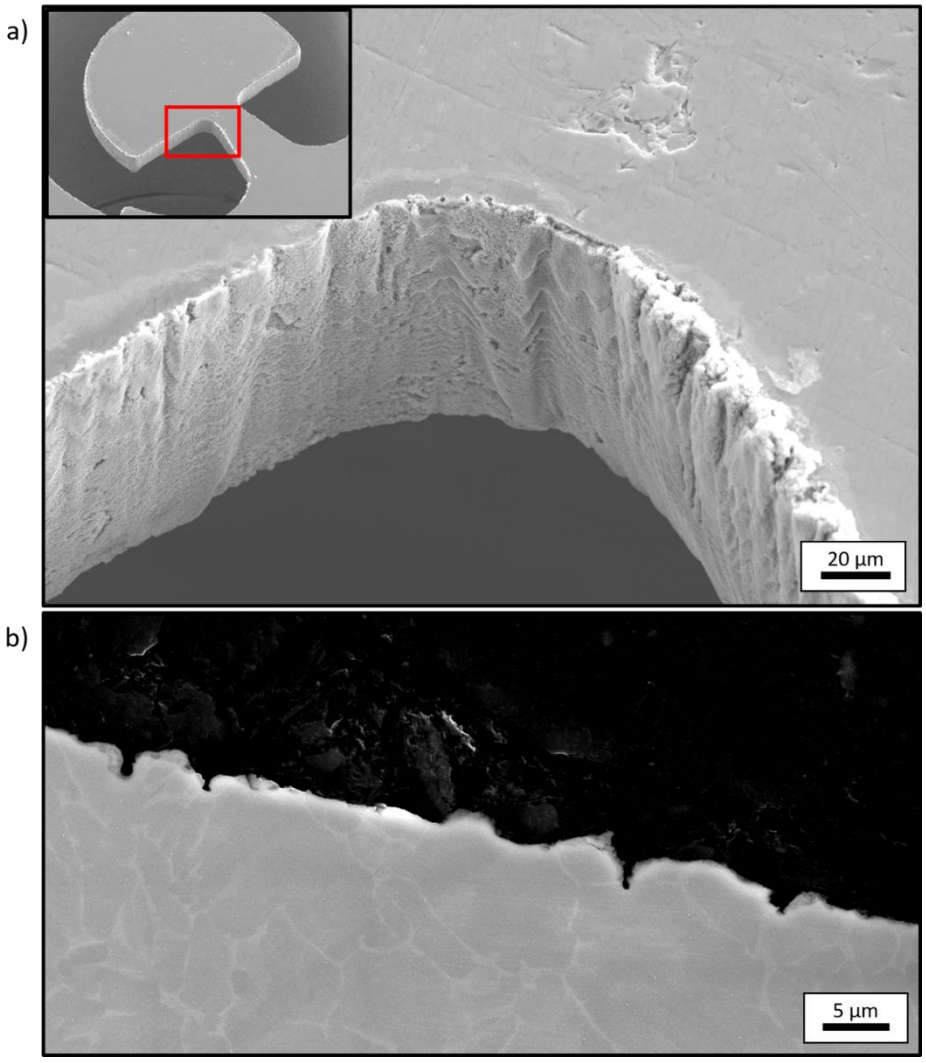



*Figure 43: Damage layer from as-received laser cut cantilever edge in Foil 1. Panel a) shows angled view of full cantilever with inset showing location. Panel b) shows cross section of an offcut in Foil 1, with Bakelite (top, dark) and titanium globular alpha microstructure (bottom, lighter).*

To resolve this, electropolishing can be used, etching material preferentially in regions with high curvature such as surface asperities. In addition to removing the undesirable laser recast layer, this finishing process will allow the foil surfaces to be polished for microstructural evaluation as well as rounding the edges. The routine used for electropolishing meso-cantilevers is built on the method from Peighambardoust *et al.* [359], followed by improvements by Dr Gong and Dr Arutyunyan.

The electropolishing routine in this case, developed primarily through iterative experiments, optimises for both the removal of the recast layer and a uniform surface finish. The composition of the electrolyte has not changed since that developed by Dr Arutyunyan, though the exact particulars of the experiment were changed in order to ensure better quality and consistency across parts.

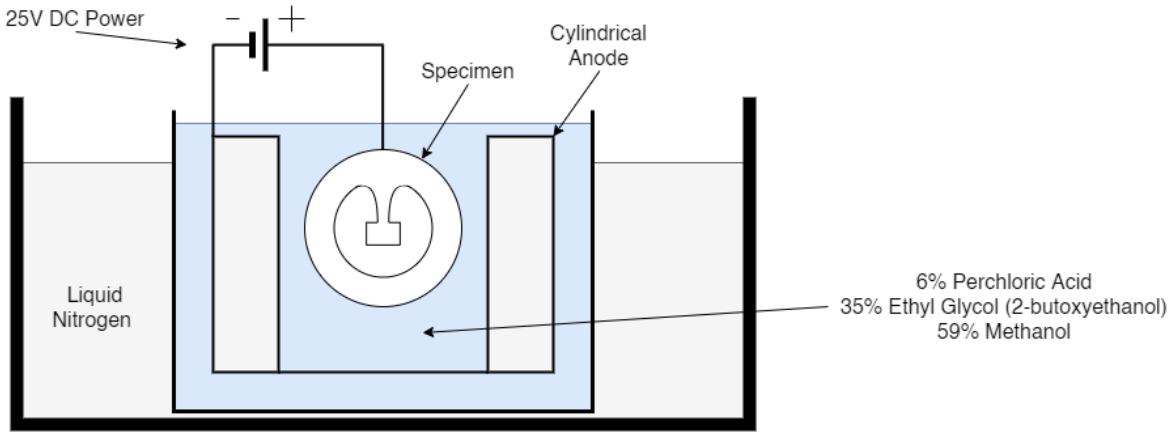



*Figure 44: Diagram of electropolishing setup, showing electrical setup, thermal containment, and chemical composition.*

A diagram of the experimental setup is shown in Figure 44. The electrolyte solution composition is as follows:

- 59% Methanol
- 35% 2-bytoxyethanol (also referred to as ethyl glycol)
- 6% Perchloric acid solution from 70% stock

The methanol is understood as reducing the concentration of the acid, while the ethyl glycol acts as both a surfactant and as a thickening agent.

200 mL of the electrolyte solution is prepared and chilled to -50 ± 5°C by placing the beaker in a liquid nitrogen bath, all in a double-walled plastic contained. Two magnetic stir bars are used, one in the beaker and one in the bath, held at 300 rpm in order to ensure uniform concentration and temperature, without introducing significant currents.

The power supply should be set up with the specimen as the anode, and a cylindrical cathode ensuring uniform electric fields should be almost fully submerged in the solution.

Each specimen is held using platinum-tipped tweezers that are electrically connected to a power supply at 25 V DC in constant voltage mode. The specimen is dipped to solution, only just below the surface, at the centre of the vortex. Using a timer, the sample is held for 10 s intervals, and the current is observed to rise rapidly to a maximum of 0.2 A, reducing exponentially to a fraction of this at the end of 20 seconds. At the end of the allotted time, the sample is immediately pulled out of solution, rapidly submerged and vigorously stirred in a separate beaker of room temperature methanol, followed by room temperature water, followed finally by a burst of compressed air to dry. The timeliness and specific parts of this process have been observed to strongly affect the quality of the polishing.

Samples are repeatedly polished and observed under an optical microscope at 20x magnification under crossed polarisers in order to evaluate the condition of the recast layer. In this state, the recast layer is often clearly visible, indicating further polishing is required. It is best practice to polish all the specimens in this manner sequentially, followed by a repeat in reverse order to re-polish, accounting for time-dependent variations. This process is repeated until the polishing quality is satisfactory – until the recast layer is no longer visible. In the case of titanium specimens, it is considered satisfactory when the edges do not contain any visible recast layer, and the microstructure can be seen through crossed polarisers.

### *Batch polishing*

When polishing large numbers of samples, it is not possible to polish all of them in one batch. This is both a consideration of practicality—polishing 100 specimens can lead to loss of specimen due to misplacement—as well as consideration of the amount of time that an electrolyte may be used. It has been observed that the polishing quality of the first specimen is consistently poor, internally hypothesised as due to the lack of titanium ions present in solution. Equally, a solution may be over-used when many samples have been polished, with the achievable quality of samples reducing when the solution has reached 1000 s of polishing time. Therefore, the common practice is to "age" the solution with a test specimen of the same material (a "throwaway" sample), and to limit the use of an electrolyte to 1000 s of polishing time.

The process by which a batch of specimens is polished therefore will begin with each sample receiving a certain amount of polishing, followed by individual evaluation leading to variable amounts of time for each sample. Table 4 shows an example table representing the polishing time for a batch of specimens. Each pass is carried out in reverse order relative to the previous pass, with the pass time indicated below in seconds.

*Table 4: Example table of polishing for a batch of specimens. Sample F8 in this case is a "throwaway" sample, and is only polished for one pass only.*

| Sample | F8 | O8 | P1 | P5 | P9 | Q4 | Q8 | R1 | R5 | R9 | S4 | S8 |
|---|---|---|---|---|---|---|---|---|---|---|---|---|
| Pass 1 /s | 30 | 30 | 30 | 30 | 30 | 30 | 30 | 30 | 30 | 30 | 30 | 30 |
| Pass 2 /s | | 30 | 30 | 30 | 30 | 30 | 30 | 30 | 30 | 30 | 30 | 30 |
| Pass 3 /s | | 60 | 50 | 30 | 30 | 30 | 30 | 60 | 20 | | | |
| Pass 4 /s | | 60 | 50 | 40 | 40 | | 40 | 60 | | | | |
| Pass 5 /s | | | 40 | 40 | 60 | | 40 | 40 | | | | |

Similarly, within each LFW foil, specimens were allocated batches in alternating order as seen in Table 5. This would divide samples from one foil into two batches, ensuring an average response across a foil.

*Table 5: Example of batch allocation across a foil. Here, the letters refer to slots in a conventional TEM Grid holder box.*

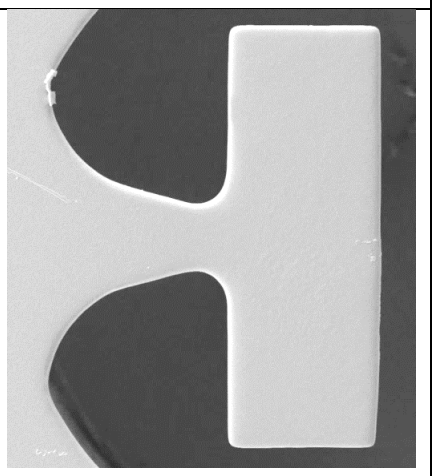
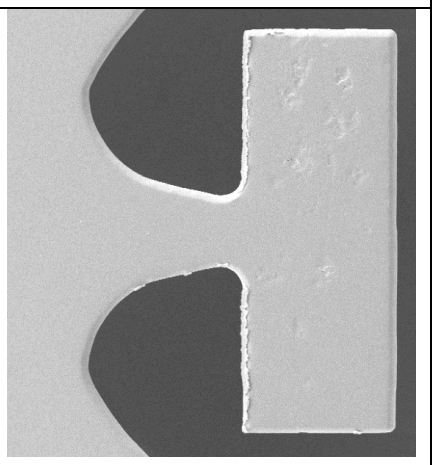
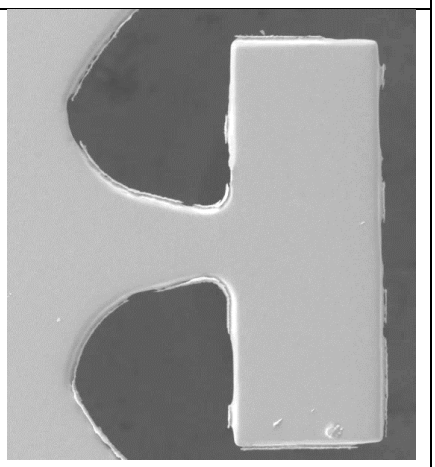
| Sample | A1 | A3 | A5 | A7 | A9 | B2 | B4 | B6 | B8 | … |
|---|---|---|---|---|---|---|---|---|---|---|
| EP Batch | 1 | 2 | 1 | 2 | 1 | 2 | 1 | 2 | 1 | … |

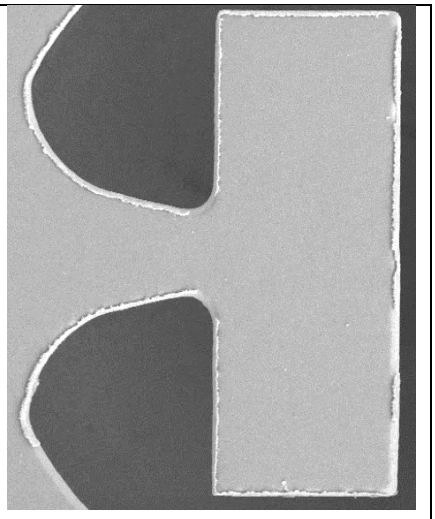
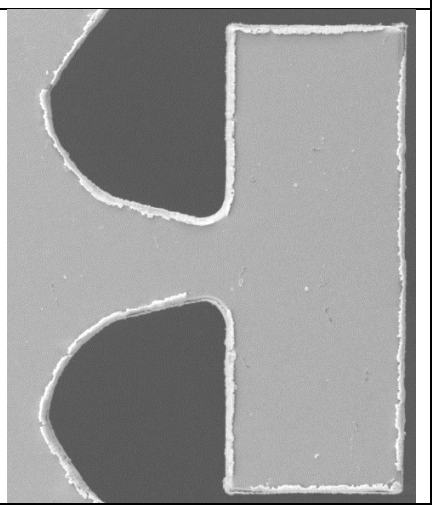
This method has been developed in order to minimise the inconsistency between specimens, mainly by attempting to control the multiple variables inherent to electropolishing. These variables however are not fully controllable, with several variables occurring within a batch of electropolishing, as well as some between batches. This list of variables is identified below:

- Inter Batch variables
  - Exact concentrations in electrolyte
  - Exact voltage on the power supply
  - Quality of electrolyte components (age of components)
- Intra-batch variables
  - Temperature of solution
  - Water content from frost
  - Fluid dynamics from stir bar rotation speed
  - Depth, position, and angle of sample held in the solution
  - Current density on the sample
  - Number of passes for a sample: either through thermal shock, or through the immediate removal of the passive oxidation layer: it is well observed that the current is dramatically higher at the beginning.
  - Time where potential difference is 0: at the beginning of each pass, between 10s increments, or at the end.
  - Concentration of titanium ions (age of solution)
  - Evaporation of solution
  - User fatigue

This list is non-exhaustive, but captures the variability in electropolishing quality. For this reason, the optical microscopy verification of polishing quality is used to determine the time required, but remains inadequate for ensuring fully polished specimens. A subjective quality metric is therefore recorded for all specimens that are measured in SEM post-electropolishing. This can be seen in Table 6.

*Table 6: Electropolishing quality rubric, showing descriptions and representative SEM micrographs as a visual aid.*

| Quality | Description | SEM Image<br><br>~300 µm<br><br>▬▬▬ |
|---|---|---|
| 10 | No recast layer remaining on the neck, smooth edges and clear microstructure. |  |
| 8 | Minimal recast layer remaining on the neck, with only small asperities. Some pitting in surface away from the neck allowed. |  |
| 6 | Some recast layer remaining on the neck, mostly on the negative (broader) side, weakly tied to the surface. |  |

| | | |
|---|---|---|
| 4 | Recast layer remaining on positive (narrower) side, strongly bonded. |  |
| 2 | Significant recast layer remaining. |  |

In later experiments (Foils 3&4 and 7-11), only samples with a quality of 6 and above were tested, with the aim to reduce the effect of this damage layer. This would provide confidence that the bulk material properties are being sampled through fatigue loading.

#### 2.4.1.8. Design and Testing of Foil 2

A second foil was cut as an intermediate test bed, also to 250 µm, for the purposes of collecting data from electropolished samples. Following a more extensive grinding step, the thickness was measured to be 70 ± 5 µm and a square size of approximately 32 x 22 cm. An added feature to the design in the foil layout was that of the crossbar on the far end of the cantilever disc, allowing for the identification of the incoming and outgoing laser side. The design was further improved,

with a reduced stress concentration of 10%, a resonant frequency of 29 kHz and an induced stress of 0.6 to 1 GPa at 70 µm with some thickness reduction. The design is shown in Figure 45.

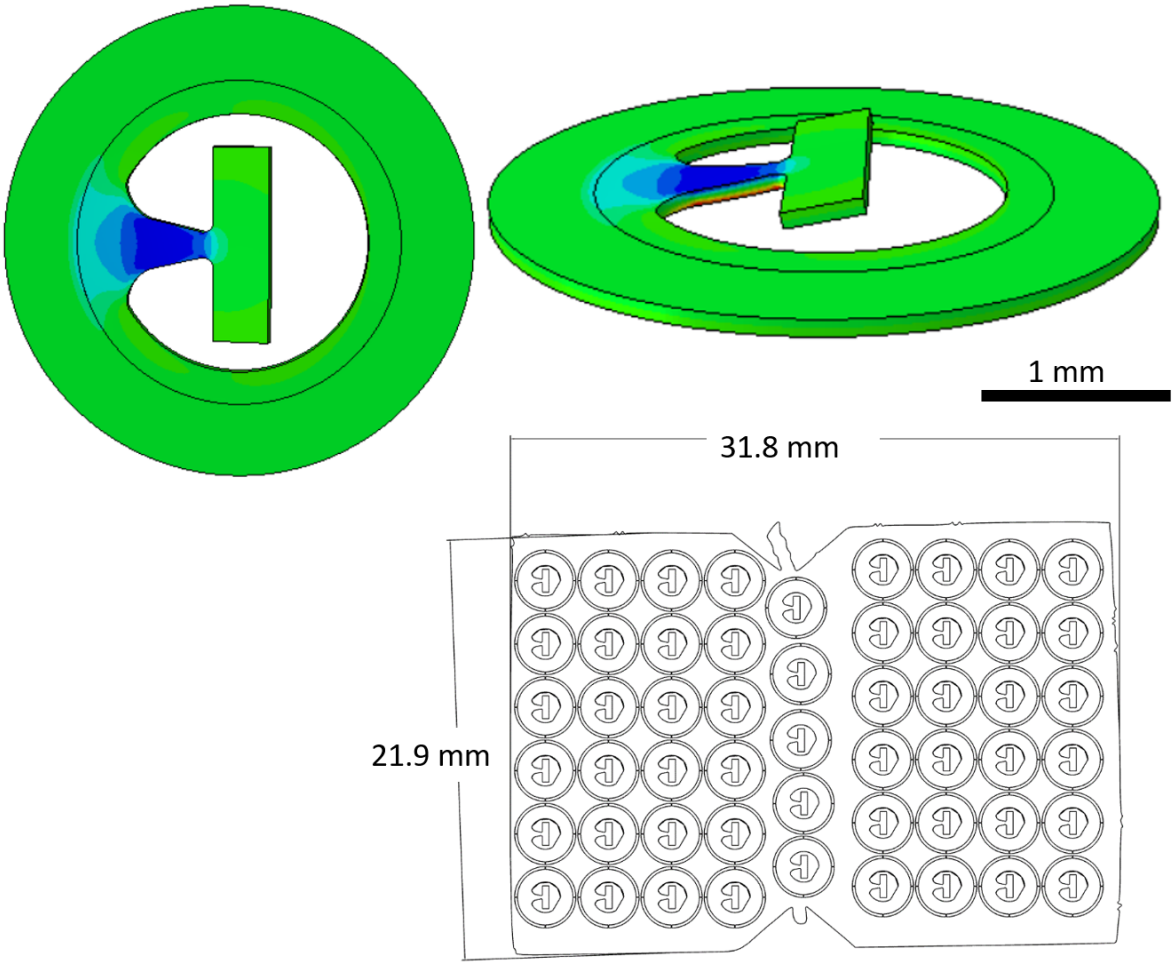



*Figure 45: Cantilever design (top), and layout on foil 2 for the second batch of specimens.*

This foil provided a basis for the development of the electropolishing routine described above. Samples in this case were polished with the above chemistry and temperature, using a range of voltages between 15 V and 20 V, and a range of duration between 10 s and 30 s. However, the quality as verified in SEM post-polishing and post-fracture remained inadequate: using the rubric above, few samples would have a quality greater than 4.

Furthermore, during electropolishing it was discovered that a mis-registration during the laser cutting caused a shift in the position of the cantilevers by approximately 400 µm. While this did

not affect the bulk specimens, the neck region of weld-line specimens were therefore primarily bimodal Heat Affected Zone (HAZ).

With these caveats, the results of the SN data recorded in a similar fashion as Foil 1 are shown in Figure 46. In this case, the Perfect Coupling corrected stresses are shown, owing to their improved estimate of bending stress.

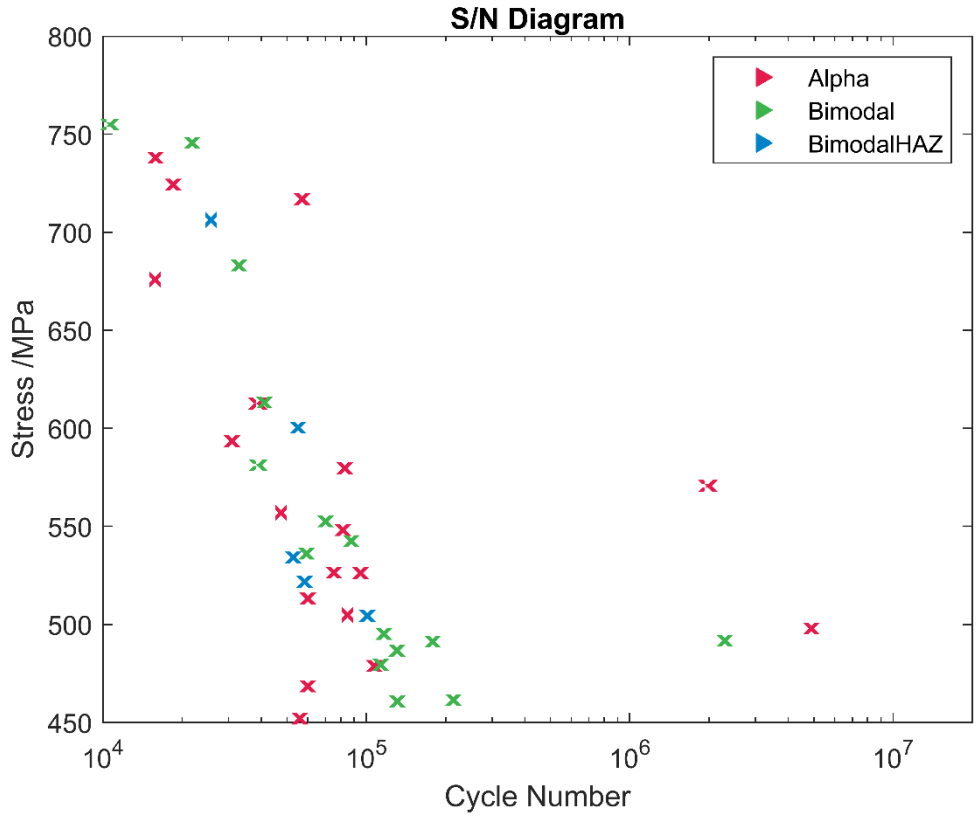



*Figure 46: Perfect coupling corrected SN plot of Foil 2 samples.*

The results of Foil 2 broadly agree with those of Foil 1 in page 91, with a fatigue limit of approximately 500 MPa. It can be seen that the fatigue response of the bulk is similar between parent materials, and the Bimodal HAZ. However, despite the electropolishing, the position of the elbow and the mean has not changed, implying little to no fatigue debit from the laser damage layer.

This seemingly surprising result warrants further investigation. Insight can be gained from observing the predicted variation in thickness from the Perfect Coupling analysis. The inferred

thicknesses varied from ~58 μm to ~78 μm, a range closer to 30%, compared to the Foil 1 range of ~ 20%. Furthermore, when measuring a subset of samples post-fracture, the variation even for those near the original design thickness was significant, with both of these results shown in Figure 47.

The results from this foil therefore show several key points:

- The sensitivity of the laser cutting process to correct registration of samples.
- The necessity for developing electropolishing routines with more consistent surface quality.
- The increased impact in geometrical variation from electropolishing.
- The limited extent to which analytical methods such as perfect coupling can be used to account for this, either in unpolished or in polished specimens.

A more detailed routine to account for the dimensional variation is necessary, in order to produce reliable fatigue data. As this experiment does not measure stress directly, and there is an interest in understanding the inherent variation in fatigue strength of materials, it is necessary to reduce as much as possible the extrinsic variations from variable surface quality or variable dynamic response.

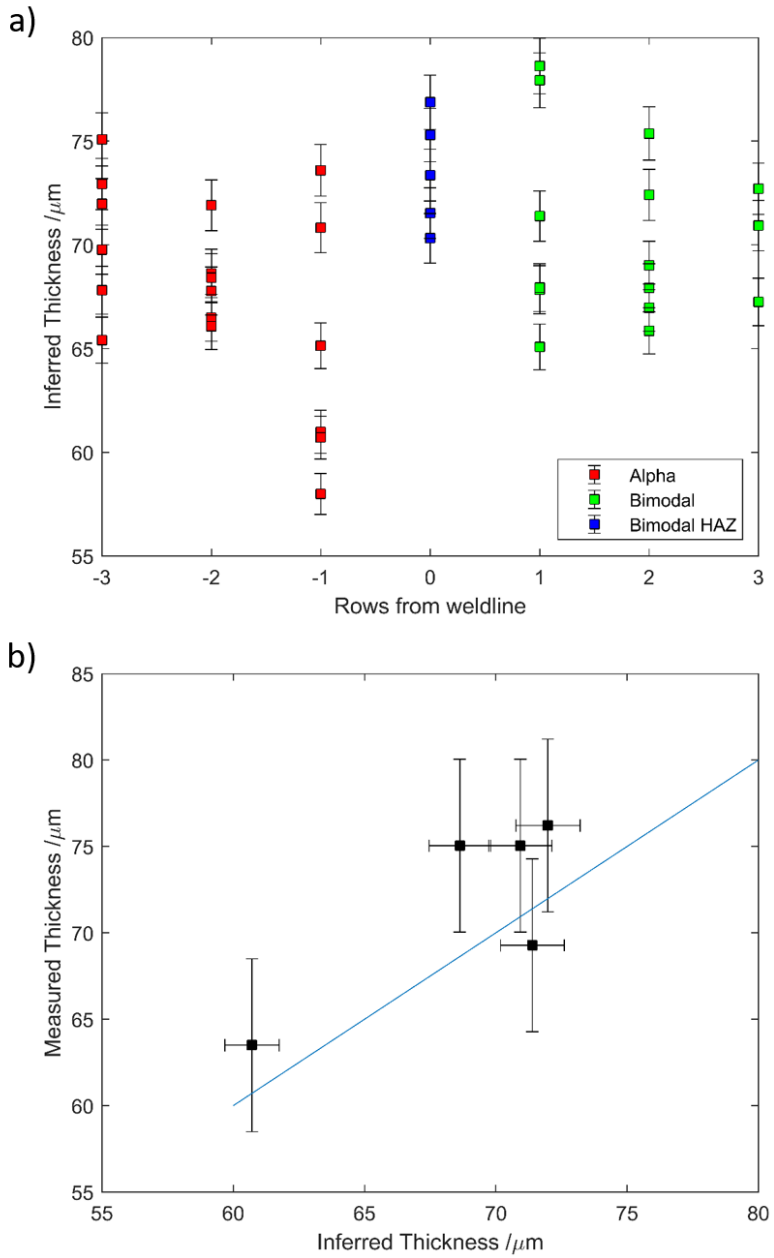



*Figure 47: Inferred thickness of samples in set Foil 2, shown in a) as a function of distance from weld line, and in b) as scatter against the post-fracture SEM measured thickness.*

#### 2.4.1.9. Dimensional Variation

In solving the challenge of removing the undesired recast layer, electropolishing creates further variability in the geometric dimensions. In part, this is due to the prioritisation of polishing quality over consistency in polishing time, leading to some samples requiring longer polishing times. In part, this is due to the challenges of controlling all the variables in electropolishing for such small samples with detailed geometries.

However, this causes amplified variations in dynamic response as the fatigue testing system is highly sensitive to geometric variations (this is discussed further in the Geometrical Analysis Section 2.4.1.11). Small variations in dimension change the system's resonant frequency, the cantilever's stiffness, and the stress induced per unit angle, often in complex relationships. It is therefore important to measure the dimensions of all of the cantilevers in order to understand each sample's individual response to a driving frequency.

This is carried out in the SEM in order to produce the most accurate measurements. The laser cut dimensions can be measured by placing 6 samples at a time in a 6-specimen holder, using the following SEM parameters for consistency:

- Working Distance: 20 mm
- Current: 1 nA
- Acceleration Voltage: 20 kV
- Magnification: 60x (or 50x if this does not capture the entire cantilever).

To reduce error and ensure accurate measurements, the SEM measurements are calibrated against known calibration samples at the same viewing parameters. When measuring the thickness of foils, the process can be expedited by mounting several at a time in a TEM grid holder. The measurement parameters are the same, save for the magnification at 500x to maximise accuracy.

Extra care must be given to measuring the foils with the side in which the laser penetrates the foil facing up. This is due to another artefact of laser cutting: tapering. As the laser ablates material during cutting, the side facing the laser is ablated more heavily than the opposing face. This leads to a slight taper in the cutting face. As this measurement would be practically challenging to measure before testing, and is a function of the geometry, the best practice developed is to measure the foil dimensions with the smaller side (incoming laser side) facing up, such that the

measurement can be carefully made at the estimated mid-point of the taper. An example figure showing these cardinal measurements is shown in Figure 48.

Nevertheless, these measured dimensions will be imprecise and inaccurate, particularly for thickness as this is measured on the edge of the circular disc, rather than with a view of the neck of the cantilever – the cantilever neck thickness remains uncertain. Furthermore, electropolishing can cause significant variation in the thickness of the foil, especially across the large distance from the neck to the edge of the disc. This can be seen clearly when viewing the samples edge on and comparing the thickness from one side to another, as seen in Figure 49.

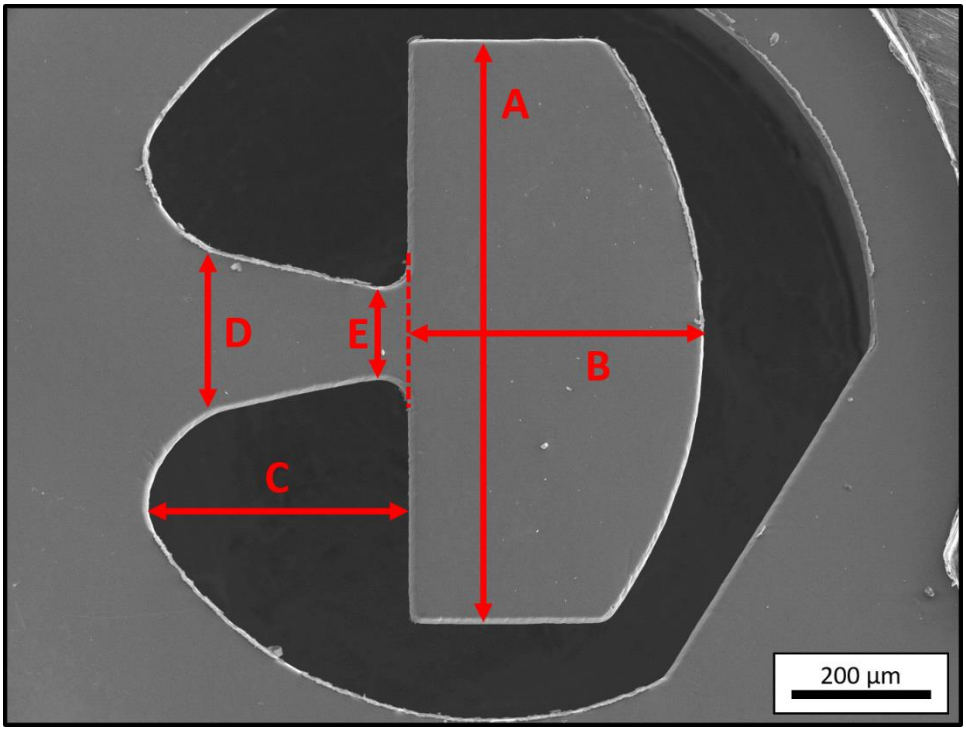



*Figure 48: Diagram of cardinal measurements made in a meso cantilever of Ti-64. This particular cantilever was M2 from sample set Foil 3&4 with a designated polishing quality of 9, and viewed with parameters as described above.*

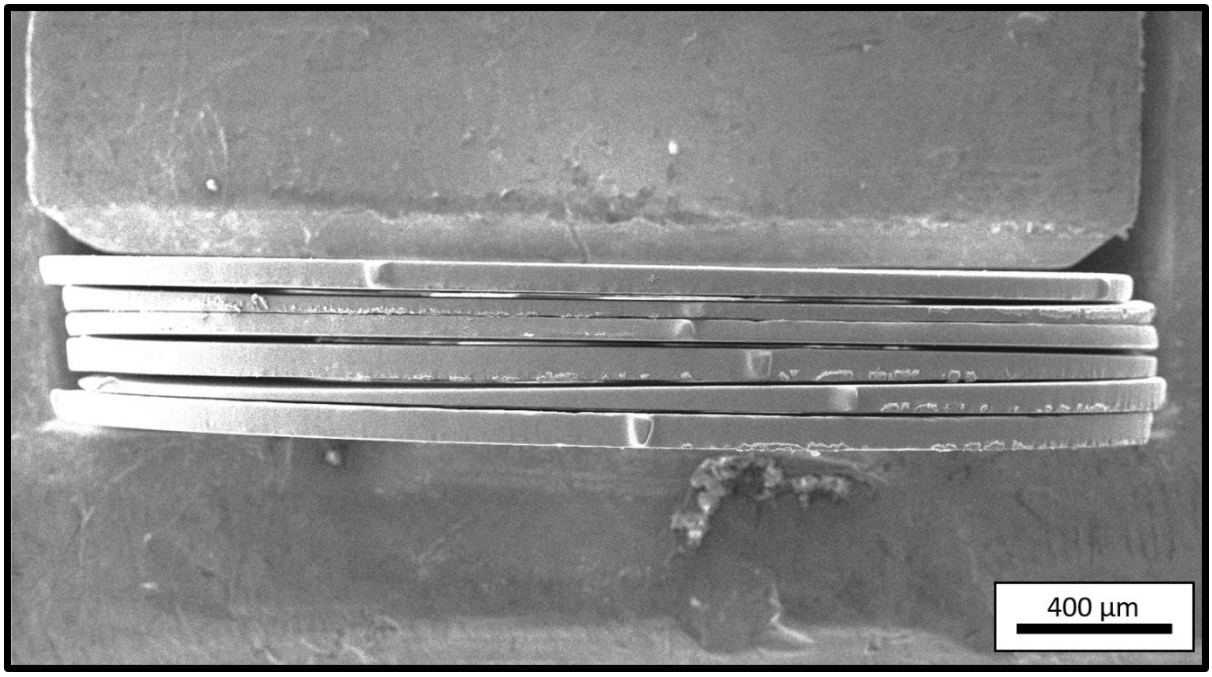



*Figure 49: Example of extreme variation in thickness on electropolished Ti-64 cantilevers in sample set Foil 3&4. Imaged in Auriga FEG SEM at 38x magnification with zero tilt.*

#### 2.4.1.10. Stiffness Measurement

The dimensions measured above can be used to calculate the cantilever resonant frequency and the stress per unit deflection angle. However, within our experimental setup, these cannot be measured directly. It is therefore instructive to validate the above dimension measurements with a quantity that can be measured experimentally: bending stiffness.

Using a KLA Tencor G200 nanoindenter, the load-displacement curve of the cantilever beam can be measured, and a beam stiffness can be collected without damaging the specimen (as loads are approximately 100 MPa). This can be compared to the FEM model beam stiffness for a specific geometry, providing insight into the accuracy of these measurements.

In carrying out these measurements, the importance lies in reducing any errors and biases that may arise. The process involves indenting a known location relative to the corners of the hammer twice: once to make a mark and the second such that the indenter tip “seats” into this mark. This technique reduces the influence of the materials bulk stiffness by plastically deforming a hole and maximising the contact area of the tip, thereby reducing the pressure on the surface. The method

also collects data for the tip retracting in air following the bending test, allowing for a correction of the “in-air”, or frame, stiffness.

The samples are held in place via a custom-machined holder shown in Figure 50. The first version held one sample per loading batch in an inner cylinder with a grub screw, nested into an outer one also held in place by grub screw. The second version allowed five samples to be loaded per batch, machined out of one single piece of aluminium to reduce compliance. The exact experimental procedure is detailed in the Appendix under Nanoindentation Stiffness Measurement Procedure on page 252.




*Figure 50: Sample holder for nanoindentation, Mark 1 (left) and Mark 2 (right).*

The excel files containing the raw load-displacement data are fed into a MATLAB script adapted from Dr Kumamoto, and iterated on to improve robustness and account for the frame stiffness. This code can be found under the GitHub repository cmmagazz/MesoCantileverStiffness (available upon request). In brief, the unloading portion of the curve is determined via a load drop of some threshold, and k-means clustering divides the unloading portion into the “on-specimen” and “in-air” sections. The unloading curve is normalised to the “in-air” section, removing the frame stiffness contribution. Of the “on-specimen” unloading curve, the first point is discarded, as

are the last 20%, in order to reduce effects from plasticity and sampling noise. An example curve is shown in Figure 51.

This process was found to be robust while sufficiently simple to confidently assess all specimens. With the steps above to mitigate compliance and variation from sample to sample, it can be shown in Table 7 that the error is on the order of 5% for the Mark 1 holder, and lower for Mark 2.

*Table 7: Methodological error measurement for nanoindentation stiffness. Four specimens from Foil 3 & 4 were chosen at random, using the Mark 1 holder.*

| Stiffness N/m | | | | | | | |
|---|---|---|---|---|---|---|---|
| Repeat 1 | 2 | 3 | 4 | Mean | Standard Deviation | Standard Error /% | Error /% |
| 4265 | 4776 | 3795 | 4507 | 4336 | 417 | 4.8 | 9.6 |
| 3779 | 4762 | 4801 | 4406 | 4437 | 473 | 5.3 | 10.7 |
| 2463 | 2563 | 2376 | 2236 | 2410 | 139 | 2.9 | 5.8 |
| 1928 | 1909 | 1876 | 1955 | 1917 | 33 | 0.9 | 1.7 |
| | | | | | Mean: | **3.5** | **6.9** |

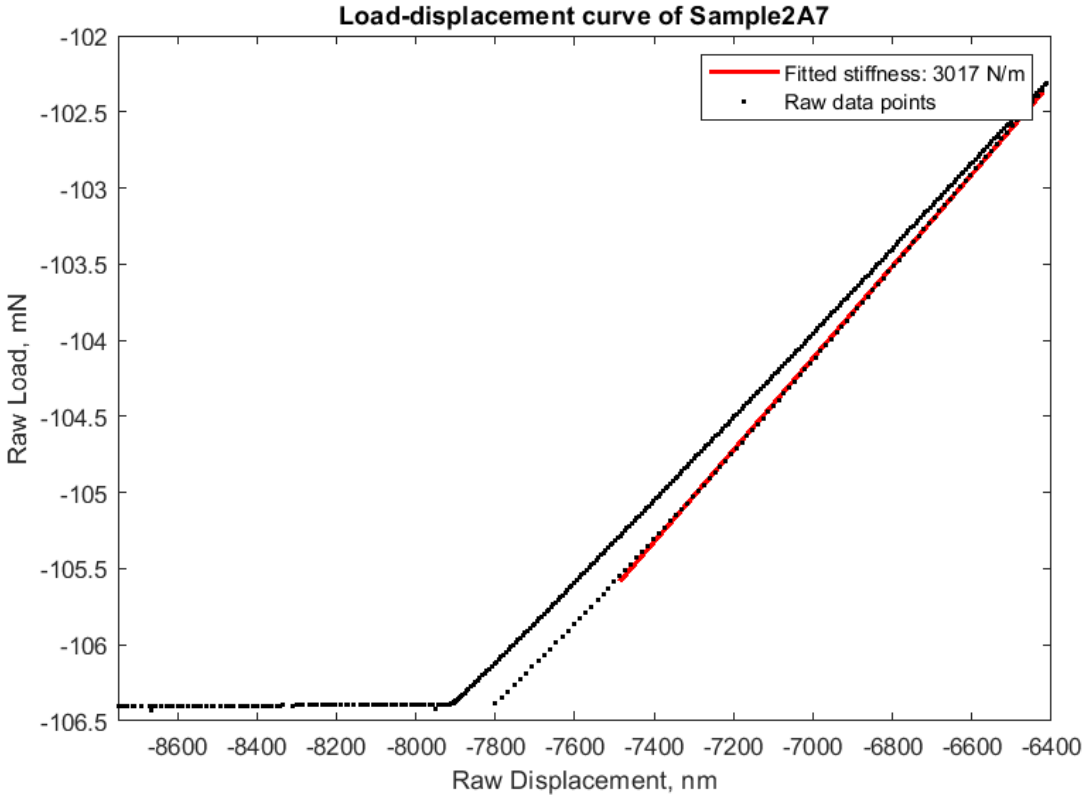



*Figure 51: Example nanoindentation dataset of sample 2A7 of the sample set Foil 7-11, showing the load-displacement curve of the second indent. The black points represent the raw data, corrected for frame stiffness. The red line represents the unloading fit to determine the beam stiffness.*

This data provides a direct measurement of the mechanical response, which can be compared to the ABAQUS simulations. Earlier experiments from Drs Gong and Arutyunyan would use this data to validate general models across samples, ensuring that the error from the experiment and simulation would be minimal. However, as shown later in results on page 110, these results would often differ from experiment to simulation by multiple integer factors, with population spreads similarly broad amongst an experimental sample set. This significant variation would need to be accounted for on a sample-by-sample basis.

#### 2.4.1.11. Geometrical Analysis

In observing the variation of thickness within a sample in Figure 49, it can be seen that the thickness variations between samples can vary by a factor of two. These variations in thickness between samples highlight a challenge in this experiment: electropolishing is necessary to remove a damage layer, but creates a highly varied sample set. Across this set, the variations of all measured lengths can dramatically affect the dynamic response during fatigue testing.

With the aim of developing a good understanding of the system, as well as to plan for corrections to post-fatigue measurements, it is better to develop parametric relationships between these geometric measurements and the relevant dynamic responses rather than single simulations for each measurement. In this way, should a specimen be measured to have a different thickness during fractography for instance, the parametric model can be used to determine the new stress per unit angle, and thereby correct for the stress tested.

A naïve approach to this would be to create N sampling points for each dimension measured, spanning the extent of measurements made. However, 10 measurements per dimensions would require $10^6$ simulations, an impractical quantity. A solution for this can be found by considering a typical dataset collected.

To better observe the variations in geometry, we can plot each recorded cardinal length on a scatter plot matrix, as seen in Figure 52.

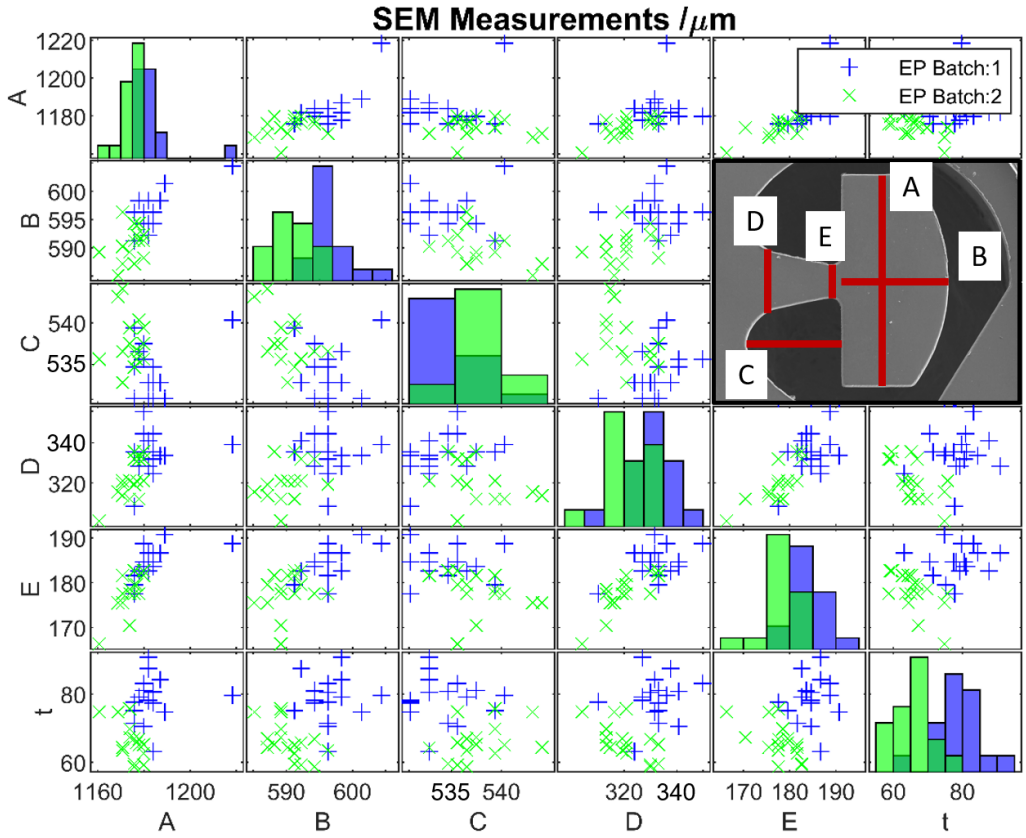



*Figure 52: Scatter plot matrix of geometric measurements across set Foil 3&4. The colour denotes the electropolishing batch, while the axes denote the cardinal lengths measured, as shown in the inset. Across the diagonal, the histograms of each measurement are shown.*

Here, it can be seen that most measurements have an approximately normal distribution. However, between measurements, for instance between A and B, there is a modest correlation. This correlation is seen, with varying strengths, across many other pairs of measurements, most strongly between A and E. This relationship is positive between measurements of material (such as A and E), and negative between measurements of material and gaps (such as C and E).

A physical explanation for this can made from the electropolishing step, where material is removed: in general, where more material has been removed on one part of the cantilever, more is removed on another. This causes correlations between respective measurements, as more-polished samples trend in a certain direction. Furthermore, the second batch of polishing can be seen to have lower measurements than batch 1, indicating that one aspect of the electropolishing routine has changed and on average, more material was removed. The correlation between the

measurements of cardinal lengths suggests that to span the space of measurements made, it is not necessary to span the entire N dimensional space defined by its maximum extents.

Principal Component Analysis (PCA) can be used to reduce the dimensionality of the dataset by considering the orthogonal axes containing the highest variance in the dataset. Detailed derivations and explanations of the PCA process can be found in the literature [360]–[362], and a brief outline is given here:

- Consider m rows of d dimensional data $\boldsymbol{X}$ as: $m \times d$
- An $d \times d$ matrix $\boldsymbol{A}$ describes the covariance of this matrix, that can be intuited as describing the correlation between one dimension to another.
- The eigenvalues $\lambda$ and eigenvectors $v$ can be found by solving the equation: $\det(\boldsymbol{A} - \lambda \boldsymbol{I}) = 0$.
- These eigenvalues and eigenvectors each satisfy the relationship: $\boldsymbol{A}v = \lambda v$, which can be thought of as defining orthogonal axes based on the covariance of the data.

This effectively creates a rotated coordinate basis for the data, which can be ordered such that the first basis vector represents the axis with the highest covariance, and subsequent axes describing the decreasing amounts of variation in the data. The data can then be rotated out of this reference frame, but omitting later basis vectors effectively projecting the data onto a small sub-space. This is carried out by considering an eigenvector matrix $\boldsymbol{W}$ of $d \times k$ size, where $k$ is the number of eigenvectors to consider. The transformation is carried out through the equation $\boldsymbol{Y} = \boldsymbol{W}' \times \boldsymbol{X}$, reducing the dimensionality of the data from $m \times d$ to $k \times d$.

Visually, this can be understood by considering a cloud of points along the x-y plane with some linear correlation. PCA determines the two eigenvectors describing the “long” axis, and the “short” axis of this data: these two vectors form the new coordinate basis for fully describing the data. The dimensionality of this data can be reduced by projecting the data onto the “long” axis alone, retaining the majority of the trend in the data. This visual example highlights a

requirement in this method: that the data be normally distributed across these axes. However, in visualising the measurement data above, this can be seen to be a reasonable assumption. The relative extent of covariance, described by the eigenvalues, often follows a bi-linear trend when plotted in a "Scree" plot as shown in Figure 53: some initial set of eigenvalues represent the bulk of the variation in the data, followed broadly by noise and other factors.

This allows for a reduction in the datasets dimensionality, allowing for the parametric fitting described above without unreasonable simulation time. N points would be spaced equally across the remaining dimensions, offering an $N^{m-k}$ times reduction in simulation time per dimension removed. For example, if the 6 dimensions were reduced to 2, 10 equally spaced points per dimension would require only $10^2$ dimensions, not $10^6$, reducing computation by a factor of $10^4$.

In effect, this method simply chooses where to place the sample points: in the visual case described above, it can be seen that it is not necessary to place sample points in the quadrants of the x-y space not covered by the data.

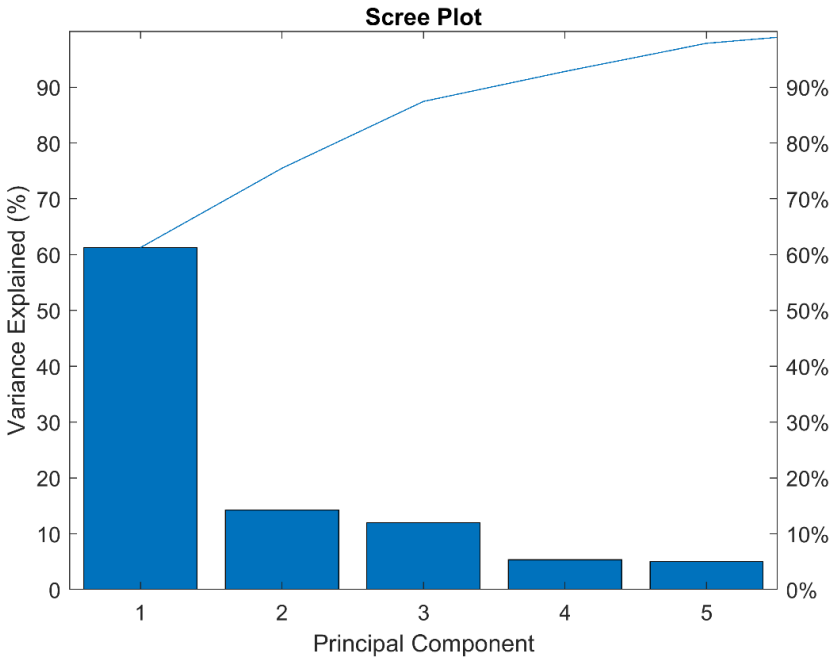



*Figure 53: Scree plot of the set Foil 3&4, showing the variance explained for each PC (blue bars), alongside the cumulative variance explained in the dataset (blue line).*

Using the example of the dataset above, a scree plot in Figure 53 shows that the first three components describes over 85% of the variance in the dataset. Using these three axes, 10 equally spaced points are used, requiring $10^3$ simulations. For ease, this can be reduced further to 5 points per component, requiring only 125 simulations for a full parametric understanding of dynamic response to a geometric variation. These simulations can be completed within a few days on a high-powered computer when using sufficient mesh density, as each computation requires approximately 30 – 60 minutes, a significant improvement to the otherwise impossible computational requirement. For visualisation purposes, the method is shown in this section using 2 principal components.

When decomposing the data in this way, each measurement obtains a coordinate value in “PC space”. Reducing dimensionality is achieved by simply considering the first *n* coordinates, with the code shown in the GitHub repository cmmagazz/AnalysisofCantileverDimensions. In this fashion, the minimum and maximum values across the dataset in those first *n* dimensions can be used to lay N equally spaced points. These points can then be re-transformed from “PC space” into “Real space”, as shown in Figure 54.

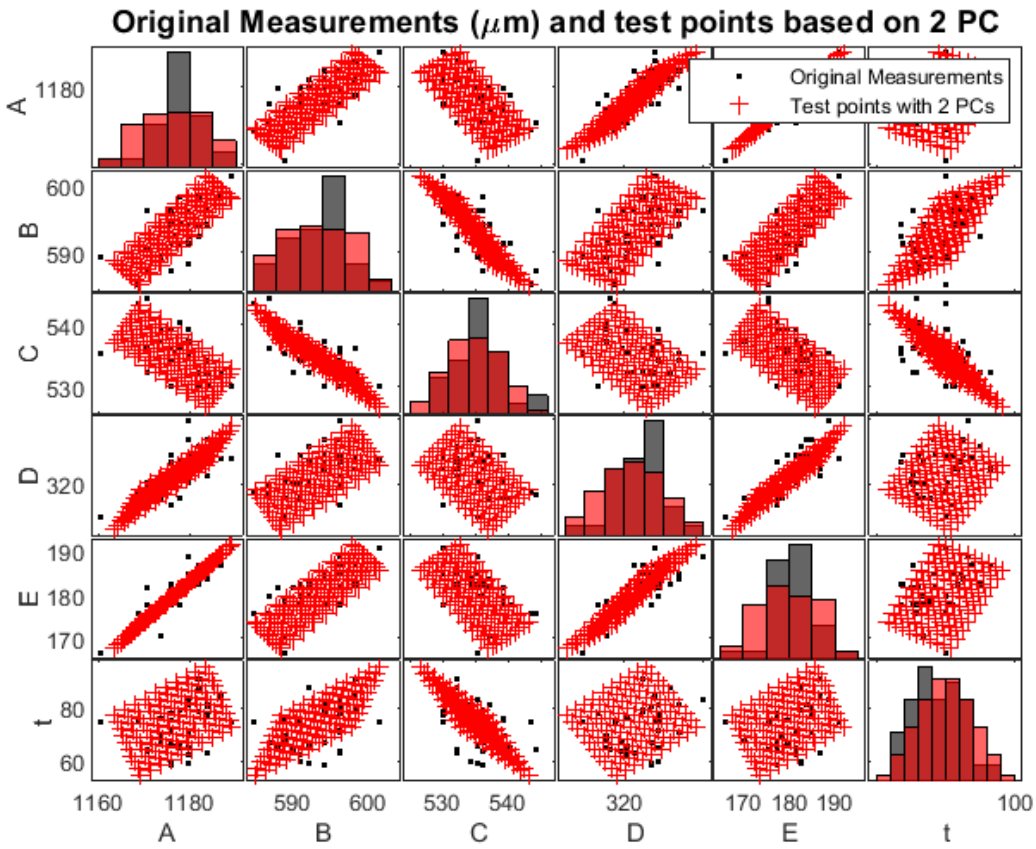



*Figure 54: Scatter plot matrix of set Foil 3&4. Here PCA analysis with 2 PCs is shown with 10 test points per component overlaid.*

It can be seen in Figure 54 that much of the variation in the data is covered by these two PCs. The 100 points can then be used to create 100 simulations, spanning 75% of the variance in the measurements. The spacing of the points in the Figure 54 shows that this method can also be broadly interpreted as finding the surface that minimises the distance from all points. Had 3 PCs been used, it would be the volume that achieves the same, *et cetera*.

These points, corresponding to geometries in real space, are used in ABAQUS to calculate the resonant frequency, stress per unit angle, and beam stiffness. A parametric function can be fitted to, in the case for 2 PCs, a surface. Figure 55 shows the simulated resonant frequency response of this surface in PC Space. With high confidence, it is therefore possible to predict the resonant frequency of another coordinate in PC space, and thereby another geometry in real space so long as it is on or near this surface. In this analysis, the decomposition to 2 principal components

implies that every measurement is projected onto this surface. As this is not truly the case, these dynamic responses are estimated.

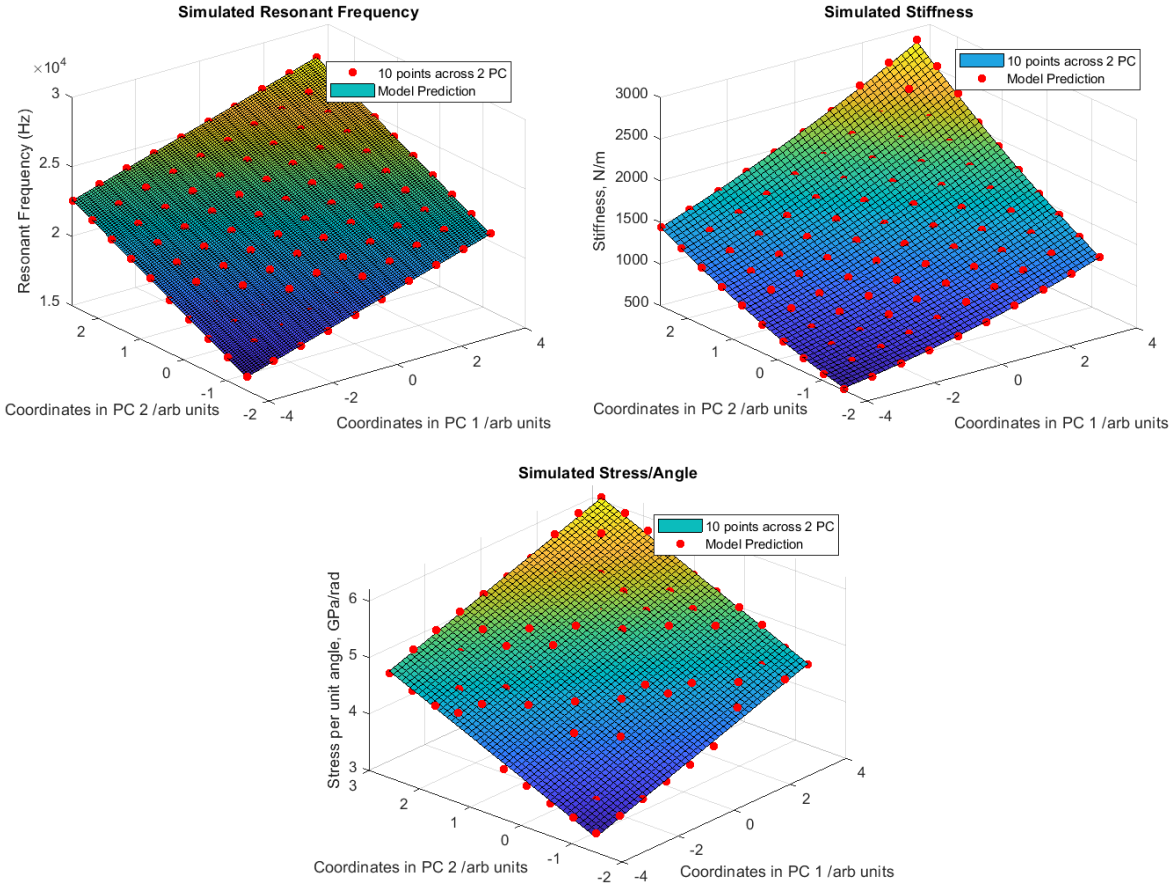



*Figure 55: Simulated dynamic responses in PC space for 2PC and 10 points per PC. Resonant Frequency and Stress Per Unit Angle are calculated with a linear model, stiffness is calculated with a quadratic. Results shown are for the design of set Foil 3&4.*

In practice, 3 PCs are used to improve accuracy: the more principal components are sampled, the more the variance is spanned, and the closer the decomposed coordinates are to their respective reduced dimension coordinate. A method to validate this choice can be seen when comparing the value obtained via PCA analysis to the simulated value obtained with the original measurements, shown in Figure 56. The error from this analysis route can therefore be estimated as the difference between these two values. It can be seen that the error when using 2 PCs is significant, implying that the projection onto this surface leads to significant change in dynamic response.

However, when sampling to 3 PCs – i.e. projecting onto the volume in PC space – the error can be seen to be minimal.

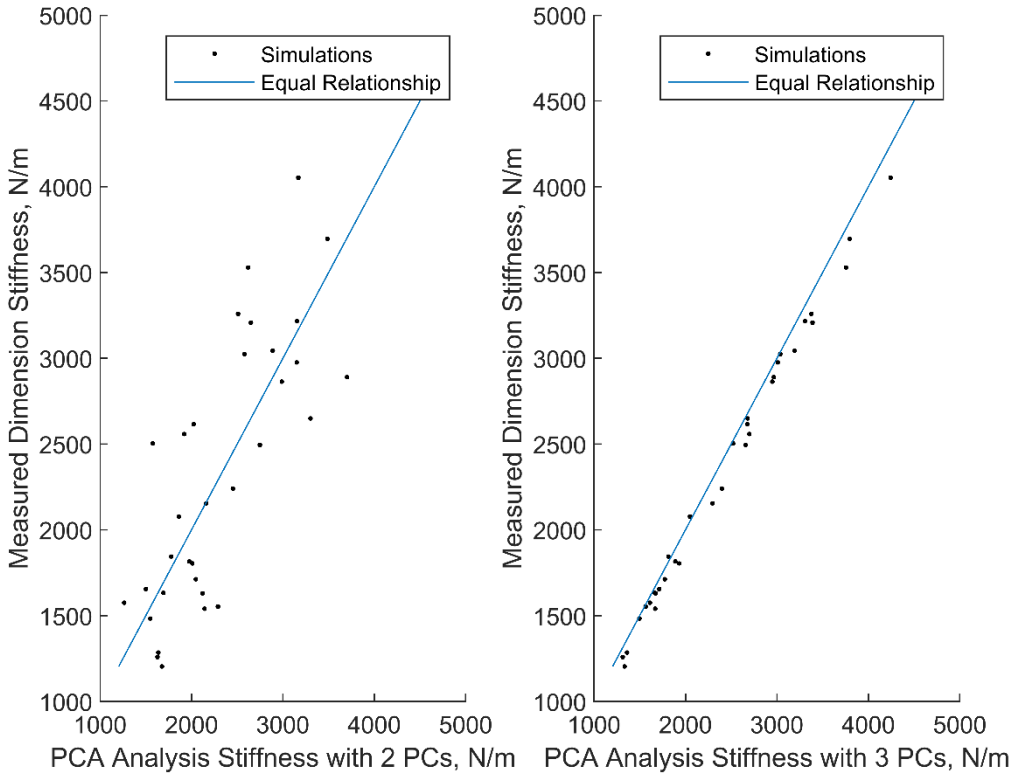



*Figure 56: ABAQUS simulation stiffness comparisons between PCA derived geometries, and SEM measured dimensions. Two principal components (left), or three principal components (right) are shown, with data points (black) along with an equal relationship as a visual guide (blue). The discrepancy between simulations is larger for 2 PCs than for 3 PCs.*

Having developed these models, it is then possible to determine the dynamic response of the cantilever specimens, each representing sample points on a parametric surface. Furthermore, it is possible to estimate dynamic responses for new measurements, so long as they remain within close proximity to this surface.

Prior to validating the experimental bending stiffness measured earlier with the simulated bending stiffness, it is worth considering the relative sensitivity of measurements. In the Stiffness Measurement section on page 108, the average error in stiffness measurement was seen to be *ca.* 5%. It is worth considering the effect of an error in the measurement of geometry on the bending stiffness: for simplicity, this can be demonstrated by perturbing the measured

dimensions, observing the effect on estimated bending stiffness and other dynamic responses in Table 8.

*Table 8: Effect of a 1% change in measurement in the average measurement on the simulated stiffness, resonant frequency, and stress per unit angle.*

| 1 % change in measurement | A | B | C | D | E | t |
|---|---|---|---|---|---|---|
| Effect on Stiffness, % | -4.0 | 2.2 | 0.2 | 1.1 | -0.6 | 3.0 |
| Effect on Resonant Frequency, % | -1.3 | 0.9 | -0.2 | 0.3 | -0.2 | 1.0 |
| Effect on Stress/Angle, % | -1.5 | 1.3 | -0.8 | 0.2 | -0.2 | 1.1 |

It can be seen that a 1% change in thickness leads to a 3% change in stiffness, indicating the sensitivity in thickness measurement. While it can also be seen that a measurement in hammer width is highly sensitive, despite not affecting stiffness physically, it must be recalled that due to the PCA analysis a measurement change in A implies a measurement change in other variables.

In repeated measurements of thickness, and observing the variation in Figure 57, the error in thickness can be estimated to be approximately 5-10 % on average. This would therefore lead, approximately, to an error of 15-30 % in stiffness.

With results discussed further in the Results section on page 175, it can be seen that there is often a significant disagreement between the experimentally measured bending stiffness, and the simulated stiffness for a given geometry.

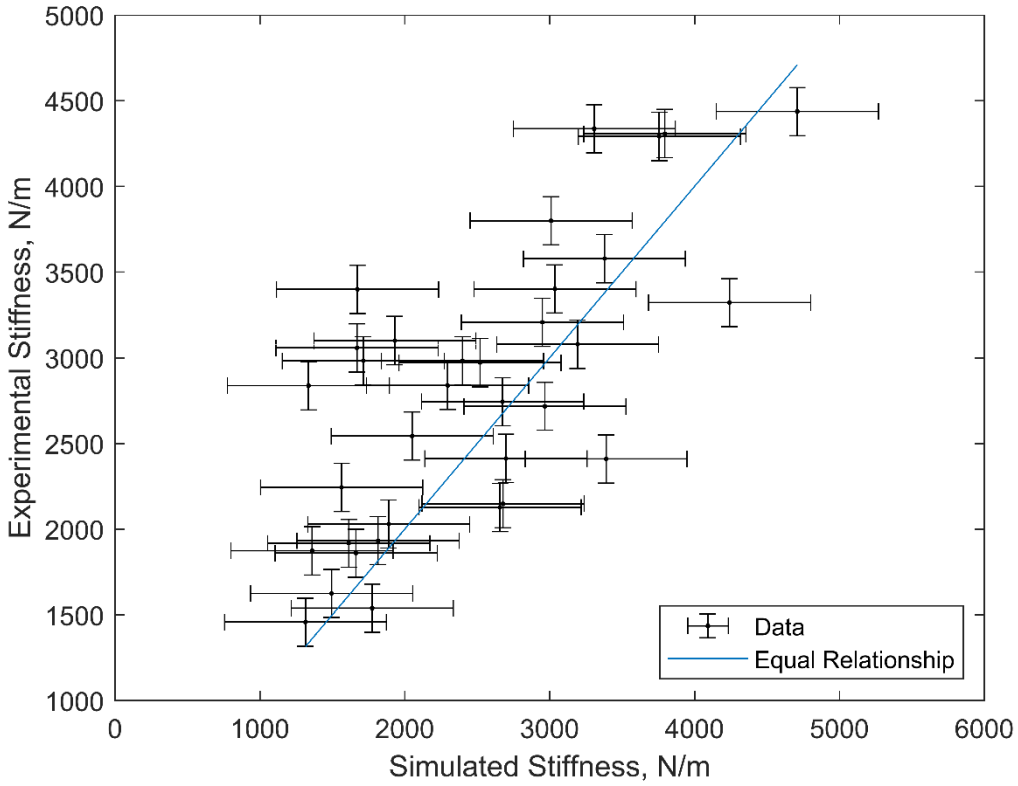



*Figure 57: Validation of simulated stiffness from measured geometry against experimental stiffness. Error bars represent average error in respective measurements, with experimental error detailed in Table 7 and simulated stiffness in Table 8 and propagating error from SEM measurement. Data shown from set Foil 3&4.*

The full benefit of this technique therefore lies in a consideration of this measurement sensitivity and error. As the sensitivity in geometrical measurement leads to a significant error in stiffness, it can be presumed the measurement in stiffness, with a lower error, would be more reliable. In particular, given the sensitivity of thickness measurements coupled with the inability to measure this thickness directly, it is prudent to rely more heavily on the more accurate measurement.

To resolve this, consider the surface shown in Figure 58 of stiffness across the 2 PCs: in effect, the location in PC space based on a measurement may be incorrect, for a given experimentally measured stiffness. Instead, consider that a given point on this surface has a stiffness measured above or below the surface, and that the height of this point has been accurately measured. It is therefore possible to find the nearest point in PC space that corresponds to this stiffness measurement, or height. In effect, solving equation (17):

$$S_{ABAQUS}(PC_1, PC_2, \dots) - S_{measured} = 0 \quad (17)$$

This new point in PC space provides measurements in real space, which can be said to represent a "predicted geometry". By using the experimental stiffness alongside a parametric understanding of the cantilever geometry, a new estimate of cardinal lengths can be found and thereby a new set of dynamic responses. A visualisation of this process is shown in Figure 58, where a point in red, seen to be a higher stiffness than its predicted stiffness, is translated in PC space to the nearest point in the surface with this stiffness.

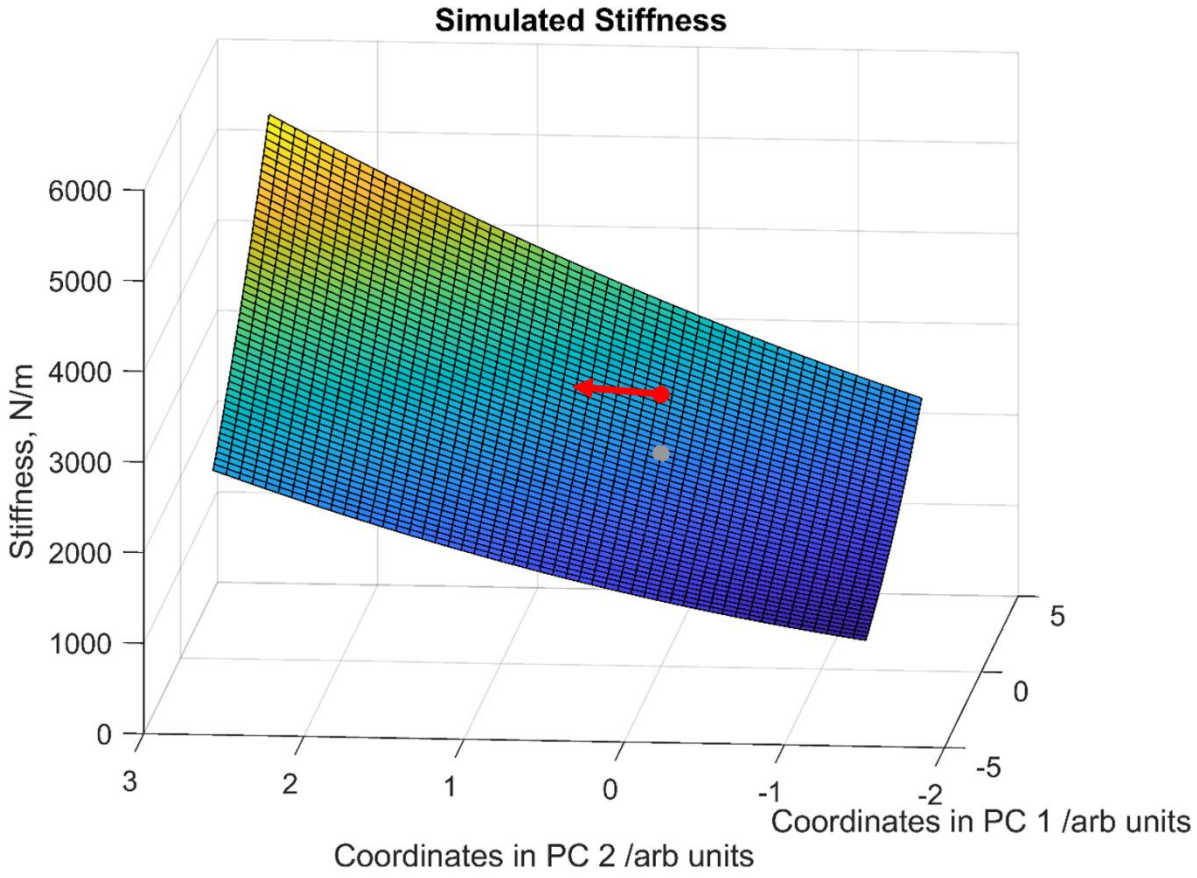



*Figure 58: Visualisation of dimension prediction from stiffness. Surface shown is ABAQUS calculated stiffness response to a change in the principle component. In red, a measured stiffness for a sample with some PC coordinates of (0,0). In grey, the stiffness of the point* $(0, 0)$*, seen to be lower in value. Red arrow shows the nearest point on the surface with that stiffness, providing new coordinates in PC space of approximately* $(1, 1)$*.*

A similar demonstration as earlier can be made in the effect of an error in stiffness measurement on these geometries, by perturbing the stiffness measurement by 5%. In this case, a 2.7% error in thickness was measured, confirming the intuition of sensitivity relationship between the two.

These dynamic responses of predicted geometries, often varying significantly from their original measurement counterparts, are necessary particularly for determining the induced stress at a given angle. The resonant frequency remains useful as a comparable measurement in observing the coupling constant for a given cantilever shown in the Geometrical Analysis section on page 111. The code for carrying out this analysis is available on GitHub at cmmagazz/AnalysisofCantileverDimensions.

This process flow, informed through the results of initial foils, allows for the design, production, and measured testing of the meso-scale cantilevers for ultrasonic testing. This is represented diagrammatically in Figure 59.

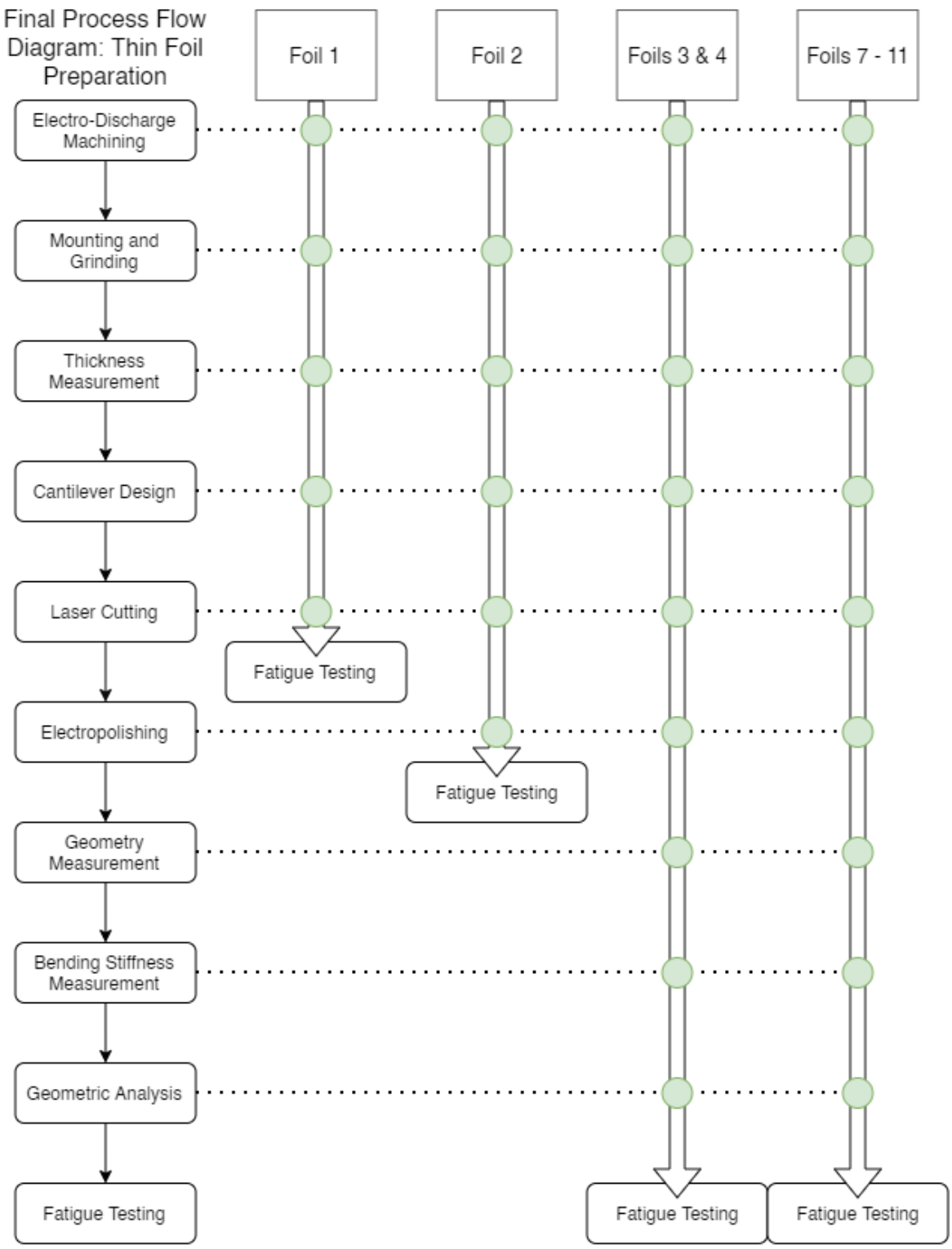



*Figure 59: Summary of process flow, showing the steps required prior to fatigue testing, and the steps carried out for the various sample sets.*

### 2.4.2. Experimental Fatigue Setup

The experimental set up for fatigue testing was built around the ultrasonic transducer, as described in the Context section on page 63. The majority of the details on operation of the transducer are included in the user manual of the manufacturer, though some details are noteworthy or tailored to the experiment carried out as in this project.

The first is the behaviour of the commercial power supply. A control board designed by Dr Gong is used to supply a signal voltage from a LabVIEW script on the control computer to the power supply, which is interpreted as a command for power to be transmitted to the transducer. In theory, a 10 Volt range is interpreted as a power control range of 0 to 100%, with each percent being 0.1 V: it is therefore instructive to consider a signal range of 0 to 100 mapping onto a power range of 0 to 100. In practice, the power supply generally interprets low signal values poorly: either responding non-linearly between 0 and 10% such that the power is the same as a 10% signal that range, or reverting to a default of 50 % power when supplied with a signal lower than 15 %. It is necessary to characterise this behaviour prior to design of the horn.

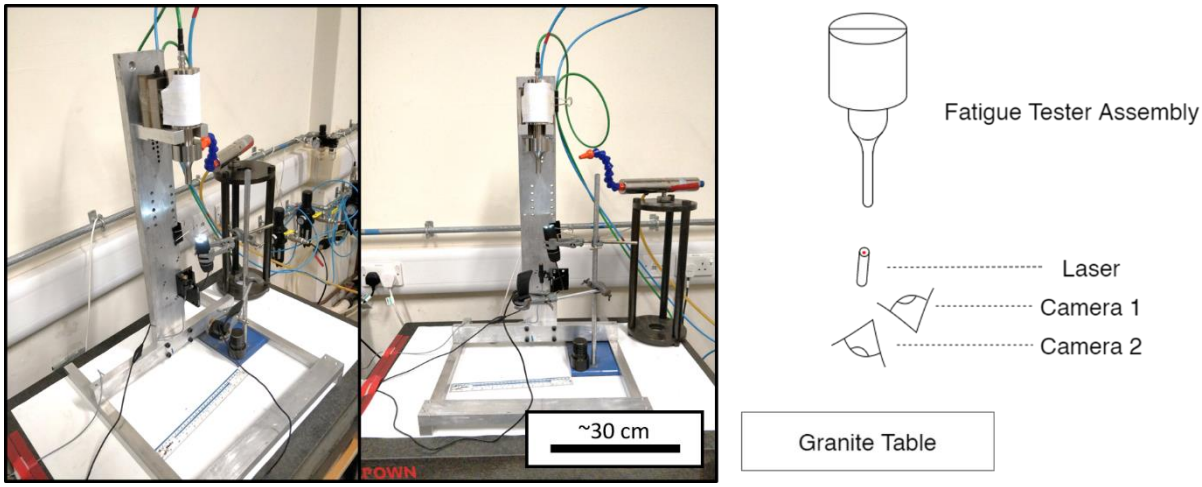



*Figure 60: Photograph of experimental fatigue setup with two views (Left and Centre), and simplified diagram.*

The second is an adapted thermal management system: owing to the large amount of power directed to a small mass, care must be taken when using experimental setup. To avoid rapid heating of the piezoelectric stack as well as the horn tip, compressed air is used to actively cool

the system when in use for more than one second. Using the laboratory compressed air infrastructure, two lines are used: the first feeds into the piezo-electric stack with the light blue line as seen in Figure 60. The second, shown as a thicker blue articulated “Loc-Line” tube with an orange tip in Figure 60, is only necessary when the power is high enough to induce significant heating in the tip. This occurs generally above 70% power. This can be used to cool the tip of the horn, and experiments have shown that unless this is significantly heated the sample’s thermal mass is low enough not to cause concern over thermal effects.

Finally, the experimental set up was placed upon a granite metrology table in order to reduce vibrations and ensure a stable position of the cameras. A photograph of this experimental setup is shown in Figure 60.

The major adaptation to allow for small scale testing involved a change to the acoustic amplification system. Rather than being used for its intended industrial use, or the testing of bulk specimens as described by C Bathias [280], these piezo electric stacks transmit power to a machined horn that amplifies the response to a tip in which the specimen holder is placed.

These horns were designed by Dr Gong with two primary properties:

1) A resonant frequency equal to that of the piezoelectric stack, within a few hundred Hertz.
2) A gain ratio as desired by the experiment.

The first dictated the length of this horn, with the 20 kHz example being 130 mm long. The second dictated the area ratio between the transducer end and the specimen end, with a reduction in this area leading to an increase in the power transmitted to the sample. This gain ratio was crucial to the successful testing of the specimens: the gain ratio needed to be sufficient to induce fatigue failure at approximately 70% power (to avoid significant heating), while low enough not to induce failure below 10% power (to avoid the non-linear regime).

To summarise, the experiment is setup as shown in Figure 60, and the supply is powered on. During the power on sequence, the power supply conducts a short frequency sweep to determine the resonant frequency of the horn. The nominal sound of this sweep is a brief squeak, indicating safe operation of the transducer-horn assembly. Further detail can be found in the relevant user manuals on visualising the resonant frequency of the horn, helpful during the design phase of the horns or if the sound is not as expected – though is out of scope for this thesis. The compressed air lines are opened, by default only the transducer line. Following this, it is possible to send a signal voltage to the power supply using the computer, a sample mounted, and a laser calibration performed.

The laser calibration is carried out in the setup described in the Context section on page 63: a sample mounted is carefully targeted with a laser, powered by computer software. Using a lower power setting, the laser can be aimed at the middle of the horn tip to ensure proper angular deflection. The focal point of the laser is set mid-way between hammer and the table: this ensures a small enough laser spot on the sample, as well as a focussed beam for measurement on the table surface. The table is covered with a sheet of white paper, and a ruler can be placed to measure the streak of the laser. A modified LabVIEW script was written to generate short pulses at regular intervals, in order to rapidly assess this behaviour, and Camera 2 (as in Figure 60) is used to record the laser response on the table. A view of the software and laser streak is shown in Figure 61.

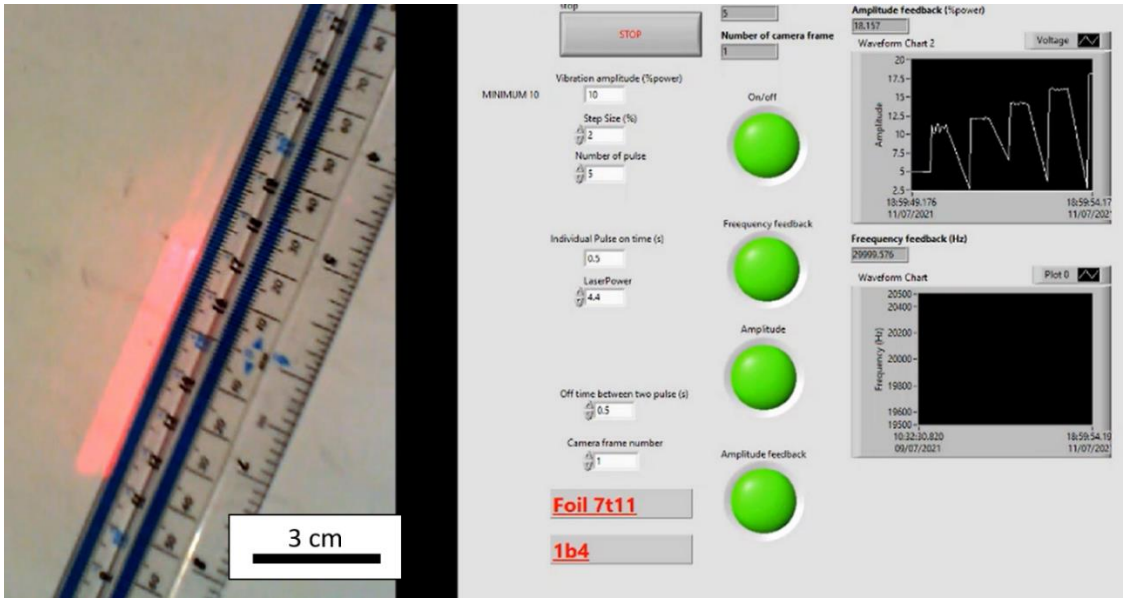



*Figure 61: Example image from laser calibration of sample 1B4 from set Foil 7-11. The sample was subjected to half-second pulses at 10, 12, 14, and 16 percent power, and is undergoing 18 % power in the image. The laser streak length was recorded as 5.7 cm. Prior to this set, a short pulse at 10 % power was used to assess whether this calibration range was safe.*

The initial laboratory setup for fatigue testing focussed on pulsed tests including the capability to capture crack growth with a microscope camera. To reduce the scope of this thesis, it was decided to optimise the setup for the rapid testing of samples under constant fatigue loading.

This consisted of two improvements: using cameras linked to the fatigue software computer as shown in Figure 60, as well as incorporating the video feed from these cameras in order to detect failures. This reduced the time taken to achieve $10^8$ cycles from ~20 hours to 1.3 hours, while retaining the ability to detect a failure to within at least 2000 cycles: by using the camera, a continuous fatigue loading could be applied and the camera used to detect the failure by observing the presence of the hammer. In addition, for ease of calibration, a second webcam is used to observe the table surface allowing for rapid laser calibration, achievable remotely.

The view from camera 1, a commercially available microscope webcam with its own light source, would be analysed with LabVIEW to measure *in situ* average brightness. Though it is beyond the scope of this thesis, this could sometimes be used to determine fatigue crack initiation and growth rate: if placed in the plane defining the bending motion of the cantilever, this would

sometimes show a brightening of the sample during larger oscillation. In all cases, this was very effective at determining the loss of a hammer at fracture, and therefore the number of cycles to failure reported in this thesis are the number of cycles until this hammer has dropped. The view from the LabVIEW software and camera input software (OBS) is shown in Figure 62.




*Figure 62: Example of fatigue testing captured via the controlling software. Large image of Camera 1 (left) showing specimen in the centre, with design of Foil 3&4. LabVIEW control software (right) showing input parameters (left column), amplitude and frequency feedback signals (centre column), and camera analysis (right column), with brightness at rest, brightness during the test, and two insets of the camera showing the view to be analysed. The failure criterion is achieved when the brightness decreases compared to the "at rest" brightness by some threshold (here defined as 3%). The Average Brightness 2 (test brightness) curve shows the initial increase as the sample approaches the oscillation amplitude (0-0.3s), the stable oscillation response (0.3-3.8s) and the increase in brightness as a crack grows (3.8s-present). In the next frame, the sample has failed, shown in the inset.*

#### 2.4.2.1. Specimen Holders

The 3 mm disc samples are held within a custom-built holder that is machined out of standard M5 grub screws. Its primary function is to tightly grip onto the outer ring of a specimen, screw tightly into the horn tip, and provide a channel for viewing the sample from the bottom. The assembly consists of a holder machined out of a grub screw including an inset for the sample and a viewing channel drilled through-thickness. A lid is made with an inner section to fit into the inset of the

holder, made slightly longer than the inset's depth, and a lip to press against the back of the hole in the horn tip. When screwed in, the lip of the lid is pressed, with a force travelling via the inner section, pinning the sample onto the holder. As the pinning of the sample affects the dynamic properties, particularly when using the coupling constant as a measure of the sample geometry, it is necessary to ensure consistency. In these experiments, this is achieved by the use of the same lid and holder for an experimental dataset, as well as tightening to a consistent torque. A torque-wrench set to 4 Nm can be used to ensure this consistent tightening. Further iterations to the design could include a mechanism to ensure consistent orientation between the lid and holder, though this was not explored in the project. The exact design and manufacturing method is detailed under the Fatigue Sample Holder Machining section of the Appendix on page 255.

## 2.5. Fatigue Testing Protocols

*This subsection on protocols, alongside the relevant literature review given in the Background section on page 48, was partially published in an article with co-authors R Rose, C Gearhart, J Gong, and AJ Wilkinson. A uniquely collaborative computational project consisting of MATLAB scripts, it must be declared that all scripts were co-authored with R Rose, with a subset adapted from C Gearhart's earlier work. The scripts therefore cannot be claimed to be original work, and resulted from discussions and live editing of scripts between R Rose and me. This subsection's text is also adapted from the similarly co-authored article titled "Bayesian Optimised Collection Strategies for Fatigue Testing – Constant Life Testing" [151].*

Two improved protocols for the collection of characteristic fatigue strength distribution parameters at a certain life are presented based on commonly used existing protocols that significantly improve estimates and collection efficiency of distribution parameters. Obtaining better estimates of fatigue strength parameters could inform more efficient engineering designs, and faster data collection enables shorter, lower cost, development cycles. The protocol

optimises the collection of fatigue data to estimate strength distribution parameters in commonly used models, and is available open source on the GitHub repository “BayesOptFatigue” [363].

### 2.5.1. Introduction

Owing to the limited number of samples to be tested in this study, it was necessary to obtain the most pertinent information relating to the material properties as possible. As described in the introduction, experiments for obtaining fundamental fatigue response parameters such as the fatigue strength distribution fall into two categories: single stress tests and multiple stress tests. This section begins with the development of a computational framework to simulate various fatigue testing protocols, followed by the description of a Bayesian Optimised fatigue collection protocol for step testing initially in constant life, followed by a “full-field” SN approach.

The Bayesian framework optimises the collection and analysis of any fatigue data where individual samples are tested at one or multiple stress levels, analysing data with a variety of candidate probability distribution models. The experimental design is optimised sequentially with each test at a specific test stress to maximise the predictive capability of the posterior based on prior information from all previous samples. A further advantage of a Bayesian approach is that the interpretation of the data allows for an expression of the Highest Posterior Density (HPD) interval of a range of model parameters rather than a confidence level in the data given the fitted model. This interpretation better accounts for the selective nature of fatigue sampling, and a basis for determining the optimal sampling strategy that would most clearly indicate likely model parameters. Furthermore, experimental data can be compared using the Bayes Information Criterion (BIC) allowing different distribution types (e.g. Normal, Log-Normal, Weibull) to be distinguished.

A selection of statistical distributions are examined to model the fixed life fatigue strength: Normal, Log-Normal, 2- and 3- parameter Weibull, Gumbell, and Frechet. The aim is to provide the user with a choice of models and care must be taken to choose an appropriate model,

particularly in the extreme value of the distribution [364]. Simulated results will be shown with a Normal distribution for simplicity, though readers are invited to the literature on the basis for fatigue strength models [203], [365], [374]–[377], [366]–[373], and are invited to evaluate the suitability of models through further experiment or statistical comparison tools such as BIC.

### 2.5.2. Computational Framework

A computational framework to simulate a material's fatigue response is constructed in order to carry out simulations and compare protocols. We generalise the fatigue response for any life as a Basquin model with an elevated fatigue limit, to determine the fatigue strength at a certain life. This modified Basquin mean response curve is defined as follows (18):

$$S_{mean} = \alpha \log(N)^{-\beta} + c \tag{18}$$

where the Basquin constants $\alpha$, $\beta$, and c are taken in this simulated system to be 600 MPa/log(cycle), 1, and 300 MPa, respectively. As such, the mean fatigue strength at $10^6$ cycles is 400 MPa. Though it is strictly not necessary to model the entire curve, it is instructive to visualise this curve and the framework lends itself to generalisation to multiple lives in further work. The fatigue curve model is also at this stage arbitrary, as we do not generalise results to a functional form across cycles. Earlier reports and theses describe the multiple curves that can fit existing fatigue data[289], [378], and for this reason the function selected does not prefer one model over another and creates the familiar SN response with an "elbow" around $10^6$ cycles.

A Monte-Carlo based method is used for generating a simulated sample set with many fatigue responses by perturbing this mean response in stress by a distribution with some characteristic spread. Thus, a sample with a determined fatigue response is a member of a sample set with a broad fatigue response. This can be written as (19):

$$S_i = \alpha \log(N)^{-\beta} + c + \delta(0, \sigma) \quad (19)$$

where $\delta(0, \sigma)$ is a random number with distribution centred about zero, and a spread in stress defined by $\sigma$. This results in a mean fatigue response at $10^6$ cycles is 400 MPa, and a spread of $\sigma$. The distribution model can be chosen at liberty and is arbitrary – for simplicity, the results shown here use a normal distribution.

In this framework, a single sample's curve is selected to be subject to the test protocol, for either a single test or multiple step tests. For the selected sample, if the fatigue strength at life $\log(N)$ is higher than the test stress, it has not failed, while if the fatigue strength is lower than the test stress, it has failed. This allows for the simulated testing of large sample sets and comparison between protocols (Figure 63).

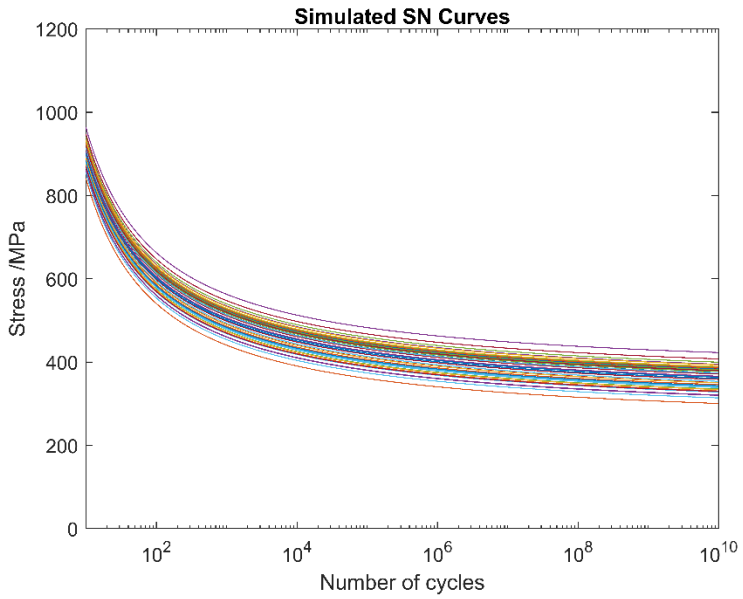



*Figure 63: Example simulated sample set with each sample modelled as a Basquin curve perturbed in stress by a normally distributed random variable*

This computational framework was used initially to investigate the role of step size and starting stress on estimated fatigue strength parameters using conventional protocols. It was also used to evaluate the confidence with which these parameters can be estimated with only a few samples, a limitation that is inherent to the meso-scale fatigue testing method but observed more widely.

To maximise the accuracy of data collected, a stress step method was preferable, though evaluating the effect of stress step damage or coaxing was out of scope for this thesis. Therefore, a larger step size would be preferable, but required determining the effects on statistical accuracy. Of note, despite the guidance described in the literature, the choice of step size and starting stress still may affect results. More importantly, however, a larger step size may induce statistical artefacts owing to a greater influence on which stress levels are involved in the testing: if the step size is comparable or larger than the spread in the sample set, sample may mostly fail from one common stress level to the next. This is referred to in this document as the step-hop effect: the design of the test will lead to testing of one stress level below the distribution, and hop to a stress level where most are expected to fail. Crucially, the measurement of distribution parameters then becomes very sensitive to the placement of these levels, and random distribution of the samples within this range.

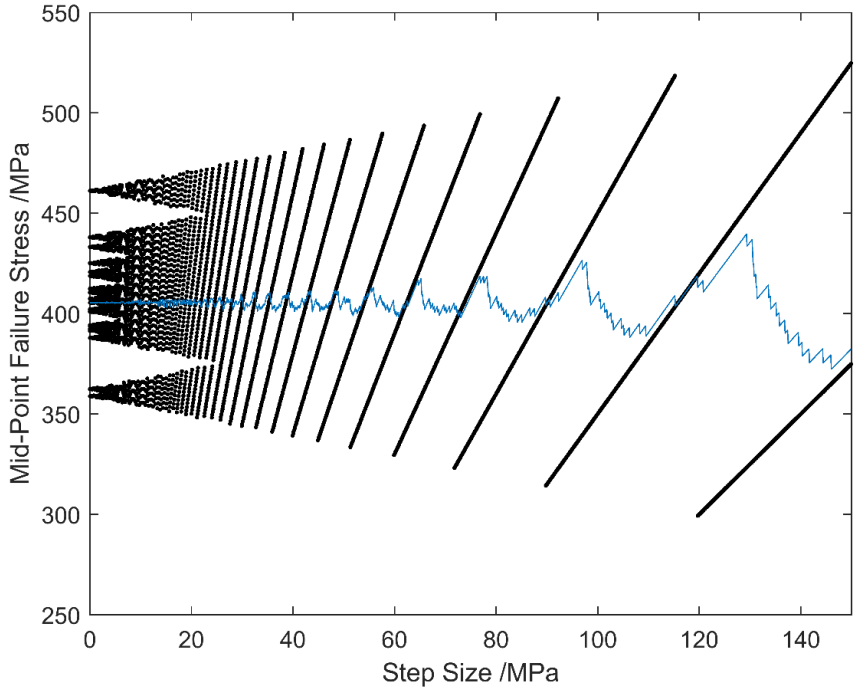



*Figure 64: Simulated stress step fatigue results, with black points showing mid-point of fatigue failure stress (between runout and failure), and the blue line showing ensemble average. Sample set consisted of 30 samples with mean of 400 MPa and standard deviation of 40 MPa. Step hop effect can be seen as a rise in the ensemble average depending on the stress step size used. For example, a step size of 110 MPa leads to an average of 390 MPa, whereas a step size of 130 MPa leads to an average of 435 MPa. Gaps in low step size arise from individual sample SN curves being located with greater accuracy, and the low number of samples, cf. Figure 63.*

For example, Figure 64 illustrates an extreme step-hop effect observed when carrying out stress step tests on specimens with some fixed starting point. In this particular case, 30 samples with a mean of 400 MPa and a spread of 40 MPa were tested with a stress step protocol with starting stress of 0 MPa. Recalling that previous tests are not being considered, it can be seen that at very large step sizes (above the spread) the ensemble mean begins to vary with step size. This effect is sensitive to starting stress (shifting this variation left to right), and the characteristics of the sample set (for small sample numbers).

This motivated a more general query on whether a protocol that was informed by the previous samples would be better. An initial attempt was made by fitting a distribution to the existing data, determining the mean, and subtracting 3 steps to re-evaluate the starting point. However, while this method did alleviate some of the step hop effect by varying the starting stress, it was very sensitive to the order of sample testing: initially, each individual sample would significantly affect the estimate of parameters. However, this was constructive as a crude precursor to the later developed Bayesian approach.

### 2.5.3. Applying Bayes Theory to Fatigue Testing

Fitting fixed life fatigue strength data typically produces estimates of model parameters describing the location, scale, and shape of the data. While regression methods are powerful for fitting to data, ideally this data has been evenly sampled across the range. However, in many experimental cases it is challenging to sample points evenly, or expensive to collect data. Fixed-life fatigue sampling presents such a challenge, requiring protocols combining multiple fixed-stress fatigue tests to generate data, owing to challenges in sampling HCF behaviour, increasing time and material cost of such tests.

Rather than estimate the relationship between the independent and response variable, a Bayesian approach evaluates the distribution of models given a set of experimental data points, extended over a distribution of models, built on Bayes rule (20):

$$P(\boldsymbol{\theta}|\boldsymbol{x}) = \frac{P(\boldsymbol{x}|\boldsymbol{\theta})P(\boldsymbol{\theta})}{P(\boldsymbol{x})} \quad (20)$$

where in this context $\boldsymbol{\theta}$ is the vector of model parameters and $\boldsymbol{x}$ represents the vector of experimental stress data. For example, a normal distribution model can be represented by the parameters mean ($\mu$) and standard deviation ($\sigma$), i.e. $\boldsymbol{\theta} = [\mu, \sigma]$. The posterior $P(\boldsymbol{\theta}|\boldsymbol{x})$ describes the probability supporting the model parameters $\boldsymbol{\theta}$ given the observations $\boldsymbol{x}$ made so far. This posterior is inferred from the prior, $P(\boldsymbol{\theta})$, which describes the probability supporting the model, the likelihood function $P(\boldsymbol{x}|\boldsymbol{\theta})$ describing the consistency of the observations with the model, and finally the marginal likelihood $P(\boldsymbol{x})$ of collecting the data which normalizes the expression.

### 2.5.4. Construction of joint posterior for fatigue strength testing

This approach allows for the evaluation of the model parameters during experimentation, beginning with a prior distribution of parameters and sequentially re-evaluated after obtaining each data point to a posterior distribution. To construct the terms in equation 1, we have extended the likelihood approach of Engler-Pinto *et al* [313], [314], to create joint posterior distributions, or the likelihood of observing a result given the model. Engler-Pinto *et al* describe this for staircase testing, while we generalise to step-type testing following the approach of Smalakys *et al* [340], represented graphically in Figure 65. The probability of recording an experimental data point $P(x_i|\boldsymbol{\theta})$ is given by Equation (21):

$$P(x_i|\boldsymbol{\theta}) = \int_{a_i}^{b_i} \phi(\mathrm{S}, \boldsymbol{\theta}) dS \quad (21)$$

where $\phi(\boldsymbol{\theta})$ is the probability density function (PDF) for the model with parameter vector $\boldsymbol{\theta}$, $a_i$ and $b_i$ are the limits in stress ($S$) determined by the data $x_i$.

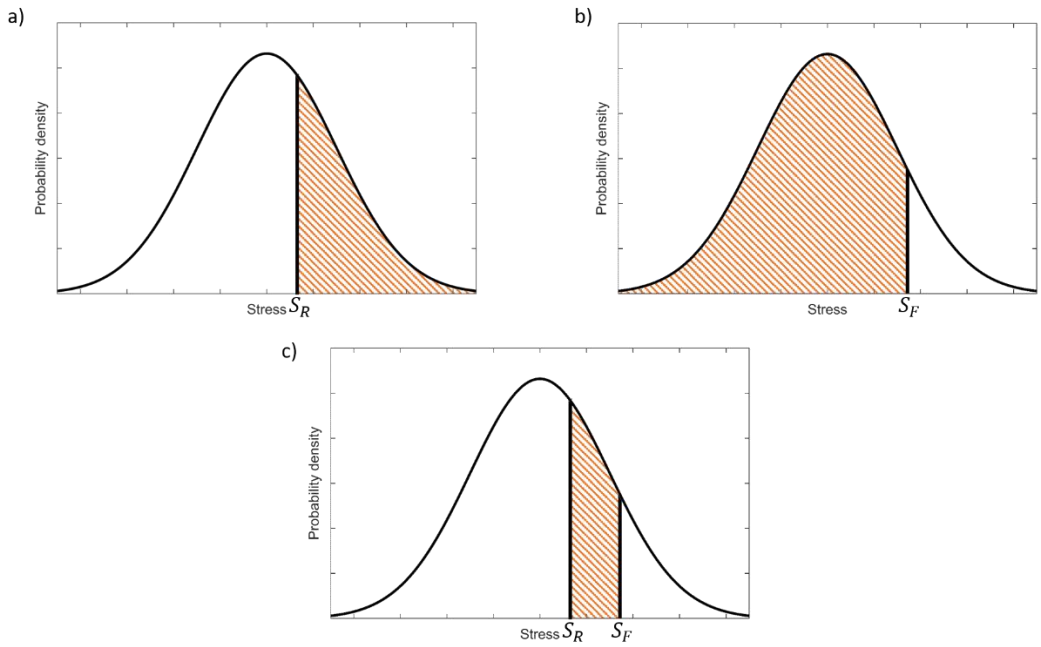



*Figure 65: Areas representing probability of model parameter combination for a) runout only b) failure only c) runout and failure*

In the case of staircase testing, a sample having failed or survived is described as an integral from one side of the distribution or the other: it is either left- or right-censored. For example, with a failed sample, the probability of recording a failure at some stress S rises to 50% at the mean failure stress, and approaches 1 at the upper limit, and the converse for runouts. Therefore, the likelihood of collecting a data-point $x_i$ denoting a failed sample can be described as integrating from negative infinity[3] to the stress at which it failed.

In a step test, the combination of requirement for both a runout and a failure at two set stresses can be described as a lower and upper limit of the integral; it is interval censored. In extremes, a step test is unlikely to be recorded: a runout and failure pair is unlikely at either low stress (owing to an unlikely failure) or high stress (owing to an unlikely runout in the preceding step). The likelihood is maximised when the runout and failure stress straddle the mean, and rise with

[3] Note: it is unphysical for a material to have a probability of failing at negative stress, though this is inconsequential as in reasonable settings, the integral from negative infinity to zero is equal to zero.

increasing step size. In these tests with multiple stresses per sample we denote the stress level by the second index $k$ in $x_{i,k}$. As we consider only step testing protocols with constant step size, the test levels denoted by $k$ start from $x_{i,1}$ and incrementing by the step size $\xi$ such that for some sample $x_i$ in equation (22):

$$x_{i,k} = x_{i,k-1} + \xi \tag{22}$$

Table 9 summarizes the possible values for $a_i$ and $b_i$ in protocols where samples are tested one or multiple times. Therefore, a step test with an infinite step size is equivalent to a single staircase test, and a sequence of steps leads to an equivalent probability of failure by some stress S as in a staircase test. It must be reiterated that this framework is only concerned with the state of the sample by some number of cycles N, and that we do not consider any mechanistic effects from previous tests – rather, we are only concerned with the experimental likelihood of model parameters given data.

*Table 9: Limits of integral for all possible experimental scenarios and expression in terms of cumulative probability distribution*

| ***Protocol*** | ***Case*** | $a_i$ | $b_i$ |
|---|---|---|---|
| One stress per sample | Failure | $-\infty$[4] | $x_i$ |
| | Runout | $x_i$ | $\infty$ |
| Multiple stresses per sample | Combined Failure and Runout | $x_{i,k-1}$ | $x_{i,k}$ |

The limits of these integrals are described in Smalakys *et al* [340] as equation (23):

[4] While we infer from the physical nature of the experiment that at 0 MPa there is no likelihood of failure, integrating from negative infinity is more reflective of the abstract distribution.

$$L_i = \begin{cases} L_i^{\text{fail}} = \Phi(s_i), & \text{left} - \text{censored} \\ L_i^{\text{step}} = \Phi(s_i) - \Phi(s_{i-1}), & \text{interval} - \text{censored} \\ L_i^{\text{runout}} = 1 - \Phi(s_i), & \text{right} - \text{censored} \end{cases} \quad (23)$$

where the likelihood of a single test $i$ is evaluated from the distribution with PDF $\phi(S)$ and cumulative distribution function (CDF) $\Phi(S)$. In this case, the integrals between limits of the PDF are equivalent to the CDF evaluations above.

The joint probability, or posterior, of recording a subsequent data $x_{i+1}$ given the model $P(\boldsymbol{\theta}|\boldsymbol{x}_{1:i})$ can then be rewritten from Bayes rule in Equation (20) to Equation (24). XXX

$$P(\boldsymbol{\theta}|\boldsymbol{x}_{1:i+1}) = \frac{P(\boldsymbol{x}_{1:i+1}|\boldsymbol{\theta})P(\boldsymbol{\theta}|\boldsymbol{x}_{1:i})}{\int \boldsymbol{d\theta} P(\boldsymbol{x}_{1:i+1}|\boldsymbol{\theta})P(\boldsymbol{\theta}|\boldsymbol{x}_{1:i})} \quad (24)$$

In Equation (24) , the prior $P(\boldsymbol{\theta}|\boldsymbol{x}_{1:i})$ is calculated from all the previous samples. The total likelihood with N samples is obtained by multiplying the likelihoods as in Nelson [379] (25):

$$L = P(\boldsymbol{x}|\boldsymbol{\theta}) = \prod_{i=1}^{N} L_i \quad (25)$$

For the first sample, a flat prior is used across a reasonable extent – a discussion of initial prior choice given in the Choice of Initial Prior section on page 142. This prior is not entirely assumption free: the extent of the prior, both in location and scale (or higher dimensions if required), imply an assertion that those parameters are equally likely to lie within this range. However, it can be shown that experiments initialised with significantly offset prior extent from the true values converge quickly. Furthermore, in experiments it is very rare to have no information on the system at all, and a mean range from 0 MPa to the Ultimate Tensile Strength represents a reasonable extent.

### 2.5.5. Applying Bayesian maximum entropy sampling to fatigue data

The goal of precisely estimating distribution parameters such as a location (such as mean, $\mu$) and scale (such as standard deviation, $\sigma$) can be thought of as generating the most compact, or tightly

constrained, joint posterior distribution for $\mu$ and $\sigma$. This tightly constrained posterior allows for better predictive capability by limiting which parameters in the distributions are likely to describe the system. To choose the next stress to test that will maximize this predictive power, Ryan, Drovandi *et al* [355] recommend maximising the expected gain in Shannon information in the joint posterior. The next stress to test is therefore chosen to maximise the expected information gain from sampling at a subsequent point $x_{i+1}$.

To do this, we use Shannon's information $I(P(\boldsymbol{x}))$, as described by Shannon (26), and evaluate the expected information (27). Often called Entropy, this expected information can be intuited as a quantitative measure of the compactness of the posterior distribution, a derivation of which can be found in [354]–[356], [380] [32]:

$$I(P(\boldsymbol{x})) = -\ln\big(P(\boldsymbol{\theta}|\boldsymbol{x})\big) \tag{26}$$

$$Ent(P(\boldsymbol{x})) = E(I) = -\int d\theta \;\; P(\boldsymbol{\theta}|\boldsymbol{x}) \ln\big(P(\boldsymbol{\theta}|\boldsymbol{x})\big) \tag{27}$$

Our aim being to maximise the compactness of the posterior distribution, we can define a gain in entropy from the addition of a possible data (a failure or runout) $X$ within the design $\boldsymbol{d}$, which for example is all possible stresses for the subsequent sample for a staircase test:

$$\Upsilon(\boldsymbol{d}, X) = Ent\big(P(\theta)\big) - Ent(P(\theta|X, \boldsymbol{d}) \tag{28}$$

As $Ent\big(P(\theta)\big)$ does not vary with data or the design, we can neglect this term. We therefore build a utility function to evaluate the expected value in the change of entropy from including the datapoint $x_{i+1}$:

$$U(\boldsymbol{d}) = -E_X\big(\Upsilon(x_{i+1})\big) = \sum_{\mathrm{X}} P(x|\boldsymbol{d}) \int d\theta \;\; P(\boldsymbol{\theta}|\boldsymbol{x}) \ln\big(P(\boldsymbol{\theta}|\boldsymbol{x})\big) \tag{29}$$

This can be intuited as evaluating the expected entropy gain of an outcome, across the expected models. The maximisation of this utility function as a function of the allowed experimental design, such as test stress, allows for the greatest expected entropy gain.

For staircase-type testing, the utility function is built by considering both possible outcomes of an experiment – a runout or failure – at some stress $S$ and evaluates this expected entropy change as a function of the test stress:

$$\mathbf{U}^{\boldsymbol{staircase}}(x_{n+1}) = \Upsilon^{\mathrm{runout}}(x_{n+1}, \boldsymbol{x})\, p^{\mathrm{runout}}(\boldsymbol{x}|S) + \Upsilon^{\mathrm{fail}}(x_{n+1}, \boldsymbol{x})\, p^{\mathrm{fail}}(\boldsymbol{x}|S) \quad (30)$$

This can be understood as determining the expected value for each possible outcome through the entropy gain, and its associated probability given the previous data. In this case, we aim to find the test stress $x_{n+1}$ which maximises $\mathbf{U}^{staircase}$. In practice, this involves considering the effect on the joint posterior of an added failure or runout to calculate $\Upsilon^{failure}$ or $\Upsilon^{runout}$ respectively by using equation (30).

For step-type testing, the design space allows for varying two test parameters: the starting stress $S_{i,0}$, as well as the step size $\xi$. The utility function is similarly built by considering possible outcomes, and their relevant likelihood and entropy gains. In this case, the outcomes are:

1) Fail a test on the first step
2) Obtain a runout and failure pair at some stress $S_{k-1}$ and $S_k$

In the first case, it is equivalent to a single staircase test. In the second case, the probabilities are interval censored. Since the sample could fail on any step – the expected $\Upsilon$ from each step contributes to the expected utility. Therefore, the utility function becomes (31):

$$\mathbf{U}^{step}(x_{n+1,1},\xi) = \Upsilon^{\text{fail}}(x_{n+1,1},\boldsymbol{x})\, p^{\text{fail}}(\boldsymbol{x}|x_{n+1,1}) + \sum_{k=2}^{N_k} \Upsilon^{\text{step}}(x_{n+1,k},\boldsymbol{x}) p^{\text{step}}(\boldsymbol{x}|x_{n+1,k}) \quad (31)$$

where the first term denotes failing on the first step, and the sum across $k$ evaluates the utility of failing at each subsequent step, recalling that $x_{n+1,k} = x_{n+1,1} + k\xi$. Here, $N_k$ is the number of possible test stresses ($k$) from the starting stress to the maximum possible test stress. The sum need only be defined up to the point where $p^{\text{step}}(\boldsymbol{x}|x_{n+1,k})$ becomes infinitesimally small, as described before – i.e. where it becomes highly unlikely to collect a result. This is used to determine a starting stress and step size that would maximise this expected utility from step testing. As shown in results, the step size is of little import in this study – rather it is the ability to optimise for starting stress when carrying out step tests at large step sizes that is beneficial.

### 2.5.6. Discretisation of the Prior

In this computational method, the prior is built as a discrete ND array with the characteristic distribution parameters, such as location and scale, along the axes. The evaluation and normalisation of the posterior is therefore (32):

$$P(\theta|\boldsymbol{x}) = \frac{P(\theta|\boldsymbol{x}_{1:i-1})P(x_i|\theta)}{\sum P(\theta|\boldsymbol{x}_{1:i-1})P(x_i|\theta)} \quad (32)$$

As such, each element in this array with coordinate of ($\theta_1, \theta_2$ …) gives the probability that these discrete parameter values represent the data. $\boldsymbol{I}$ is therefore calculated by summing the probability contributions from every possible combination of model parameters of the desired distribution. For simplicity $\boldsymbol{U}$ is calculated for a normal distribution in this work (i.e. $\boldsymbol{\theta} = \langle \boldsymbol{\mu}, \boldsymbol{\sigma} \rangle$), but many other distributions are supported.

The prior is initialised by creating an array of equal values such that $\sum P(\theta|x_0) = 1$. The extent of this prior can be chosen with reasonable limits such as minimum of 0 MPa for location and scale,

and ~ UTS and half of the UTS as a maximum. However, these arbitrary limits are given as examples, and it can be shown that they do not significantly affect the performance of the protocol. Practically, it is more convenient to use the logarithm of the probabilities as this avoid numerical issues with small values. In this way, Equation (6) is in practice carried out as the sum of logarithms. A more detailed view of this process is included in the README of the GitHub repository [363].

### 2.5.7. Choice of Initial Prior

The choice of using a flat prior, as opposed to the non-informative prior, can be justified by both an argument of simplicity as well a notable feature in the trend of Shannon information at low specimen number. Two non-informative priors were investigated. As suggested by Box and Tiao [34], for inference based on the normal distribution the Jeffreys prior in equation (33) promotes models with small standard deviations.

$$P(\theta|x_0) \propto \sigma^{-1} \tag{33}$$

This form can be shown to be non-informative according to Box and Tiao's data translated likelihood criteria [34] as well as by Jeffreys rule for transformation invariance [35]. Alternatively, a constant prior over a range is used, which has the advantage that it is mathematically equivalent to a maximum likelihood approach.

When using a Jeffreys prior the Shannon information drops significantly after approximately 10 samples (Figure 66). This is generally observed as an initial under-estimation of the standard deviation, in line with the prior construction, followed by an increase in the estimate and uncertainty in the standard deviation. This overconfidence in a low standard deviation was deemed, particularly in the context of fatigue testing, as sub-optimal, despite the subsequent faster convergence to the same parameter values. For these reasons, a fully flat prior was used in the testing and simulation reported in this work.

However, it must be clear that a flat prior is not assumption-free. Rather, the standard deviation is deemed equally likely to lie within the extent that is specified in the permitted 2D parameter space.

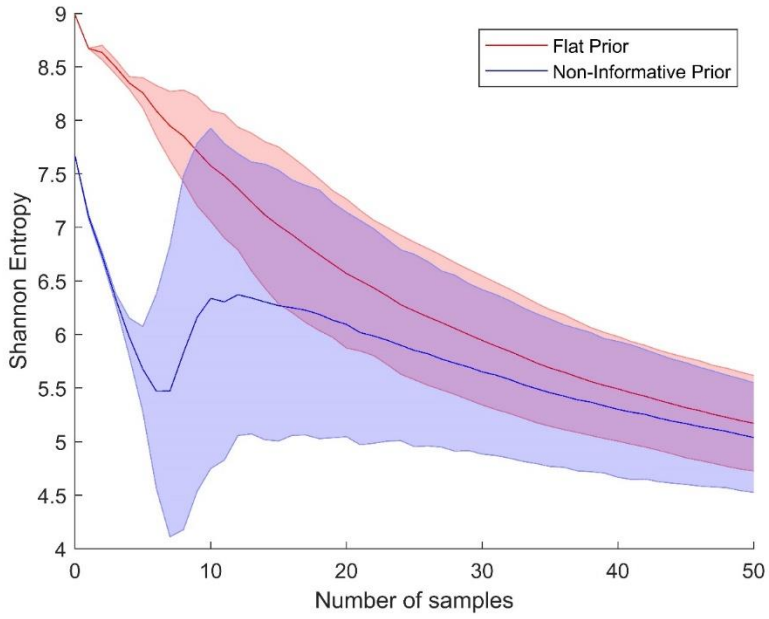



*Figure 66: Comparison of Shannon Information between tests with priors initialised as: uniform probability (red), and non-informative (blue). The tests were performed on a simulated set with strength 400MPa and distribution width 40MPa at $10^6$ cycles for 100 specimens using the Bayesian Staircase protocol. The shaded error bars represent the standard deviation between repeats. The simulations were repeated 500 times.*

### 2.5.8. Bayesian Staircase Protocol

The Bayesian Staircase collection strategy (Figure 67) broadly resembles the conventional staircase method in three ways: the interpretation of the algorithm's behaviour, an approximate similarity in collection in the initial points, and an analysis based on a sample set containing failed specimens and runout data.

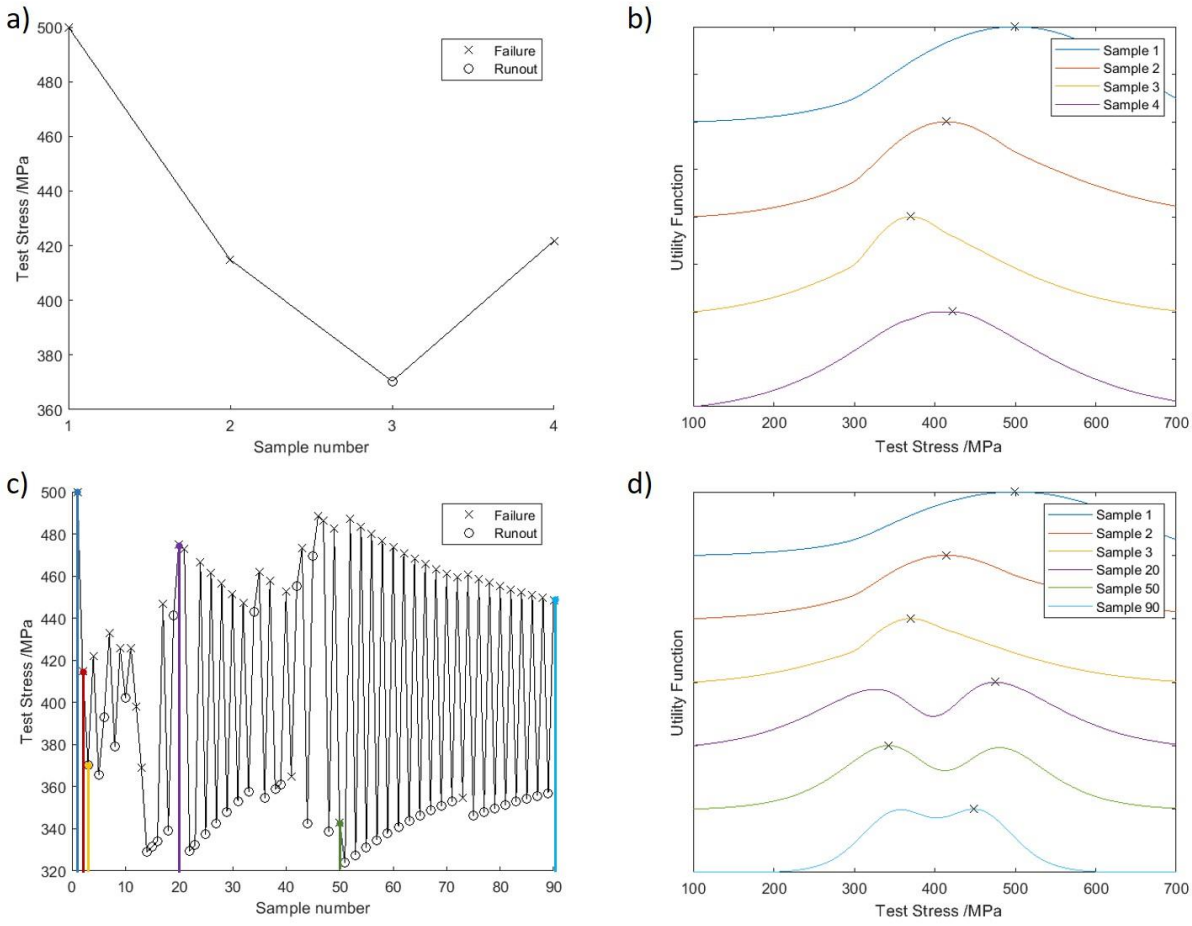



*Figure 67: Staircase plot (a, c) and associated utility function plots (b, d) for 4, and 90 samples. The simulated sample set had a mean of 400 MPa and distribution width of 40 MPa.*

The original staircase algorithm implicitly infers that a test stress is above the mean if a sample has failed, or below the mean if a sample has run out, thereby setting the stress level for the subsequent test. This inference is seen more concretely in the Bayesian staircase method, with the added consideration of all previous data and a variable stress increment between tests and incorporating testing at the optimal location not at an arbitrarily pre-defined stress.

The first few specimens perform a binary search for the mean failure strength to establish a constraint on the mean. As the estimate of mean becomes more precise, there is less information to be gained by testing at the centre of the distribution, and the algorithm then tries to determine the standard deviation. This is reflected in the expected information curve as a transition to a bimodal distribution (Figure 67) with peaks at approximately one standard deviation from the mean. This transition quantifies the intuitive approach of determining the stress range to test by

measuring the mean, followed by sampling the spread of the sample set, and is similar in behaviour to Never's D-optimal test strategy [341]. Figure 68 shows that the mean is generally well constrained after 10 samples, while the standard deviation requires more specimens for convergence.

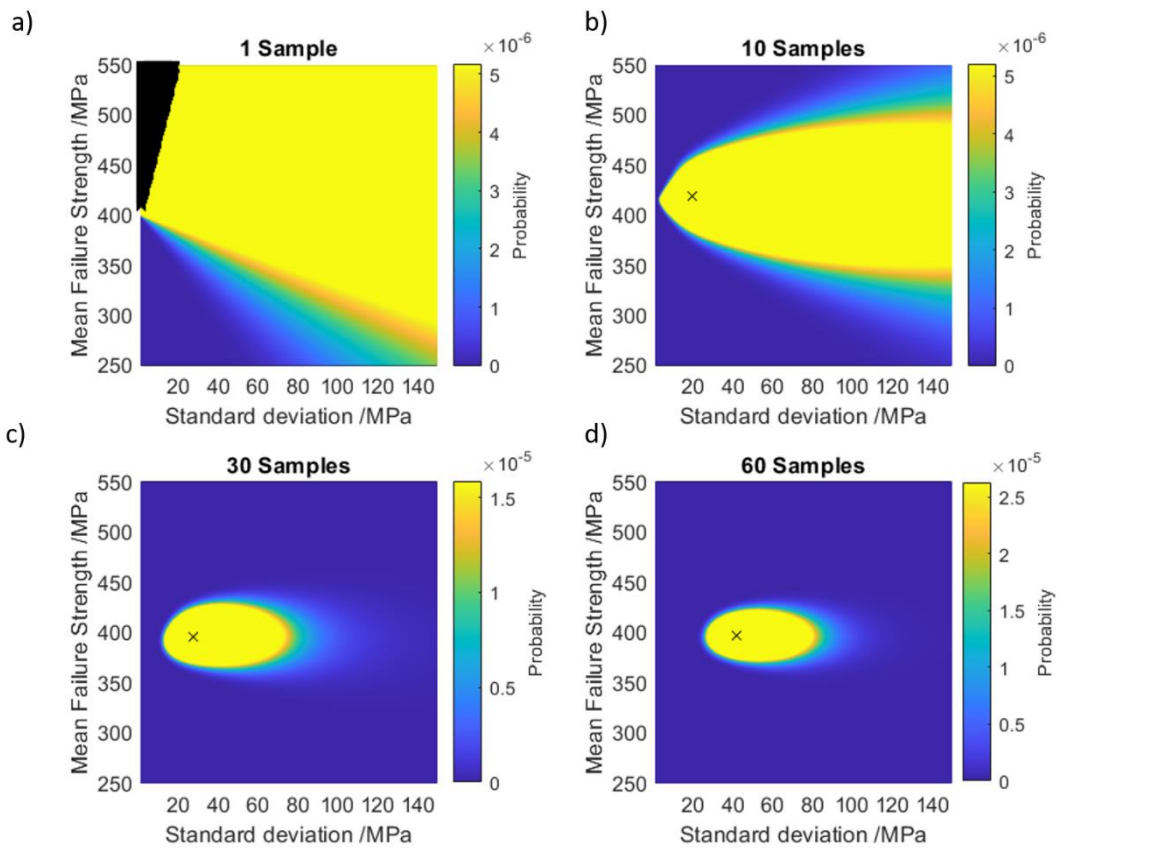



*Figure 68: Evolution of joint posterior surface with a) 1, b) 10, c) 30, d) 60 samples. The simulated sample set had a mean of 400 MPa and a distribution width of 40 MPa. The first specimen ran out at 400 MPa, showing the relative preference for the parameters to lie above 400 MPa. Yellow represents the region of parameters space within the 95% HPD interval, and black crosses show the MAP.*

The Bayesian protocol has several advantages to the regular staircase method: very little information is required about the sample set prior to testing, testing parameters are not reliant on prior knowledge, and a faster convergence is obtained. The first two points follow from the protocol's process, and the latter can be seen in Figure 69. This figure shows the trend in error as a function of sample number for various protocol parameters, as well as the error after 100 samples as a function of the ratio of stress increment to the true distribution standard deviation.

The percentage error is calculated relative to the known true distribution parameters, for example for the mean: $Error_{\mu} = 100 * \frac{\mu_{estimate} - \mu_{real}}{\mu_{real}}$.

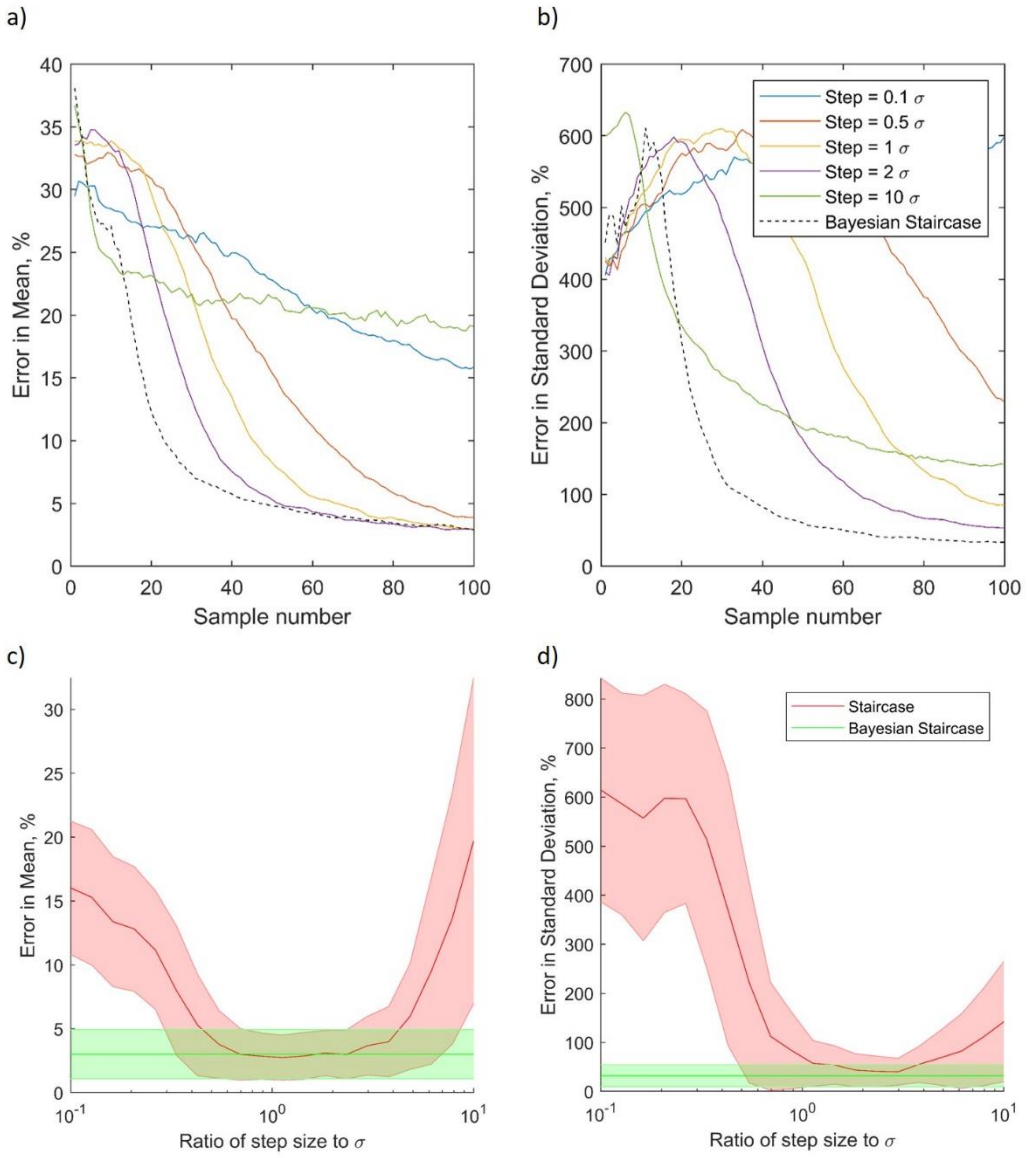



*Figure 69: Convergence plot of a) mean and b) standard deviation for a variety of step sizes, and comparison of error after 100 samples in c) mean and d) standard deviation between Staircase (red) and Bayesian Staircase (green) protocol. The simulated sample set had a mean of 400 MPa and a distribution with of 40 MPa, and the simulations in c) and d) are repeated 200 times to generate a standard deviation in the values (shaded regions). The comparison plot in c) and d) can be seen to be a cross section of a) and b) after 100 samples for a larger number of step ratios. a) and b) lines are smoothed in the x axis with a window of 5 samples.*

The rate of reduction in error for a set of protocol parameters, and the error at some benchmark number of samples varies significantly. The primary observations are:

- The strong variation in the conventional staircase method's rate of error reduction as a function of the sample number.
- The improved rate of error reduction in the Bayesian counterpart, outperforming all possible conventional parameter choices.

### 2.5.9. Bayesian Step Protocol

In comparison to staircase protocols, stress step methods have the advantage that all specimens are tested to failure. However, there is significant debate over the reliability of step test data due to concerns over the effect of previous tests, through damage or coaxing [205], [305], [315]–[318]. Furthermore, as each sample is tested multiple times, the experimental time taken per sample can be higher than staircase testing.

For these reasons, step sizes are generally advised to be above 5% of the fatigue limit [307]. However, this requires prior knowledge of material properties and is dependent on the life being tested, as well as causing debate over whether this is sufficient to avoid damage/coaxing. While larger step sizes reduce the effect of loading history, there is a trade-off between accuracy and precision: the details of sample distribution are lost when carrying out tests at larger step size. Crucially, having a fixed set of stress levels to test reduces the ability of larger step sizes to be used for precise estimation of parameters: if the step size is larger than the distribution width of fatigue strengths, samples will always fail on the same step.

To that end, we create a protocol that finds an optimal step size and starting stress, setting out the stress levels for an individual sample. The utility calculated in Equation (12) for a range of step sizes and starting stresses creates a utility surface as shown in Figure 70, where the maximum value corresponds to the optimum parameters for the next sample to test. For constant life testing, the optimum step size is always the smallest step size as it provides the smallest interval of fatigue strength for the sample. This trivial result reflects the trade-off described above, but without regard for damage effects. Therefore, the benefit of this Bayesian approach in

comparison to the conventional protocol arises when using larger step sizes: where damage is less of a concern and the role of starting stress can greatly influence accuracy.

Thus, the dimensionality of the utility surface can be reduced to only considering varying the starting stress with a constant step size. Here, we choose 160 MPa, or 4 times the standard deviation, shown in Figure 70. This significantly larger step size can be increased further, and is used only as a demonstrator of the effect of starting stress.

Generally, the protocol follows similar behaviour to the Bayesian Staircase protocol. The starting stress has large variations at low numbers of samples where varying the possible failure stresses gives a quicker estimation of the mean fatigue strength. When the step size is larger than the width of the sample strength distribution, the starting stress tends towards testing the same point at large numbers of samples where the stress levels intersect stresses approximately one standard deviation away from the mean, analogous to the behaviour noted in the Bayesian Staircase protocol. Conversely, when the step size is much smaller than the width of the sample strength distribution, there is comparatively less to gain by varying starting stresses.

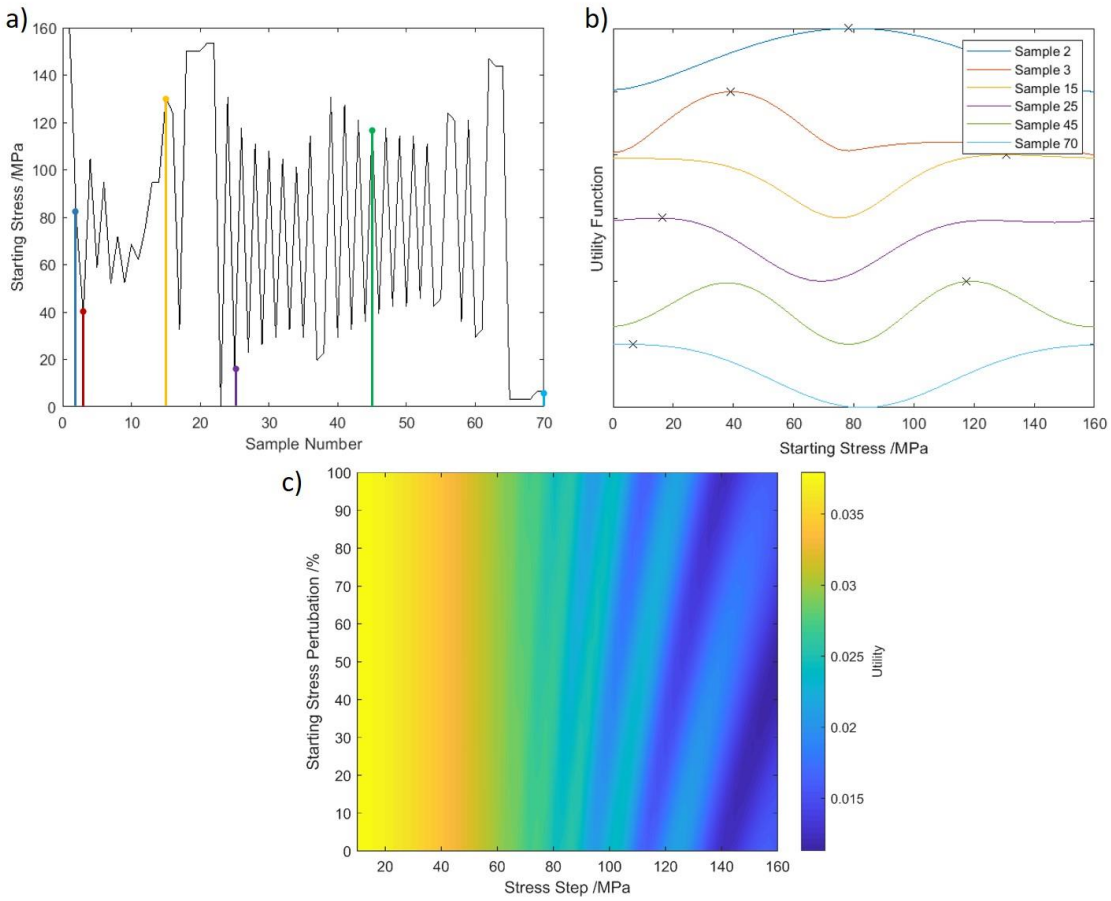



*Figure 70: a) Staircase plot of the Bayesian Stress Step protocol, showing the starting stress as a function of sample number. The specimens simulated had a mean strength of 400MPa and a distribution width of 40 MPa. The stress step was 160 MPa, with a maximum starting stress of 160 MPa. b) Utility function showing the relative utility of various starting stresses, at a selection of specimen numbers, colour-coded as in a). c) Utility at 70 samples is shown when allowing for a variation in step size, showing the preference for smaller step sizes. In this case, the vertical slice at a stress step of 160 MPa is equal to the curve at 70 specimens in b), and the stress perturbation represents the variation in starting stress from 160 MPa to 160 – 100% * step size.*

As in the case of the staircase protocols, a comparison can be made between the conventional stress step protocol and its Bayesian counterpart, as a function of the stress increment size shown in Figure 71.

In this case, the lowest error after 100 samples is given by testing with the smallest step size, an intuitive result when recalling that these simulations do not investigate the role of damage. It can also be seen that the Bayesian counterpart performs identically for small step sizes. It should also be noted that the error level, even at this reduced number of specimens, is lower than for staircase testing at small step sizes. This is in line with common practice, highlighting the trade-off in choosing protocols between efficiency and concern about damage.

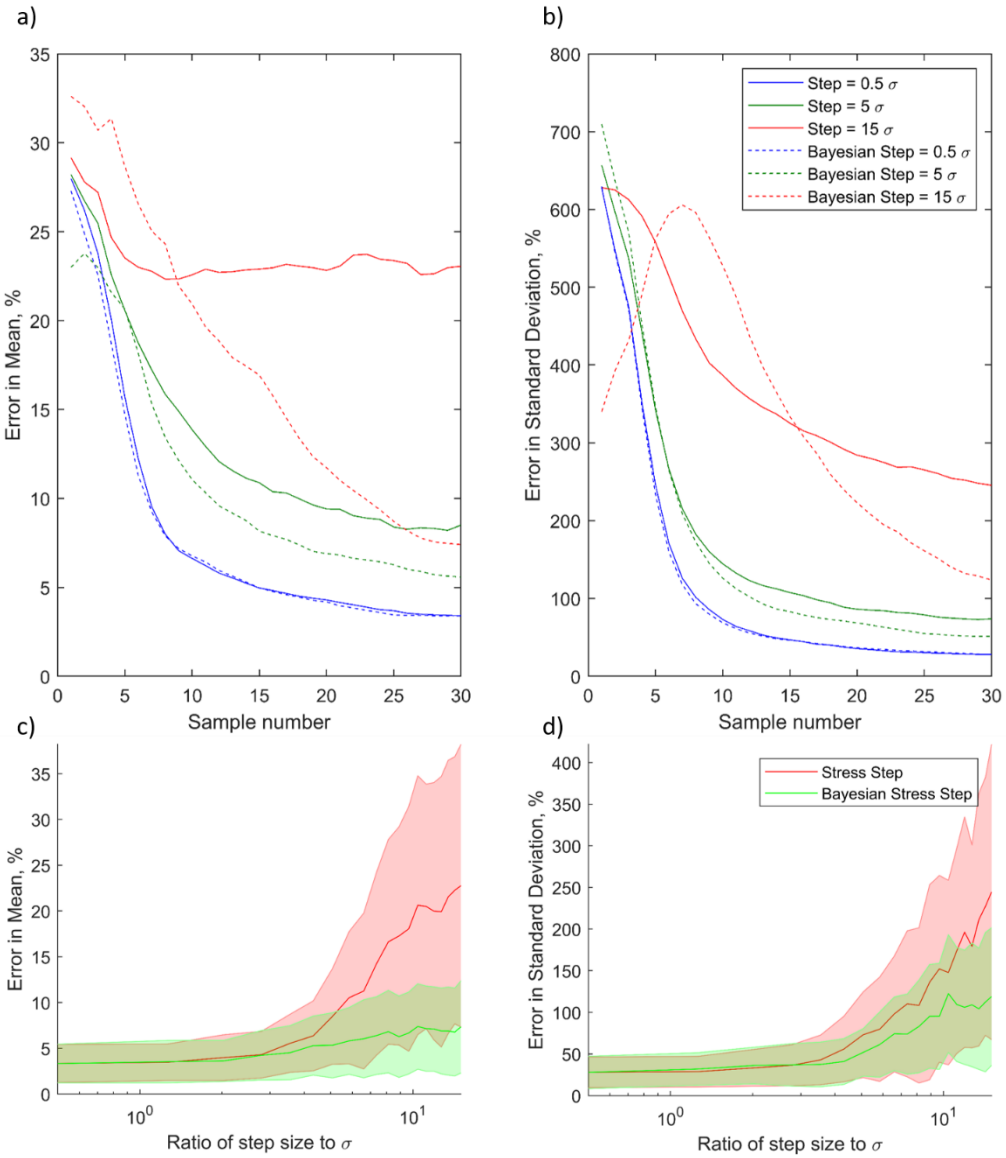



*Figure 71: Convergence plot of a) mean and b) standard deviation for a variety of step sizes, and comparison of error after 30 samples in c) mean and d) standard deviation between conventional (red) and Bayesian (green) for a variety of ratios between step size and true distribution width. The simulated sample set had a mean of 400 MPa and a distribution with of 40 MPa, and the simulations in c) and d) are repeated 200 to generate a standard deviation in the values (shaded regions). The comparison plot in c) and d) can be seen to be a cross section of a) and b) after 30 samples for a larger number of step ratios. a) and b) lines are smoothed in the x axis with a window of 5 samples.*

The benefit from the Bayesian Step protocol comes when using larger step sizes and the relative difference of starting a fraction of a step away (Figure 71). For these larger step sizes, the Bayesian protocol has a significantly better performance in estimating both mean and standard

deviation. For example, the Bayesian protocol with a 15 σ step size and obtained a better estimate of mean than a conventional step protocol with 5 σ step after 30 samples.

Note that in the initial phases of data collection, particularly for estimates of standard deviation, the error in the Bayesian protocol is higher than for conventional protocols. This is an artefact complicated by the distribution in the error: in a conventional protocol, an experimentalist may achieve an accurate measurement, but is highly unlikely to. This can be seen when observing the distribution in the error after 5 samples, shown in Figure 72.

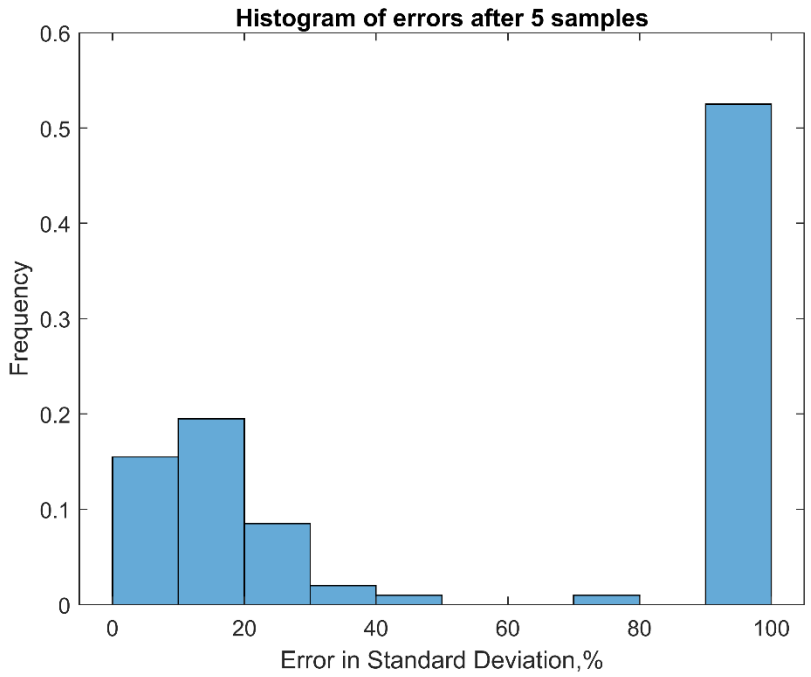



*Figure 72: Histogram of errors after 5 samples, for 200 repeats, at a step size 5 times the true spread of the simulation dataset. This simulation dataset had a mean of 400 MPa and a spread of 40 MPa. A bimodal distribution can be seen, with most repeats having an error of 90-100 %, and some having a low error of approximately 20%.*

This complication can be resolved by considering the mode of the error: what is the most likely error that an experimentalist is likely to incur during the experiment. This is shown in Figure 73.

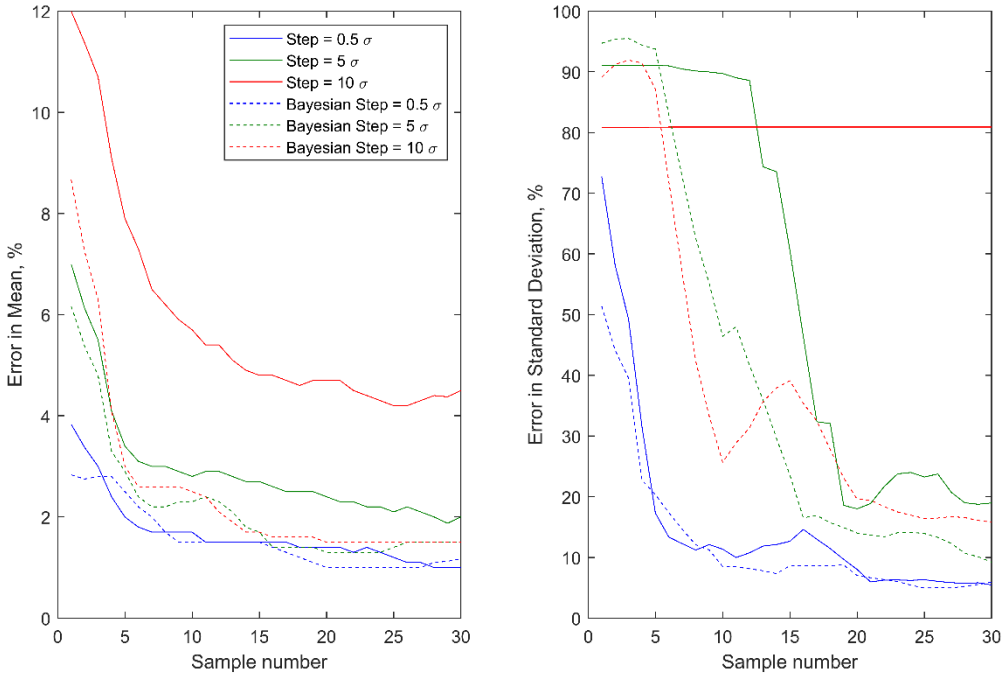



*Figure 73: Convergence plot of the mode of the error in the mean (left) and standard deviation (right) for a variety of step sizes. The simulated sample set had a mean of 400 MPa and a distribution with of 40 MPa.*

Stress step tests can therefore be used with comparatively less concern over damage by using significantly larger step sizes and varying the starting stress. Compared to the conventional protocol, a stress step size approximately twice as large can be used to obtain the same error level for a set number of samples.

### 2.5.10.Statistical Model Selection

Fatigue strength data is often extrapolated to low probability of failure to give acceptable tolerances in service. However, the choice of statistical distribution model to describe this fatigue strength will strongly affect the extreme value statistics. This has motivated work in determining model suitability [203], [365], [374]–[376], [366]–[373]. We provide a tool for the comparison of different statistical models given experimental data collected, such that model suitability can be explored.

This work focusses on Bayes Information Criterion (BIC), shown in equation (34). BIC is based on the maximum log-likelihood $\hat{L}$, number of observations $n$, and the number of parameters $k$ in the

model. The term with number of parameters penalizes against models with more parameters as they will be more liable to overfitting. Models with a lower BIC should be selected over other models.

$$BIC = k\ln(n) - 2\ln(\hat{L}) \tag{34}$$

$$\hat{L} = \max P(\boldsymbol{x}|\boldsymbol{\theta}, M) \tag{35}$$

$\hat{L}$ is the maximum value of the likelihood function (35) which describes the probability of observing data given a model $M$, data $\boldsymbol{x}$, and parameters $\boldsymbol{\theta}$. Thus, $\hat{L}$ gives a measure of the goodness of fit of the data to the best model of that functional form. Following Kass and Raftery [381], the value of the BIC can give evidence for a model over another model with lower values indicating more evidence. To compare two models, $\Delta BIC$ can be defined as $\Delta BIC = BIC_1 - BIC_2$, and shows evidence for $BIC_1$ if it is negative. Values of $\Delta BIC$ between 0 and 2 indicates weak evidence, 2 and 6 indicates substantial evidence, and 6 to 10 indicates strong evidence for the lower BIC.

The ability of this criterion to select from these distributions is dependent on the protocol used as well as the model of the input sample distribution, with step-type protocols resolving the distribution type much more effectively than staircase-type protocols as shown in Figure 74. Generally, step-type protocols with smaller distribution width relative to step size are easier to distinguish, and it is harder to distinguish Log-Normal from Normal. Repeat experiments comparing to 3-parameter Weibull, Gumbell, and Frechet produced similar distinction between distribution models, with stress-step methods providing stronger distinction between distributions.

However, it must be noted that the distinction between these distributions remains unclear after testing 80 samples in simulation, and further testing is required to develop a confident distinction

with these protocols. This does suggest the possibility of developing a utility function with an experimental aim to maximise the distinction between distributions.

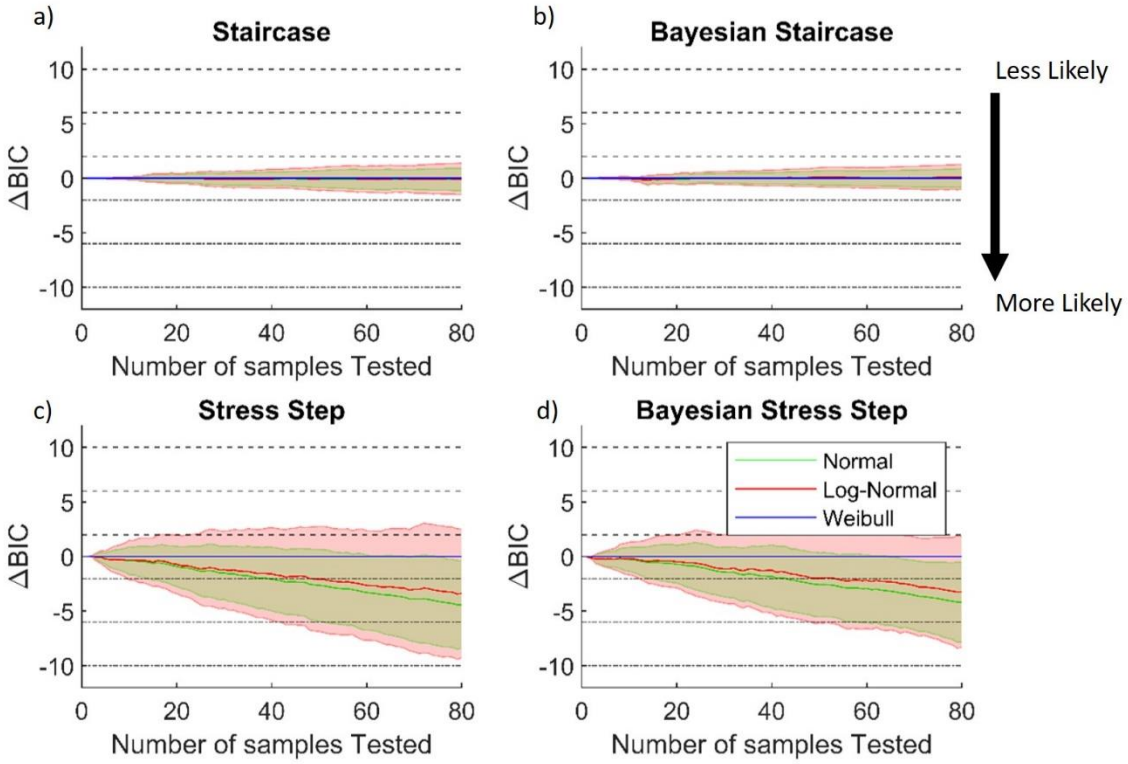



*Figure 74: Evolution in $\Delta BIC$ (difference in Bayes Information Criterion) for data with Normal distribution and mean of 400 MPa with standard deviation 40 MPa. $\Delta BIC$ is calculated relative to $BIC$ for 2-Parameter Weibull distributions, with the lowest BIC indicating a distribution with stronger evidence. a) Staircase, b) Bayesian Staircase, c) Stress Step, d) Bayesian Stress Step protocols based on 100 repeats (shaded region corresponding to one standard deviation). Step Size/increment was 40 MPa and starting stress was 380 MPa for Staircase and 120 MPa for Step. The dashed lines represent the level of evidence shown as in Kass and Raftery* [381].

### 2.5.11.Comparing Protocols and limitations

The comparison between conventional and Bayesian-type protocols as shown in Figure 69 and Figure 71 are a result of our definition of convergence. However, this visualisation significantly reduces the information present in the simulations, and our definition of convergence is just one of many ways to compare results. The current definition only considers the deviation of the Maximum *A Posteriori* (MAP) from the true value. Further considerations can be made, for instance, by observing the gradient at which the MAP reaches a value and does not change, the number of samples required for this converged value not to change by some threshold, and analysis considering the distribution in parameter probabilities. However, regardless of the

definition, it was observed that Bayesian counterparts to conventional methods lead to faster, narrower, and more accurate estimates of both parameters, independent of prior knowledge. Furthermore, in comparing the protocols considered in this analysis, there is a clear difference between the rate of convergence between single-stress tests and multiple-stress tests. Stress step methods may be favourable when fewer samples are available, whereas single-stress tests may be favourable when conducting tests in a shorter amount of time or without concern of loading history.

Examining further, these results also give an insight into the common practice of the conventional protocols. The staircase method can be seen to have the lowest error in determining the mean when the stress increment is near the standard deviation, reflecting the common practice discussed as early as in the original Dixon-Mood reports [306]. However, it can also be seen that this common practice forgoes the nuance in this decision. Figure 75 shows the convergence plot as shown in Figure 69 with only the staircase results after 100 samples, overlaid with the errors as obtained after 30 and 60 samples.

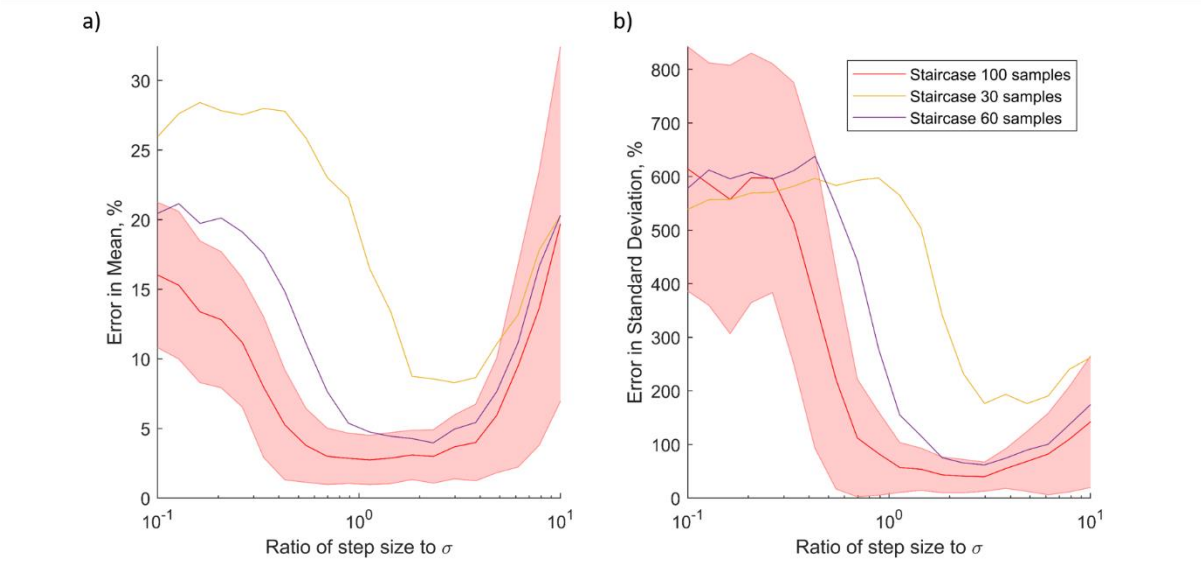



*Figure 75: Comparison of error in a) mean and b) standard deviation as shown in Figure 51 c) and d) examining only the staircase protocol for a variety of sample numbers.*

While the optimal increment for measuring the mean to the lowest error is indeed equal to the standard deviation, this is not true for measuring the standard deviation. Furthermore, the

optimal increment for measuring both mean and standard deviation changes with sample number. Initially, it is more effective to collect data with a larger increment, a result that is reflected in the Bayesian protocol during the binary search and ensuing collection. This highlights the significant advantage of the Bayesian protocol: an evolving sequential adaptation of the testing parameters to the data.

However, whilst the Bayesian methods avoid requiring estimates of the fatigue system to be measured in determining starting stress or step size, the construction of the prior itself is necessary. Both the range in parameters values as well as the coarseness of this discrete mesh require some broad estimation, though this requirement is substantially more flexible: the binary search is sufficiently quick at determining the mean if it is within the extent of the prior. Coarseness of the discrete mesh is only a concern when, for reasons of computational efficiency, the mesh has been coarsened to such a degree that the model predicts likelihood for one set of parameters, and zero probability for neighbouring parameters. During collection of either simulated or experimental results, this can be easily visualised and amended.

This method lends itself to generalisation to allow for a broader set of experimental goals. From earlier discussions of distribution types, it may be possible to generate a utility function that maximises the distinction between distribution types [356]. This represents a potential for future work, highlighting the need in engineering practice to ensure predictive capability at the extremes of the distribution.

An experimental validation of the above simulations was carried out by R Rose to confirm the basis of the Monte Carlo sample set and demonstrate the protocols in a physical laboratory setting. These results can be found in the publication, but are omitted in this thesis in favour of results on the Ti-64 LFW.

These results, until now only applied to constant life, show the benefits of developing protocols aimed with maximising the information for every subsequent sample. Within single-stress tests, it permits for faster convergence on model parameters. Within multiple-stress tests, it permits the use of a larger step size while retaining accuracy. The ancillary tools of distribution distinction also provide a basis to estimate underlying behaviours, and highlight the impact of protocols on such metrics.

### 2.5.12.Extension to PSN Curves

The methodology detailed above allows for the incorporation of the information on runouts or failures into protocol details sequentially, allowing for an understanding of the fatigue strength at some life to be understood during collection. However, currently omitted is the number of cycles to failure. In much of the literature on constant life fatigue testing, as described above, the number of cycles to failure is not reported. While life-testing models provide for the inclusion of such data, it once again is evident that collecting data in the higher cycle regimes remains challenging. What is necessary is a framework for constant life data collection that would allow for the inference of behaviour based on when the sample failed.

Consider that a sample failing very early in the test can inform the experimentalist of something different to a sample failing close to the designated number of cycles in the test – the runout cycle. We can show this diagrammatically in Figure 76, where two samples tested in a staircase test at a stress to a given number of cycles are shown to have failed at drastically different cycle numbers. This highlights the importance in measuring not only aleatoric uncertainty (broadly defined as errors relating to the experimental data), but epistemic uncertainty. That is to say, part of the experimental aim lies in measuring the system's uncertainty, or the spread in response relating to the sample set.

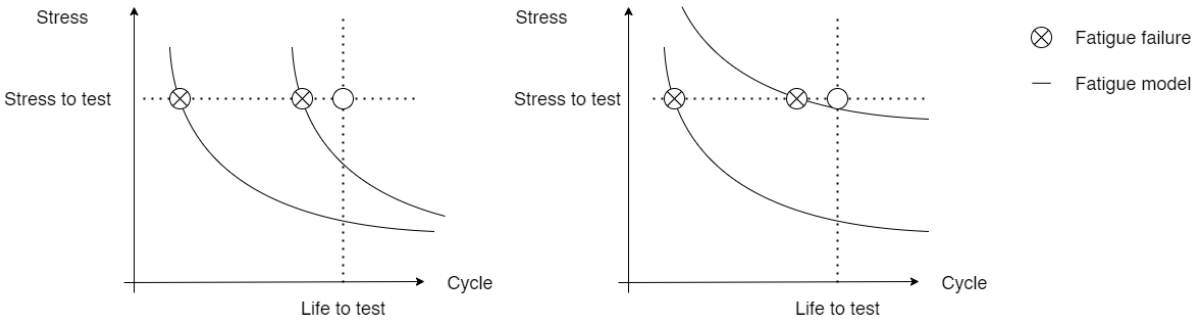



*Figure 76: Diagram of two example fatigue tests conducted at the same stress and runout life (empty circle). Cross-filled circle shows the location in cycles of the failure of each respective sample. Two interpretations of this data with the same fatigue model are shown: the left side shows a life-scattered interpretation, and the right side shows a stress-scattered interpretation. Further data is required to distinguish between the two.*

In this context, this has been framed as, “Is fatigue data life-scattered or stress-scattered?” [309] To illustrate this question, consider the example above modelled with a simple modified Basquin curve with similar parameters to draw the SN behaviour of this system. This figure shows two possibilities to explain the variation between them: that the samples were scattered in life, or that the samples were scattered in stress. Further complexity can be introduced by considering whether the scatter varies across the field: is the scatter homoscedastic (constant across the range) or heteroscedastic (varying across the range)?

Various models that are more complex can model such data with more nuance, however the majority of models imply some SN behavioural curve. In an engineering context, it is trivial to note that both the form of the SN curve, as well as the form of the spread, significantly affect design considerations.

A further aim of this thesis therefore was to determine whether the weld-line SN curve behaves in some different manner to the parent material. With a minimal number of samples, it was deemed not possible to observe statistically significant deviation from one model to another, and a method independent of conventional SN models was developed. This more “cycle agnostic” method can be constructed by considering the behaviour at each life as independent. Using the framework described earlier, this is achieved by considering a set of posteriors describing the constant life behaviour at a set of lives: the SN curve is divided into several “life slices” in which to

study the fatigue strength. This is shown in Figure 77, where three life slices are considered: one at LCF, one at the “elbow”, one at HCF.

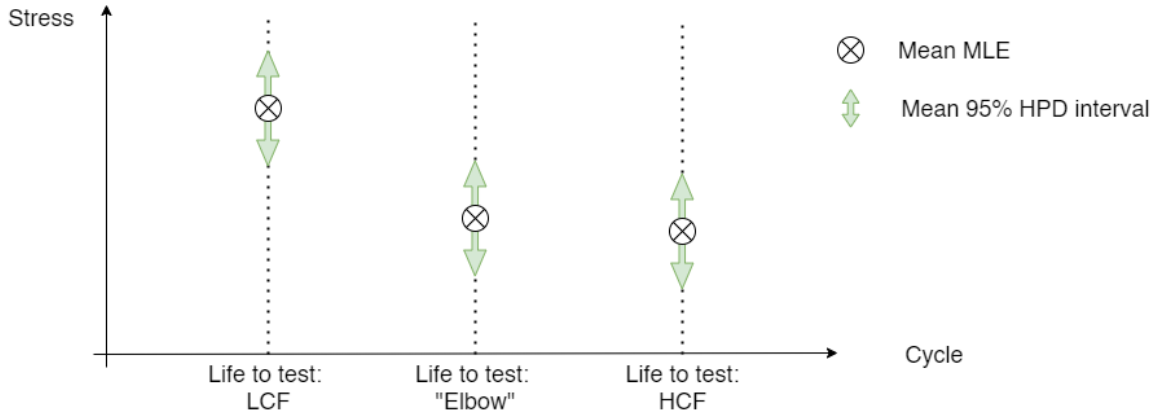



*Figure 77: Diagram of SN curve divided into three "life slices": LCF, Elbow, and HCF. In this case, an MLE with its 95 % HPD interval shows the range of possible mean values.*

Notably, this permits any SN behaviour and defines the SN curve with a subtle but robust structure that at every life there is some defined fatigue strength, which can be modelled with a location and scale. This explicit definition is given to highlight the trivial result that the converse is not true: at every stress there may not be a defined fatigue life within a reasonable range[5].

It is worth highlighting that the purpose of this construction is not to model existing data, but to act as a formalisation of experimental aims during data collection. This unique approach to a fatigue experiment is helpful particularly in the context of comparing the life behaviour for a set of samples at very specific regions of the SN curve: for instance, it permits optimising the sampling to determine the behaviour at very long life, at the “elbow”, and at relatively shorter

[5] While this is reminiscent of debates regarding the existence of a fatigue limit [403], this thesis does not explore the behaviour beyond the range of $10^0$ - $10^9$ cycles. Within this range, there can be some fatigue limit defined, though within the construction defined this is better described as simply the fatigue strength at $10^9$ cycles.

lives. The data gathered from this independent modelling of the SN curve can then be used to validate SN models, and is particularly useful for doing so at (V)HCF.

To illustrate the structure of this, an example of such results is shown in Figure 78. Three slices are shown with sufficient data to constrain the posterior to a narrow set of parameters. It can be seen that each MAP reflects the trend expected from the underlying Basquin curve, but crucially that the high cycle fatigue slices are equally constrained.

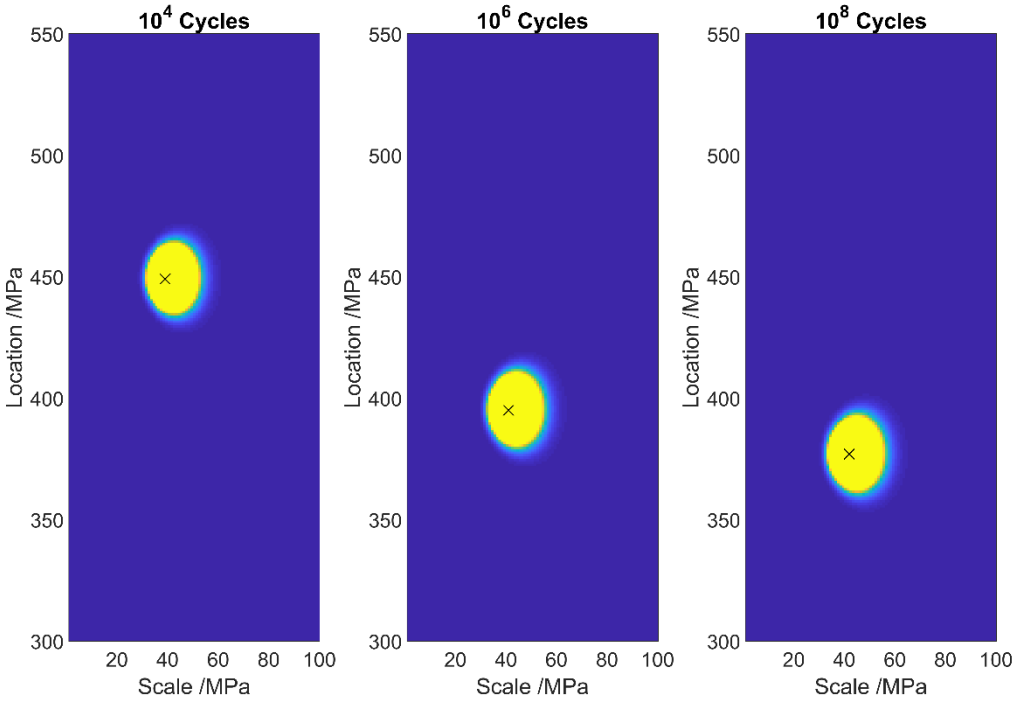



*Figure 78: Simulated PSN results for three slices at log(cycle) 4, 6, and 8. Results obtained are from a total of 90 stress step samples at 10 MPa step size starting from 0 MPa with 30 carried out at each life. The simulated sample set is the same functional form and parameters as described in earlier sections, with a mean 450, 400, and 375 MPa at each respective life and a constant Normal spread of 40 MPa.*

With this construction, the earlier example can be reanalysed: does the location of the failure cycle relative to the lives under analysis affect our understanding of the fatigue response? Does

the posterior of LCF behaviour change if a sample tested to HCF were to survive past LCF? Does it change if it failed before LCF? [6]

It is therefore intuitive, when carrying out tests across several lives, to incorporate the information regarding failure cycles from one test into the posterior of other life slices. This propagation of information can be shown diagrammatically in Figure 79, where a variety of scenarios for a given single- or multiple-stress test provides information on the posterior for a set of life slices.

[6] In practice, it is common practice for experimentalists to implicitly consider this information. This approach can be seen in a formalised manner in the British Standard guides for determining HCF behaviour: initial tests consist of life testing followed by a staircase (or similar) test, the former indicating an approximate range of where to carry out a more rigorous test based on when the samples are failing [309].

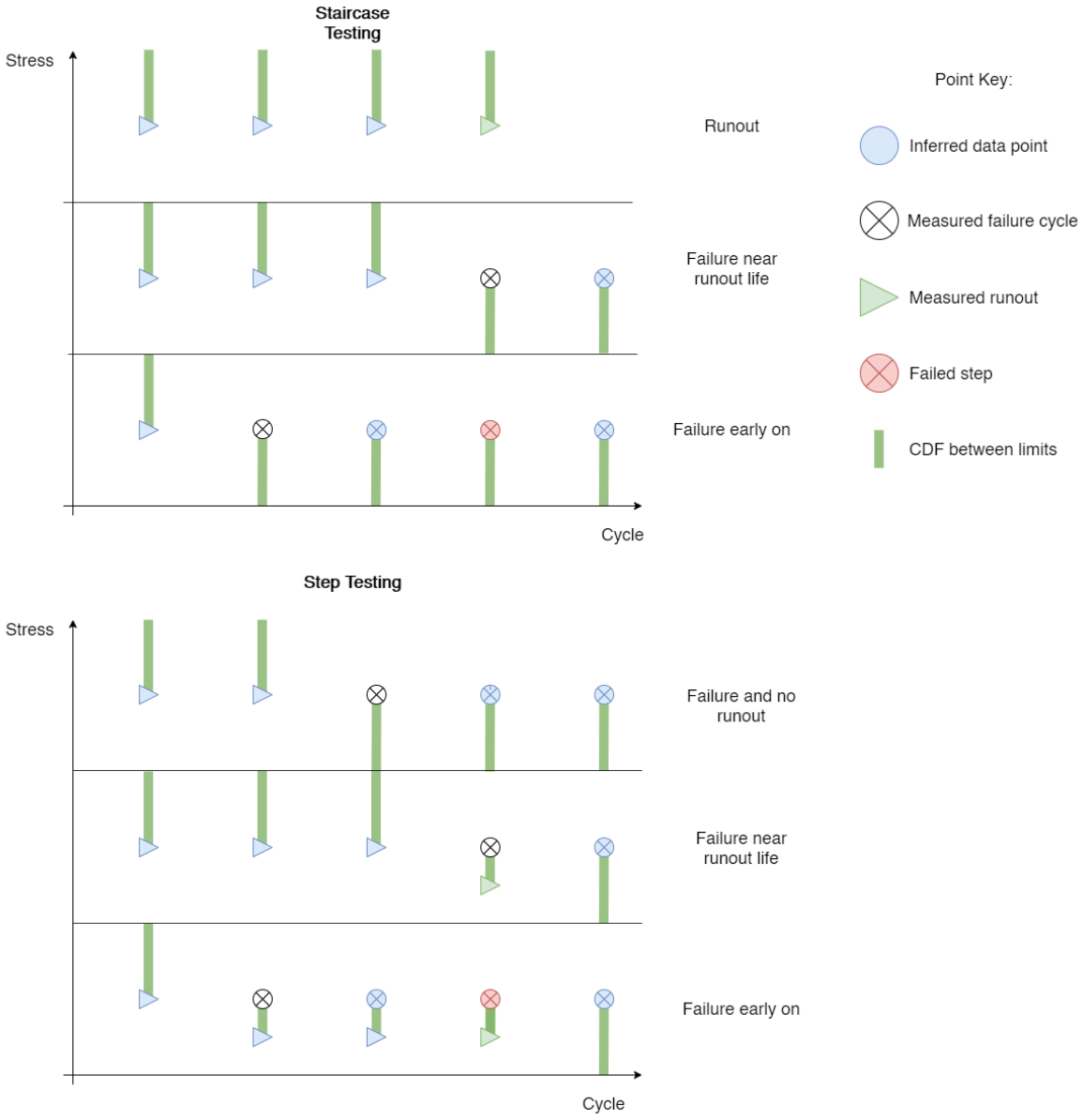



*Figure 79: Diagram of logic propagation from a single-stress test (top) or a stress step test (bottom). Various scenarios are shown with runouts or failures occurring near or far from the runout cycle. Green bars can be interpreted as highlighting regions in stress where the mean is likely to lie.*

The experimental aim can therefore be to maximise the sum of expected information gain across all these lives, also written based on Equation (10) as:

$$U(\boldsymbol{d}) = -\sum_{\boldsymbol{C}} E_X\left(\Upsilon_{\mathrm{C_i}}(x_{i+1})\right) = \sum_{\boldsymbol{C}}\sum_{\mathrm{X}} P_{C_i}(x|\boldsymbol{d}) \int d\theta \; P_{C_i}(\boldsymbol{\theta}|\boldsymbol{x}) \ln\left(P_{C_i}(\boldsymbol{\theta}|\boldsymbol{x})\right) \tag{36}$$

Here, the expected utility is summed across all the lives in a set $C_i \in \boldsymbol{C}$, where for instance $\boldsymbol{C} = \{10^3, 10^4, 10^5, 10^6, 10^7, 10^8, 10^9\}$ represents evenly log-spaced slices between $10^3$ and $10^9$. This simple extension to a variety of lives allows for the optimal collection of fatigue data for the SN field without any parametric SN curve model.

However, the evaluation of $P_{C_i}$ requires careful attention. In this case, the probability of collecting a data-point within some slice $C_i$ is no longer the probability of the sample achieving a certain state by the end of the test (such as a failure or a runout) as described earlier, but rather the probability of failing within some number of cycles. Simply, it is the probability of failing at some cycle $N$, or the location in the cycle axis of the measured failure cycle in Figure 79. Strictly, as the cycle axis (or time axis) has been discretised into specific life slices, the question becomes what the probability of recording a failure between two life slices.

For a single test at some stress $S$, the probability of failing within some interval in cycles is similar to the case of multiple tests across stress. I.e. this can be thought of as an integral between two limits in life of the fatigue life probability distribution function. However, as we do not evaluate fatigue life probability distributions, the probability of failing between two slices can be evaluated in terms of the fatigue strength cumulative distributions. This is written as the difference between running out on some slice $c - 1$ at stress $S$ and failing on slice $c$ at that same stress $S$:

$$P_N = \begin{cases} P_N = \Phi_{C_1}(S), & for\ N < C_1 \\ P_N = \Phi_{\chi}(S) - \Phi_{\chi-1}(S), & for\ C_{\chi-1} < N < C_{\chi} \\ P_N = 1 - \Phi_{\max C}(S), & for\ runouts \end{cases} \quad (37)$$

Recalling that the likelihood is evaluated from the cumulative distribution function (CDF) $\Phi(S)$. This formulation of the problem can be verified by considering that the sum of all the probabilities of failing before the runout slice is intuitively equal to the final CDF of the runout slice.

To illustrate the probability quantities determined above, it is possible to generate figures of the probabilities of failing at a certain point in SN space as well as the probability of having failed by some certain point – or, the PDF and CDF in this SN space. This is shown in Figure 80, where the CDF at some life can be intuited as the sum of all values to the left of that slice in the PDF figure. These plots show the motivation of such a construction: this formulation permits the simple consideration of the probability of a certain state by some number of cycles at some stress, or the fatigue life at some stress.

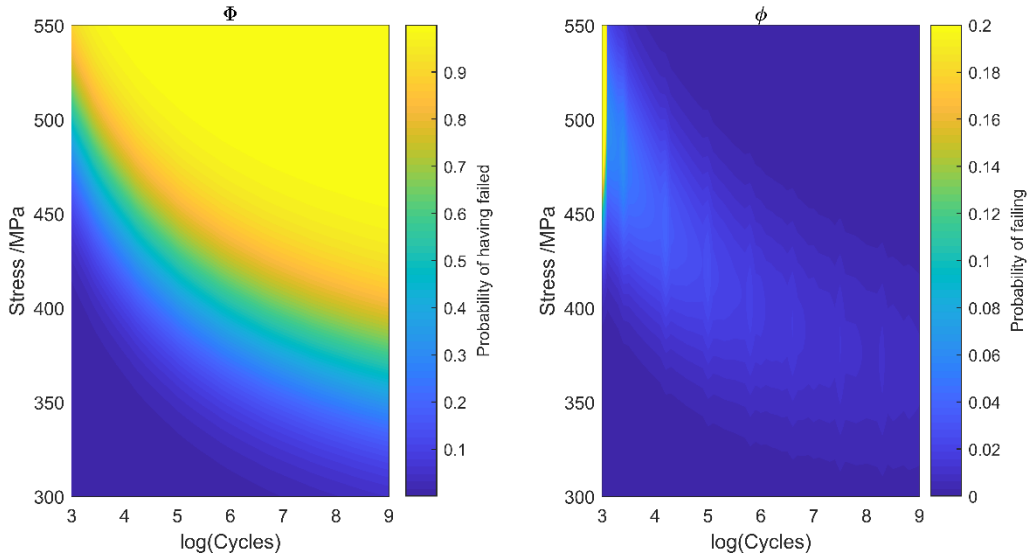



*Figure 80: Simulated PSN results showing CDF (left) and PDF (right) from a perfect posterior based on the sample set described earlier. Prior slices cover the range of 3 to 9 $log(cycles)$ in steps of $0.1$ $log(cycles)$, and each posterior is null save for the correct parameters at that cycle. Discretisation lines can be seen as artefacts in the PDF example.*

In practice, fewer life slices would be considered, and visualisation of such data requires care owing to the discretisation of this data – a consideration necessary when discretising any data.

To evaluate the probabilities of failing at some SN coordinate for a multiple-stress test, this question becomes further nuanced: consider a step test whereby the stress at some step is equal to mean fatigue strength. It is therefore expected that 50% of the samples fail at this step. When determining the probability of failing at some cycle $N$ on the next step, we must consider that the experiment has effectively carried out a proof-test, and that the mean number of cycles to failure may differ from that of an equally stressed single-stress test for purely statistical reasons. This is

inspired from the approach of Ganser *et al* [382] where the truncated distribution is carried forward for the next step. Diagrammatically, this is shown in Figure 81.

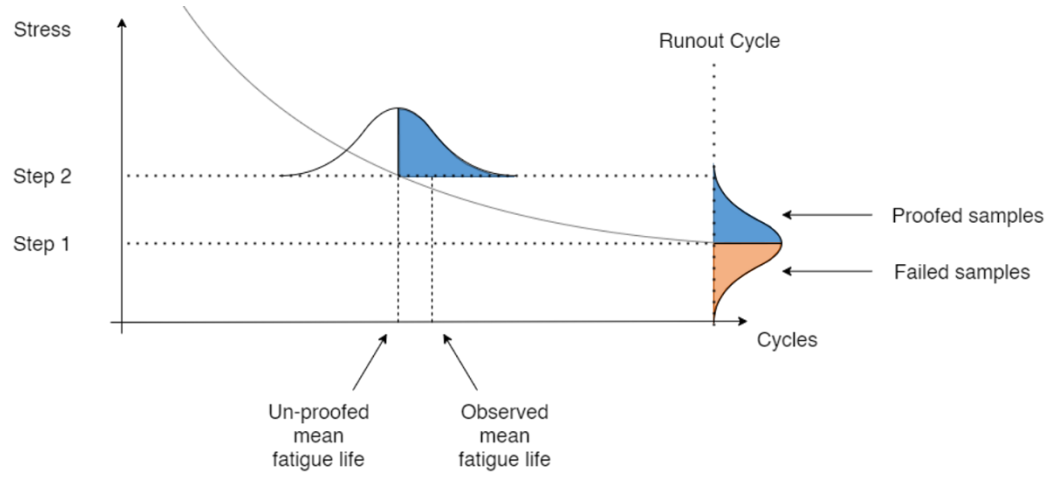



*Figure 81: Diagram showing the proof-test effect on step tests. A set of samples are tested to step 1, with half of them failing. The remaining half are tested to step 2, and the proofed samples exhibit a higher mean fatigue life than the un-proofed full sample set.*

The assumption this analysis implies is that strong samples are strong at every life, and weak samples are weak at every life. In other words, that the SN curves of each individual samples do not cross. This assumption underpins the computational framework as well, and while competing fracture mechanisms may cause individual SN curves to cross, within a small number of samples that are not characterised to determine defect population, this assumption is reasonable.

In practice, this achieved by determining the probability of surviving the test at the previous stress, and considering only the percentage that may survive this. This is repeated cumulatively, and it can be shown that the sum of the probabilities of failing at some cycle $N$ is equal to the step interval probability as described earlier.

Figure 82 shows the calculations for two different step testing protocols, one where small steps are taken, one where larger steps are taken, and a comparison to the single-test approach. These simulations are run from a starting stress of 130 MPa, leading to a 50% failure rate at approximately 370 MPa for each stress step test. It can be seen that samples are expected to fail at approximately 4.5 log(cycles) for single stress tests, but are barely expected to fail at all in small

step size tests (owing to them all having failed by this point), and expected to begin failing at 5.1 log(cycles) for larger step tests. The importance in such nuance is in adequately calculating the probability of samples failing at certain times, in order to calculate the expected utility of such a result. However, these results highlight the care needed when analysing stress step data: regardless of any physical damage or loading history mechanism, there are significant statistical effects in the results when considering the number of cycles to failure. The state results of failures or runouts (representing truly constant life data) are not affected by this statistical biasing.

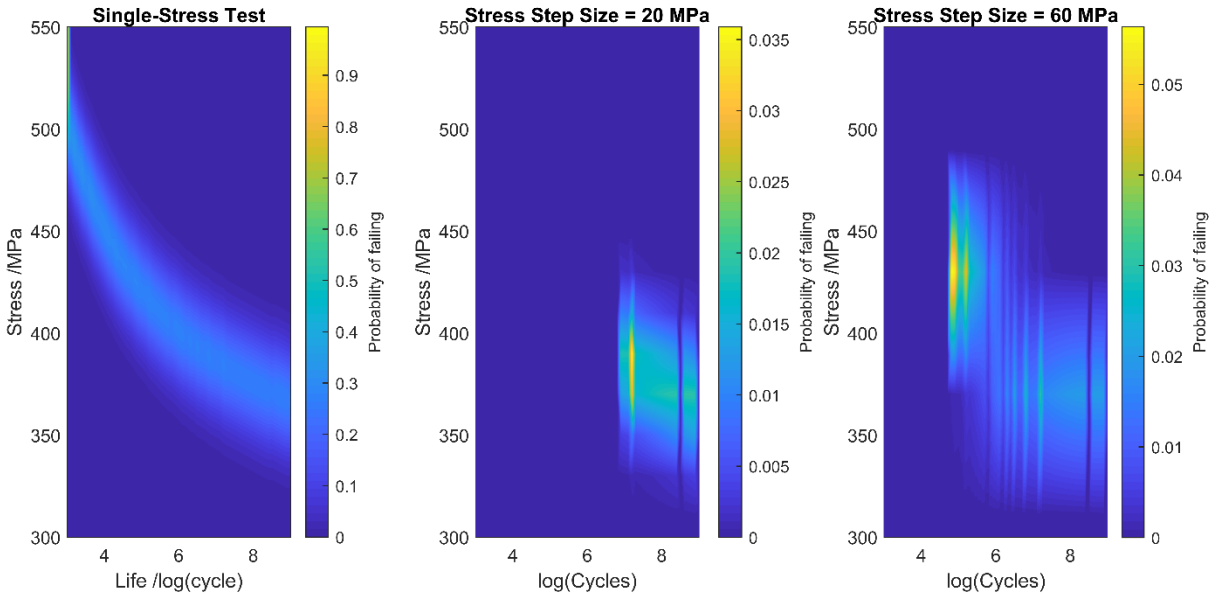



*Figure 82: Visualisation of truncation effect in step testing. Single stress test (left) as shown in Figure 62 (RHS) shows the original expected failure distribution. Small step size (centre) shows accumulation near the HCF region, with some discretisation artefacts. Larger step size (right) shows truncation and statistically extended fatigue life for tests conducted at 430 MPa.*

In this framework, a fatigue test can be considered as travelling along the x-axis of the above PDF figures at a certain stress. This reflects the experimental reality of such tests, where by definition it is only possible to conduct tests – even constant life tests – as a combination of constant stress tests.

With the defined probability of failing at a certain point, it is possible to calculate the utility function in the general case of any single- or multiple-stress test as:

$$\mathrm{U}^{PSN\ Single}(x_{n+1}, R)$$

$$= \sum_{C_i=C_1}^{R} \Upsilon^{\mathrm{fail}}(x_{n+1}, C_i)\ \phi^{\mathrm{fail}}(x_{n+1}, C_i) \qquad (38)$$

$$+ \Upsilon^{\mathrm{survive}}(x_{n+1}, R)\ \Phi^{\mathrm{survive}}(x_{n+1}, R)$$

Here, the first term evaluates the expected entropy change for a sample failing at any point up to the runout cycle. The second term evaluates the expected entropy change for a sample not failing by this point. The terms have been simplified for readability, representing the same quantities as in the constant life case with implied prior data and displaying only the variables of next stress ($x_{n+1}$) and runout cycle ($R$). Note that the sum of the PDF evaluations $\sum_{C_i=C_1}^{R} \phi^{\mathrm{fail}}(C_i)$ is equal to the CDF evaluation $\Phi^{fail}$.

For multiple-stress tests, we consider the equivalent expansion as above:

$$\mathrm{U}^{PSN\ Multiple}\left(x_{n+1,1}, \xi, R\right)$$

$$= \sum_{C_i=C_1}^{R} \Upsilon^{\mathrm{fail}}(x_{n+1}, C_i)\ \phi^{\mathrm{fail}}(x_{n+1}, C_i) \qquad (39)$$

$$+ \sum_{C_i=C_1}^{R} \sum_{k=2}^{N_k} \Upsilon^{\mathrm{step}}\left(x_{n+1,k}, C_i\right) \phi^{\mathrm{step}}(x_{n+1,k}, C_i)$$

Here again, we consider the expected entropy change from failing at any point prior to runout in the first step (first term), followed by the equivalent term for all subsequent steps. The variables present to optimise utility are the starting stress, the step size, and the runout cycle. It can be seen here that, unlike in the constant life method, the optimal step size may not be the smallest permitted size: a larger step size may be optimal in order to probe the number of cycles to fail at high stress and low cycles, providing information across a large range of cycles.

The utility function can be seen to become quite complex, and conventional methods for function optimisation can easily fall into local minima. For this reason, the utility function must be evaluated across the full field. For the case of the PSN step protocol, this requires calculation

across the entire step size, starting stress, and runout cycle volume, providing scope for further work to reduce computational intensity.

However, these two utility functions provide unique protocols for fatigue testing across a range of desired runout cycles, with user-defined parameters such as range of step size and starting stresses. Prior to reporting experimental results, it is instructive to observe the behaviour of these full-field SN protocols on simulated datasets.

#### 2.5.12.1. A note about Propagation

The propagation diagram shown in Figure 79 shows the full propagation of information: all life slices are informed of a result irrespective of its nature. This includes cycles before the failure cycle, between failure cycle and runout cycle, and beyond runout cycles. It has been observed in simulation experiments that this propagation is effective for life testing (where the runout cycle is set as the maximum considered life slice and is unchanged), but induces biases for large datasets with large standard deviation when using other protocols. An explanation for this biasing has not been found. However, it has been shown through significant numbers of simulations that propagating between failure cycle and runout cycle – so called “medium propagation” – does not induce these biases in the analysis of results. Therefore, only medium-propagation results are considered for experimental results, and some no-propagation results are shown for illustration. This is discussed further in the Discussion section on page 206.

### 2.5.13.PSN Single-Stress Protocol

The PSN single-stress protocol behaves somewhat similarly to the conventional and Bayesian single stress (staircase) protocol, with initial samples constraining the range of possible mean values followed by sampling near the standard deviation to determine spread. Figure 83 shows the utility function and result of the first sample, followed by the second, followed by the steady-state response after several hundred data-points are collected at each life.

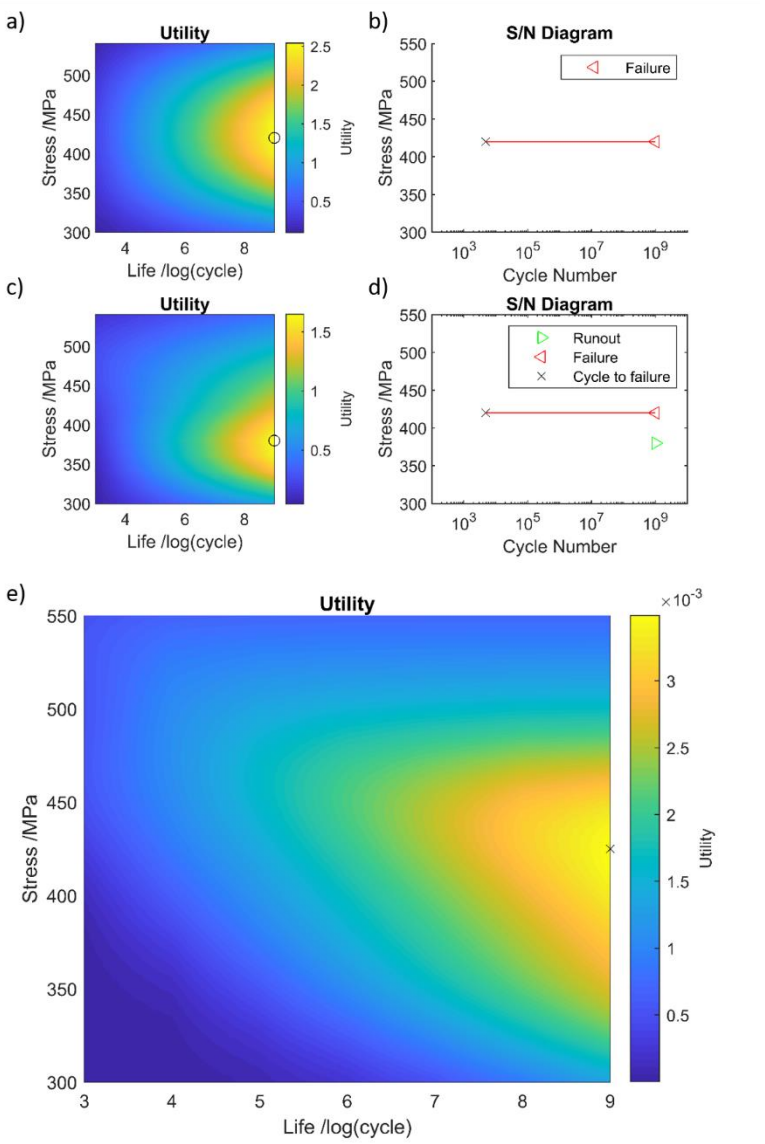



*Figure 83: Simulated PSN Single-Test Protocol. Utility function (a) and subsequent result (b) for the first sample, followed by the second sample (c), (d). The steady state utility function is shown in e) after several hundred data points are added to each life slice. Runouts considered are the orders of magnitude between 3 and 9, with simulated dataset with parameters as described above.*

The figure shows an initial tendency for high-cycle fatigue, centred about the middle of the stress range as in the constant life equivalent. The second specimen is tested at a lower stress as the first sample failed, again reflecting the behaviour of the constant life protocol. The steady state response, however, retains the HCF and higher stress preference. This can be understood as due to the medium-propagation of information: for a single test, more information is gained for relatively early failures, as many life slices are informed. For illustration, the comparison between

the utility function with medium-propagation and with no-propagation of this same steady state posterior is made in Figure 84.

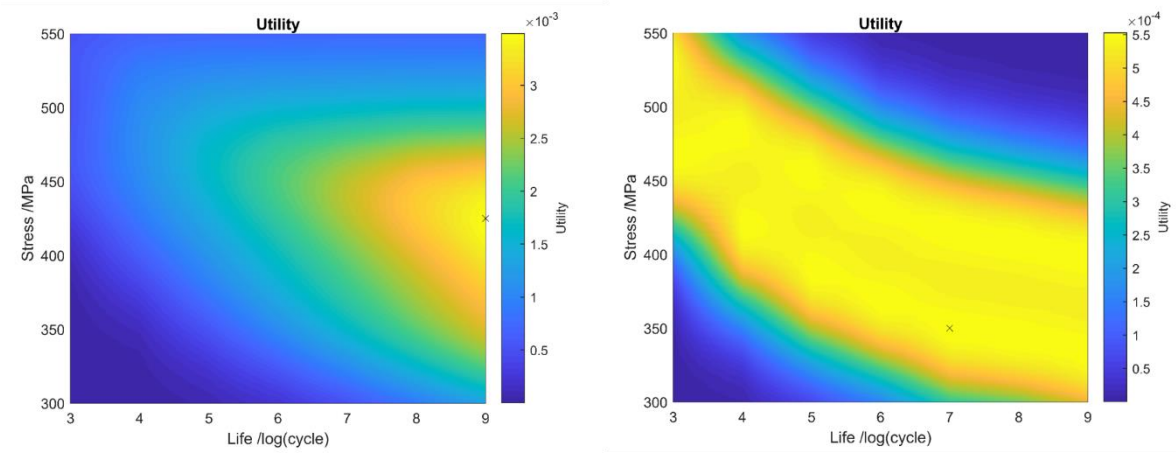



*Figure 84: Simulated PSN plots comparing the steady state utility surface with medium propagation (left) and no propagation (right). Runouts considered are the orders of magnitude between 3 and 9, with simulated dataset with parameters as described above.*

The no-propagation graph can be seen to have a trough in the middle of an SN-curve-shaped band. A cross section in life of this curve produces the same bimodal distribution seen in the constant life example at steady state as seen in Figure 67, as without any propagation this experiment is equivalent to a combination of multiple constant life experiments. The inclusion of logic propagation allows for the generation of a full-field inference on model parameters, and the utility function allows for sampling only where the expected information is the highest. In the case of single-stress tests, it can be intuited that this will always be in the high stress HCF region at steady state.

An example of the SN results in a steady state single-test PSN protocol are shown in Figure 85, comparing between medium propagation and no propagation. While the medium propagation does not test at any other life than HCF, owing to the increased information from early failures, the protocol accurately and precisely estimates the fatigue strength parameters of the sample set.

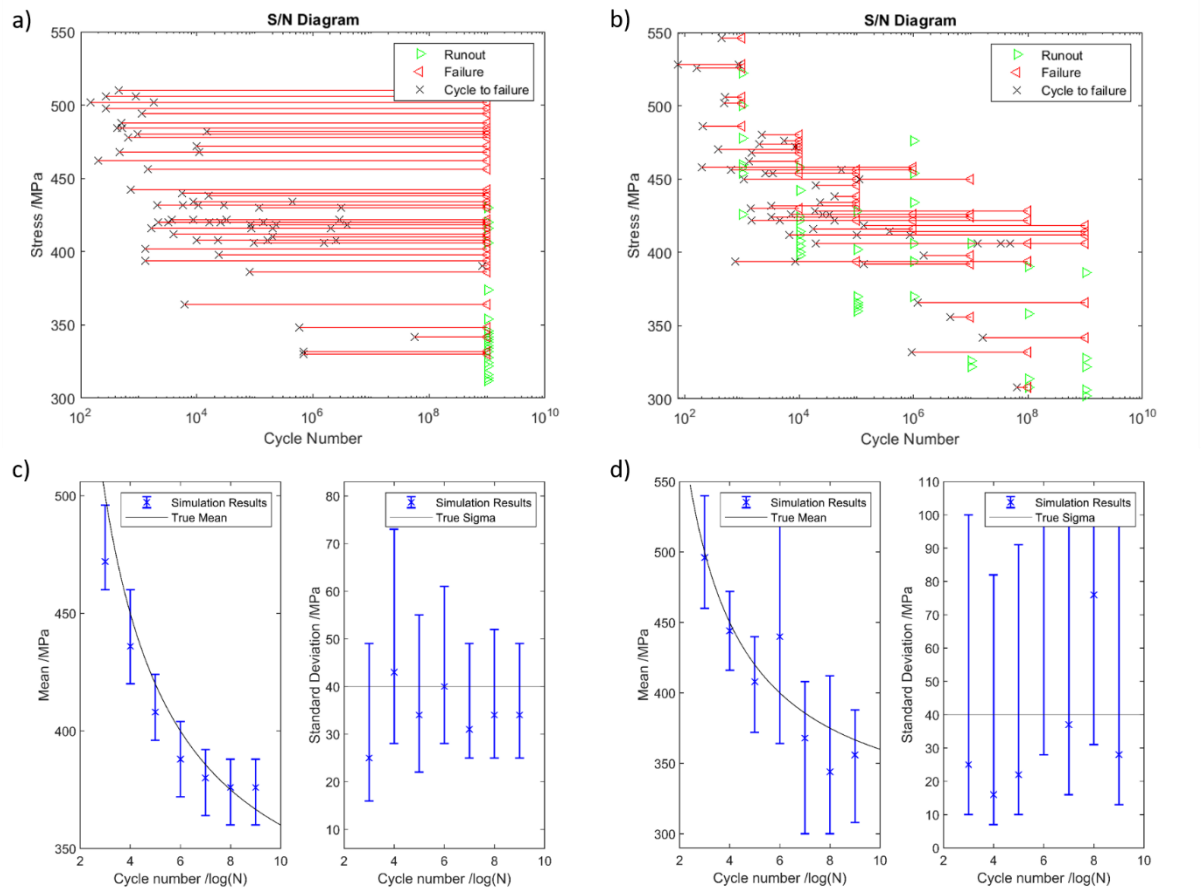



*Figure 85: Simulation PSN Single-test on 100 samples showing medium propagation (left) and no propagation (right). The SN plots are shown in a) and b). The results of the posterior are shown in comparison to the underlying simulation set in c) and d) with MLE and 95% CI. It can be seen that the medium propagation protocol preferentially tests at HCF, though creates a narrower and accurate estimate of fatigue strength across all lives.*

However, as single-stress tests invariably lead to lower precision for low number of samples, it was decided that for the LFW experiments, a multiple-stress protocol would be used. Care was taken to keep a minimal step size that was sufficient to avoid concerns of damage. Prior to discussion of experimental results, it is worth observing the behaviour of the PSN multiple-stress protocol.

### 2.5.14.PSN Multiple Stress Protocol

The multiple stress PSN protocol can be designed with a series of degrees of freedom: starting stress, step size, and runout cycle are all variable. Projections of these variables allow for simpler experiments, such as only allowing starting stress and runout cycle to vary, or even runout cycle alone.

In the case of allowing only runout cycles to vary, the behaviour of the protocol reflects the intuitive approach: one sample is generally tested at every life, unless the sample has failed very early in which case the SN curve can be inferred to be shallow. Following this, samples are tested broadly evenly. This initial behaviour is shown in Figure 86.

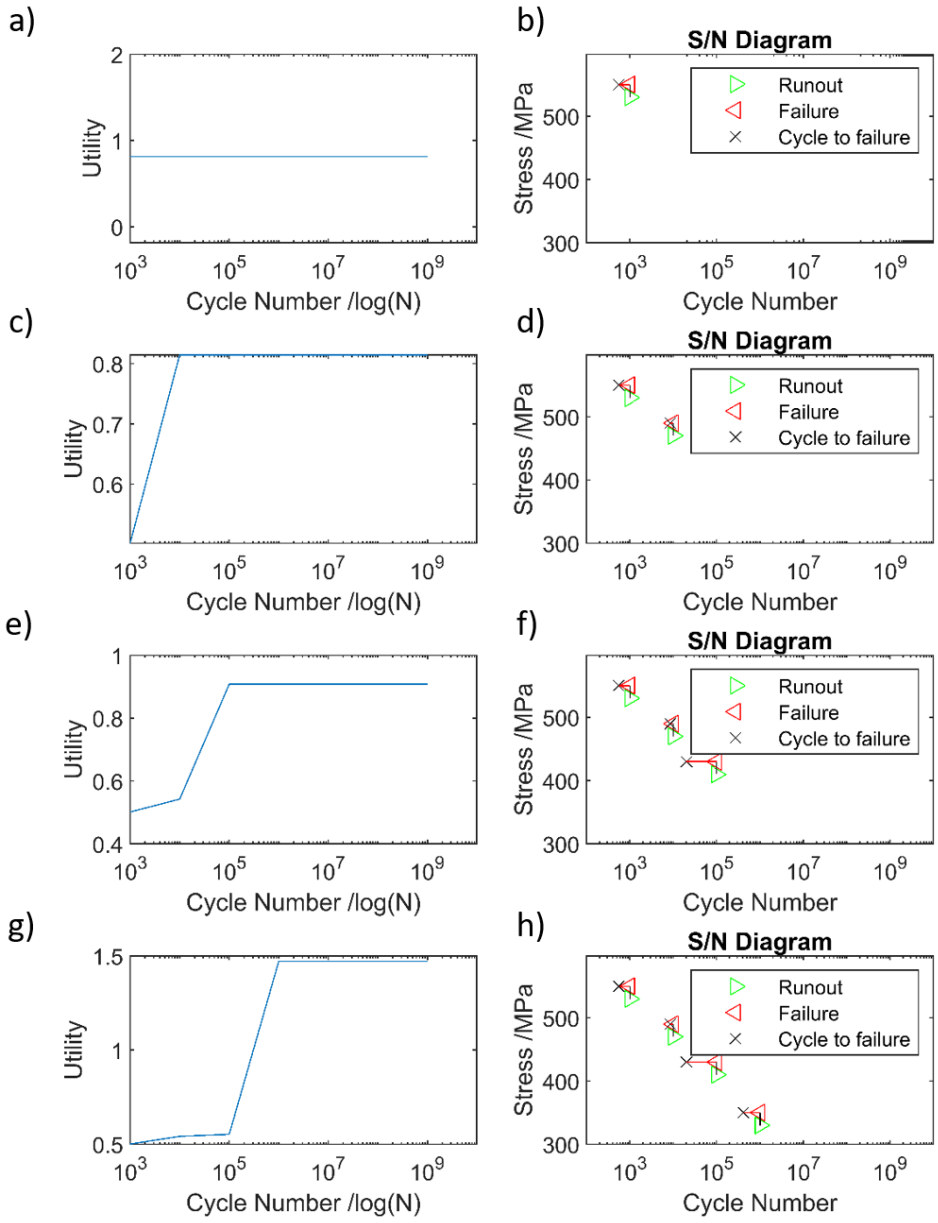



*Figure 86: Simulated PSN multiple stress protocol with utility (left) and subsequent SN plot (right) for the first 4 samples. Runouts considered are the orders of magnitude between 3 and 9, with simulated dataset with parameters as described above.*

This simple case can be seen to have a flat utility function for the first sample – all runout cycles are expected to provide the same information. Choosing the first of this equal set, it sequentially samples at higher runout cycles, eventually having obtained information relating to all life slices.

Figure 87 shows the simulation result of a fully varying (in step size, starting stress, and runout cycle) PSN multiple stress protocol after 50 samples. The SN plot and subsequent utility volume are shown, with a complex structure. Larger step sizes can be seen to give greater expected utility as a result of early failures giving insight into early SN behaviour. The SN plot after 50 samples therefore shows a variety of step sizes, starting stresses, and selected runout lives, and the resulting posterior shows estimates that are in line with the simulated sample set. This advanced protocol is used for the final experimental dataset in the thesis.

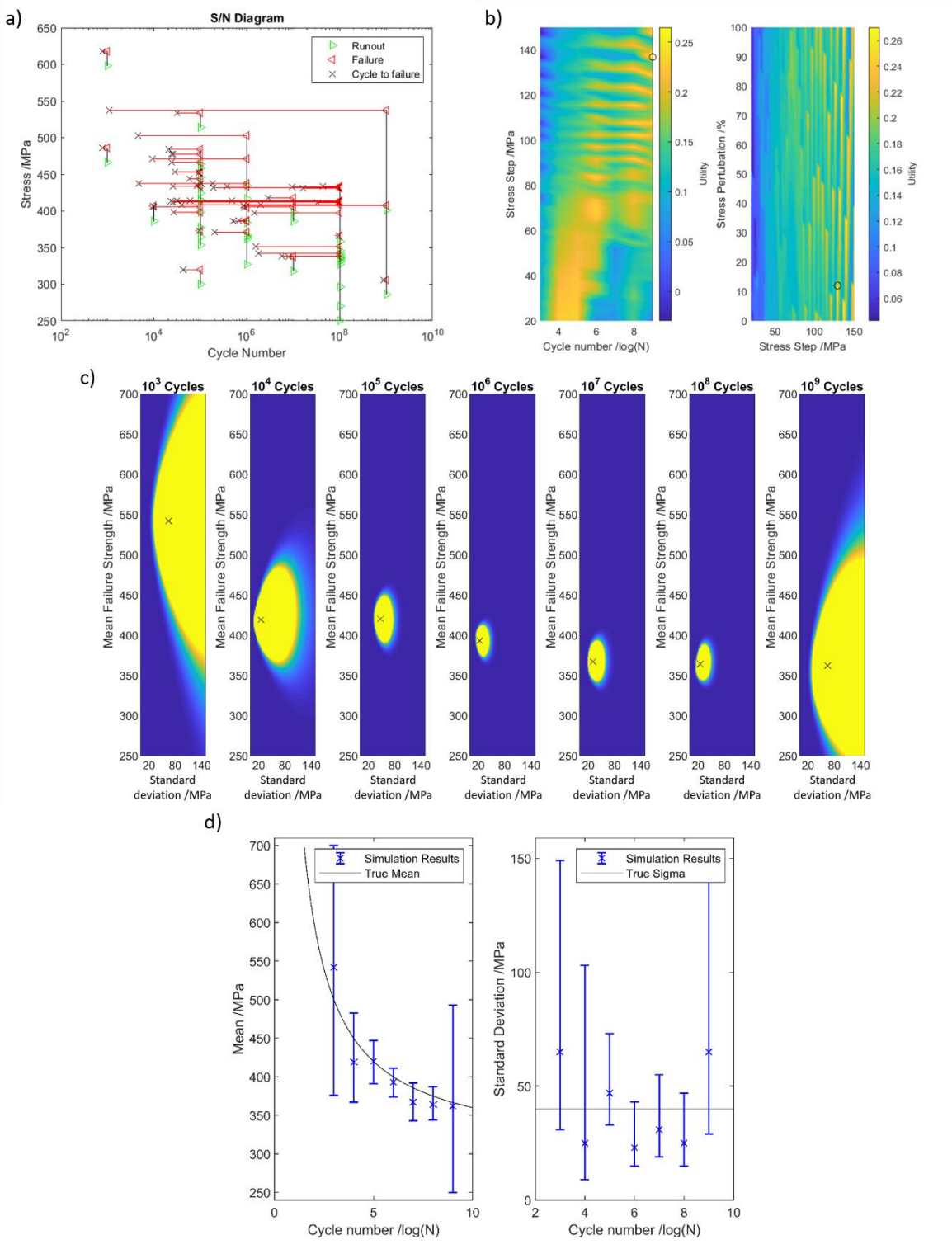



*Figure 87: PSN step protocol with varied step size, starting stress, and life. a) SN plot with 50 samples, b) projection of utility volume for subsequent sample, and c) HPD surface of posterior for life slices of interest. Lives between $10^3$ and $10^9$ are considered, and a simulated sample set as described earlier. Panel d) shows the comparison of posterior estimates to the underlying simulation set curve with MLE and 95% CI.*

## 2.6. Experimental Results

Having outlined the experimental developments as well as the protocols used, the experimental results of the two sample sets, Foil 3&4 and Foils 7-11, can be reported. Owing to the low number of weld-specimens, samples in set Foil 3&4 were tested to a single constant runout life of $10^6$ cycles. This was chosen in order to sample the "elbow" of the SN curve, as well as to provide HCF data within a reasonable amount of experimental time.

Samples in set Foil 7-11 were tested to a range of runout lives ranging from $10^5$, $10^6$, and $10^7$. Similarly as above, this was motivated to sample the behaviour before, at, and after the "elbow" while acknowledging the limited number of samples available.

### 2.6.1. Results of Foil 3&4

Four foils were cut with the purpose of following the complete procedure listed. These were designated the names Foil 3, 4, 5, and 6. The foils were EDM wire cut to 150 µm and trimmed to a narrow width of approximately 10 mm such that all four equally sized foils could be placed on the grinder ensuring a consistent thickness across the foils. The foil was measured to be 100 µm thick following the grinding step, and as the electropolishing results from Foil 2 indicated a thickness reduction of approximately 10-15 µm, a design was made for a cantilever with thickness of 90 µm. Shown in Figure 88, this had a stress concentration of approximately 10% and an achieved stress of 600 MPa at 40 µm of vibration amplitude. The resonant frequency at 95 µm was 26 kHz, decreasing to 22 kHz at 80 µm, in case electropolishing caused more thinning than expected.

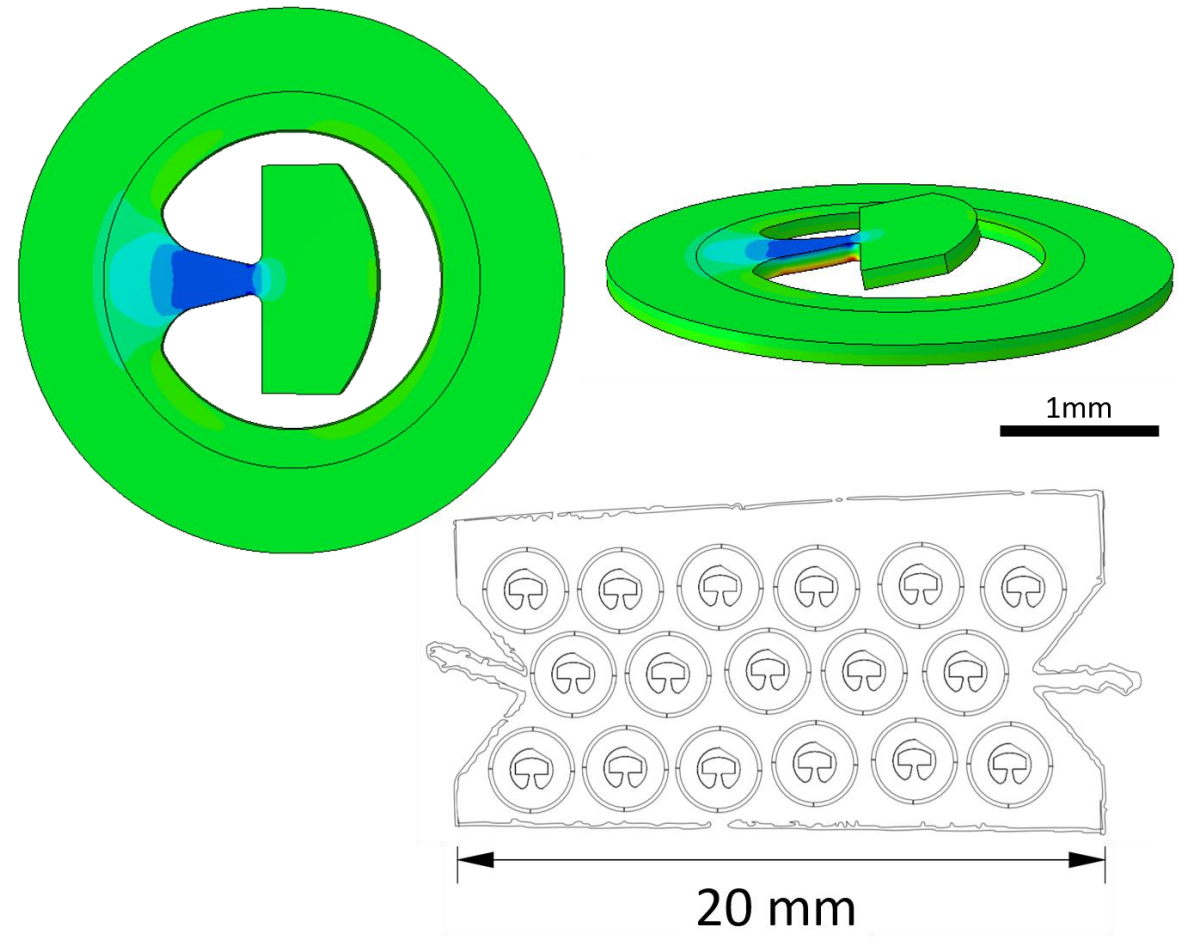



*Figure 88: Cantilever design (top), and layout on foils 3, 4, 5 and 6 as shown in one example (bottom). An asymmetric cut is added to the design of each cantilever on the far end in order to distinguish between the incoming and outgoing laser direction. The weld-line can be seen by the flash extending beyond either side of the horizontal line in the middle of the foil. Five specimens can be laid out along this line, with the alignment of the weld-line in the centre of the cantilever neck.*

The samples were polished in an electropolishing campaign with two batches as described in the Electropolishing section on page 95. Samples from foils 5 & 6 were used for developing the polishing routine, and results are therefore not reported owing to their highly varying quality. The dimensions of all samples in foils 3 & 4 were subsequently measured in the SEM. Figure 89 shows an example of one such measured sample, and Figure 52 showed the results of the dimension measurements.

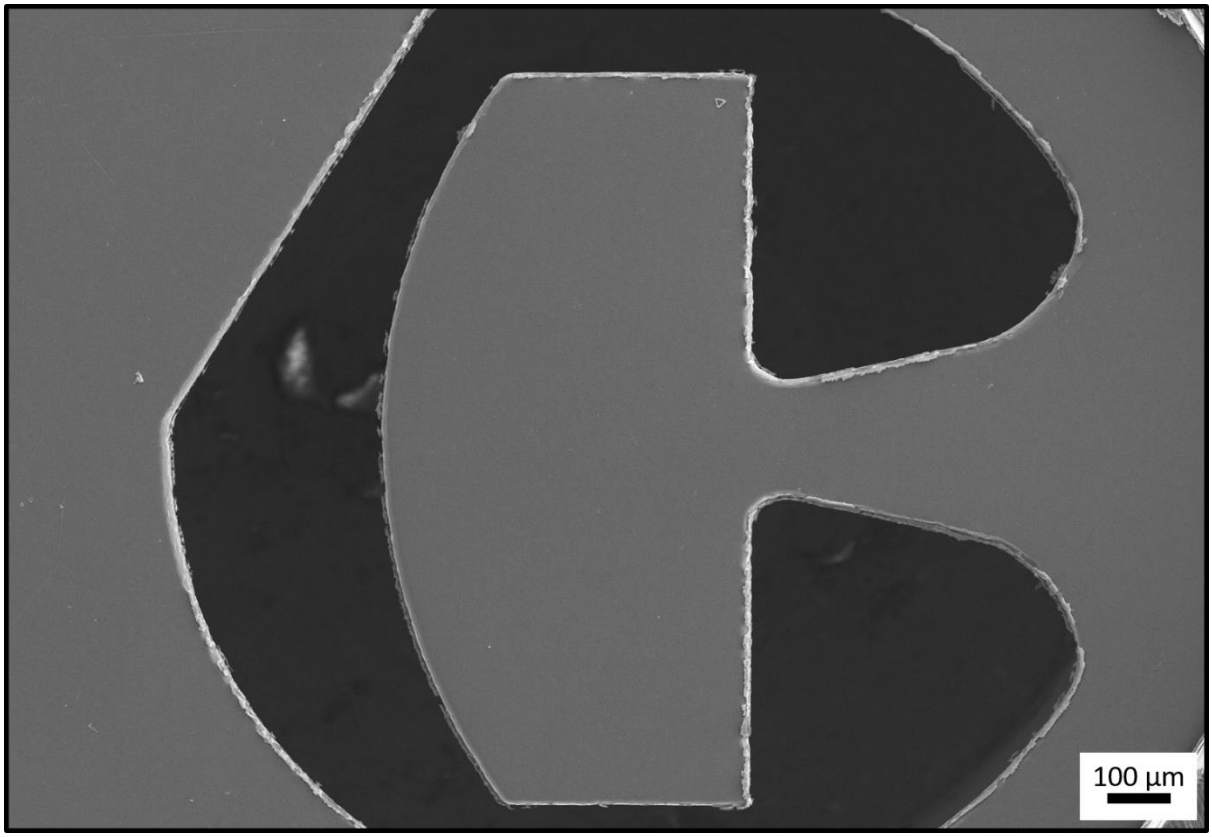



*Figure 89: Sample K8 from set Foil 3&4 following electropolishing step. Sample was polished for 120 s and was measured to have the following dimensions: hammer width 1180 µm, hammer length 594 µm, neck length 537, neck width base 329 µm, neck width end 184 µm, and thickness 81 µm. The quality was deemed a seven out of ten, representative of the average specimen. The asymmetric cut can be seen on the top left of the image, indicating that this is the incoming laser side of the cantilever – for this reason, the taper can be seen, and measurements are made on the mid-point of the taper. SEM image was taken at 60x magnification in secondary electron mode, 20 mm working distance, and 20 kV voltage.*

Details of this particular set of dimensional measurements are outlined in the Geometrical Analysis section on page 111, where 3 principal components were used to model the dynamic responses. The nanoindentation method outlined was used to determine the experimental stiffness, and these results are shown in Figure 57 in the section on page 111. The large discrepancy between experimental and modelled stiffness suggests significant error in some measurement. The standard error in the indentation stiffness was shown to be approximately 8%, while the SEM measurement of thickness has a 5-10% error. It was shown in the Geometrical Analysis section on page 111 that a 1% error in thickness leads to a 3% error in stiffness. Meanwhile, propagating the measurement errors of stiffness via Monte-Carlo simulations shows

that the 8% error in stiffness leads to a 2.7% error in predicted thickness. This result intuitively reflects the sensitivity of bending beam stiffness on the thickness of a square beam: $F \propto t^3$.

The predicted geometries can be calculated based on the experimental stiffness and the SEM estimates, and are shown in Figure 90. It can be seen that, particularly for the single outlier, points are generally drawn to align with the cohort's trend. Save for the outlier, most points do not change significantly, and the measurements of thickness and neck dimensions are most sensitive. This aligns with the aim of this procedure: the method can be thought of as reducing the sensitivity to individual measurement error by aggregating the data set to a trend.

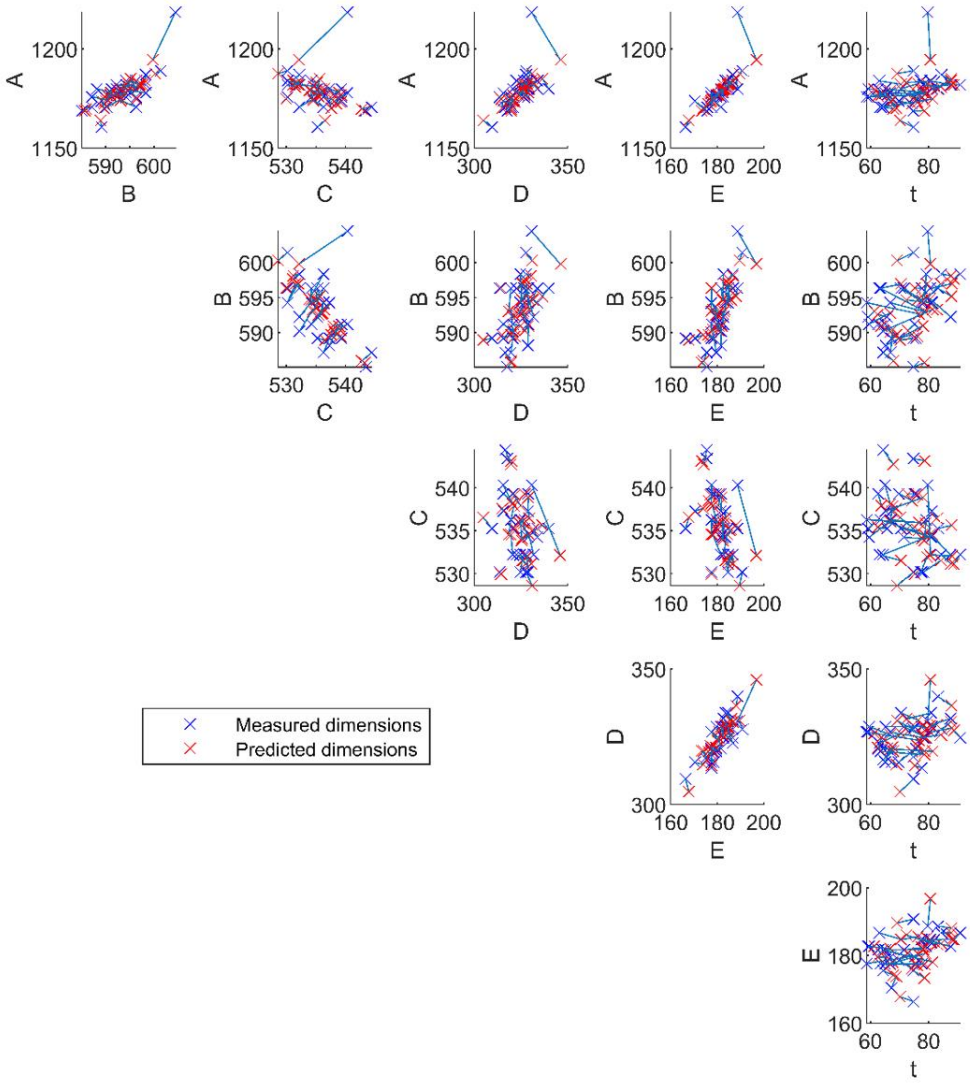



*Figure 90: Dimensions scatter matrix of set Foil 3&4 with measured dimensions (blue) and predicted dimensions (red). Connectors are drawn between corresponding points, and all measurements are in µm.*

With these predicted geometries, a new set of resonant frequencies and stress per unit angle are calculated, with the data shown in Table 10. As in foil 2, it was discovered that a mis-registration during the laser cutting in foil 4 caused a shift in the position of the cantilevers by approximately 200 μm. While this did not affect the bulk specimens, the neck region of weld-line specimens were therefore primarily alpha HAZ.

*Table 10: Dynamic responses for samples in Foil 3&4, including sample name, microstructure material type. Dynamic responses are given for measured dimension simulations alongside experimental stiffness in order to calculate the predicted dimensions. Values are given in 3 significant figures for comparison purposes. By definition, the stiffness of the predicted dimensions equal the experimental stiffness. The naming convention for samples is given by their location in a standard TEM grid box. This is provided for comparison to fracture surfaces in results.*

| Sample | Material | Measured Dimension Simulations | | | | Predicted Dimensions | |
|---|---|---|---|---|---|---|---|
| | | Resonant Frequency Hz | Stress / angle GPa/rad | Stiffness N/m | Experimental Stiffness N/m | Resonant frequency Hz | Stress / angle GPa/rad |
| K2 | Alpha | 22700 | 5.25 | 3260 | 4340 | 24800 | 5.80 |
| K4 | Alpha | 24700 | 5.74 | 4190 | 3320 | 22700 | 5.25 |
| K6 | Alpha | 22000 | 5.09 | 2960 | 3800 | 23800 | 5.54 |
| K8 | Alpha | 22900 | 5.28 | 3330 | 3580 | 23300 | 5.39 |
| K10 | Alpha | 22000 | 5.12 | 2920 | 2720 | 21400 | 4.98 |
| O2 | Alpha | 21300 | 4.89 | 2620 | 2740 | 21500 | 4.93 |
| O4 | Alpha | 18200 | 4.14 | 1550 | 3400 | 23000 | 5.34 |
| O6 | Alpha | 18200 | 4.14 | 1550 | 3060 | 22200 | 5.15 |
| O8 | Alpha | 16900 | 3.78 | 1140 | 2840 | 21700 | 4.98 |
| O10 | Alpha | 18400 | 4.14 | 1570 | 2980 | 22000 | 5.04 |
| P1 | Alpha | 21000 | 4.79 | 2470 | 2970 | 22200 | 5.08 |
| L1 | Alpha | 20100 | 4.60 | 2210 | 2840 | 21600 | 4.95 |
| L3 | Bimodal | 25500 | 5.98 | 4640 | 4440 | 25000 | 5.85 |
| L5 | Bimodal | 21100 | 4.86 | 2620 | 2150 | 19600 | 4.71 |
| L7 | Bimodal | 23700 | 5.51 | 3750 | 4310 | 24700 | 5.77 |
| L9 | Bimodal | 23600 | 5.46 | 3720 | 4290 | 24700 | 5.73 |
| M2 | Bimodal | 22500 | 5.19 | 3150 | 3080 | 22200 | 5.13 |
| M4 | Bimodal | 21800 | 5.01 | 3000 | 3400 | 22700 | 5.22 |
| P3 | Bimodal | 19600 | 4.59 | 1970 | 2540 | 21000 | 4.82 |
| P5 | Bimodal | 19100 | 4.40 | 1820 | 3100 | 22300 | 5.14 |
| P7 | Bimodal | 21400 | 5.07 | 2630 | 2130 | 19900 | 4.59 |
| P9 | Bimodal | 17000 | 3.79 | 1160 | 1870 | 18900 | 4.33 |
| Q2 | Bimodal | 17600 | 3.93 | 1320 | 1630 | 18100 | 4.06 |
| Q4 | Bimodal | 19100 | 4.34 | 1800 | 2030 | 19500 | 4.48 |
| M6 | Weld | 22900 | 5.28 | 3350 | 2410 | 20500 | 4.67 |
| M8 | Weld | 17700 | 4.01 | 1400 | 2240 | 20000 | 4.70 |
| M10 | Weld | 21800 | 5.04 | 2900 | 3210 | 22400 | 5.19 |
| N1 | Weld | 20500 | 4.71 | 2330 | 2980 | 22000 | 5.07 |
| N3 | Weld | 21300 | 4.87 | 2640 | 2410 | 20600 | 4.69 |
| Q6 | Alpha HAZ | 18100 | 4.06 | 1490 | 1920 | 19200 | 4.37 |
| Q8 | Alpha HAZ | 18800 | 4.26 | 1700 | 1930 | 19200 | 4.39 |
| Q10 | Alpha HAZ | 18600 | 4.22 | 1660 | 1540 | 17700 | 4.00 |
| R1 | Alpha HAZ | 18200 | 4.11 | 1540 | 1860 | 18900 | 4.30 |
| R3 | Alpha HAZ | 16800 | 3.74 | 1100 | 1460 | 17400 | 3.89 |

It must be also noted that the polishing route has caused several specimens to have resonant frequencies below the testing frequency. These sub-resonant specimens are unlikely to provide useful data: during crack growth, the resonant frequency decreases as the stiffness reduces, leading to a lowering in bending angle and therefore test stress. This process can continue to the point that the sample will never fully fracture, dependant on the morphology of the crack and the above factor competing with the concentration on the crack tip. However, for samples that did fracture, results can be reported as crack initiation dominates in this (V)-HCF region. For this reason, samples in the Alpha HAZ region were completely disregarded, and samples P7, P9 were disregarded.

Due to the large variety of resonant frequencies, several horns were used for testing with varying gain ratios ranging from 1:2.5, 1:5, and 1:10. However, this does not affect the consistency of results: the deflection angle alone is used for determining stress, and as perfect coupling is not used in the analysis of the results, the measurements of the vibration amplitude of the horn are not necessary.

Each specimen was loaded as described, and following a set of low-amplitude pulses to determine the dynamic response, were calibrated to within a safe range (at least 150 MPa below test stress). As occasionally, particularly for samples near resonance, this corresponded to a very low amplitude, samples would be re-calibrated in between steps: i.e. if a sample survived steps 1 and 2 at stress 200 MPa and 300 MPa, the range of stresses to calibrate could be increased from 0-50 MPa to 0-150 MPa. The consequence of this however was that, despite using the Bayesian optimised starting stress, the effective starting stress would be shifted (owing to an uneven step size). Using this protocol, samples were tested to failure at $10^6$ cycles, with a maximum starting stress of 100 MPa and a step size of 50 MPa. Six alpha samples (K10, L1, L8, O2, O6, and O10) were tested prior to the development of this method, initiating the motivation for the

development of such a method. For this reason, SN results are not included in the analysis of this set, though measurements of thickness and coupling constant are used for the validation step.

The full loading history of each sample is shown in Figure 91, where it is clear that the weld specimens have a higher mean fatigue strength than the parent material.

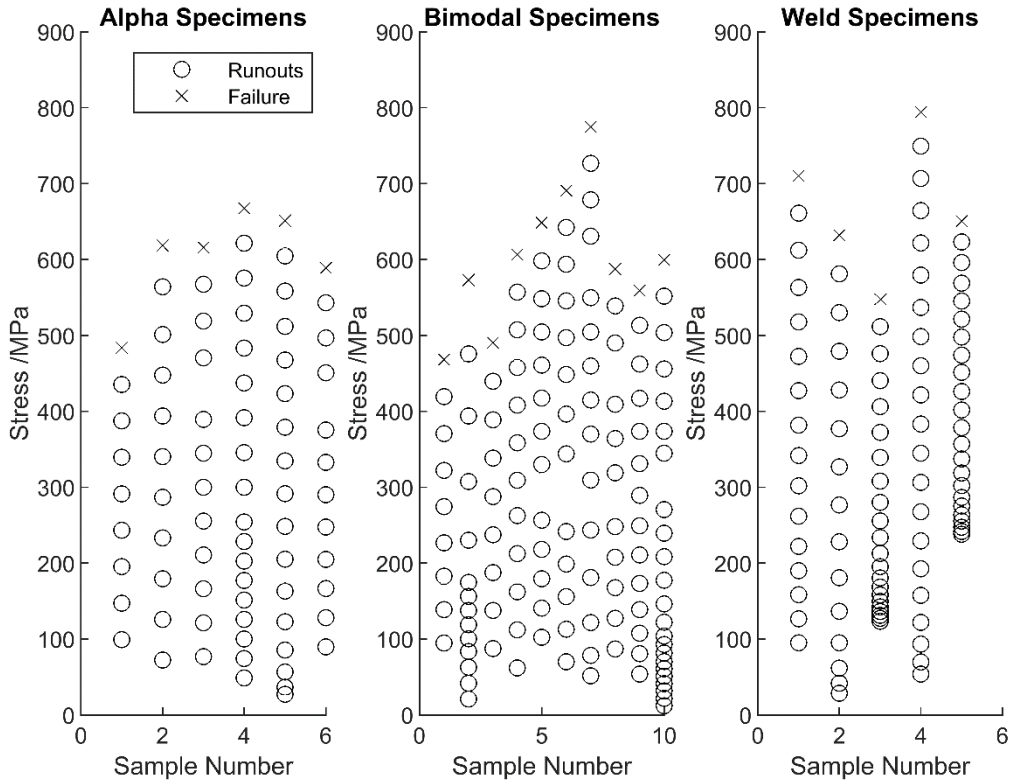



*Figure 91: Full loading history of set Foil3&4, showing Alpha, Bimodal, and Weld specimens tested to failure at $10^6$ cycles.*

The SN plot of these results, coloured by microstructure, is shown in Figure 92, showing more clearly this fatigue credit. It can be seen that the elbow of the SN curve occurs roughly in the same number of cycles, at approximately $5 \times 10^5$ cycles, which can suggest that the different materials have slightly different offsets in their fatigue strength rather than fatigue life.

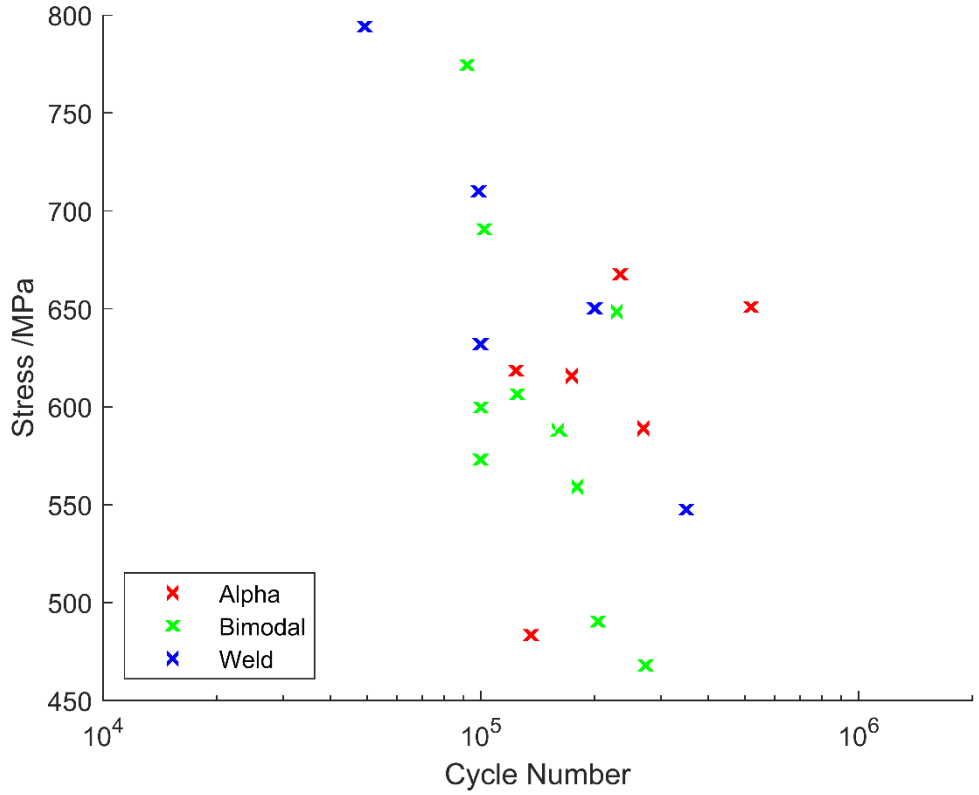



*Figure 92: SN plot of data in set Foil3&4 showing number of cycles to failure at final stress level, coloured by microstructure. Runouts are hidden for clarity, and error in life is approximately 1000 cycles, while errors in stress are approximately 10%.*

Having tested these samples to failure, it is possible to validate the PCA-based analysis route by measuring the fracture surface thickness. While thickness variations along the length of the neck are possible, for simplicity it is considered that the thickness at the fracture surface represents a more accurate estimate than the thickness on the edge of the ring.

Figure 93 shows the comparison of the measured fracture thickness for all these tested specimens and the original measurement or PCA-derived predicted geometry. It can clearly be seen that the PCA derived thicknesses are better estimates of the fracture surface thickness. The thickness of several samples had been under-estimated in the original SEM measurement—seen in the general bias to the left hand side of the equal relationship curve—likely owing to these samples having been over-polished on the outer ring.

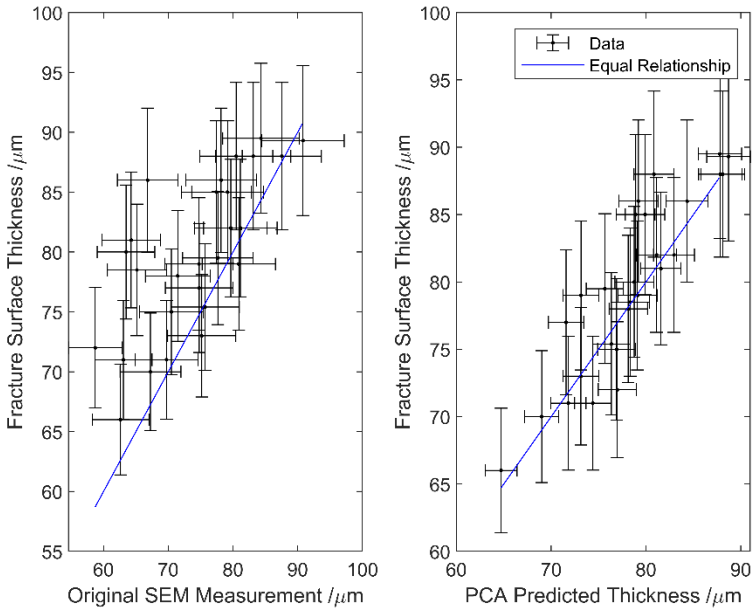



*Figure 93: Comparison of Original (left) and PCA Predicted (right) thicknesses to the post-fracture SEM measurement of fracture surface thickness. Error bars in SEM measurements are 7%, while the PCA predicted thickness error is 2.5%. Equal relationship (blue line) is shown as a guide to the eye.*

The PCA route can be further validated by considering the coupling constant: samples driven closer to resonance are expected to have greater coupling constant. This comparison is shown in Figure 94, and the resonant frequencies calculated via PCA predicted geometry clearly show a stronger resemblance to the dynamic response in Figure 32 of the Cantilever Design section on page 80.

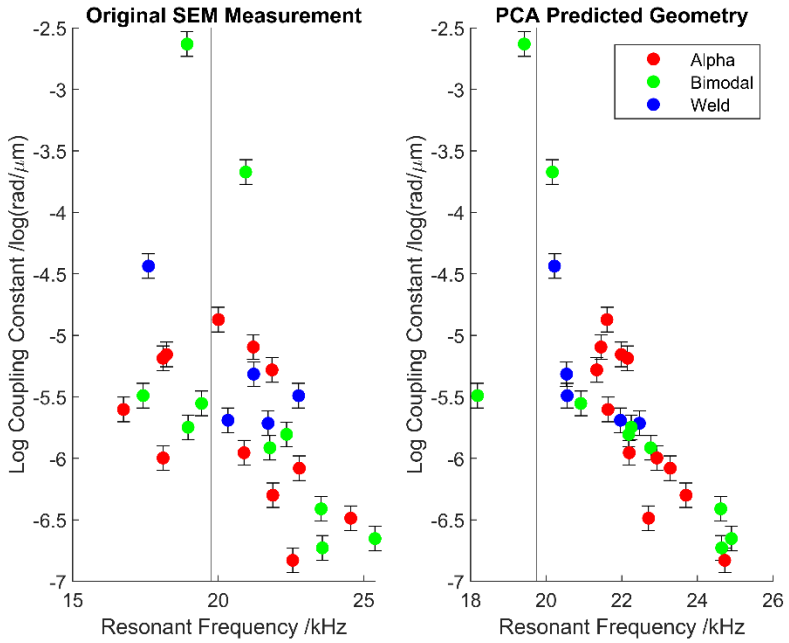



*Figure 94: Comparison of Original (left) and PCA Predicted (right) resonant frequencies plotted against the log of the coupling constant. Points are coloured by microstructure, and the testing frequency of 19750 Hz is shown as a guide to the eye. For simplicity, error bars are not shown on the frequency axis but correspond to ca. 10% on the original measurements and 2.5% on the PCA predicted geometry. Error in coupling constant is 0.1 log(rad/μm).*

With this validation of the PCA predicted geometry, the fatigue results can be more closely analysed. Figure 95 shows the joint posterior of model parameters calculated for this dataset, modelled as a normal distribution, with a summary shown in Table 11.

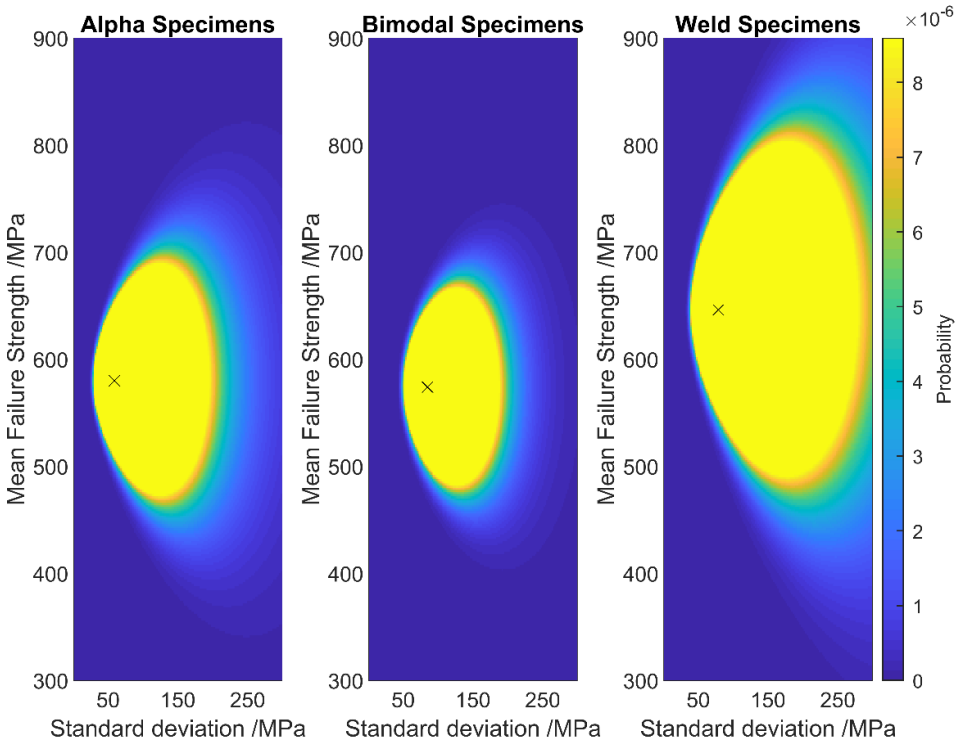



*Figure 95: Joint posterior for Alpha, Bimodal, and Weld specimens (left, centre, and right, respectively), calculated from the 6 alpha, 10 bimodal, and 5 weld specimens that were tested to failure at $10^6$ cycles. Marked point shows the MAP.*

It can be seen that the joint posterior is much more constrained for the datasets containing a larger number of samples, but that nonetheless the MAP of the weld material lies approximately 70 MPa above the parent material. The standard deviations are approximately similar, with the weld material more likely to exhibit a higher spread. Observing the convergence of these values provides insight into comparing the differently sized datasets, shown in Figure 96. This provides a more nuanced approach to the analysis, but showing that the trends for each type of material is similar – the results are expected to agree in their relative order and approximate magnitude of difference.

*Table 11: Results of set Foil 3&4 after 6 Alpha, 10 Bimodal, and 5 Weld samples. Data is modelled with a normal distribution. MAP and 95% HPD ranges are given, rounded to the nearest 10 MPa.*

| Material | Estimate of Mean: MAP [95% HPD range] /MPA | Estimate of Standard Deviation: MAP [95% HPD range] /MPA |
|---|---|---|
| Alpha | 580 [470, 690] | 60 [30, 190] |
| Bimodal | 570 [480, 660] | 85 [50, 185] |
| Weld | 650 [490, 800] | 80 [40, 280] |

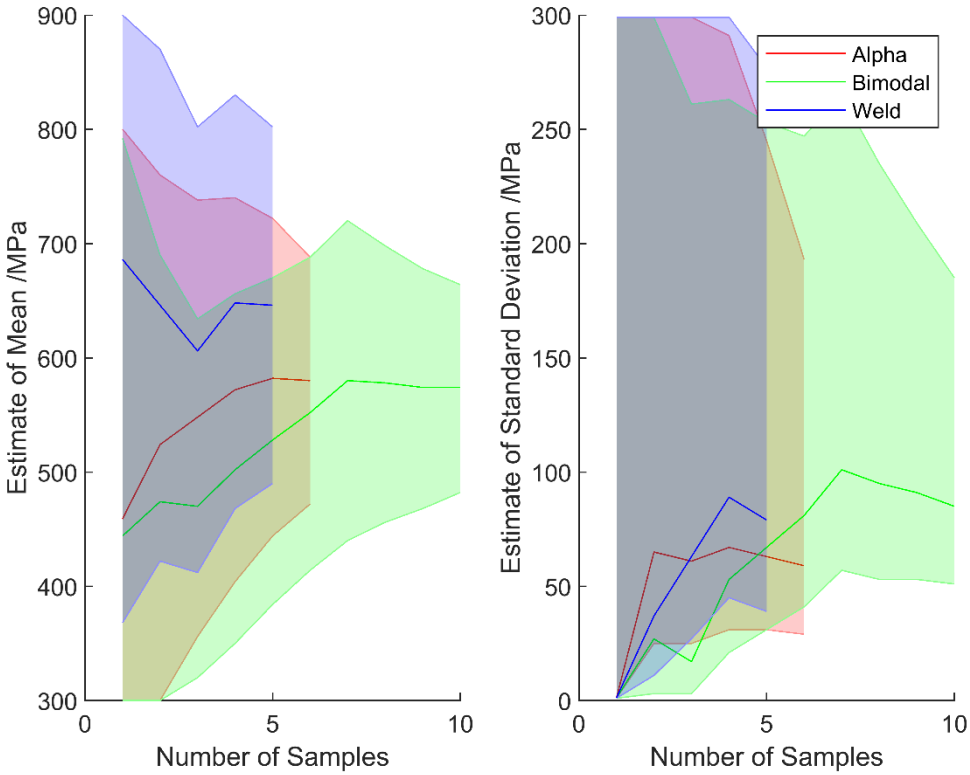



*Figure 96: Convergence plots of experimental Foil3&4 joint posterior results with mean (left) and standard deviation (right) shown for each type of material.*

These are in alignment with literature values: alpha and bimodal material having fatigue strengths of approximately 450-600 MPa [20], [172], [383], [384], [176], [185], [211], [212], [227], [281], [284], [358]. Further insights into the fatigue response of these different types of material can be seen by observing the fractography. A selection of the fracture surfaces for each material are shown from Figure 97 to Figure 101, with the unique fractography of meso-scale cantilevers showing strong crystallographic influence. The first shows the fracture surface of an alpha material specimen, where the three fatigue crack growth stages can be seen:

- Initiation followed by crystallographic facets as a crack cleaves individual grains,
- Cyclical crack growth, often showing striation-like features (in this case influenced again by the relatively large grain size and visible within grain facets),
- Final fracture showing significant plastic deformation no longer influenced by the grain structure.

A secondary crack can be seen to bisect the front of the fracture surface near the initiation side, suggesting the complex interplay between crystallographic orientations on local vs global stress states.

Observing Figure 98, the bimodal fracture surface can be seen to have some similarities with the alpha surface: the clear stages of crack growth with visible crystallographic facets, a transition to a different mode of crack growth, and finally a “stage III”-like ductile rupture. This particular example is chosen for some of the unique features observed, such as the nano-metre scale “fish-scale” features that suggest a possible interaction with the grain morphology, such as laths or degenerate mis-orientation with the activation of multiple slip planes.

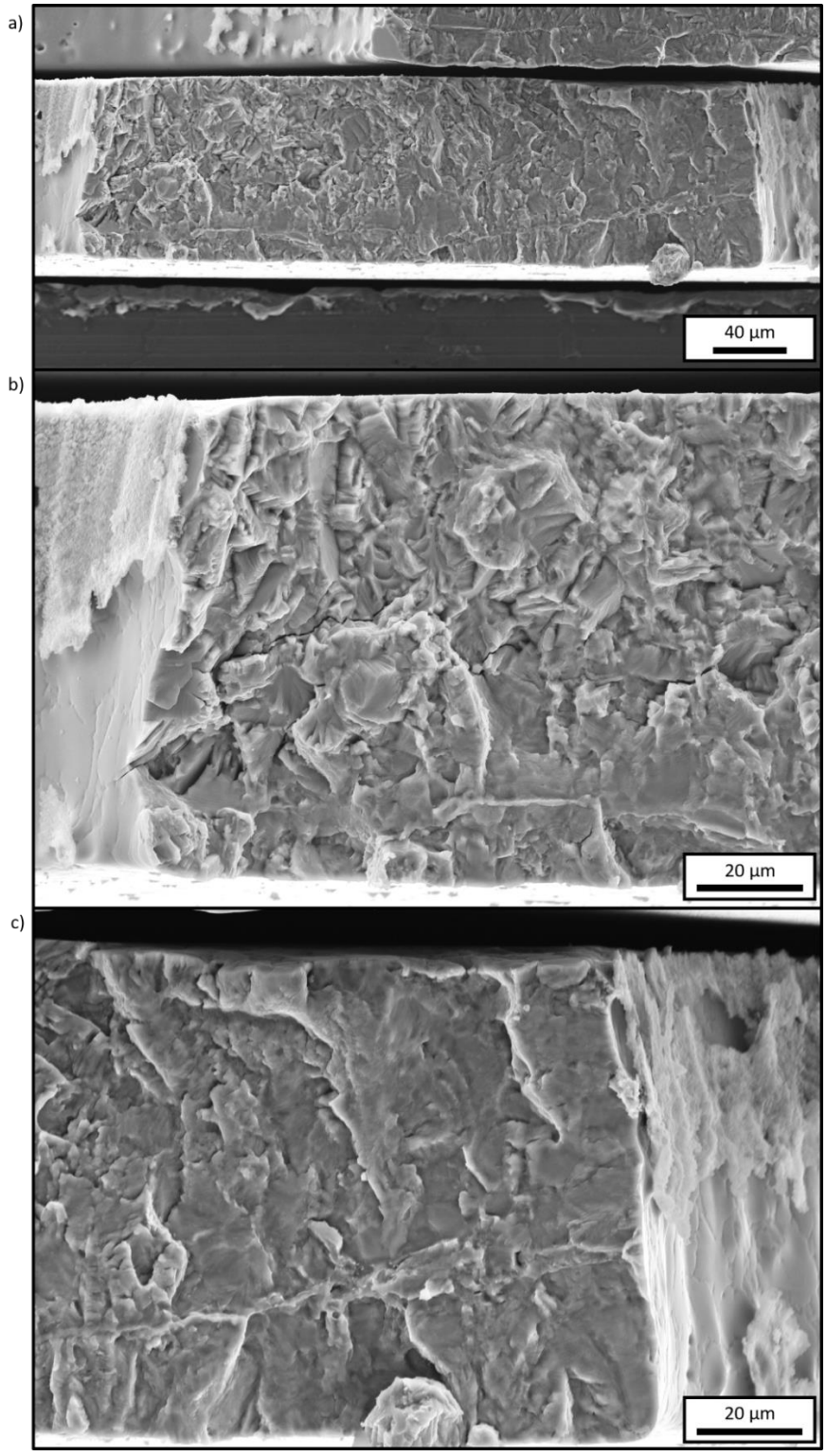



*Figure 97: Fracture surface of sample K4 from set Foil 3&4. This alpha sample underwent $10^6$ cycles at 515 MPa, followed by fracturing after $1.25 \times 10^5$ cycles at a stress of 565 MPa. Panel a) shows the full fracture surface, with an initiation on the top-left hand portion of the image with faceted crack growth, followed by crack growth away from this corner, followed by final fracture in the bottom-right hand corner of the specimen with significant plastic deformation. Panel b) shows the initiation site in closer detail, with many crystallographic facets visible, some containing striations further away from the corner as the crack propagation transitions to stage II. A secondary crack can be seen to cut across mid-way through the plane, suggesting strong crystallographic influence on the crack plane direction owing to its angle away from the dominant crack surface. Panel c) shows the right side of the fracture surface in detail, showing the final fracture.*

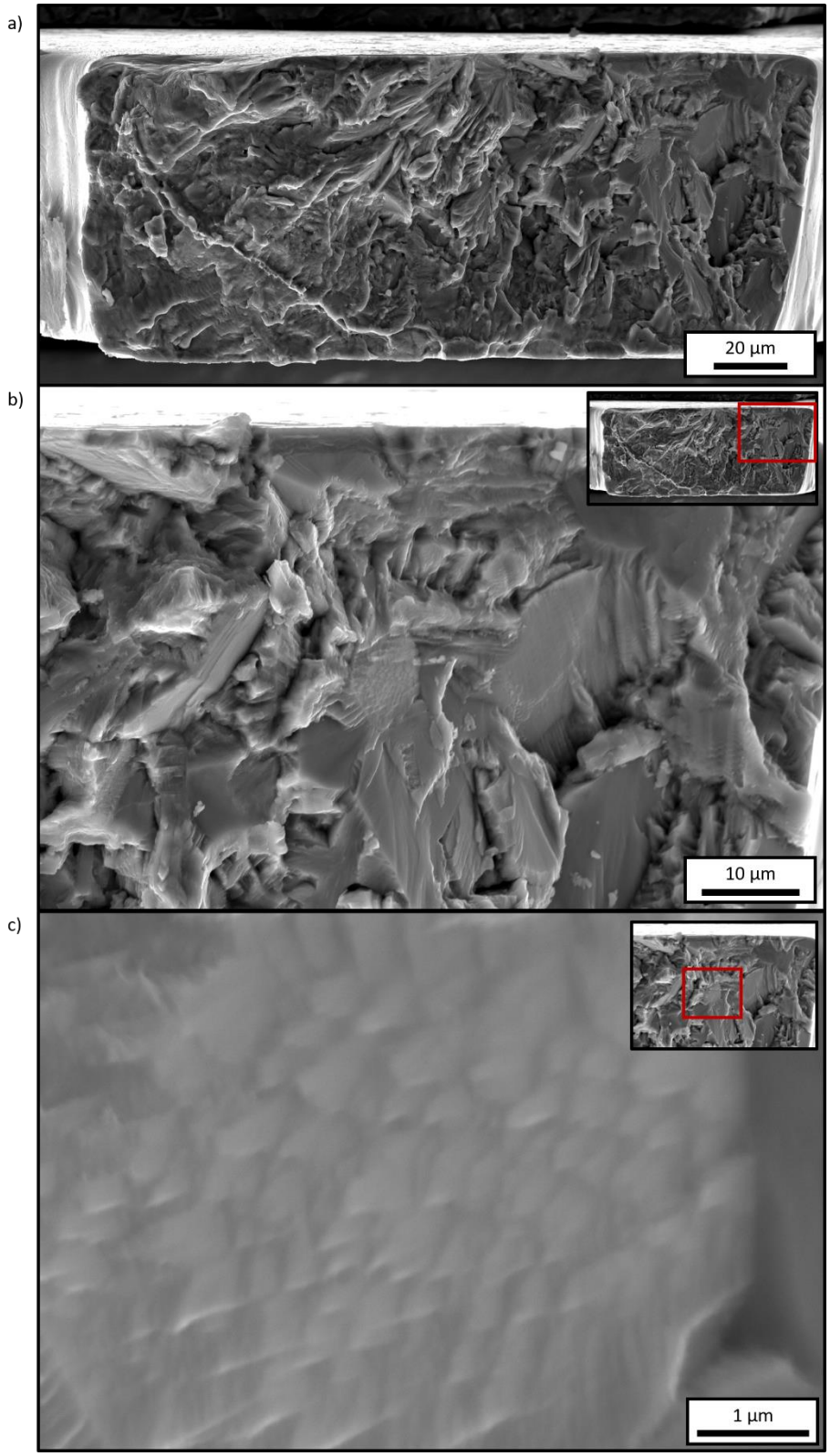



*Figure 98: Fracture surface of sample M2 from set Foil 3&4. This bimodal sample underwent $10^6$ cycles at 570 MPa, followed by fracturing after $2.3 \times 10^5$ cycles at a stress of 620 MPa. Panel a) shows the full fracture surface, with an initiation on the top-right hand portion of the image with faceted crack growth, followed by crack growth away from this corner, followed by final fracture in the bottom-left hand corner of the specimen. Panel b) shows the initiation site in closer detail, with several facets containing striation-like features. A single grain is shown in panel c) showing complex crack surface morphology with "fish-scale" markings, likely showing the interplay between the crack growth direction and microstructural or crystallographical features.*

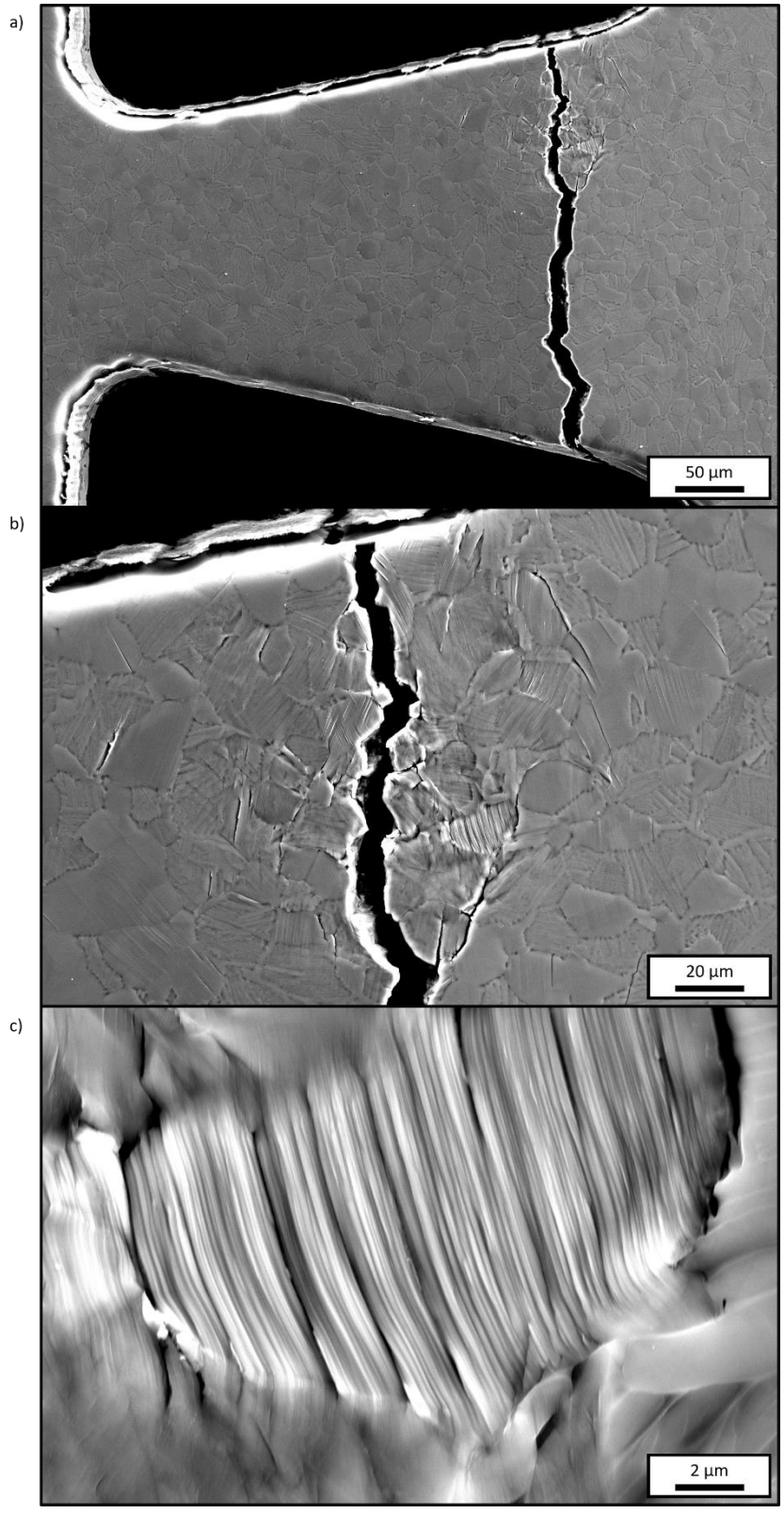



*Figure 99: Fractured sample M2 from set Foil 3&4 as shown from the top in Figure 11. The crack, growing from the edge of the sample on the bottom of the image, can be seen to follow a torturous path along the neck. The initiation point can be seen to be smooth, representing the behaviour of the underlying material. Towards the top of the neck, as shown in Panel b) and c), the stress during the compressive bending portion of the cycle can be seen to have significantly deformed certain grains, with slip lines clearly visible in the topology. One such grain, shown in panel c), can be seen to be excessively deformed, with banding of ca. 200nm in spacing. These bands also change direction across grain boundaries, with a 30° change in the bottom left, likely due to crystallographic effects.*

Figure 99 shows the fracture surface from the top. This shows further the effect of the crystallography on the path of the crack: the crack, initiating from the bottom of the image, can be seen to follow closely along certain directions within grains, or along grain boundaries depending on the combination of orientation and local stress state. This can be seen particularly clearly in Figure 98 panel b) and c) where certain grains, likely oriented in the “weak” direction relative to the stress, are significantly deformed and initiating secondary cracks.

Finally, Figure 100 and Figure 101 show the fracture surface of a weld specimen. Figure 100 shows the fracture surface, with a much more conventional morphology in part owing to a more conventional grain size to sample size ratio. Facets are difficult to observe at such scales, but modes remain clearly visible with the crack in this case extending from top-left to bottom right. Figure 101 shows a top-down view of the same sample, with a secondary crack seen to extend partially along the thickness of the sample.

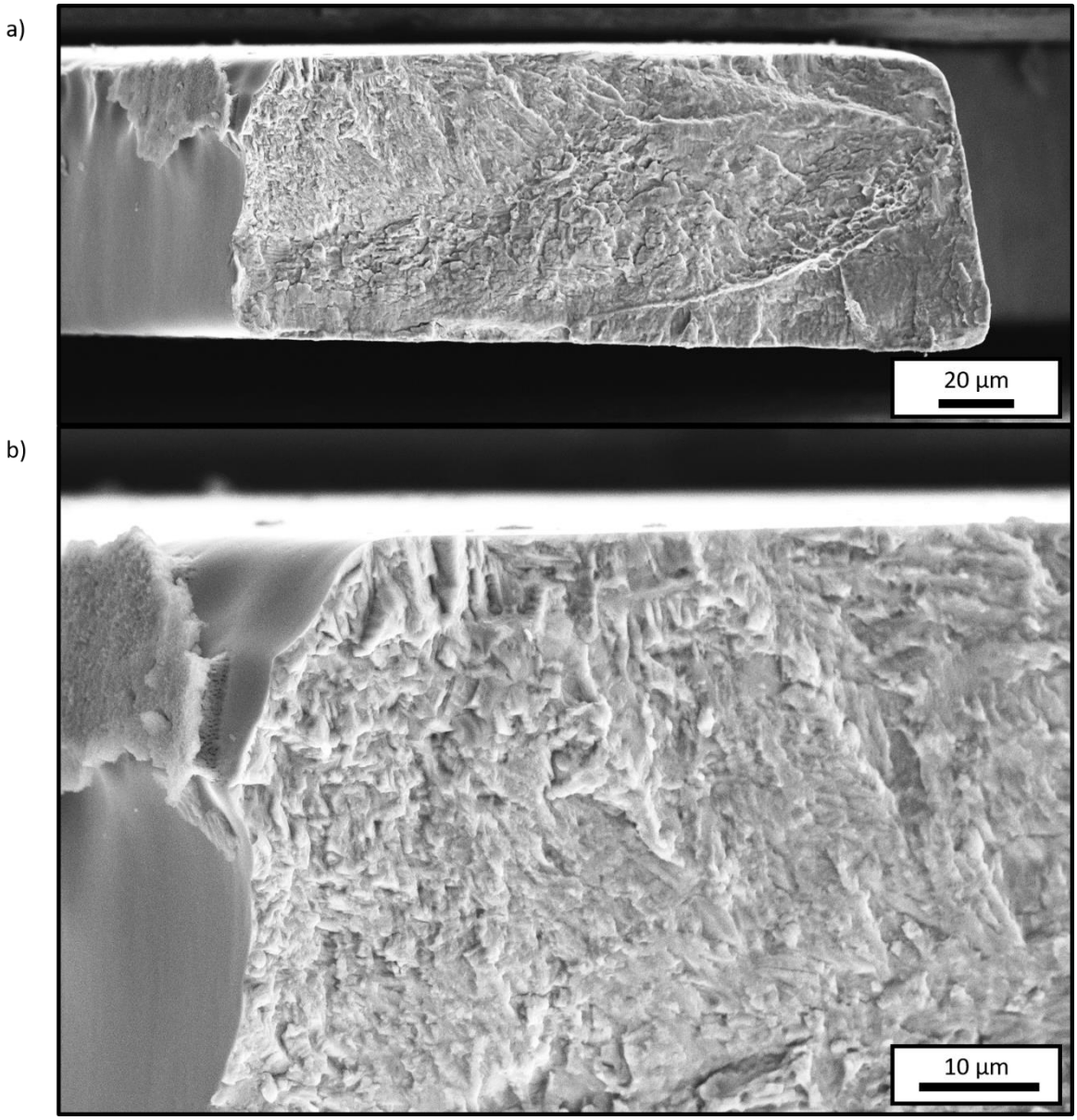



*Figure 100: Fractured sample N1 from set Foil 3&4. This weld sample underwent $10^6$ cycles at 790 MPa, followed by fracturing after $5 \times 10^4$ cycles at a stress of 840 MPa. The morphology of the fracture surface is finer owing to the greater number of grains across the sample. The crack, growing from the top left corner, can be seen to progress across the face of the fracture surface, with a characteristic "fish eye" demarcation between stage II and stage III on the bottom right.*

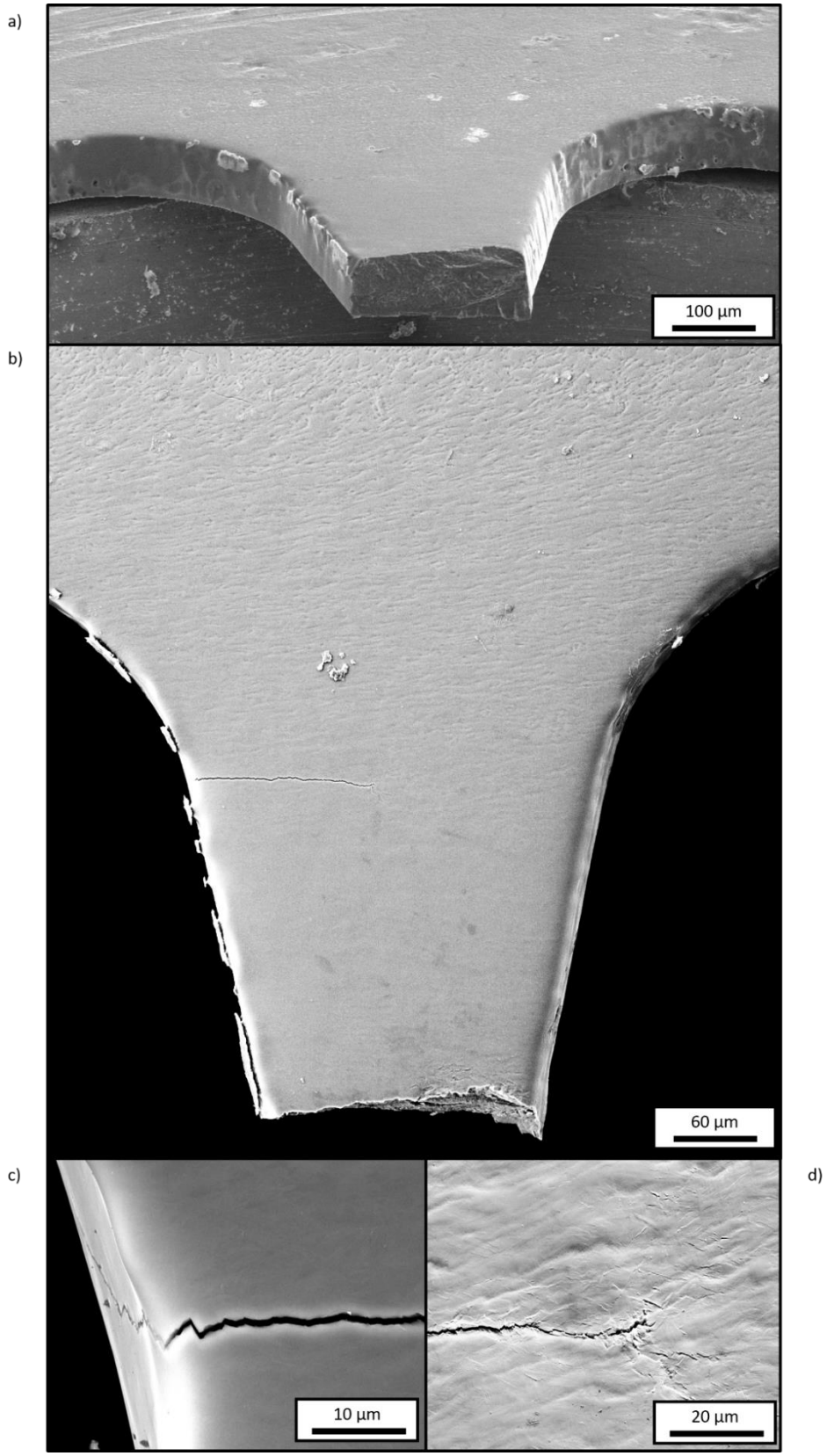



*Figure 101: Fractured sample N1 from set Foil 3&4 as shown from the top in Figure 13. The fracture surface can be seen in panel a) with a more top down view in b) showing the etched microstructure of the weld line clearly along the neck. A secondary crack can be seen towards the base of the neck, with the initiation point shown in panel c), and panel d) shows the point where the crack arrested. This point can be seen to be partially microstructurally induced: with slip lines extending at approximately 45°.*

This fractography show a unique perspective in the fatigue analysis of meso-scale cantilevers: owing to the comparatively low number of grains in parent material specimens, isolated tests on microstructural regions of interest or further characterisation of fatigue crack propagation mechanisms are possible.

Immediately, the results provide confidence in the method of data collection: these results can be interpreted to be representative of these similar volumes of parent and weld-line material, particularly as the fractographs do not point to a processing route defect. Therefore, a more confident comparison in fatigue strength between these three materials can be made.

### 2.6.2. Results of Foil 7-11

Following the methodology validation in the previous section, a larger dataset of samples can be produced. Five foils were cut to a target thickness of 180 µm, ground and each foil was measured individually to be 85±7 µm. From the lessons of sample set Foil 3&4 with a maximum thickness reduction of 35 µm, a cantilever was designed such that the resonant frequency would be significantly above 21 kHz even at a reduced electropolished thickness of 50 µm. To this end, a design was made with a resonant frequency of 27 kHz at 50 µm thickness, achieving 650 MPa at 50 µm vibration amplitude. This design is shown in Figure 102.

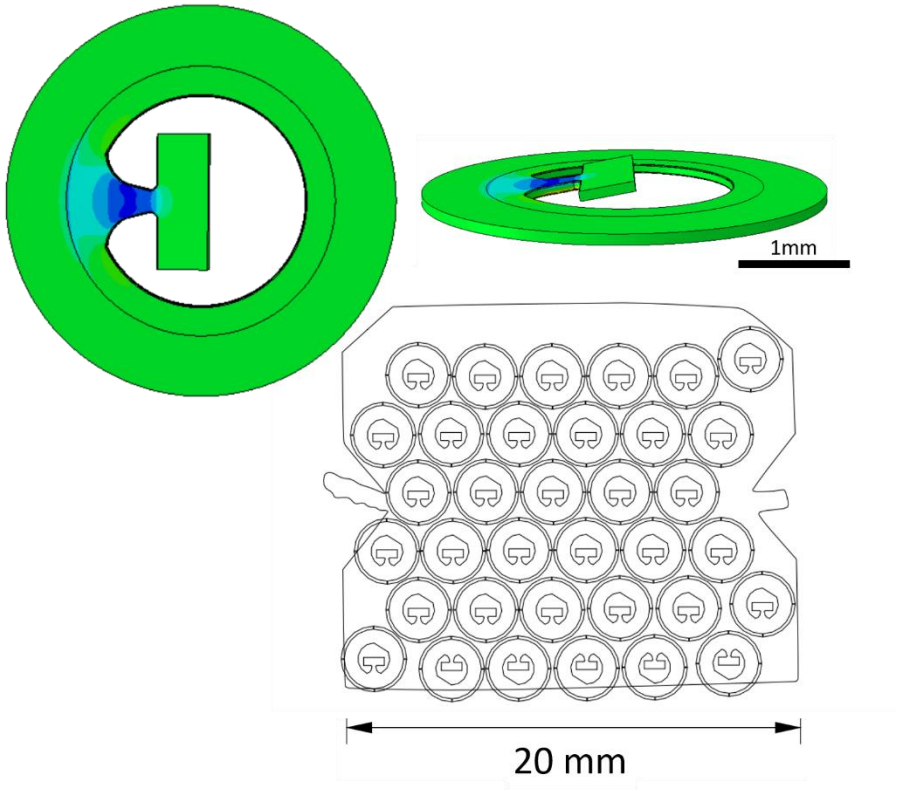



*Figure 102: Design of cantilever for sample set Foil 7-11. Top section shows top-view and side-view of cantilever during oscillation, with stress distribution along the neck shown in blue (compression) and red (tension). The stress shown purely for visualisation purposes is induced from a vibration amplitude of 50 µm. The bottom shows the layout of the samples on the foil, with 5 cantilevers placed along the weld-line. Of note is that several samples are not complete: these are used for the purposes of calibrating the electropolishing set up and are not used for data: only complete cantilevers are used for data gathering.*

Out of five foils, 153 cantilevers were cut, of which 18 contained significant gaps due to them being cut on the edge of the foils. 114 cantilevers were individually polished using the route described in the Electropolishing section on page 95, with polishing times ranging from 60 - 350 seconds. Each specimen was measured in the SEM, and those that had achieved a minimum quality of 6 out of 10 were nanoindented to measure the stiffness. This set contained 73 specimens, of which 25 weld, 26 bimodal, and 22 alpha material.

The PCA analysis route was followed in order to calculate the predicted geometries of the samples. An example of a cantilever is shown in Figure 103, with dimensions and quality measured as described in the caption.

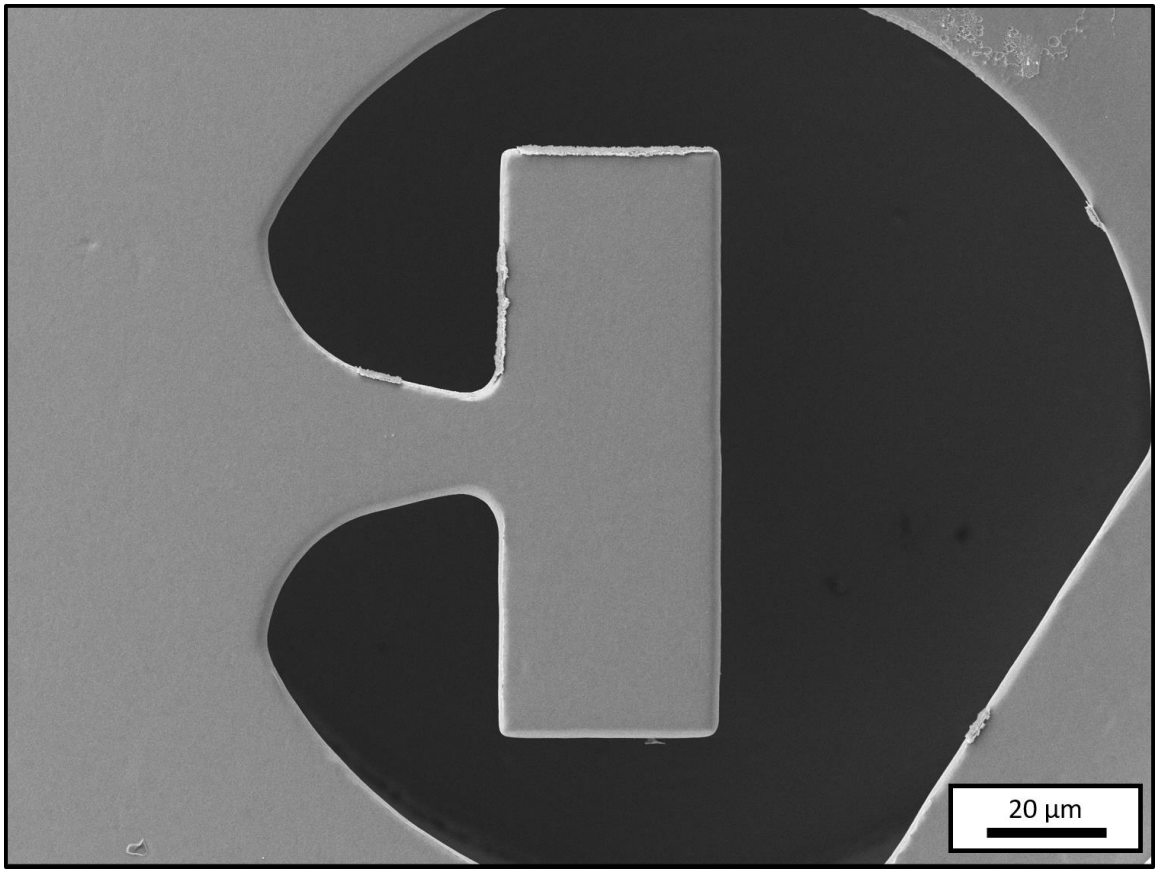



*Figure 103: Sample 1A1 from set Foil 7-11 following electropolishing step. Sample was polished for 120 s and was measured to have the following dimensions: hammer width 970 µm, hammer length 362 µm, neck length 392, neck width base 258 µm, neck width end 158 µm, and thickness 81 µm. The quality was deemed an eight out of ten, representative of the average specimen. The asymmetric cut can be seen on the bottom right of the image, indicating that this is the incoming laser side of the cantilever – for this reason, the taper can be seen, and measurements are made on the mid-point of the taper. SEM image was taken at 60x magnification in secondary electron mode, 10 mm working distance, and 15 kV voltage.*

The scatter matrix of measured dimensions, coloured by electropolishing batch, is shown in Figure 104. This figure shows similar trends to the results of Foil 3&4: measurements of material tend to decrease while measurements of gaps tend to increase, with most of these co-correlating owing to the physical action of the electropolishing step. This gives further credence to the benefit of the PCA methodology, with a scree plot shown in Figure 105.

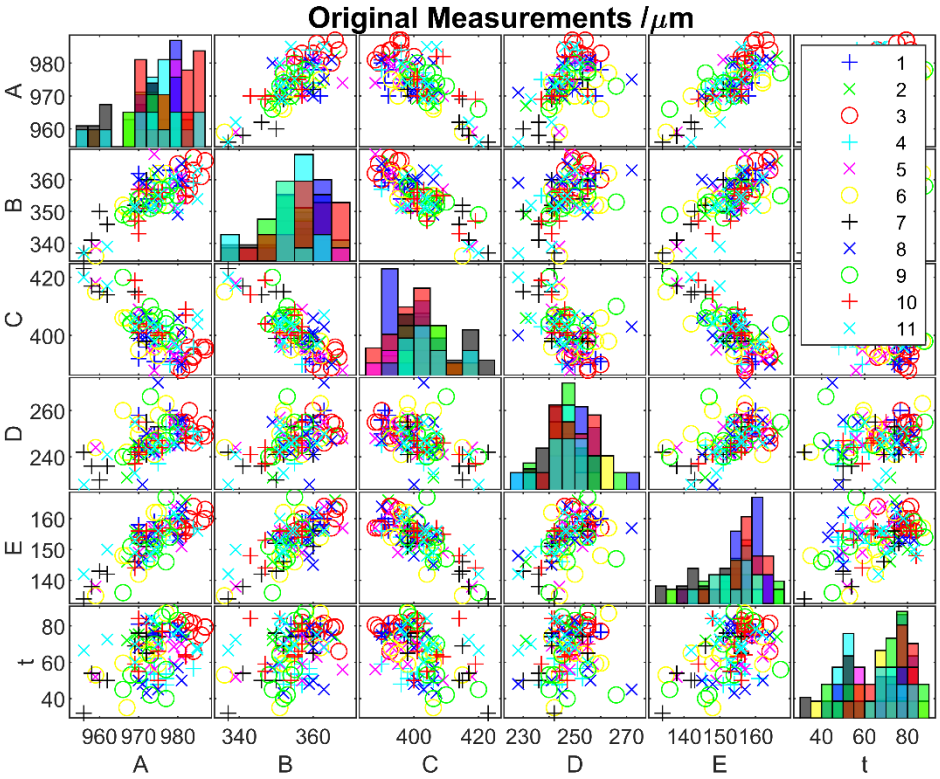



*Figure 104: Scatter plot matrix of SEM measured dimensions of sample set Foil 7-11. Points correspond to each sample, with 114 shown. Markers correspond to different electropolishing batches, and cardinal measurements are as given in Figure 48. Diagonal elements in the matrix are histogram of measurements, while off-diagonal elements are correlations between corresponding row and column measurements. All measurements given in µm.*

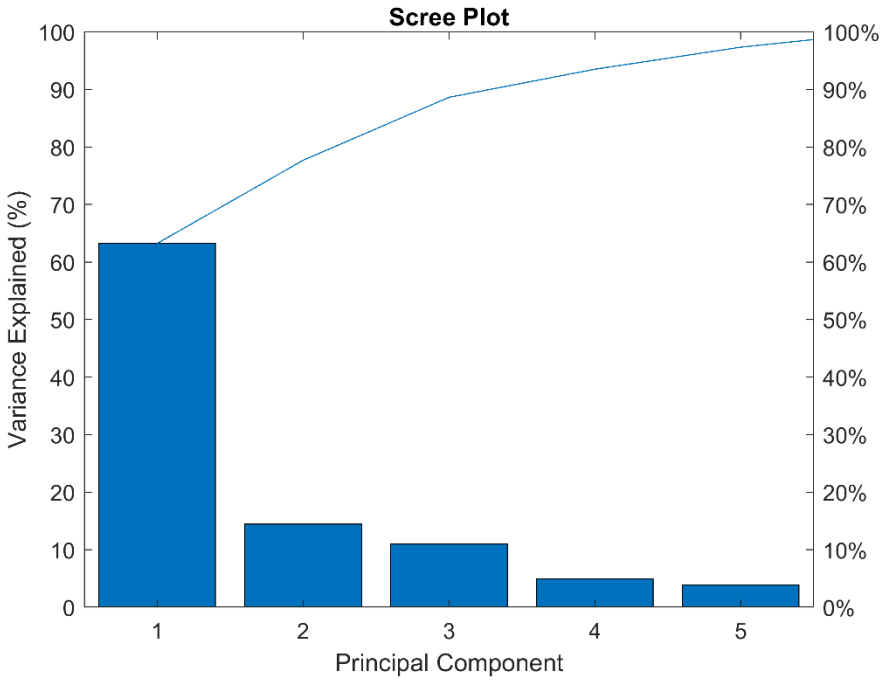



*Figure 105: Scree pot of PCA analysis of dimensions in sample set Foil 7-11, showing the variance explained for each PC (blue bars), alongside the cumulative variance explained in the dataset (blue line).*

Using 3 principal components, 90% of the variance can be captured and modelled, such that parametric evaluations of the dynamic responses can be calculated. From the experimental stiffness, as described in the Stiffness Measurement section on page 108, a predicted geometry can be found, which on average deviated from the original measurements by 8% for thickness values. The dynamic responses of the 77 samples to be tested are shown in Table 12 with only predicted geometry values shown.

This data shows a significant caveat in this testing methodology: though in this sample set no specimen had a resonant frequency below 20 kHz, the requirement for high polishing quality lead to significant variations in the polishing time and therefore the geometric variation. This lead to a large range in resonant frequency, with many samples resonating above 35 kHz. Initial test on the 20 kHz transducer showed insufficient angular deviation owing to the large discrepancy between testing and resonant frequencies. Therefore, a 30 kHz transducer was used for samples with a resonant frequency greater than 32.5 kHz. A discussion on the comparison of results between 20 and 30 kHz is given later.

The specimens were then tested to the PSN variable step size multiple stress protocol described in the PSN Multiple Stress Protocol section on page 171, with a minimum step size of 50 MPa and a maximum starting stress of 330 MPa. These values were based on safe estimates from the experience gained in the constant life results of Foil 3&4. The various runout lives allowed for this test were $10^5$, $10^6$, and $10^7$ cycles.

The SN diagram for each microstructure is shown in Figure 106, showing some of the load history for each sample through the penultimate test and the final test.

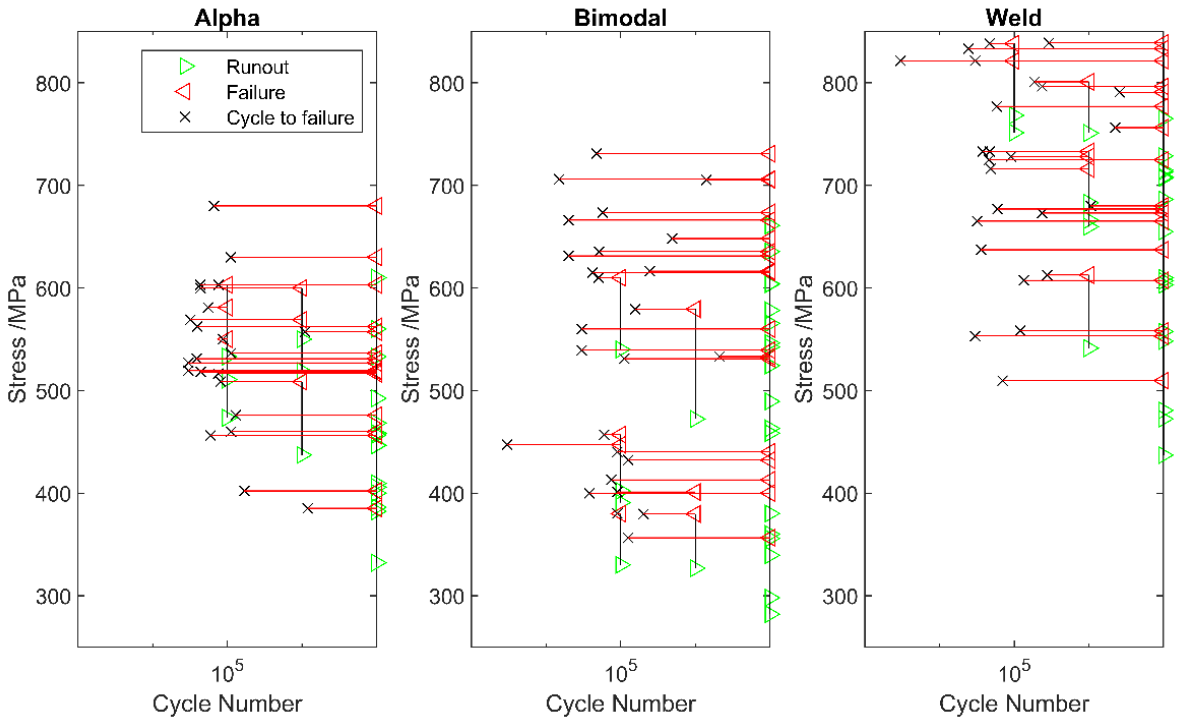



*Figure 106: Experimental SN plot for sample set Foil 7-11, with 22 alpha, 26 bimodal, and 25 weld samples. Samples are tested to lives between 5, 6, and 7 $log(cycles)$, and with stress step protocols with varying step sizes with a minimum step size of 50 MPa and a maximum starting stress of 330 MPa. SN data is divided by microstructure type, with alpha (left) bimodal (centre) and weld (right) shown. Error in life is approximately 1000 cycles, while errors in stress are approximately 10%.*

*Table 12: Dynamic responses of all tested samples in Foil 7-11, ordered by material type and sample name. Dynamic responses are derived from predicted geometry through ABAQUS simulations, and are given as values with 3 significant figures for comparative purposes only. Naming convention, as in the former sample set, is given by the position of the sample in a standard TEM grid box, with the addition of a prefix number for box number.*

| Material | Sample | Resonant Frequency Hz | Stress / angle GPa/rad | … | | | |
|---|---|---|---|---|---|---|---|
| Alpha | 1D4 | 34400 | 4.93 | Bimodal | 1I9 | 30100 | 4.24 |
| Alpha | 1D6 | 45800 | 6.56 | Bimodal | 1J2 | 33800 | 4.65 |
| Alpha | 1D10 | 45100 | 6.46 | Bimodal | 1O8 | 36000 | 5.08 |
| Alpha | 1E1 | 42700 | 6.11 | Bimodal | 2A9 | 44800 | 6.18 |
| Alpha | 1K4 | 35900 | 5.12 | Bimodal | 2B4 | 37900 | 5.35 |
| Alpha | 1K6 | 35200 | 4.89 | Bimodal | 2B10 | 28000 | 4.01 |
| Alpha | 1K8 | 33800 | 4.82 | Bimodal | 2G9 | 34700 | 4.67 |
| Alpha | 1K10 | 34400 | 4.87 | Bimodal | 2H4 | 35300 | 4.78 |
| Alpha | 1L1 | 36900 | 5.19 | Bimodal | 2H6 | 38800 | 5.42 |
| Alpha | 1L3 | 39800 | 5.52 | Bimodal | 2H8 | 38200 | 5.39 |
| Alpha | 1R3 | 41300 | 5.87 | Bimodal | 2H10 | 35500 | 4.82 |
| Alpha | 1R5 | 37300 | 5.22 | Bimodal | 2I1 | 39900 | 5.67 |
| Alpha | 1R7 | 34500 | 4.84 | Weld | 1C3 | 40700 | 5.77 |
| Alpha | 1R9 | 37400 | 5.31 | Weld | 1C5 | 40700 | 5.74 |
| Alpha | 1S2 | 26800 | 3.56 | Weld | 1C7 | 44100 | 6.25 |
| Alpha | 2D8 | 32000 | 4.48 | Weld | 1C9 | 44100 | 6.33 |
| Alpha | 2D10 | 30100 | 4.22 | Weld | 1D2 | 43900 | 6.24 |
| Alpha | 2E3 | 39800 | 5.59 | Weld | 1J4 | 36700 | 5.19 |
| Alpha | 2J8 | 37500 | 5.25 | Weld | 1J6 | 28800 | 3.97 |
| Alpha | 2K2 | 35500 | 4.92 | Weld | 1J8 | 36500 | 5.17 |
| Alpha | 2K4 | 37500 | 5.21 | Weld | 1J10 | 34900 | 4.99 |
| Alpha | 2K6 | 43300 | 6.01 | Weld | 1K2 | 31100 | 4.36 |
| Bimodal | 1A1 | 46300 | 6.59 | Weld | 1Q4 | 37200 | 5.27 |
| Bimodal | 1A3 | 44100 | 6.32 | Weld | 1Q6 | 30900 | 4.29 |
| Bimodal | 1A7 | 40900 | 5.87 | Weld | 1Q8 | 30200 | 4.17 |
| Bimodal | 1A9 | 45600 | 6.44 | Weld | 1Q10 | 28700 | 3.93 |
| Bimodal | 1B4 | 44000 | 6.29 | Weld | 1R1 | 27900 | 3.89 |
| Bimodal | 1B6 | 42100 | 6.02 | Weld | 2C3 | 34900 | 4.97 |
| Bimodal | 1H2 | 31100 | 4.39 | Weld | 2C5 | 26500 | 3.58 |
| Bimodal | 1H4 | 32900 | 4.66 | Weld | 2C7 | 35900 | 5.01 |
| Bimodal | 1H6 | 31500 | 4.48 | Weld | 2C9 | 39500 | 5.59 |
| Bimodal | 1H8 | 29700 | 4.15 | Weld | 2D2 | 29100 | 3.95 |
| Bimodal | 1H10 | 30300 | 4.22 | Weld | 2I3 | 34100 | 4.76 |
| Bimodal | 1I3 | 34500 | 4.86 | Weld | 2I5 | 35300 | 4.95 |
| Bimodal | 1I5 | 29800 | 4.18 | Weld | 2I7 | 33100 | 4.55 |
| … | | | | Weld | 2I9 | 35700 | 5.07 |

Figure 106 shows the collection of fatigue life across all three runout cycles to be investigated. The samples are also spaced across the stress axis with varying starting stresses and varying step size. The number of cycles to failure is shown as well, indicating the form of the SN curve with an elbow at $10^6$ cycles. For alpha specimens, this elbow is approximately found at 525 MPa. There is a bimodal distribution in the bimodal samples, with a cluster of samples at approximately 400 MPa and another at 600 MPa. Finally, weld samples can be seen to have an elevated but broad elbow at approximately 700 MPa.

As in the former sample set, the dataset can be used to validate some of the methodology, such as the PCA derived geometry. The most direct measurement of dynamic response in this experimental set up is the coupling constant exhibited between transducer power and angular deflection. Figure 107 shows the comparison of this data to both original measurement-derived resonant frequencies, and the PCA-derived resonant frequencies. The closer alignment to the dynamic response curve in Figure 32 of the Methods section on page 78 can be seen in the PCA derived frequencies, for both the 20 kHz and 30 kHz tested specimens. As horns are not calibrated to their vibration amplitude in this experiment, each horn will introduce a factor difference in effective vibration amplitude to a certain power input. Despite these differences, however, the rise in coupling constant when the resonant frequency approaches the testing frequency can be seen.

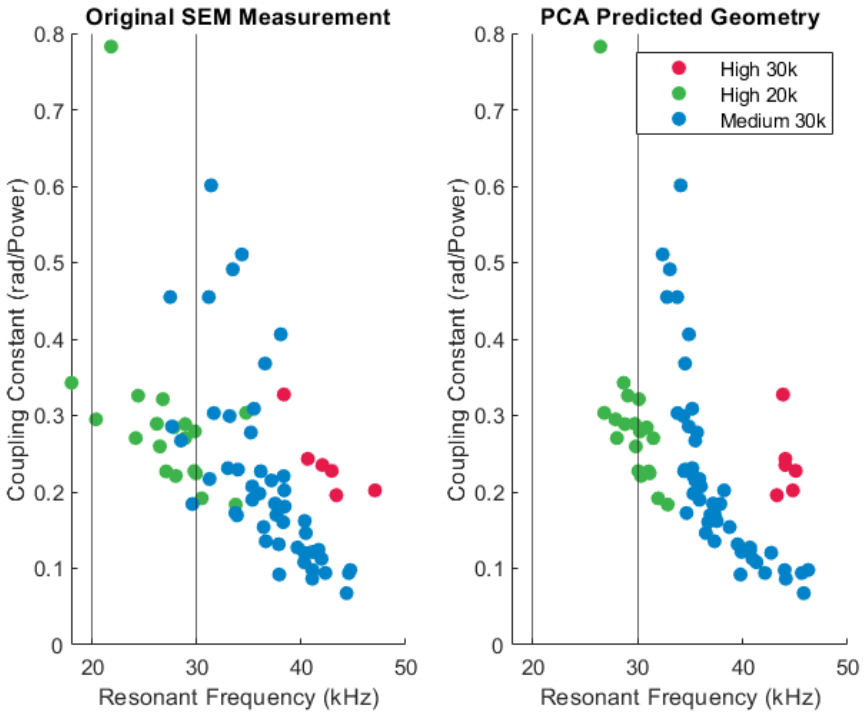



*Figure 107: Coupling constant measurement for samples in set Foil 7-11. All 73 samples are shown, coloured by the amplification horn used and the test frequency. Two vertical lines at 20 and 30 kHz are shown as a guide to the eye. Error bars are not shown for clarity, but error is approximately 10% in measurement of coupling constant.*

The final validation of the PCA derived geometry would be to measure the fracture surface thickness, as done in the earlier sample set, though this was deemed out of scope. The SN results can be further analysed by considering the joint posterior for each allowed runout life, considering all the data collected, as described in the Extension to PSN section on page 157. This posterior, for each material, is shown in Figure 108. These results show more clearly the estimates that can be obtained for the fatigue strength at a variety of cycles. These results can be described as the MAP and 95% HPD interval for both the mean and spread of fatigue strength at a given cycle life. These results are summarised in Table 13.

*Table 13: Results from joint posterior analysis shown in Figure 108. All values given in MPa, with mean and 95% HPD range in square brackets.*

| Material | $10^5$ Cycles | | $10^6$ Cycles | | $10^7$ Cycles | |
|---|---|---|---|---|---|---|
| | Mean | Standard Deviation | Mean | Standard Deviation | Mean | Standard Deviation |
| Alpha | 520 [480, 560] | 50 [30, 90] | 500 [450, 550] | 65 [40, 115] | 485 [430, 540] | 70 [45, 130] |
| Bimodal | 500 [420, 580] | 115 [75, 205] | 500 [420, 580] | 115 [80, 200] | 520 [440, 600] | 115 [75, 195] |
| Weld | 680 [610,750] | 90 [60, 160] | 665 [605, 725] | 90 [60, 150] | 660 [595,730] | 95 [60, 165] |

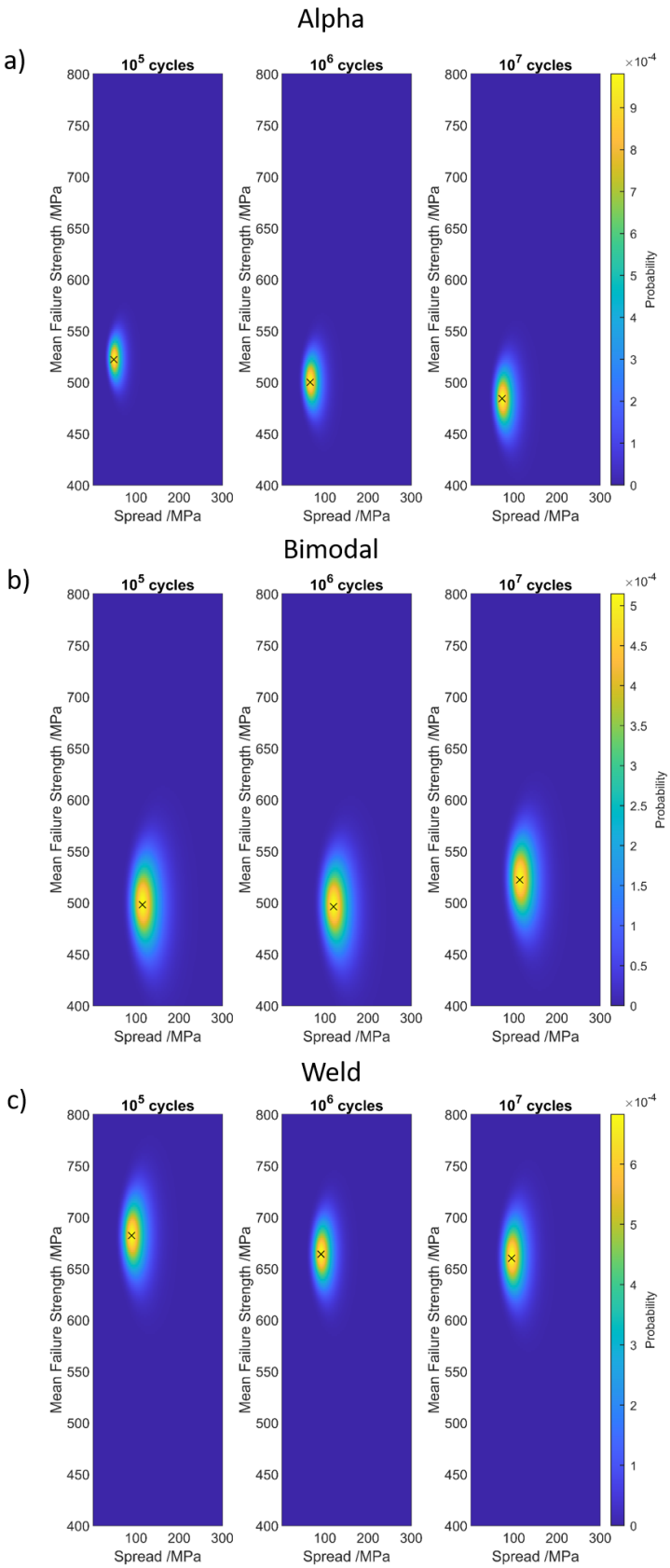



*Figure 108: Joint posterior for sample set Foil 7-11 with 73 samples tested: 22 alpha, 26 bimodal, and 25 weld. Results show the constant life joint posterior for the three runout cycles set in test campaign: $10^5$ cycles, $10^6$ cycles, and $10^7$ cycles. Crosses mark the MAP, with values outlined in Table 4.*

With the description in the uncertainty of the results above, Figure 109 shows the SN curve with the MAP values comparing parent material with weld material, following a calculation of a joint posterior for all parent material samples.

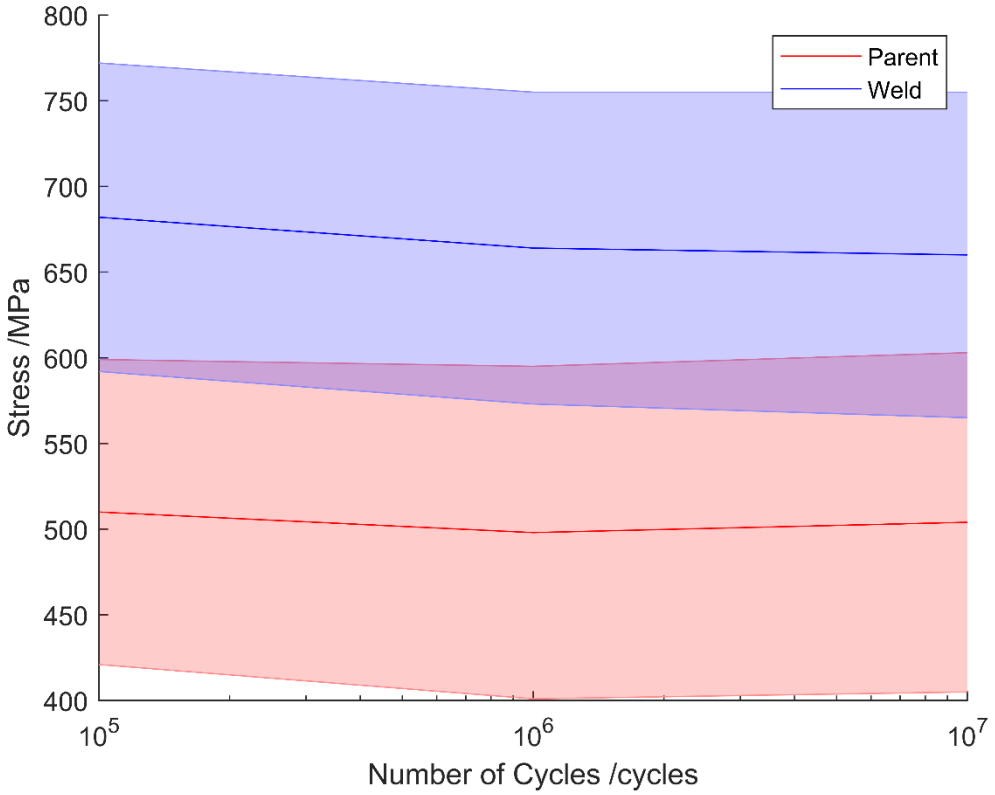



*Figure 109: SN diagram of parent material comparing mean (line) and one standard deviation (shaded area) across all 3 tested lives for parent material (48 samples, red) and weld material (25 samples, blue).*

This result confirms the earlier findings in Foil 3&4: the parent material has a fatigue strength at $10^6$ cycles of approximately 500 MPa with a spread of approximately 50 MPa in the alpha and 100 MPa in the bimodal material. More crucially, the weld material has an elevated fatigue strength across all lives of approximately 100-150 MPa above parent material, with a spread of approximately 100 MPa. It can also be seen that the minimal overlap in the spread between the parent and weld material implies that bulk tests are likely to fail in the parent material (in addition to the often greater volume of parent material tested).

To compare all datasets collected, Figure 110 shows the SN plot of all samples failed in all four fatigue test campaigns. These results show the significant degree of scatter that is obtained

across these test campaigns. It can be seen that there is broad agreement between datasets, with weld specimens of sets Foil 3&4 and Foil 7-11 showing higher mean fatigue strength, likely due to the improved polishing quality and accounting for geometric variation. The fatigue debit from unpolished specimens cannot be seen in parent material, with bimodal specimens in Foil 7-11 performing worse than in the unpolished Foil 1. This plot may suggest an effect from loading history, though competing effects of poor polish and geometrical control cannot be distinguished.

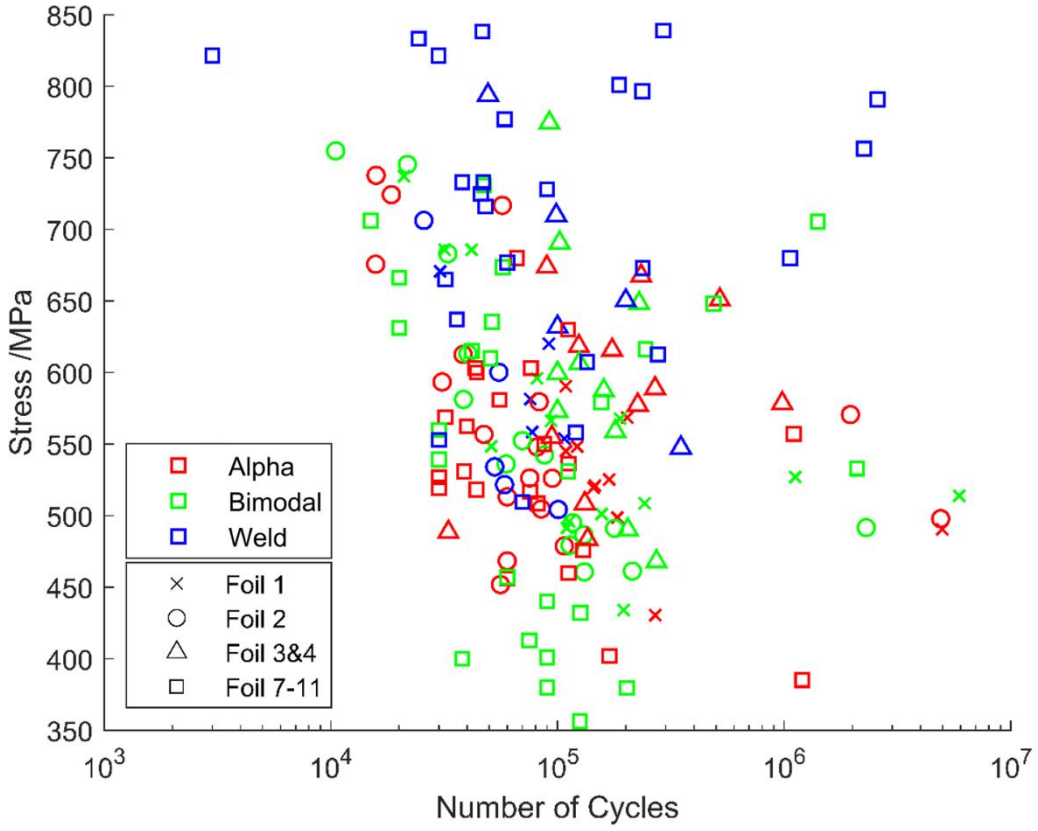



*Figure 110: SN Plot of data collected in all fatigue test campaigns, coloured by microstructure. Plot shows data from set Foil 1 (x markers), Foil 2 (o), Foil 3&4 (Δ), and Foil 7-11 (□). Colours represent material microstructure with alpha (red), bimodal (green), and weld (blue). In this case, the first 6 samples of Foil 3&4 are shown for completeness. 167 points are shown, with 29, 38, 27, and 73 points shown in sets Foil 1, 2, 3&4, and 7-11 respectively.*

## 2.7. Discussion

The data shown in the results highlight the complexity of this methodology. The results of each portion within the process flow are discussed and synthesised to contextualise the confidence with which to interpret them.

The process for producing samples represents a solution to the issue tasked in this thesis, but presents multiple opportunities for improvement. The primary challenge remains to produce a statistically relevant number of samples with similar geometries, and to do so in a manner that produces fatigue results reflective of the underlying behaviour. To do so implies producing parts with no microstructural change from the bulk material, and with no surface effects that introduce stress states that would not be seen in the bulk.

Using a foil based method followed by laser cutting and electropolishing is scalable, but limited by the consistency in electropolishing. In addition to the challenges in reliably producing parts to the specifications above, any success in this naturally introduces significant variation in geometry, which are challenging in such a dynamic system. Methods such as the PCA analysis can reduce the computational complexity of accounting for these variations, and indeed reflect the underlying mechanism of material removal by electropolishing, but remain approximate measures whose precision is difficult to estimate. This difficulty in error estimation is owed to the significant non-trivial combination of SEM measurement error with the stiffness correction function. Though Monte-Carlo simulations suggest a reduction in error propagated from this method of 2:1, the original surfaces determined by the SEM measurements may be displaced due to the random error of individual points changing the direction of the principal axes. This displacement is likely to be sensitive to the position of a measurement relative to the average measurement, in addition to the response functions non-linearity. Therefore, these errors should be interpreted as indicative.

This limitation is notable in the Perfect Coupling method described earlier. In light of the discussion above, this method can be thought of as approximating all errors in dimensional measurement as an error in the thickness measurement. The average measurements of the cantilever geometry from the top-down view in both Foil 1 and post-electropolished Foil 2 were taken as correct, with the variable of thickness taken as a free variable. This approximation is

further limited by the assumption that the vibration amplitude of the horn tip is perfectly coupled to the sample, which is known to vary by approximately 20%. For this reason, in combination with the low surface quality, experiments from Foil 1 and 2 are not considered as part of the results of this thesis.

When considering the experimental set up as a whole, it is worth highlighting the opportunities for introductions of error. While the transducer can be calibrated, the excitation of the meso-cantilever can only be measured via deflection angle. This is the primary source of error in this method: in addition to the geometric variations described above, the material parameters in the ABAQUS simulation cannot be independently validated to sufficient precision. The stiffness of the cantilever can be measured via nanoindentation, but is coupled with the dimensions of the cantilever, as well as the requirement for knowledge of any voids or irregularities. Furthermore, it does not reflect fully the dynamic response: measurements of hammer width affect dynamic but not static properties. This can be globally understood as the difference between the static beam stiffness, the material stiffness, and the dynamic stiffness. Furthermore, owing to the strongly non-linear response of cantilevers to excitation frequencies near their resonant frequencies, and to the error in the coupling of vibrations from the horn tip to the cantilever itself, the dynamic stiffness cannot be precisely understood even with significant calibration on the horn tip.

During collection of fatigue life, there are temporal challenges of working at very high frequency: though not necessary for this analysis, it is not possible with the current cameras in the lab to observe the fatigue response with a temporal resolution finer than 50 ms, corresponding to 1000 cycles.

A further challenge lies in a fatigue loading experiment where load is not directly measured: during crack growth, the resonant frequency will decrease and approach the testing frequency. This positive feedback loop causes a significant increase in stress, and a significant but non-linear reduction in the crack growth life. While some indication of the crack growth life can be gleaned

from changes in brightness curves as shown before, this is highly dependent on the optics in the current setup, and the scope of these experiments remain in practicality limited to full fracture tests. Some inroads by colleagues have been made in measuring crack growth through monitoring of the laser streak during testing, with some progress also made in adaptively reducing the vibration amplitude in response, in order to keep deflection angle constant. However, such methods are not mature at the time of writing, and the question remains on whether bending fatigue tests should remain at constant angle in order to maintain constant stress. Therefore, this ultrasonic mesocantilever test method emphasises initiation stages over crack growth.

This discussion leads to the previously discussed consideration of the implication of results in such small-scale fatigue tests. The primary concern in the use of such small-scale mechanical data is often the size effect, which combines mechanistic effects (e.g. Gao-Nix, scale hardening [60], [268], [269] Hall Petch, to name a few) and statistical effects (from a reduced volume being observed). However, in materials with complex microstructures, it remains critical to carry out tests in volumes representative of the variation in order to obtain information from each component of this “composite” structure.

More broadly, the limitations and benefits of this fatigue test can be summarised in the effort to determine local stresses and the behaviour of material to these local stress states. The experimental challenges lie in accurately determining the former, while the motivation of this project is described by the latter. This method is far removed from approved testing standards, and is not primarily aimed at generating databases for lifing bulk engineering components. Indeed, not only must care be given in the design phase to choose the loading to be service-relevant, but a cantilever design itself promotes crack initiation at surface defects compared to conventionally seen HCF failure from internal defects. Instead, the benefit lies in probing local

fatigue debit and credit in materials where processes have led to locally altered microstructures, for use in detailed analysis during process development and component design.

Finally, the effect of frequency must be investigated. While earlier studies discussed in the Background section on page 56 show no frequency effect in titanium, or if at all a fatigue credit at higher frequency, Figure 111 shows the data from set Foil 7-11, with markers differentiated for samples tested at 20 kHz (x markers) and at 30 kHz (o).

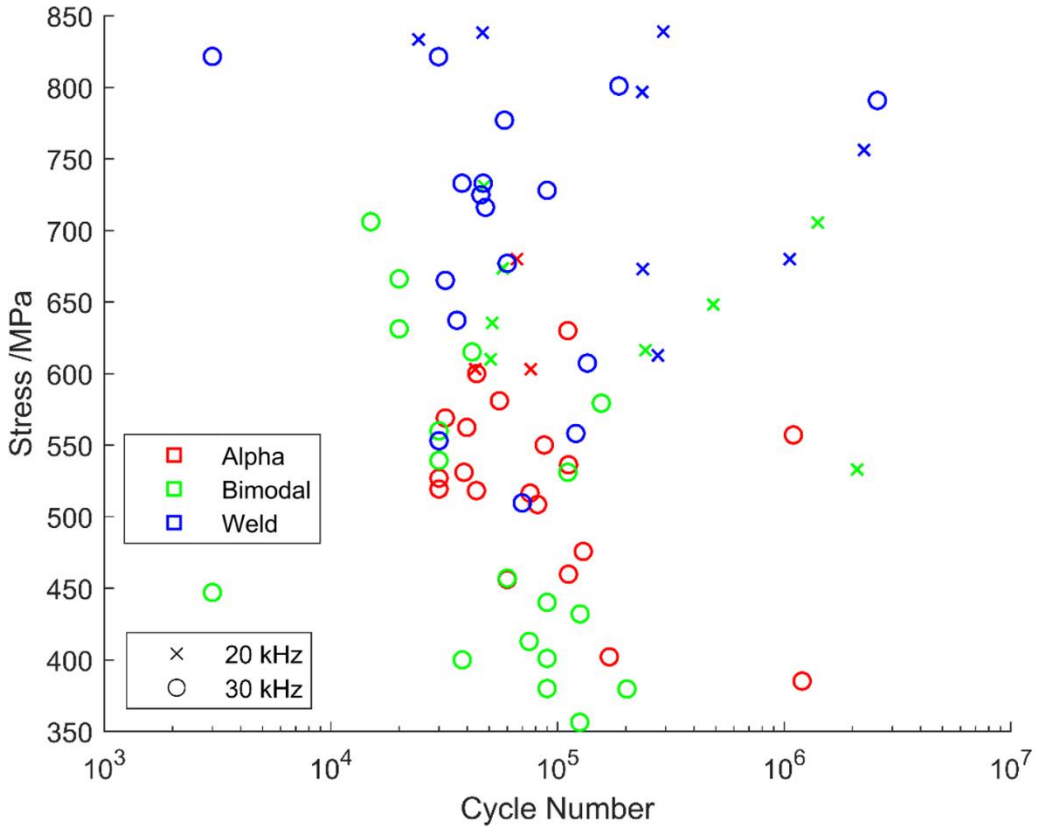



*Figure 111: SN Plot shown of data in set Foil 7-11 with differentiation between material (colours) and test frequency with 20 kHz shown with x markers, and 30 kHz shown with o markers. Colours represent material microstructure with alpha (red), bimodal (green), and weld (blue).*

This represents the only dataset of meso-scale cantilevers with similar designs tested at both 20 kHz and 30 kHz. The bimodal specimens in particular can be seen to have a wide range and clear distinction between the test frequencies, likely accounting for the bimodal distribution seen in earlier results. Though the analysis of samples only tested at 30 kHz provide similar conclusions to those described above, this contributes to the uncertainty and complexity of the interpretation of

such results. Recalling that the use of two testing frequencies was a result of variations in resonant frequency owing to a need to achieve consistent polishing quality, the trade-offs inherent to this experimental design are made clear.

This brings the discussion to the details of the experimental protocol. As discussed in the introduction, step testing, or as later described “multiple stress” protocols inherently require concern on the loading history of individual specimens. Though literature describes these effects in terms of damage or coaxing, with some studies investigating this effect and others utilising this for accelerated life testing methods, this study does not investigate the extent of damage. This is justified through two main arguments: data efficiency and cautious use of large step sizes.

As discussed earlier, the collection of high cycle fatigue data with low sample number presents a data challenge. Without the availability of damage models that may be unfounded in novel microstructures, step testing provides the benefit of greater data efficiency with a lower and upper bound for strength. Furthermore, while no damage model is used in this analysis, all models in the literature suggest a smaller effect with larger step sizes. Building on the work of Dr Arutyunyan in CP titanium, which indicates that a 5 MPa step size shows small effects in the range of $10^5 – 10^7$ cycles, it can be reasonably assumed that a 50 MPa produces minimal effects.

This larger step size causing a reduction in accuracy motivates the development of the Bayesian optimised protocol with varied starting stress. This study reports an early use of such a method in practice for the study of materials with success. Despite the experimental challenges linked with determining calibration constants, leading to the re-evaluation of test stresses and thereby changing the effective starting stress, the protocol’s robust adaptive response leads to a method which provides more information than the equivalent experiment with a rigid stress scale. However, these experimental challenges cannot be understated. It can be seen that for many specimens, the step size was not uniform and the start stress did not lie in the range of 50-100

MPa. This can be explored by displaying the intended starting stress and the actual starting stress, shown in Figure 112.

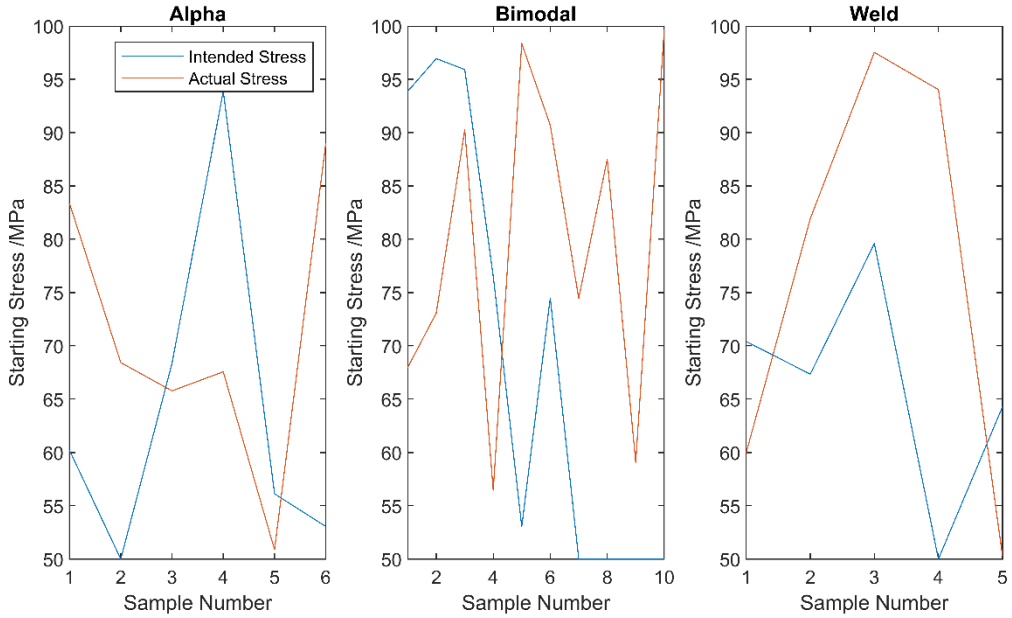



*Figure 112: Comparison between intended and actual starting stresses for each progressive sample in set Foil 3&4 during the Bayesian step constant life protocol.*

This shows the difficulty inherent to this experiment, suggesting that the protocol did not significantly improve parameter estimates in this case. Furthermore, in observing Figure 71 describing the convergence in the Bayesian step protocol, it can be seen that at this step size and number of samples, the Bayesian protocol did not significantly improve the precision of the estimates. However, through Figure 73 it can be seen that the Bayesian protocol is more consistent in its precision: with one experiment, it is impossible to determine the error due to protocol.

The PSN protocol suffered from challenges linked to its construction. The initial motivation of this protocol was the natural extension of the constant life approach, with the intention not to include a fatigue life model in order to minimise assumptions. The development of this protocol provides insights into interpretation of fatigue behaviour: evaluating probability of failure is significantly more tractable through fatigue strength than fatigue life as there is a defined fatigue strength for

every life, but not vice versa. To demonstrate this, consider the often-used phrase that “fatigue is life-scattered at low cycle, and stress scattered at high-cycle”. A consideration of the shape of the SN curve suggests that this phrase describes the direction of the spread relative to the curve, rather than its nature. In order to characterise the spread independently of this curve, as shown in many graphs describing the probability (or cumulative) distribution functions of failure, it is necessary to decide on the direction: probabilities are evaluated in stress or in life. Conventionally, these curves are shown to sum to unity for probability distribution functions (or tend to unity at the limit for cumulative functions). At high stress, this is feasible for both life and stress functions, with often life curves shown as these describe more practical applications of this curve. However, at low stress this is not necessarily practically feasible: near or below the fatigue limit, the fatigue life is not determined. Therefore, the only practicable method is to draw this curve in stress. This may explain the phrase described earlier, but may also suggest that stress scatter can be used to describe the fatigue curve at all lives. Simply put, the fatigue strength at every life is determined, unlike the fatigue life at every stress.

In combination with the motivation not to assume a functional form for the SN curve, the consideration that every cycle number contains a defined fatigue strength permits the construction of such a PSN model with discretised runout cycles that are explored: so-called life-slices. However, the Bayesian approach to collecting data in order to satisfy the utility functions described above require further work. The main limitation is the bias originating from the maximisation of utility at different propagation methods. This includes the as-yet un-explained bias from full propagation of information, as well as the slight bias for a flat SN curve in the medium propagation. This discussion will explore these issues in multiple-stress tests, as used in this study.

The first arises during full propagation. Consider Figure 113, showing a large amount of data collected at several VHCF, with the PSN CDF field shown. It can be seen that in comparing

between medium and full propagation, there is a significant bias with an increased slope in the curve and a decreased estimate in spread. One interpretation is that outliers at high stress and high cycle are excessively affecting the estimate of mean at lower cycles, and vice versa for low stress low cycle outliers, which is only relevant when considering single stress contributions (i.e. the unbounded integrals). This effect disappears when ignoring these single stress contributions. However, it is unclear why this biasing is so marked in this method and further study is required.

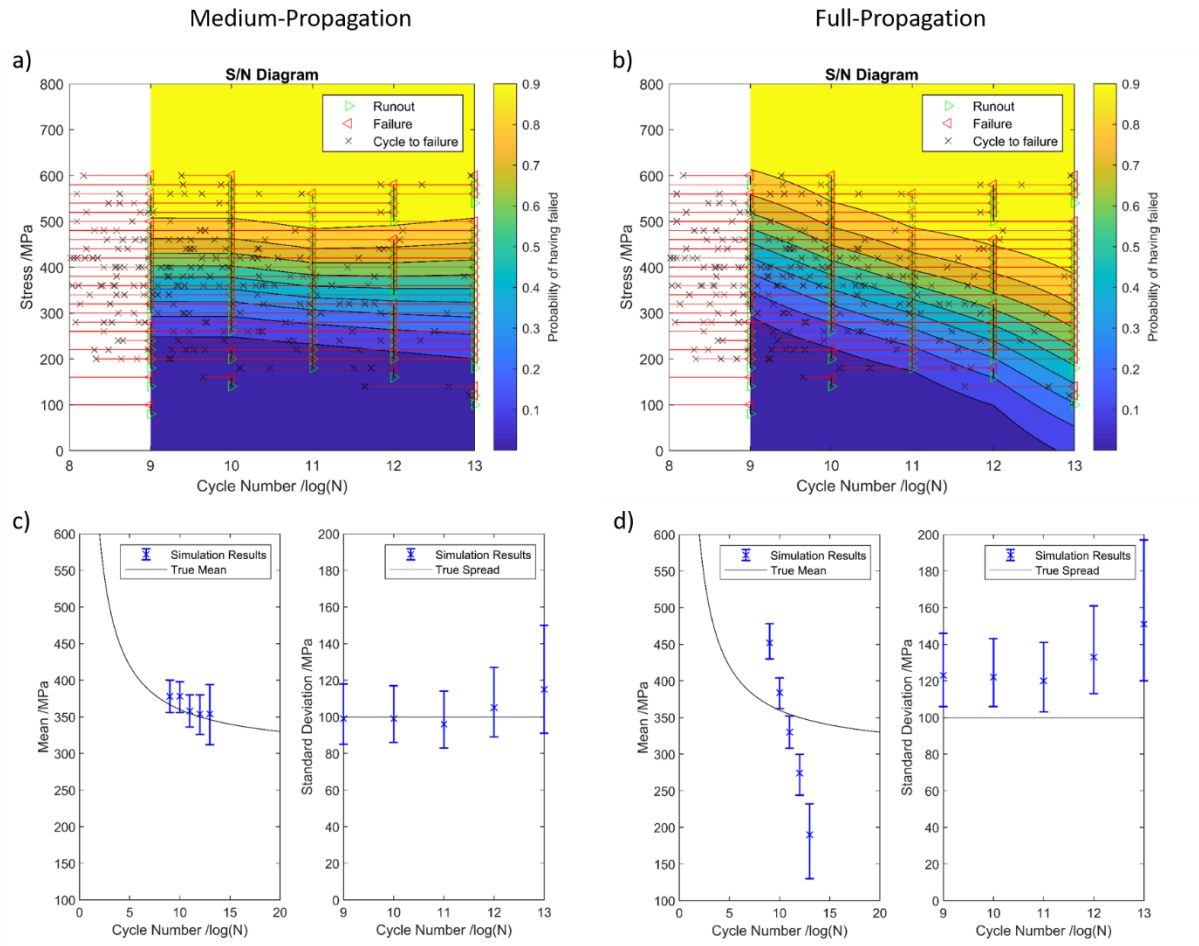



*Figure 113: Comparison between medium propagation (left) and full-propagation (right) with SN diagram (Panels a) and b)) with failure probability field and posterior result with MLE and 95% HPD error bars (Panels c) and d)). The sample set had a modified Basquin curve with parameters as in the methods section on page 48, and a constant spread of 100 MPa. 50 samples were tested with a step test regime at runout values of 9 – 13 $log(cycles)$ in steps of 1 $log(cycle)$ with a step size of 20 MPa and a starting stress of 0 MPa. Panels c) and d) show the true simulation set response in black.*

During the collection with medium propagation, there also existed an unstable equilibrium if a sample failed early: if the estimate of the mean is similar across the lives to study, there is a higher expected utility at higher lives as it is expected that the sample will fail early from one step

to the next. This bias can be entrenched in tests with large step size, and the experimentalist is required to override the preference for HCF testing in this case. This can be explained as a preference for the Bayesian system to observe SN curves with a flat mean response curve.

These limitations show the interplay between the experimentalist's knowledge and expectation of such systems and this – more simplified – Bayesian approach. This model limits itself to a fundamental approach that does not consider the functional form of the SN curve, though some aspects of this curve are known even with minimal assumptions.

It is possible to incorporate functional SN models into the Bayesian approach through a parametric approach. For instance, rather than independent estimates for mean and spread (and scale) for each cycle, a posterior can be constructed for the parameters in the model to study. Such a model could be as in the simulation set shown in equations (40) and (41):

$$S(N) = \alpha \log(N)^{\beta} + c \tag{40}$$

$$\sigma(N) = \gamma N + \delta \tag{41}$$

In this case, the mean curve is set to follow a modified Basquin law with the parameters $\alpha, \beta, c$, and the spread is allowed to vary linearly with parameters $\gamma, \delta$. However, early work in this showed strong "structure" in this posterior space, i.e. that the regions of high likelihood were highly varying with little cohesion, and therefore sub-optimal for discretisation frameworks. In addition, significant computational resources was needed to capture a sufficiently resolved parameter space.

Finally, the choice of distribution must be further discussed. This report models the fatigue strength using the normal distribution, though literature has shown more suitable models in fatigue data such as Weibull or log-normal [300], [303], [389]–[398], [364], [399]–[401], [365], [368], [377], [385]–[388]. However, the results shown in the complete publication on the Bayesian methodology shows that, at low sample number, there is little ability to distinguish between models and little credibility in extrapolating results to extreme values. For this reason,

the normal distribution is used as an illustrative and simple model to capture the spread in fatigue strength. This can be further demonstrated using Bayes Information Criterion (BIC), as seen in Figure 114. This figure does not show any significant evidence for or against any of the first three distribution models, with evidence against Gumbell, Frechet, and 3-parameter Weibull. This methodology is discussed in detail in the publication of this method [151], and is omitted from this report as it does not show any significant result, but suggests that the normal distribution may be used in this report without any misleading conclusions within the scope of the experimental results.

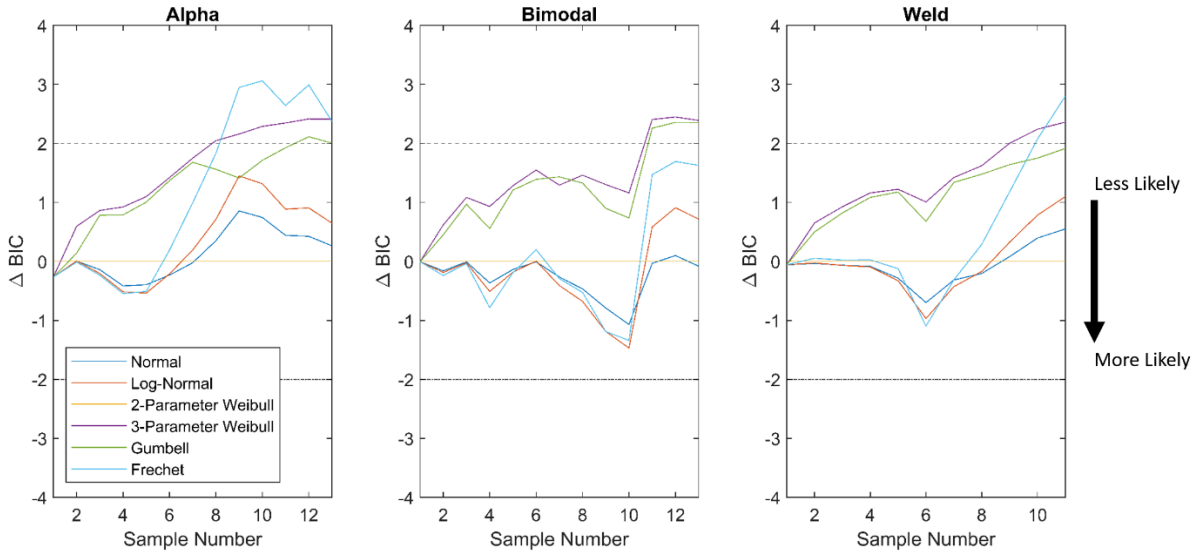



*Figure 114: BIC evolution for alpha (left) bimodal (centre) and weld (right) specimens that were tested to $10^6$ cycles in sample set Foil 3&4 and Foil 7-11. A comparison is made between the models in the legend to the 2-parameter Weibull, which equals the null result. A more negative result indicates a more likely candidate distribution, with a BIC greater than 2 representing "substantial evidence" according to Kass and Raftery* [381]*. Therefore, there is no evidence for a single distribution that clearly describes the data better than another does.*

Further work building on the results of this thesis can be divided into two parts: further development of the protocol, and further investigation in the fractography and fatigue mechanisms in these specimens. In the first instance, it is clear that the PSN protocol requires investigation into the source of the biases described above, and the incorporation of parametrised models, with great promise to develop data-driven methods that can aid the experimentalist in more rapidly validating fatigue models and determining material behaviour.

In the second instance, closer analysis of fractography can be used to inform models describing the failure mechanism of such unique microstructures. Detailed fractography, HR-EBSD to measure strains and dislocation density, and crack path analysis are methods for post-fractured samples, as well as experiments to measure crack growth rate. However, in part due to the limited scope and in part due to mitigating circumstances from the COVID-19 pandemic, these were replaced in favour of the data-driven methodologies described above.

## 2.8. Conclusion

This novel method for measuring the fatigue response of advanced manufactured microstructures offers unique data that can inform production methods. The challenges addressed in this chapter required developing:

1) A processing route for the generation of meso-scale test samples from a bulk specimen
2) The determination of the stress state in varying samples in a complex fatigue test setup
3) The consistent and confident determination of fatigue response at HCF with few specimens.

This work emphasises the importance in experimental procedure to carefully examine the local stress state of specimens undergoing fatigue loading, especially under more the complex testing regimes seen in micro-mechanical testing. This report outlines these advances through:

1) A process flow for the reliable generation of high surface quality test specimens with microstructures representative of bulk material
2) The development of data-driven methods for combining uncertain geometric measurements with bending stiffness measurements to predict dynamic behaviour
3) The development of a Bayesian Optimised testing protocol for constant life and full-field SN characterisation.

The advances above allow for further meso-scale sample production with dynamic property validation (points 1&2) and reliable data collection of (V)HCF constant life data with optimised protocols (point 3). These material agnostic tools can be used to collect, at high efficiency and spatial resolution, novel fatigue data in challenging sampling domains.

Crucially, however, this work has uniquely delivered the first direct estimate of the high-cycle fatigue credit in the central weld-zone of linear friction welded Ti-64 under bending fatigue axially in the forging direction. It has been shown that the weld material has an elevated fatigue strength approximately 150 MPa higher than parent material, with similar spread across the cycle ranges of $10^5$ – $10^7$ cycles. This quantified increase in fatigue strength can be incorporated into existing models for analysing component behaviour, and for further manufacturing process development.

The tools described enable further work, from detailed study of fatigue crack behaviour in such localised microstructures, to statistically rigorous studies of HCF strength behaviour particularly in the context of advanced manufacturing processes.

# 3. Project Conclusions

This thesis responds to the need to understand refined microstructures following developments in advanced manufacturing, and presents two methods for assessing local property. The first, a correlative nanoindentation mapping method, permits the rapid collection of structure property relationships as well as diagnostics through a visual multi-modal approach. The second, a meso-scale ultrasonic fatigue testing setup carried out with a novel protocol, permits the efficient collection of dynamic property data in otherwise difficult to measure regions.

Nanoindentation mapping permits the collection of mechanical property over a large area (~mm range) and at high resolution (~500 nm). Crystallographic effects on these properties such as orientation mechanical anisotropy or grain boundary effects can be observed when used in combination with EBSD.

Meso-scale ultrasonic fatigue testing provides several unique collection benefits:

- Rapid collection of high cycle fatigue data
- Extraction of fatigue property of small volumes of material

Using a newly developed Bayesian PSN multiple stress protocol, a quantitative description of the confidence in data collection can be used to optimise the efficiency of experiments in this challenging field.

Applied onto this case study, this method permits the collection of (V)HCF data in the weld-line, a result otherwise difficult to obtain due to the preference for parent material failure. When applied to the Ti-64 LFW, both methods provide adequately high resolution data to relate the microstructural variation from parent material to weld-line, extracting structure property relationships that describe this in static loading, as well as in VHCF fatigue loading. The results of the nanoindentation work suggests that the weld-line contains material approximately 30% harder than the parent material. While the fatigue loading is perpendicular to the main

nanoindentation direction, and therefore does not include the orientation strengthening, the fatigue strength credit results are broadly aligned.

These methods, presented through the above case study, are largely material system agnostic, and are valuable as a suite of tools and analytical techniques for approaching complex experimental challenges with data analytics. Manufacturing processes have developed highly advanced methodologies for creating complex high-performing materials to be used in demanding conditions. This project delivered tools allowing for experimental evaluation with similarly local (comparable to microstructure), and similarly advanced (using computational methods) approaches to enable the modern experimentalist to determine material properties at scale and at pace.

# 4. References


[1] C. M. Magazzeni, “Towards a Local Property Assessment of Materials,” *J. Eng. Integr. Soc.*, no. 51, pp. 34–36, Sep. 2021.

[2] SmarTech, “Additive Manufacturing in Aerospace : Strategic Implications,” *SmarTech Mark. Publ.*, no. August, pp. 1–5, 2014.

[3] D. Wee, R. Kelly, R. Mathis, and M. Breunig, “Industry 4.0 after the initial hype Where manufacturers are finding value and how they can best capture it,” 2016.

[4] M. Breunig, R. Kelly, R. Mathis, and D. Wee, “Getting the most out of Industry 4.0,” 2016.

[5] W. Gao *et al.*, “The status, challenges, and future of additive manufacturing in engineering,” *CAD Comput. Aided Des.*, vol. 69, pp. 65–89, Dec. 2015.

[6] D. Walton and H. Moztarzadeh, “Design and Development of an Additive Manufactured Component by Topology Optimisation,” *Procedia CIRP*, vol. 60, pp. 205–210, Jan. 2017.

[7] S. Ren and S. Galjaard, “Topology Optimisation for Steel Structural Design with Additive Manufacturing,” *Model. Behav.*, pp. 35–44, 2015.

[8] J. Podroužek, M. Marcon, K. Ninčević, and R. Wan-Wendner, “Bio-Inspired 3D Infill Patterns for Additive Manufacturing and Structural Applications,” *Mater. 2019, Vol. 12, Page 499*, vol. 12, no. 3, p. 499, Feb. 2019.

[9] G. Constantinides, K. S. Ravi Chandran, F. J. Ulm, and K. J. Van Vliet, “Grid indentation analysis of composite microstructure and mechanics: Principles and validation,” *Mater. Sci. Eng. A*, vol. 430, no. 1–2, pp. 189–202, Aug. 2006.

[10] S. Singamneni, Y. Lv, A. Hewitt, R. Chalk, W. Thomas, and D. Jordison, “Additive Manufacturing for the Aircraft Industry: A Review,” *J Aeronaut Aerosp. Eng*, vol. 8, no. 1, p. 215, 2019.

[11] P. D. Mangalgiri, “Composite materials for aerospace applications,” *Bull. Mater. Sci*, vol. 22, no. 3, pp. 657–664, 1999.

[12] A. P. Mouritz, M. K. Bannister, P. J. Falzon, and K. H. Leong, “Review of applications for advanced three-dimensional fibre textile composites,” *Compos. Part A Appl. Sci. Manuf.*, vol. 30, no. 12, pp. 1445–1461, Dec. 1999.

[13] C. Soutis, “Fibre reinforced composites in aircraft construction,” *Prog. Aerosp. Sci.*, vol. 41, no. 2, pp. 143–151, Feb. 2005.

[14] P. C. Collins, D. A. Brice, P. Samimi, I. Ghamarian, and H. L. Fraser, “Microstructural Control of Additively Manufactured Metallic Materials,” 2016.

[15] Y. M. Arısoy, L. E. Criales, T. Özel, B. Lane, S. Moylan, and A. Donmez, “Influence of scan strategy and process parameters on microstructure and its optimization in additively manufactured nickel alloy 625 via laser powder bed fusion,” *Int. J. Adv. Manuf. Technol.*, vol. 90, no. 5–8, pp. 1393–1417, 2017.

[16] E. Alabort *et al.*, “Alloys-by-design: Application to titanium alloys for optimal superplasticity,” *Acta Mater.*, vol. 178, pp. 275–287, Oct. 2019.

[17] Y. T. Tang *et al.*, “Alloys-by-design: Application to new superalloys for additive manufacturing,” *Acta Mater.*, vol. 202, pp. 417–436, Jan. 2021.

[18] J. H. Panchal, S. R. Kalidindi, and D. L. McDowell, “Key computational modeling issues in Integrated Computational Materials Engineering,” *Comput. Des.*, vol. 45, pp. 4–25, 2013.

[19] A. A. Salem, J. B. Shaffer, D. P. Satko, S. L. Semiatin, and S. R. Kalidindi, “Workflow for integrating mesoscale heterogeneities in materials structure with process simulation of titanium alloys,” *Integrating Materials and Manufacturing Innovation*, vol. 3, no. 1. Springer Berlin Heidelberg, pp. 322–343, 16-Dec-2014.

[20] G. Lütjering and J. C. Williams, *Titanium*. Springer, 2003.

[21] T. B. Britton, F. P. E. Dunne, and A. J. Wilkinson, “On the mechanistic basis of deformation at the microscale in hexagonal close-packed metals,” *Proceedings of the Royal Society A: Mathematical, Physical and Engineering Sciences*, vol. 471, no. 2178. 2015.

[22] H. L. Ewalds, “The effect of environment on fatigue crack closure in aluminium alloys,” *Eng. Fract. Mech.*, vol. 13, no. 4, pp. 1001–1007, 1980.

[23] I. Weiss and S. L. Semiatin, “Thermomechanical processing of alpha titanium alloys - An overview,” *Materials Science and Engineering A*, vol. 263, no. 2. Elsevier, pp. 243–256, 15-May-1999.

[24] J. C. Williams, R. G. Baggerly, and N. E. Paton, “Deformation behavior of HCP Ti-Al alloy single crystals,” in *Metallurgical and Materials Transactions A: Physical Metallurgy and Materials Science*, 2002, vol. 33, no. 3, pp. 837–850.

[25] H. W. ROSENBERG, “TITANIUM ALLOYING IN THEORY AND PRACTICE,” in *The Science, Technology and Application of Titanium*, Elsevier, 1970, pp. 851–859.

[26] G. Lütjering, “Influence of processing on microstructure and mechanical properties of (α+β) titanium alloys,” *Mater. Sci. Eng. A*, vol. 243, no. 1–2, pp. 32–45, Mar. 1998.

[27] M. Peters, J. Kumpfert, C. H. Ward, and C. Leyens, “Titanium alloys for aerospace applications,” *Advanced Engineering Materials*, vol. 5, no. 6. Wiley-Blackwell, pp. 419–427, 26-Jun-2003.

[28] S. Nishikawa and S. Kikuchi, “Diffraction of cathode rays by mica [4],” *Nature*, vol. 121, no. 3061. pp. 1019–1020, 1928.

[29] B. L. Adams, S. I. Wright, and K. Kunze, “Orientation imaging: The emergence of a new microscopy,” *Metall. Trans. A*, vol. 24, no. 4, pp. 819–831, Apr. 1993.

[30] N. C. K. Lassen, D. J. Jensen, and K. Conradsen, “Image processing procedures for analysis of electron back scattering patterns,” *Scanning Microsc.*, vol. 6, no. 1, pp. 115–121, 1992.

[31] H. N. Southworth, “Scanning Electron Microscopy and Microanalysis,” in *Physicochemical Methods of Mineral Analysis*, vol. 15, no. 9, 1975, pp. 421–450.

[32] J. Goldstein, D. E. Newbury, J. R. Michael, N. W. M. Ritchie, J. H. J. Scott, and D. C. Joy, *Scanning electron microscopy and x-ray microanalysis*. .

[33] T. B. Britton *et al.*, “Tutorial: Crystal orientations and EBSD — Or which way is up?,” *Mater. Charact.*, vol. 117, pp. 113–126, 2016.

[34] A. P. Day, “Spherical EBSD,” in *Journal of Microscopy*, 2008, vol. 230, no. 3, pp. 472–486.

[35] P. N. Quested, P. J. Henderson, and M. McLean, “Observations of Deformation and Fracture Heterogeneities in a Nickel-Base Superalloy Using Electron Back Scattering Patterns,” *Acta mater.*, vol. 36, no. 10, pp. 2743–2752, 1988.

[36] A. J. Wilkinson, G. Meaden, and D. J. Dingley, “High-resolution elastic strain measurement from electron backscatter diffraction patterns: New levels of sensitivity,” *Ultramicroscopy*, vol. 106, no. 4–5, pp. 307–313, Mar. 2006.

[37] T. B. Britton *et al.*, “Factors affecting the accuracy of high resolution electron backscatter diffraction when using simulated patterns,” *Ultramicroscopy*, vol. 110, no. 12, pp. 1443–1453, Nov. 2010.

[38] T. B. Britton and A. J. Wilkinson, “High resolution electron backscatter diffraction measurements of elastic strain variations in the presence of larger lattice rotations,” *Ultramicroscopy*, vol. 114, pp. 82–95, Mar. 2012.

[39] A. J. Wilkinson, G. Meaden, and D. J. Dingley, “Elastic Strain Tensor Mapping - Extending the Limits of EBSD Analysis,” *Microsc. Microanal.*, vol. 11, no. S02, pp. 520–521, Aug. 2005.

[40] A. J. Wilkinson, G. Meaden, and D. J. Dingley, “High resolution mapping of strains and rotations using electron backscatter diffraction,” *Mater. Sci. Technol.*, vol. 22, no. 11, pp. 1271–1278, Nov. 2006.

[41] J. Jiang, T. B. Britton, and A. J. Wilkinson, “Measurement of geometrically necessary dislocation density with high resolution electron backscatter diffraction: Effects of detector binning and step size,” *Ultramicroscopy*, vol. 125, pp. 1–9, 2013.

[42] M. Calcagnotto, D. Ponge, E. Demir, and D. Raabe, “Orientation gradients and geometrically necessary dislocations in ultrafine grained dual-phase steels studied by 2D and 3D EBSD,” *Mater. Sci. Eng. A*, vol. 527, no. 10–11, pp. 2738–2746, Apr. 2010.

[43] W. Pantleon, “Resolving the geometrically necessary dislocation content by conventional electron backscattering diffraction,” *Scr. Mater.*, vol. 58, no. 11, pp. 994–997, Jun. 2008.

[44] J. Jiang, T. B. Britton, and A. J. Wilkinson, “Evolution of dislocation density distributions in copper during tensile deformation,” *Acta Mater.*, vol. 61, no. 19, pp. 7227–7239, Nov. 2013.

[45] T. Ben Britton, S. Birosca, M. Preuss, and A. J. Wilkinson, “Electron backscatter diffraction study of dislocation content of a macrozone in hot-rolled Ti-6Al-4V alloy,” *Scr. Mater.*, vol. 62, no. 9, pp. 639–642, 2010.

[46] A. Vilalta-Clemente, M. Meisnar, S. Lozano-Perez, and A. J. Wilkinson, “Characterization of Elastic Strain Field and Geometrically Necessary Dislocation Distribution in Stress Corrosion Cracking of 316 Stainless Steels by Transmission Kikuchi Diffraction,” *Microsc. Microanal.*, vol. 21, no. S3, pp. 605–606, 2015.

[47] F. P. E. Dunne, D. Rugg, and A. Walker, “Lengthscale-dependent, elastically anisotropic, physically-based hcp crystal plasticity: Application to cold-dwell fatigue in Ti alloys,” *Int. J. Plast.*, vol. 23, no. 6, pp. 1061–1083, Jun. 2007.

[48] F. Weber, I. Schestakow, F. Roters, and D. Raabe, “Texture evolution during bending of a single crystal copper nanowire studied by EBSD and crystal plasticity finite element simulations,” *Adv. Eng. Mater.*, vol. 10, no. 8, pp. 737–741, Aug. 2008.

[49] P. D. Littlewood and A. J. Wilkinson, “Local deformation patterns in Ti-6Al-4V under tensile, fatigue and dwell fatigue loading,” *Int. J. Fatigue*, vol. 43, pp. 111–119, Oct. 2012.

[50] P. D. Littlewood and A. J. Wilkinson, “Geometrically necessary dislocation density distributions in cyclically deformed Ti-6Al-4V,” *Acta Mater.*, vol. 60, no. 15, pp. 5516–5525, Sep. 2012.

[51] D. Di Maio and S. G. Roberts, “Measuring fracture toughness of coatings using focused-ion-beam-machined microbeams,” *J. Mater. Res.*, vol. 20, no. 2, pp. 299–302, 2005.

[52] J. Gong and A. J. Wilkinson, “A microcantilever investigation of size effect, solid-solution strengthening and second-phase strengthening for 〈a〉 prism slip in alpha-Ti,” *Acta Mater.*, vol. 59, no. 15, pp. 5970–5981, Sep. 2011.

[53] E. O. Hall, “The deformation and ageing of mild steel: II Characteristics of the Lüders deformation,” *Proc. Phys. Soc. Sect. B*, vol. 64, no. 9, pp. 742–747, 1951.

[54] N. J. Petch and P. Stables, “Delayed Fracture of Metals under Static Load,” *Nature*, vol. 169, no. 4307, pp. 842–843, May 1952.

[55] D. J. Dunstan and A. J. Bushby, “Grain size dependence of the strength of metals: The Hall-Petch effect does not scale as the inverse square root of grain size,” *Int. J. Plast.*, vol. 53, pp. 56–65, Feb. 2014.

[56] W. C. Oliver and G. M. Pharr, “An improved technique for determining hardness and elastic modulus using load and displacement sensing indentation experiments,” *J. Mater. Res.*, vol. 7, no. 6, pp. 1564–1583, 1992.

[57] G. M. Pharr and W. C. Oliver, “Measurement of Thin Film Mechanical Properties Using Nanoindentation,” *MRS Bull.*, vol. 17, no. 7, pp. 28–33, 1992.

[58] N. A. Fleck, G. M. Muller, M. F. Ashby, and J. W. Hutchinson, “Strain gradient plasticity: Theory and experiment,” *Acta Metall. Mater.*, vol. 42, no. 2, pp. 475–487, Feb. 1994.

[59] B. Merle, V. Maier-Kiener, T. J. Rupert, and G. M. Pharr, “Current trends in nanomechanical testing research,” *J. Mater. Res. 2021 3611*, vol. 36, no. 11, pp. 2133–2136, Jul. 2021.

[60] M. D. Uchic, D. M. Dimiduk, J. N. Florando, and W. D. Nix, “Sample dimensions influence strength and crystal plasticity,” *Science (80-. ).*, vol. 305, no. 5686, pp. 986–989, Aug. 2004.

[61] Z. W. Shan, R. K. Mishra, S. A. Syed Asif, O. L. Warren, and A. M. Minor, “Mechanical annealing and source-limited deformation in submicrometre- diameter Nicrystals,” *Nat. Mater.*, vol. 7, no. 2, pp. 115–119, 2008.

[62] D. Rugg, T. B. Britton, J. Gong, A. J. Wilkinson, and P. A. J. Bagot, “In-service materials support for safety critical applications - A case study of a high strength Ti-alloy using advanced experimental and modelling techniques,” *Mater. Sci. Eng. A*, vol. 599, pp. 166–173, Apr. 2014.

[63] F. Roters, P. Eisenlohr, L. Hantcherli, D. D. Tjahjanto, T. R. Bieler, and D. Raabe, “Overview of constitutive laws, kinematics, homogenization and multiscale methods in crystal plasticity finite-element modeling: Theory, experiments, applications,” *Acta Mater.*, vol. 58, no. 4, pp. 1152–1211, Feb. 2010.

[64] J. Gong and A. J. Wilkinson, “Micro-cantilever testing of a prismatic slip in commercially pure Ti,” *Philos. Mag.*, vol. 91, no. 7–9, pp. 1137–1149, Mar. 2011.

[65] J. Gong and A. Wilkinson, “Investigation of elastic properties of single-crystal α-Ti using microcantilever beams,” *Philos. Mag. Lett.*, vol. 90, no. 7, pp. 503–512, Jul. 2010.

[66] J. Gong and A. J. Wilkinson, “Anisotropy in the plastic flow properties of single-crystal α titanium determined from micro-cantilever beams,” *Acta Mater.*, vol. 57, no. 19, pp. 5693–5705, Nov. 2009.

[67] R. Ding, J. Gong, A. J. Wilkinson, and I. P. Jones, “Transmission electron microscopy of deformed Ti-6Al-4V micro-cantilevers,” in *Philosophical Magazine*, 2012, vol. 92, no. 25–27, pp. 3290–3314.

[68] R. K. Basukala, K. J. Park, D. Y. Choi, and S. J. Han, “Secure mobile IP communication in residential networks,” in *24th IEEE International Conference on Advanced Information Networking and Applications Workshops, WAINA 2010*, 2010, no. 2009, pp. 357–362.

[69] I. Bhamji, M. Preuss, P. L. Threadgill, and A. C. Addison, “Solid state joining of metals by linear friction welding: A literature review,” *Materials Science and Technology*, vol. 27, no. 1. Taylor & Francis, pp. 2–12, 12-Jan-2011.

[70] R. Turner, J. C. Gebelin, R. M. Ward, and R. C. Reed, “Linear friction welding of Ti-6Al-4V: Modelling and validation,” *Acta Mater.*, vol. 59, no. 10, pp. 3792–3803, Jun. 2011.

[71] A. Kermanpur, H. Sepehri Amin, S. Ziaei-Rad, N. Nourbakhshnia, and M. Mosaddeghfar, “Failure analysis of Ti6Al4V gas turbine compressor blades,” *Eng. Fail. Anal.*, vol. 15, no. 8, pp. 1052–1064, 2008.

[72] I. Bhamji, M. Preuss, P. L. Threadgill, R. J. Moat, A. C. Addison, and M. J. Peel, “Linear friction welding of AISI 316L stainless steel,” *Mater. Sci. Eng. A*, vol. 528, no. 2, pp. 680–690, Dec. 2010.

[73] W. Li, A. Vairis, M. Preuss, and T. Ma, *Linear and rotary friction welding review*, vol. 61, no. 2. Taylor & Francis, 2016, pp. 71–100.

[74] X. Y. Wang, W. Y. Li, T. J. Ma, and A. Vairis, “Characterisation studies of linear friction welded titanium joints,” *Mater. Des.*, vol. 116, pp. 115–126, Feb. 2017.

[75] A. R. McAndrew, P. A. Colegrove, C. Bühr, B. C. D. Flipo, and A. Vairis, “A literature review of Ti-6Al-4V linear friction welding,” *Progress in Materials Science*, vol. 92. Pergamon, pp. 225–257, 01-Mar-2018.

[76] X. Kong, J. Li, C. Bennett, W. Collins, and S. Laflamme, “Numerical simulation and experimental validation of a large-area capacitive strain sensor for fatigue crack monitoring,” *Meas. Sci. Technol.*, vol. 27, p. 124009, 2016.

[77] A. Vairis and M. Frost, “High frequency linear friction welding of a titanium alloy,” *Wear*, vol. 217, no. 1, pp. 117–131, Apr. 1998.

[78] A. Vairis and M. Frost, “Modelling the linear friction welding of titanium blocks,” vol. 292, no. 1, pp. 8–17, Nov. 2000.

[79] A. L. Pilchak, “The effect of friction stir processing on the microstructure, mechanical properties and fracture behavior of investment cast Ti-6Al-4V.” 2009.

[80] P. Wanjara and M. Jahazi, “Linear friction welding of Ti-6Al-4V: Processing, microstructure, and mechanical-property inter-relationships,” *Metall. Mater. Trans. A Phys. Metall. Mater. Sci.*, vol. 36, no. 8, pp. 2149–2164, Aug. 2005.

[81] J. C. Stinville, F. Bridier, D. Ponsen, P. Wanjara, and P. Bocher, “High and low cycle fatigue behavior of linear friction welded Ti-6Al-4V,” *Int. J. Fatigue*, vol. 70, pp. 278–288, Jan. 2015.

[82] G. D. Wen, T. J. Ma, W. Y. Li, J. L. Li, H. Z. Guo, and D. L. Chen, “Cyclic deformation behavior of linear friction welded Ti6Al4V joints,” *Mater. Sci. Eng. A*, vol. 597, pp. 408–414, Mar. 2014.

[83] A. R. McAndrew, P. A. Colegrove, A. C. Addison, B. C. D. Flipo, and M. J. Russell, “Energy and Force Analysis of Ti-6Al-4V Linear Friction Welds for Computational Modeling Input and Validation Data,” *Metall. Mater. Trans. A Phys. Metall. Mater. Sci.*, vol. 45, no. 13, pp. 6118–6128, Dec. 2014.

[84] C. M. Magazzeni *et al.*, “Nanoindentation in multi-modal map combinations: a correlative approach to local mechanical property assessment,” *J. Mater. Res.*, vol. 36, no. 11, pp. 2235–2250, Jan. 2021.

[85] M. Quaresimin, “Modelling the fatigue behaviour of bonded joints in composite materials,” in *Multi-scale Modelling of Composite Material Systems*, C. Soutis and P. W. R. Beaumont, Eds. Cambridge, UK: Woodhead, 2005, pp. 469–494.

[86] E. Le Pen, D. Baptiste, and G. Hug, “Multi-scale fatigue behaviour modelling of Al-Al2O3 short fibre composites,” *Int. J. Fatigue*, vol. 24, pp. 205–214, 2002.

[87] K. Sai and G. Cailletaud, “Multi-mechanism models for the description of ratchetting: Effect of the scale transition rule and of the coupling between hardening variables,” *Int. J. Plast.*, vol. 23, pp. 1589–1617, 2007.

[88] Y. Xiong *et al.*, “Cold Creep of Titanium: Analysis of stress relaxation using synchrotron diffraction and crystal plasticity simulations,” Mar. 2020.

[89] Y. Guo, D. M. Collins, E. Tarleton, F. Hofmann, A. J. Wilkinson, and T. Ben Britton, “Dislocation density distribution at slip band-grain boundary intersections,” *Acta Mater.*, vol. 182, pp. 172–183, Jan. 2020.

[90] S. Das, F. Hofmann, and E. Tarleton, “Consistent determination of geometrically necessary dislocation density from simulations and experiments,” *Int. J. Plast.*, vol. 109, pp. 18–42, Oct. 2018.

[91] E. Tarleton and S. G. Roberts, “Dislocation dynamic modelling of the brittle-ductile transition in tungsten,” *Philos. Mag.*, vol. 89, no. 31, pp. 2759–2769, Nov. 2009.

[92] A. L. Pilchak and J. C. Williams, “The effect of friction stir processing on the mechanical properties of investment cast and hot isostatically pressed Ti-6Al-4V,” in *Metallurgical and Materials Transactions A: Physical Metallurgy and Materials Science*, 2011, vol. 42, no. 6, pp. 1630–1645.

[93] W. Y. Li *et al.*, “Microstructure characterization and mechanical properties of linear friction welded Ti-6Al-4V alloy,” *Adv. Eng. Mater.*, vol. 10, no. 1–2, pp. 89–92, Feb. 2008.

[94] P. Frankel, M. Preuss, A. Steuwer, P. J. Withers, and S. Bray, “Comparison of residual stresses in Ti-6Al-4V and Ti-6Al-2Sn-4Zr-2Mo linear friction welds,” *Mater. Sci. Technol.*, vol. 25, no. 5, pp. 640–650, May 2009.

[95] C. Qiu *et al.*, “Influence of processing conditions on strut structure and compressive properties of cellular lattice structures fabricated by selective laser melting,” *Mater. Sci. Eng. A*, vol. 628, pp. 188–197, Mar. 2015.

[96] D. E. J. Armstrong, A. J. Wilkinson, and S. G. Roberts, “Measuring anisotropy in Young’s modulus of copper using microcantilever testing,” *J. Mater. Res.*, vol. 24, no. 11, pp. 3268–3276, 2009.

[97] F. J. Humphreys, “Review Grain and subgrain characterisation by electron backscatter diffraction.”

[98] T. B. Britton, H. Liang, F. P. E. Dunne, and A. J. Wilkinson, “The effect of crystal orientation

on the indentation response of commercially pure titanium: Experiments and simulations," *Proc. R. Soc. A Math. Phys. Eng. Sci.*, vol. 466, no. 2115, pp. 695–719, 2010.

[99] F. F. Dear *et al.*, "Combined APT, TEM and SAXS characterisation of nanometre-scale precipitates in titanium alloys," *Microsc. Microanal.*, vol. 25, no. S2, pp. 2516–2517, 2019.

[100] Y. Chang *et al.*, "Characterizing solute hydrogen and hydrides in pure and alloyed titanium at the atomic scale," *Acta Mater.*, vol. 150, pp. 273–280, May 2018.

[101] X. Llovet, A. Moy, P. T. Pinard, and J. H. Fournelle, "Electron probe microanalysis: a review of recent developments and applications in materials science and engineering," *Prog. Mater. Sci.*, p. 100673, May 2020.

[102] A. J. Wilkinson, E. E. Clarke, T. B. Britton, P. Littlewood, and P. S. Karamched, "High-resolution electron backscatter diffraction: An emerging tool for studying local deformation," *J. Strain Anal. Eng. Des.*, vol. 45, no. 5, pp. 365–376, Jul. 2010.

[103] T. B. Britton, ) D Randman, and A. J. Wilkinson, "Nanoindentation study of slip transfer phenomenon at grain boundaries," 2017.

[104] D. Rugg, M. Dixon, and F. P. E. Dunne, "Effective structural unit size in titanium alloys."

[105] T. S. Jun, D. E. J. Armstrong, and T. B. Britton, "A nanoindentation investigation of local strain rate sensitivity in dual-phase Ti alloys," *J. Alloys Compd.*, vol. 672, pp. 282–291, Jul. 2016.

[106] M. Mayo, R. Siegel, Y. Liao, and W. Nix, "Nanoindentation of nanocrystalline ZnO," *J. Mater. Res.*, vol. 7, no. 4, pp. 973–979, 1992.

[107] H. Somekawa and C. A. Schuh, "High-strain-rate nanoindentation behavior of fine-grained magnesium alloys," *J. Mater. Res.*, vol. 27, no. 9, pp. 1295–1302, May 2012.

[108] S. Shim, H. Bei, M. K. Miller, G. M. Pharr, and E. P. George, "Effects of focused ion beam milling on the compressive behavior of directionally solidified micropillars and the nanoindentation response of an electropolished surface," *Acta Mater.*, vol. 57, no. 2, pp. 503–510, Jan. 2009.

[109] D. R. P. Singh, N. Chawla, G. Tang, and Y. L. Shen, "Micropillar compression of Al/SiC nanolaminates," *Acta Mater.*, vol. 58, no. 20, pp. 6628–6636, Dec. 2010.

[110] S. Korte, R. J. Stearn, J. M. Wheeler, and W. J. Clegg, "High temperature microcompression and nanoindentation in vacuum," *J. Mater. Res.*, vol. 27, no. 1, pp. 167–176, Jan. 2012.

[111] S. Korte and W. J. Clegg, "Micropillar compression of ceramics at elevated temperatures," *Scr. Mater.*, vol. 60, no. 9, pp. 807–810, May 2009.

[112] E. M. Grieveson, D. E. J. Armstrong, S. Xu, and S. G. Roberts, "Compression of self-ion implanted iron micropillars," *J. Nucl. Mater.*, vol. 430, no. 1–3, pp. 119–124, Nov. 2012.

[113] P. Sudharshan Phani and W. C. Oliver, "A critical assessment of the effect of indentation spacing on the measurement of hardness and modulus using instrumented indentation testing," *Mater. Des.*, vol. 164, Feb. 2019.

[114] B. Vignesh, W. C. Oliver, G. S. Kumar, and P. S. Phani, "Critical assessment of high speed nanoindentation mapping technique and data deconvolution on thermal barrier coatings," *Mater. Des.*, vol. 181, Nov. 2019.

[115] E. D. Hintsala, U. Hangen, and D. D. Stauffer, "High-Throughput Nanoindentation for

Statistical and Spatial Property Determination," *JOM*, vol. 70, no. 4. pp. 494–503, 2018.

[116] M. Sebastiani, R. Moscatelli, F. Ridi, P. Baglioni, and F. Carassiti, "High-resolution high-speed nanoindentation mapping of cement pastes: Unravelling the effect of microstructure on the mechanical properties of hydrated phases," *Mater. Des.*, vol. 97, pp. 372–380, May 2016.

[117] N. X. Randall, M. Vandamme, and F. J. Ulm, "Nanoindentation analysis as a two-dimensional tool for mapping the mechanical properties of complex surfaces," *J. Mater. Res.*, vol. 24, no. 3, pp. 679–690, 2009.

[118] E. P. Koumoulos, K. Paraskevoudis, and C. A. Charitidis, "Constituents Phase Reconstruction through Applied Machine Learning in Nanoindentation Mapping Data of Mortar Surface," *J. Compos. Sci.*, vol. 3, no. 3, p. 63, Jun. 2019.

[119] C. Tromas, J. C. Stinville, C. Templier, and P. Villechaise, "Hardness and elastic modulus gradients in plasma-nitrided 316L polycrystalline stainless steel investigated by nanoindentation tomography," *Acta Mater.*, vol. 60, no. 5, pp. 1965–1973, Mar. 2012.

[120] C. Tromas, M. Arnoux, and X. Milhet, "Hardness cartography to increase the nanoindentation resolution in heterogeneous materials: Application to a Ni-based single-crystal superalloy," *Scr. Mater.*, vol. 66, no. 2, pp. 77–80, Jan. 2012.

[121] D. Goldbaum, R. R. Chromik, N. Brodusch, and R. Gauvin, "Microstructure and Mechanical Properties of Ti Cold-Spray Splats Determined by Electron Channeling Contrast Imaging and Nanoindentation Mapping," *Microsc. Microanal.*, vol. 21, no. 3, pp. 570–581, 2015.

[122] J. M. Wheeler, "Mechanical phase mapping of the Taza meteorite using correlated high-speed nanoindentation and EDX," *J. Mater. Res.*, pp. 1–11, Aug. 2020.

[123] K. Herrmann, N. M. Jennett, W. Wegener, J. Meneve, K. Hasche, and R. Seemann, "Progress in determination of the area function of indenters used for nanoindentation," *Thin Solid Films*, vol. 377–378, pp. 394–400, Dec. 2000.

[124] H. M. Gardner *et al.*, "Quantifying the effect of oxygen on micro-mechanical properties of a near-alpha titanium alloy," *J. Mater. Res.*, vol. 36, no. 12, pp. 2529–2544, Sep. 2021.

[125] J. B. Pethica and W. C. Oliver, "Mechanical Properties of Nanometre Volumes of Material: use of the Elastic Response of Small Area Indentations," *MRS Proc.*, vol. 130, 1988.

[126] X. Li and B. Bhushan, "A review of nanoindentation continuous stiffness measurement technique and its applications," *Mater. Charact.*, vol. 48, no. 1, pp. 11–36, Feb. 2002.

[127] M. A. Monclús, S. Lotfian, and J. M. Molina-Aldareguía, "Tip shape effect on hot nanoindentation hardness and modulus measurements," *Int. J. Precis. Eng. Manuf.*, vol. 15, no. 8, pp. 1513–1519, 2014.

[128] G. Nolze, "Image distortions in SEM and their influences on EBSD measurements," *Ultramicroscopy*, vol. 107, no. 2–3, pp. 172–183, Feb. 2007.

[129] "MATLAB version R2019a." The MathWorks Inc., Natick, Massachusetts, 2019.

[130] M. R. Bache, W. J. Evans, V. Randle, and R. J. Wilson, "Characterization of mechanical anisotropy in titanium alloys," *Mater. Sci. Eng. A*, vol. 257, no. 1, pp. 139–144, Nov. 1998.

[131] W. A. Soer and J. T. M. De Hosson, "Detection of grain-boundary resistance to slip transfer using nanoindentation," *Mater. Lett.*, vol. 59, no. 24–25, pp. 3192–3195, Oct. 2005.

[132] T. B. Britton, D. Randman, and A. J. Wilkinson, “Nanoindentation study of slip transfer phenomenon at grain boundaries,” *J. Mater. Res.*, vol. 24, no. 3, pp. 607–615, Mar. 2009.

[133] Y. Su, C. Zambaldi, D. Mercier, P. Eisenlohr, T. R. Bieler, and M. A. Crimp, “Quantifying deformation processes near grain boundaries in α titanium using nanoindentation and crystal plasticity modeling,” *Int. J. Plast.*, vol. 86, pp. 170–186, Nov. 2016.

[134] E. Bayerschen, • A T Mcbride, • B D Reddy, and • T Böhlke, “Review on slip transmission criteria in experiments and crystal plasticity models.”

[135] Y. Guo, T. B. Britton, and A. J. Wilkinson, “Slip band-grain boundary interactions in commercial-purity titanium,” *Acta Mater.*, vol. 76, pp. 1–12, Sep. 2014.

[136] S. Miura and Y. Saeki, “Plastic deformation of aluminum bicrystals 〈100〉 oriented,” *Acta Metall.*, vol. 26, no. 1, pp. 93–101, Jan. 1978.

[137] J. Kacher and I. M. Robertson, “In situ and tomographic analysis of dislocation/grain boundary interactions in α-titanium,” *Philos. Mag.*, vol. 94, no. 8, pp. 814–829, Mar. 2014.

[138] S. Sodha, “An Implementation of Sobel Edge Detection,” *Project Rhea*. [Online]. Available: https://www.projectrhea.org/rhea/index.php/An_Implementation_of_Sobel_Edge_Detection. [Accessed: 23-Jul-2020].

[139] G. Evangelidis, “ECC image alignment algorithm (image registration) ,” *MATLAB Central File Exchange*, 06-Apr-2020. [Online]. Available: https://uk.mathworks.com/matlabcentral/fileexchange/27253-ecc-image-alignment-algorithm-image-registration. [Accessed: 06-Apr-2020].

[140] G. D. Evangelidis and E. Z. Psarakis, “Parametric Image Alignment Using Enhanced Correlation Coefficient Maximization.”

[141] S. Seitz *et al.*, “Homography, Transforms, Mosaics,” New York.

[142] N. J. Petch, “The cleavage strength of polycrystals,” *J. Iron Steel Inst.*, vol. 174, no. 1, pp. 25–28, 1953.

[143] D. Drouin, A. R. Couture, D. Joly, X. Tastet, V. Aimez, and R. Gauvin, “CASINO V2.42—A Fast and Easy-to-use Modeling Tool for Scanning Electron Microscopy and Microanalysis Users,” *Scanning*, vol. 29, no. 3, pp. 92–101, May 2007.

[144] P. Gopon, J. Fournelle, P. E. Sobol, and X. Llovet, “Low-Voltage electron-probe microanalysis of Fe-Si compounds using soft X-rays,” *Microsc. Microanal.*, vol. 19, no. 6, pp. 1698–1708, Dec. 2013.

[145] J. R. Goldstein, J., Newbury, D.E., Joy, D.C., Lyman, C.E., Echlin, P., Lifshin, E., Sawyer, L., Michael, *Scanning Electron Microscopy and X-ray Microanalysis*. Springer US, 2003.

[146] A. J. Wilkinson and T. Ben Britton, “Strains, planes, and EBSD in materials science,” *Materials Today*, vol. 15, no. 9. Elsevier, pp. 366–376, 01-Sep-2012.

[147] S. J. B. Reed, *Electron microprobe analysis and scanning electron microscopy in geology*, vol. 9780521848756. Cambridge University Press, 2005.

[148] J. D. Livingston and B. Chalmers, “Multiple slip in bicrystal deformation,” *Acta Metall.*, vol. 5, no. 6, pp. 322–327, Jun. 1957.

[149] J. Kacher, B. P. Eftink, B. Cui, and I. M. Robertson, “Dislocation interactions with grain boundaries,” *Curr. Opin. Solid State Mater. Sci.*, vol. 18, no. 4, pp. 227–243, Aug. 2014.

[150] F. Javaid, H. Pouriayevali, and K. Durst, “Dislocation–grain boundary interactions: recent advances on the underlying mechanisms studied via nanoindentation testing,” *J. Mater. Res.*, vol. 36, no. 12, pp. 2545–2557, Jun. 2021.

[151] C. M. Magazzeni, R. Rose, C. Gearhart, J. Gong, and A. J. Wilkinson, “Bayesian Optimised Collection Strategies for Fatigue Testing-Constant Life Testing.”

[152] W. A. J. Albert, “Uber Treibseile am Harz. Archiv ffir Mineralogie, Georgnosie.,” *Bergbau Undhiittenkd.*, vol. 10, pp. 215–234, 1837.

[153] A. Kahlow, “Materials in 19Th Century Germany,” *Hist. Technol.*, vol. 7, no. 3–4, pp. 255–266, Jul. 1991.

[154] A. Wöhler, “Versuche zur Ermittelung der auf die Eisenbahnwagen-Achsen einwirkenden Kräfte und der Widerstandsfähigkeit der Wagen-Achsen,” *Z. Bauw.*, vol. 10, pp. 583–616, 1860.

[155] W. Schütz, “A history of fatigue,” *Eng. Fract. Mech.*, vol. 54, no. 2, pp. 263–300, May 1996.

[156] S. Suresh, *Fatigue of Materials*. Cambridge University Press, 1998.

[157] A. Wöhler, “Uber die Festigkeitversuche mit Eisen und Stahl,” *Zeitschrift für Bauwes.*, 1870.

[158] O. H. Basquin, “The exponential law of endurance tests,” *Proc. Am. Soc. Test. Mater.*, vol. 10, pp. 625–630, 1910.

[159] C. M. Sonsino, “Course of SN-curves especially in the high-cycle fatigue regime with regard to component design and safety,” *Int. J. Fatigue*, vol. 29, no. 12, pp. 2246–2258, Dec. 2007.

[160] S. Subramanyan, “A cumulative damage rule based on the knee point of the S-N Curve,” *J. Eng. Mater. Technol. Trans. ASME*, vol. 98, no. 4, pp. 316–321, Oct. 1976.

[161] Y. Murakami, T. Takagi, K. Wada, and H. Matsunaga, “Essential structure of S-N curve: Prediction of fatigue life and fatigue limit of defective materials and nature of scatter,” *Int. J. Fatigue*, vol. 146, p. 106138, May 2021.

[162] H. O. Fuchs, R. I. Stephens, and H. Saunders, “Metal Fatigue in Engineering (1980),” *J. Eng. Mater. Technol.*, vol. 103, no. 4, pp. 346–346, 1981.

[163] R. REED, J. SMITH, and B. CHRIST, “The economic effects of fracture in the United States,” *Natl. Bur. Stand. Spec. Publ.*, no. 647, pp. 1–7, 1983.

[164] J. A. Ewing and J. C. W. Humfrey, “The Fracture of Metals under Repeated Alternations of Stress,” *Philos. Trans. R. Soc. A Math. Phys. Eng. Sci.*, vol. 200, no. 321–330, pp. 241–250, Jan. 1903.

[165] N. Thompson, N. Wadsworth, and N. Louat, “Origin of fatigue fracture in copper,” *Philos. Mag.*, vol. 1, pp. 113–126, 1956.

[166] O. Helgeland, “Cyclic hardening and fatigue of copper single crystals,” *J. Inst. Met.*, vol. 93, pp. 570–5, 1965.

[167] P. J. E. Forsyth, “A two-stage process of fatigue crack growth,” in *Proc. Crack Propagation Symposium. Vol. 1*, London: HMSO, 1962, pp. 76–94.

[168] H. I. Kaplan and C. Laird, “On the mechanism of stage I crack propagation in fatigue,” *Trans. Met. Soc. AIME*, vol. 239, pp. 1017–1025, 1967.

[169] P. Paris and F. Erdogan, “A critical analysis of crack propagation laws,” *J. Fluids Eng. Trans. ASME*, vol. 85, no. 4, pp. 528–533, Dec. 1963.

[170] A. Mesgarnejad, A. Imanian, and A. Karma, “Phase-field models for fatigue crack growth,” *Theor. Appl. Fract. Mech.*, vol. 103, p. 102282, Oct. 2019.

[171] G. P. Sendeckyj, “Constant life diagrams — a historical review,” *Int. J. Fatigue*, vol. 23, no. 4, pp. 347–353, Apr. 2001.

[172] R. J. Morrissey, D. L. McDowell, and T. Nicholas, “Frequency and stress ratio effects in high cycle fatigue of Ti-6Al-4V,” *Int. J. Fatigue*, vol. 21, no. 7, pp. 679–685, 1999.

[173] K. S. Chan, “A Microstructure-Based Fatigue-Crack-Initiation Model,” *Metall. Mater. Trans. A*, vol. 34A, 2003.

[174] C. C. Wojcik, K. S. Chan, and D. A. Koss, “Stage I fatigue crack propagation in a titanium alloy,” *Acta Metall.*, vol. 36, no. 5, pp. 1261–1270, 1988.

[175] T. Connolley, P. E. Mchugh, and M. Bruzzi, “A review of deformation and fatigue of metals at small size scales,” *Fatigue Fract. Eng. Mater. Struct.*, vol. 28, no. 12, pp. 1119–1152, Dec. 2005.

[176] R. K. Nalla, B. L. Boyce, J. P. Campbell, J. O. Peters, and R. O. Ritchie, “Influence of microstructure on high-cycle fatigue of Ti-6Al-4V: Bimodal vs. lamellar structures,” in *Metallurgical and Materials Transactions A: Physical Metallurgy and Materials Science*, 2002, vol. 33, no. 3, pp. 899–918.

[177] E. Castillo and A. Fernández-Canteli, “A unified statistical methodology for modeling fatigue damage,” *A Unified Stat. Methodol. Model. Fatigue Damage*, pp. 1–232, 2009.

[178] M. C. Baietto, E. Pierres, A. Gravouil, B. Berthel, S. Fouvry, and B. Trolle, “Fretting fatigue crack growth simulation based on a combined experimental and XFEM strategy,” *Int. J. Fatigue*, vol. 47, pp. 31–43, 2013.

[179] S. Hémery, P. Villechaise, and D. Banerjee, “Microplasticity at Room Temperature in α/β Titanium Alloys,” *Metall. Mater. Trans. A Phys. Metall. Mater. Sci.*, vol. 51, no. 10, pp. 4931–4969, Oct. 2020.

[180] S. M. Beden, S. Abdullah, A. K. Ariffin, S. M. Beden, S. Abdullah, and A. K. Ariffin, “Review of Fatigue Crack Propagation Models for Metallic Components,” *Eur. J. Sci. Res.*, vol. 28, no. 3, pp. 364–397, 2009.

[181] A. Carpinteri, A. Spagnoli, and S. Vantadori, “Reformulation in the frequency domain of a critical plane-based multiaxial fatigue criterion,” *Int. J. Fatigue*, vol. 67, pp. 55–61, Oct. 2014.

[182] M. Dehghani, R. Tremblay, and M. Leclerc, “Fatigue failure of 350WT steel under large-strain seismic loading at room and subfreezing temperatures,” *Constr. Build. Mater.*, vol. 145, pp. 602–618, Aug. 2017.

[183] M. R. Bache, W. J. Evans, and W. Voice, “The resistance to impact damage and subsequent fatigue response of two titanium alloys,” *Mater. Sci. Eng. A*, vol. 333, no. 1–2, pp. 287–294, Aug. 2002.

[184] S. Stanzl-Tschegg, “Very high cycle fatigue measuring techniques,” *Int. J. Fatigue*, vol. 60, no. March, pp. 2–17, 2014.

[185] M. Papakyriacou, H. Mayer, C. Pypen, H. Plenk, and S. Stanzl-Tschegg, “Influence of loading

frequency on high cycle fatique properties of b.c.c and h.c.p. metals," *Mater. Sci. Eng. A*, vol. 308, no. 1–2, pp. 143–152, Jun. 2001.

[186] V. Hakim and A. Karma, "Laws of crack motion and phase-field models of fracture," *J. Mech. Phys. Solids*, vol. 57, no. 2, pp. 342–368, Feb. 2009.

[187] R. O. Ritchie, "Incomplete self-similarity and fatigue-crack growth," *Int. J. Fract. 2005 1323*, vol. 132, no. 3, pp. 197–203, Apr. 2005.

[188] H. Henry and H. Levine, "Dynamic instabilities of fracture under biaxial strain using a phase field model," *Phys. Rev. Lett.*, vol. 93, no. 10, p. 105504, Sep. 2004.

[189] D. L. McDowell, "Basic issues in the mechanics of high cycle metal fatigue," *Int. J. Fract.*, vol. 80, no. 2, pp. 103–145, Apr. 1989.

[190] C. P. Przybyla and D. L. McDowell, "Simulated microstructure-sensitive extreme value probabilities for high cycle fatigue of duplex Ti-6Al-4V," in *International Journal of Plasticity*, 2011, vol. 27, no. 12, pp. 1871–1895.

[191] F. Bridier, P. Villechaise, and J. Mendez, "Analysis of the different slip systems activated by tension in a α/β titanium alloy in relation with local crystallographic orientation," *Acta Mater.*, vol. 53, no. 3, pp. 555–567, Feb. 2005.

[192] N. E. Paton, R. G. Baggerly, and J. C. Williams, "Deformation and solid solution strengthening of titanium-aluminum single crystals," *Rockwell Rep. SC 526.7FR*, p. 24, 1976.

[193] A. P. Jirandehi and M. M. Khonsari, "General quantification of fatigue damage with provision for microstructure: A review," *Fatigue Fract. Eng. Mater. Struct.*, vol. 44, no. 8, pp. 1973–1999, Aug. 2021.

[194] A. Muth, R. John, A. Pilchak, S. R. Kalidindi, and D. L. McDowell, "Analysis of Fatigue Indicator Parameters for Ti-6Al-4V microstructures using extreme value statistics in the transition fatigue regime," *Int. J. Fatigue*, vol. 153, p. 106441, Dec. 2021.

[195] J. Isaac, "Rigid-Flex Technology: Mainstream Use but More Complex Designs," 2007.

[196] F. P. E. E. Dunne, A. Walker, and D. Rugg, "A systematic study of hcp crystal orientation and morphology effects in polycrystal deformation and fatigue," *Proc. R. Soc. A Math. Phys. Eng. Sci.*, vol. 463, no. 2082, pp. 1467–1489, Jun. 2007.

[197] Z. Zheng, D. S. Balint, and F. P. E. Dunne, "Investigation of slip transfer across HCP grain boundaries with application to cold dwell facet fatigue," *Acta Mater.*, vol. 127, pp. 43–53, Apr. 2017.

[198] W. Zhang, Y. Gao, Y. Xia, and H. Bei, "Indentation Schmid factor and incipient plasticity by nanoindentation pop-in tests in hexagonal close-packed single crystals," *Acta Mater.*, vol. 134, pp. 53–65, Aug. 2017.

[199] D. Lunt, J. Q. da Fonseca, D. Rugg, and M. Preuss, "Microscopic strain localisation in Ti-6Al-4V during uniaxial tensile loading," *Mater. Sci. Eng. A*, vol. 680, pp. 444–453, 2017.

[200] A. Carpinteri and M. Paggi, "A unified interpretation of the power laws in fatigue and the analytical correlations between cyclic properties of engineering materials," *Int. J. Fatigue*, vol. 31, no. 10, pp. 1524–1531, Oct. 2009.

[201] A. Fernández-Canteli, C. Przybilla, M. Nogal, M. L. Aenlle, and E. Castillo, "ProFatigue: A Software Program for Probabilistic Assessment of Experimental Fatigue Data Sets,"

*Procedia Eng.*, vol. 74, pp. 236–241, Jan. 2014.

[202] Y. Wang, R. Serra, and E. P. Argoul, "Adapted Locati method used for accelerated fatigue test under random vibrations," *Procedia Struct. Integr.*, vol. 19, pp. 674–681, Jan. 2019.

[203] O. P. Yadav, V. Rathod, A. Rathore, and R. Jain, "Probabilistic modeling of fatigue damage accumulation for reliability prediction," *Int. J. Qual. Stat. Reliab.*, vol. 2011, 2011.

[204] K. Hectors and W. De Waele, "Cumulative Damage and Life Prediction Models for High-Cycle Fatigue of Metals: A Review," *Met. 2021, Vol. 11, Page 204*, vol. 11, no. 2, p. 204, Jan. 2021.

[205] P. Zioupos and A. Casinos, "Cumulative damage and the response of human bone in two-step loading fatigue," *J. Biomech.*, vol. 31, no. 9, pp. 825–833, Sep. 1998.

[206] F. P. E. Dunne and D. Rugg, "On the mechanisms of fatigue facet nucleation in titanium alloys," *Fatigue Fract. Eng. Mater. Struct.*, vol. 31, no. 11, pp. 949–958, Nov. 2008.

[207] W. J. Evans and M. R. Bache, "Dwell-sensitive fatigue under biaxial loads in the near-alpha titanium alloy IMI685," *Int. J. Fatigue*, vol. 16, no. 7, pp. 443–452, Jan. 1994.

[208] V. Sinha, J. E. Spowart, M. J. Mills, and J. C. Williams, "Observations on the faceted initiation site in the dwell-fatigue tested Ti-6242 alloy: Crystallographic orientation and size effects," *Metall. Mater. Trans. A Phys. Metall. Mater. Sci.*, vol. 37, no. 5, pp. 1507–1518, 2006.

[209] K. S. Chan, "Roles of microstructure in fatigue crack initiation," *Int. J. Fatigue*, vol. 32, no. 9, pp. 1428–1447, 2010.

[210] S. Mounsey *et al.*, "Study of Low Cycle Fatigue in Heat-Treated Al- Mg Alloys," *Int. J. Fatigue*, vol. 23, no. 1, pp. 447–468, 2016.

[211] M. R. R. Bache, W. J. J. Evans, B. Suddell, and F. R. M. R. M. Herrouin, "The effects of texture in titanium alloys for engineering components under fatigue," vol. 23, Jan. 2001.

[212] E. E. Sackett, L. Germain, and M. R. Bache, "Crystal plasticity, fatigue crack initiation and fatigue performance of advanced titanium alloys," *Int. J. Fatigue*, vol. 29, no. 9–11, pp. 2015–2021, Sep. 2007.

[213] H. Abdolvand, J. Wright, and A. J. Wilkinson, "Strong grain neighbour effects in polycrystals," *Nat. Commun.*, vol. 9, no. 1, 2018.

[214] S. Hémery, A. Nait-Ali, M. Guéguen, and P. Villechaise, "Mechanical study of crystalline orientation distribution in Ti-6Al-4V: An assessment of micro-texture induced load partitioning," *Mater. Des.*, vol. 137, pp. 22–32, Jan. 2018.

[215] M. S. Duval-Chaneac *et al.*, "Fatigue crack growth in IN718/316L multi-materials layered structures fabricated by laser powder bed fusion," *Int. J. Fatigue*, vol. 152, p. 106454, Nov. 2021.

[216] S. Rajan, P. Wanjara, J. Gholipour, and A. S. Kabir, "Microstructure, Tensile Properties, and Fatigue Behavior of Linear Friction-Welded Ti-6Al-2Sn-4Zr-2Mo-0.1Si," *Materials (Basel).*, vol. 14, no. 1, p. 30, Dec. 2020.

[217] J. M. García and T. F. Morgeneyer, "Strength and fatigue strength of a similar Ti-6Al-2Sn-4Zr-2Mo-0.1Si linear friction welded joint," *Fatigue Fract. Eng. Mater. Struct.*, vol. 42, no. 5, pp. 1100–1117, May 2019.

[218] S. Romano, A. Brückner-Foit, A. Brandão, J. Gumpinger, T. Ghidini, and S. Beretta, “Fatigue properties of AlSi10Mg obtained by additive manufacturing: Defect-based modelling and prediction of fatigue strength,” *Eng. Fract. Mech.*, vol. 187, pp. 165–189, Jan. 2018.

[219] T. Ghidini and C. D. Donne, “Fatigue life predictions using fracture mechanics methods,” *Engng Fract. Mech.*, vol. 76, pp. 134–148, 2009.

[220] S. Beretta and S. Romano, “A comparison of fatigue strength sensitivity to defects for materials manufactured by AM or traditional processes,” *Int. J. Fatigue*, vol. 94, pp. 178–191, Jan. 2017.

[221] P. Edwards and M. Ramulu, “Fatigue performance evaluation of selective laser melted Ti-6Al-4V,” *Mater. Sci. Eng. A*, vol. 598, pp. 327–337, 2014.

[222] P. Li, D. H. Warner, A. Fatemi, and N. Phan, “Critical assessment of the fatigue performance of additively manufactured Ti-6Al-4V and perspective for future research,” *Int. J. Fatigue*, vol. 85, pp. 130–143, Apr. 2016.

[223] H. Gong, K. Rafi, H. Gu, G. D. Janaki Ram, T. Starr, and B. Stucker, “Influence of defects on mechanical properties of Ti-6Al-4V components produced by selective laser melting and electron beam melting,” *Mater. Des.*, vol. 86, pp. 545–554, Dec. 2015.

[224] K. Solberg, “Fatigue design for metallic components produced by additive,” 2021.

[225] S. Liu and Y. C. Shin, “Additive manufacturing of Ti6Al4V alloy: A review,” *Mater. Des.*, vol. 164, p. 107552, Feb. 2019.

[226] T. M. Mower and M. J. Long, “Mechanical behavior of additive manufactured, powder-bed laser-fused materials,” *Mater. Sci. Eng. A*, vol. 651, pp. 198–213, 2016.

[227] J. Günther *et al.*, “Fatigue life of additively manufactured Ti–6Al–4V in the very high cycle fatigue regime,” *Int. J. Fatigue*, vol. 94, pp. 236–245, Jan. 2017.

[228] K. Solberg and F. Berto, “What is going on with fatigue of additively manufactured metals?,” *Mater. Des. Process. Commun.*, vol. 1, no. 5, p. e84, Oct. 2019.

[229] D. T. S. Lewis, R. J. Lancaster, S. P. Jeffs, H. W. Illsley, S. J. Davies, and G. J. Baxter, “Characterising the fatigue performance of additive materials using the small punch test,” *Mater. Sci. Eng. A*, vol. 754, pp. 719–727, Apr. 2019.

[230] J. W. Gao *et al.*, “Fatigue and damage tolerance assessment of induction hardened S38C axles under different foreign objects,” *Int. J. Fatigue*, vol. 149, p. 106276, Aug. 2021.

[231] S. Luo, X. Nie, L. Zhou, Y. Li, and W. He, “High Cycle Fatigue Performance in Laser Shock Peened TC4 Titanium Alloys Subjected to Foreign Object Damage,” *J. Mater. Eng. Perform. 2018 273*, vol. 27, no. 3, pp. 1466–1474, Jan. 2018.

[232] Z. Zhao, L. Wang, C. Liu, L. Liu, and W. Chen, “Prediction of High-Cycle Fatigue Performance of 1Cr11Ni2W2MoV Stainless Steel Plate after Foreign Object Damage,” *Int. J. Aerosp. Eng.*, vol. 2020, 2020.

[233] S. Leuders *et al.*, “On the mechanical behaviour of titanium alloy TiAl6V4 manufactured by selective laser melting: Fatigue resistance and crack growth performance,” *Int. J. Fatigue*, vol. 48, pp. 300–307, Mar. 2013.

[234] M. Simonelli, Y. Y. Tse, and C. Tuck, “Effect of the build orientation on the mechanical properties and fracture modes of SLM Ti-6Al-4V,” *Mater. Sci. Eng. A*, vol. 616, pp. 1–11, 2014.

[235] M. Simonelli, Y. Y. Tse, and C. Tuck, “Further undestanding of ti-6al-4v selective laser melting using texture analysis,” in *23rd Annual International Solid Freeform Fabrication Symposium - An Additive Manufacturing Conference, SFF 2012*, 2012, pp. 480–491.

[236] K. S. Ravichandran, “Near threshold fatigue crack growth behavior of a titanium alloy: Ti-6A1-4V,” *Acta Metall. Mater.*, vol. 39, no. 3, pp. 401–410, Mar. 1991.

[237] Y. Liu and F. P. E. Dunne, “The mechanistic link between macrozones and dwell fatigue in titanium alloys,” *Int. J. Fatigue*, vol. 142, p. 105971, Jan. 2021.

[238] K. U. Yazar, M. Shamitha, and S. Suwas, “Texture-dependent dwell fatigue response of titanium,” *https://doi.org/10.1080/14786435.2021.1916116*, vol. 101, no. 12, pp. 1443–1470, 2021.

[239] I. Bantounas, T. C. Lindley, D. Rugg, and D. Dye, “Effect of microtexture on fatigue cracking in Ti-6Al-4V,” *Acta Mater.*, vol. 55, no. 16, pp. 5655–5665, 2007.

[240] D. P. Satko *et al.*, “Effect of microstructure on oxygen rich layer evolution and its impact on fatigue life during high-temperature application of α/β titanium,” *Acta Mater.*, vol. 107, pp. 377–389, Apr. 2016.

[241] T. Chapman, “The effect of environment on fatigue mechanisms in aerospace titanium alloys,” Imperial College London, London, 2015.

[242] E. C. Reed and J. A. Viens, “The influence of surface residual stress on fatigue limit of titanium,” *J. Manuf. Sci. Eng. Trans. ASME*, vol. 82, no. 1, pp. 76–78, 1960.

[243] K. Yang *et al.*, “Enhanced extra-long life fatigue resistance of a bimodal titanium alloy by laser shock peening,” *Int. J. Fatigue*, vol. 141, p. 105868, Dec. 2020.

[244] S. Pasta and A. P. Reynolds, “Residual stress effects on fatigue crack growth in a Ti-6Al-4V friction stir weld,” *Fatigue Fract. Eng. Mater. Struct.*, vol. 31, no. 7, pp. 569–580, Jul. 2008.

[245] C. You *et al.*, “The effects of surface pits and intermetallics on the competing failure modes in laser shock peened AA7075-T651: Experiments and modelling,” *Int. J. Fatigue*, vol. 155, p. 106568, Feb. 2022.

[246] A. G. Sanchez *et al.*, “Effects of laser shock peening on the mechanisms of fatigue short crack initiation and propagation of AA7075-T651,” *Int. J. Fatigue*, vol. 143, p. 106025, Feb. 2021.

[247] E. Maawad, Y. Sano, L. Wagner, H. G. Brokmeier, and C. Genzel, “Investigation of laser shock peening effects on residual stress state and fatigue performance of titanium alloys,” *Mater. Sci. Eng. A*, vol. 536, pp. 82–91, 2012.

[248] X. Pan *et al.*, “Fatigue performance improvement of laser shock peened hole on powder metallurgy Ni-based superalloy labyrinth disc,” *Surf. Coatings Technol.*, vol. 409, p. 126829, Mar. 2021.

[249] S. Luo, W. He, K. Chen, X. Nie, L. Zhou, and Y. Li, “Regain the fatigue strength of laser additive manufactured Ti alloy via laser shock peening,” *J. Alloys Compd.*, vol. 750, pp. 626–635, Jun. 2018.

[250] M. R. Bache and W. J. Evans, “Impact of texture on mechanical properties in an advanced titanium alloy,” *Mater. Sci. Eng. A*, vol. 319–321, pp. 409–414, Dec. 2001.

[251] K. Le Biavant, S. Pommier, and C. Prioul, “Local texture and fatigue crack initiation in a Ti-6Al-4V titanium alloy,” *Fatigue Fract. Eng. Mater. Struct.*, vol. 25, no. 6, pp. 527–545, Jun.

2002.

[252] F. Bridier, P. Villechaise, and J. Mendez, “Slip and fatigue crack formation processes in an α/β titanium alloy in relation to crystallographic texture on different scales,” *Acta Mater.*, vol. 56, no. 15, pp. 3951–3962, Sep. 2008.

[253] H. Kuroki *et al.*, “Fatigue Characteristic of Linear Friction Welded Ti-6Al-4V Joints,” *Lect. Notes Mech. Eng.*, pp. 3–15, Jun. 2019.

[254] Z. Liu, Y. Wang, S. Ji, and D. Yan, “Fatigue Properties of Ti-6Al-4V Titanium Alloy Friction Stir Welding Joint,” *J. Mater. Eng. Perform.*, vol. 27, no. 8, pp. 4308–4316, Aug. 2018.

[255] J.-M. Garcia, “Mechanical characterization of Linear Friction Welded Titanium alloys,” Université Paris sciences et lettres, 2019.

[256] A. M. M. García, “BLISK Fabrication by Linear Friction Welding,” in *Advances in Gas Turbine Technology*, 2011, pp. 411–435.

[257] I. Bhamji, A. C. Addison, P. L. Threadgill, and M. Preuss, “Linear friction welding in aerospace engineering,” *Weld. Join. Aerosp. Mater.*, pp. 95–122, Jan. 2012.

[258] A. Mateo *et al.*, “Materials Science and Technology Welding repair by linear friction in titanium alloys Welding repair by linear friction in titanium alloys,” 2013.

[259] C. He, Y. Liu, J. Dong, Q. Wang, D. Wagner, and C. Bathias, “Fatigue crack initiation behaviors throughout friction stir welded joints in AA7075-T6 in ultrasonic fatigue,” *Int. J. Fatigue*, vol. 81, pp. 171–178, Dec. 2015.

[260] G. M. Castelluccio, W. D. Musinski, and D. L. McDowell, “Computational micromechanics of fatigue of microstructures in the HCF–VHCF regimes,” *Int. J. Fatigue*, vol. 93, pp. 387–396, 2016.

[261] S. Lavenstein and J. A. El-Awady, “Micro-scale fatigue mechanisms in metals: Insights gained from small-scale experiments and discrete dislocation dynamics simulations,” *Curr. Opin. Solid State Mater. Sci.*, vol. 23, no. 5, p. 100765, Oct. 2019.

[262] M. A. Haque and M. T. A. Saif, “A review of MEMS-based miroscale and nanoscale tensile and bending testing,” *Exp. Mech.*, vol. 43, no. 3, pp. 248–255, 2003.

[263] S. Fu, L. Wang, G. Chen, D. Yu, and X. Chen, “A tension-torsional fatigue testing apparatus for micro-scale components,” *Rev. Sci. Instrum.*, vol. 87, no. 1, p. 015111, Jan. 2016.

[264] K. J. Hemker and W. N. Sharpe, “Microscale characterization of mechanical properties,” *Annual Review of Materials Research*, vol. 37. pp. 92–126, 2007.

[265] Y. Murakami and S. Beretta, “Small Defects and Inhomogeneities in Fatigue Strength: Experiments , Models and Statistical Implications,” *Extremes*, vol. 2, no. 2, pp. 123–147, 1999.

[266] W. D. Nix and H. Gao, “Indentation size effects in crystalline materials: A law for strain gradient plasticity,” *J. Mech. Phys. Solids*, vol. 46, no. 3, pp. 411–425, Mar. 1998.

[267] J. Ast, M. Ghidelli, K. Durst, M. Göken, M. Sebastiani, and A. M. Korsunsky, “A review of experimental approaches to fracture toughness evaluation at the micro-scale,” *Mater. Des.*, vol. 173, p. 107762, Jul. 2019.

[268] B. N. Jaya and M. Z. Alam, “Small-scale mechanical testing of materials,” *Curr. Sci.*, vol. 105, no. 8, pp. 1073–1099, 2013.

[269] C. P. Frick, B. G. Clark, S. Orso, A. S. Schneider, and E. Arzt, “Size effect on strength and strain hardening of small-scale [1 1 1] nickel compression pillars,” *Mater. Sci. Eng. A*, vol. 489, no. 1–2, pp. 319–329, Aug. 2008.

[270] S. E. Stanzl-Tschegg, “Fracture mechanisms and fracture mechanics at ultrasonic frequencies,” *Fatigue Fract. Eng. Mater. Struct.*, vol. 22, no. 7, pp. 567–579, Jul. 1999.

[271] R. Mitsche, S. Stanzl, and D. Burkert, “Hochfrequenzkinematographie in der Metallforschung,” *Wissenschaftlicher Film*, vol. 14, no. 3, p. 10, 1973.

[272] I. Marines *et al.*, “Ultrasonic fatigue tests on bearing steel AISI-SAE 52100 at frequency of 20 and 30 kHz,” in *International Journal of Fatigue*, 2003, vol. 25, no. 9–11, pp. 1037–1046.

[273] C. Bathias, “Gigacycle fatigue of bearing steels,” *Mater. Sci. Technol.*, vol. 28, pp. 27–33, 2012.

[274] Z. Huang, D. Wagner, C. Bathias, and P. C. Paris, “Subsurface crack initiation and propagation mechanisms in gigacycle fatigue,” *Acta mater.*, vol. 58, pp. 6046–6054, 2010.

[275] I. Marines-Garcia, D. Galvan-Montiel, and C. Bathias, “Fatigue life assessment of high-strength, low-alloy steel at high frequency,” *Arab. J. Sci. Engng*, vol. 33, pp. 237–247, 2008.

[276] H. Tao and C. Bathias, “Etude expérimentale du fretting-fatigue à très haute fréquence,” *Rev. Métall.*, vol. 93, pp. 687–695, 1996.

[277] Q. Wang, M. K. Khan, and C. Bathias, “Current understanding of ultra-high cycle fatigue,” *Theor. Appl. Mech. Letts*, vol. 2, p. 31002, 2012.

[278] Q. Y. Wang, J. Y. Berard, A. Dubarre, G. Baudry, S. Rathery, and C. Bathias, “Gigacycle fatigue of ferrous alloys,” *Fatigue <html_ent glyph="@amp;" ascii="&"/> Fract. Eng. Mater. Struct.*, vol. 22, no. 8, pp. 667–672, Aug. 1999.

[279] C. Bathias and P. C. Paris, *Gigacycle Fatigue in Mechanical Practice*. Marcel Dekker, 2004.

[280] C. Bathias, “There is no infinite fatigue life in metallic materials,” *Fatigue Fract. Eng. Mater. Struct.*, vol. 22, no. 7, pp. 559–565, Jul. 1999.

[281] H. Mayer, *Recent developments in ultrasonic fatigue*, vol. 39, no. 1. John Wiley & Sons, Ltd, 2016, pp. 3–29.

[282] B. Pyttel, D. Schwerdt, and C. Berger, “Very high cycle fatigue - Is there a fatigue limit?,” *Int. J. Fatigue*, vol. 33, no. 1, pp. 49–58, 2011.

[283] J. H. Zuo, Z. G. Wang, and E. H. Han, “Effect of microstructure on ultra-high cycle fatigue behavior of Ti-6Al-4V,” *Mater. Sci. Eng. A*, vol. 473, no. 1–2, pp. 147–152, 2008.

[284] R. J. Morrissey and T. Nicholas, “Fatigue strength of Ti–6Al–4V at very long lives,” *Int. J. Fatigue*, vol. 27, no. 10–12, pp. 1608–1612, Oct. 2005.

[285] M. Janeček *et al.*, “The very high cycle fatigue behaviour of Ti-6Al-4V alloy,” in *Acta Physica Polonica A*, 2015, vol. 128, no. 4, pp. 497–502.

[286] J. Petit, C. Sarrazin-Baudoux, J. Martinez, S. Stanzl-Tschegg, and H. Mayer, “Very High Cycle Fatigue behavior of a Ti6246 alloy in air and in high vacuum,” in *VHCF-4 - 4th International Conference on Very High Cycle Fatigue*, 2007, pp. 399–408.

[287] E. TAKEUCHI, Y. FURUYA, N. NAGASHIMA, and S. MATSUOKA, “The effect of frequency on the giga-cycle fatigue properties of a Ti–6Al–4V alloy,” *Fatigue Fract. Eng. Mater. Struct.*, vol. 31, no. 7, pp. 599–605, Jul. 2008.

[288] J. Kohout and S. Věchet, “New function for fatigue curves characterization and its multiple merits,” *Int. J. Fatigue*, vol. 23, no. 2, pp. 175–183, Jan. 2001.

[289] J. F. Barbosa *et al.*, “A comparison between S-N Logistic and Kohout-Věchet formulations applied to the fatigue data of old metallic bridges materials https://orcid.org/0000-0003-3553-6107,” vol. 48, pp. 400–410, 2019.

[290] H. S. Kim and S. Huang, “S-n curve characterisation for composite materials and prediction of remaining fatigue life using damage function,” *J. Compos. Sci.*, vol. 5, no. 3, p. 76, Mar. 2021.

[291] H. S. Kim and J. Zhang, “Fatigue Damage and Life Prediction of Glass/Vinyl Ester Composites,” *J. Reinf. Plast. Compos.*, vol. 20, no. 10, pp. 834–848, Sep. 2001.

[292] Q. Guo, X. Guo, J. Fan, R. Syed, and C. Wu, “An energy method for rapid evaluation of high-cycle fatigue parameters based on intrinsic dissipation,” *Int. J. Fatigue*, vol. 80, pp. 136–144, Nov. 2015.

[293] A. Nourian-Avval and M. M. Khonsari, “Rapid prediction of fatigue life based on thermodynamic entropy generation,” *Int. J. Fatigue*, vol. 145, p. 106105, Apr. 2021.

[294] Y. X. Zhao and H. B. Liu, “Weibull modeling of the probabilistic S–N curves for rolling contact fatigue,” *Int. J. Fatigue*, vol. 66, pp. 47–54, Sep. 2014.

[295] P. Strzelecki and T. Tomaszewski, “Application of Weibull distribution to describe S-N curve with using small number specimens,” *AIP Conf. Proc.*, vol. 1780, no. 1, p. 020007, Oct. 2016.

[296] M. Kamal and M. M. Rahman, “Advances in fatigue life modeling: A review,” *Renew. Sustain. Energy Rev.*, vol. 82, pp. 940–949, Feb. 2018.

[297] C. Li, S. Wu, J. Zhang, L. Xie, and Y. Zhang, “Determination of the fatigue P-S-N curves – A critical review and improved backward statistical inference method,” *Int. J. Fatigue*, vol. 139, no. June, p. 105789, 2020.

[298] L. Xie, J. Liu, N. Wu, and W. Qian, “Backwards statistical inference method for P–S–N curve fitting with small-sample experiment data,” *Int. J. Fatigue*, vol. 63, pp. 62–67, Jun. 2014.

[299] J. Gao, Z. An, and B. Liu, “A new method for obtaining P-S-N curves under the condition of small sample,” *Proc. Inst. Mech. Eng. Part O J. Risk Reliab.*, vol. 231, no. 2, pp. 130–137, Apr. 2017.

[300] S. Shimizu, K. Tosha, and K. Tsuchiya, “New data analysis of probabilistic stress-life (P-S-N) curve and its application for structural materials,” *Int. J. Fatigue*, vol. 32, no. 3, pp. 565–575, Mar. 2010.

[301] P. Strzelecki, “Accuracy of determined S-N curve for constructional steel by selected models,” *Fatigue Fract. Eng. Mater. Struct.*, vol. 43, no. 3, pp. 550–557, 2020.

[302] J. Schijve, *Fatigue of structures and materials*. Dordrecht: Springer Netherlands, 2009.

[303] A. Fernández-Canteli, S. Blasón, B. Pyttel, M. Muniz-Calvente, and E. Castillo, *Considerations about the existence or non-existence of the fatigue limit: implications on practical design*, vol. 223. Springer, 2020, pp. 189–196.

[304] D. L. DuQuesnay and P. R. Underhill, “Fatigue life scatter in 7xxx series aluminum alloys,” *Int. J. Fatigue*, vol. 32, no. 2, pp. 398–402, Feb. 2010.

[305] T. Nicholas, “Step loading for very high cycle fatigue,” *Fatigue Fract. Eng. Mater. Struct.*, vol. 25, no. 8–9, pp. 861–869, Sep. 2002.

[306] W. J. Dixon and A. M. Mood, “A Method for Obtaining and Analyzing Sensitivity Data,” *J. Am. Stat. Assoc.*, vol. 43, no. 241, pp. 109–126, 1948.

[307] ASTM, “A tentative guide for fatigue testing and the statistical anaylsis of fatigue data.,” 1958.

[308] F. G. Pascual and W. Q. Meeker, “Analysis of Fatigue Data with Runouts Based on a Model with Nonconstant Standard Deviation and a Fatigue Limit Parameter,” *J. Test. Eval.*, vol. 25, no. 3, pp. 292–301, 1997.

[309] ISO 12107, “Metallic materials — Fatigue testing — Statistical planning and analysis of data - ISO 12107,” *Test*, vol. 2006, p. 13, 2006.

[310] W. Nelson, “Accelerated Life Testing - Step-Stress Models and Data Analyses,” *IEEE Trans. Reliab.*, vol. R-29, no. 2, pp. 103–108, 1980.

[311] S. K. Lin, Y. L. Lee, and M. W. Lu, “Evaluation of the staircase and the accelerated test methods for fatigue limit distributions,” *Int. J. Fatigue*, vol. 23, no. 1, pp. 75–83, Jan. 2001.

[312] R. D. Pollak, “Analysis of Methods for Determining High Cycle Fatigue Strength of a Material with Investigation of Ti-6Al-4V Gigacycle Fatigue Behavior,” *Fac. Grad. Sch. Eng. Manag. Force Inst. Technol.*, p. 278, 2005.

[313] C. C. Engler-Pinto, J. V. Lasecki, R. J. Frisch, and J. E. Allison, “Statistical approaches applied to very high cycle fatigue,” in *VHCF-4 - 4th International Conference on Very High Cycle Fatigue*, 2007, pp. 369–376.

[314] C. C. Engler-Pinto Jr *et al.*, “Statistical approaches applied to fatigue test data analysis,” 2005.

[315] L. XI and Z. SONGLIN, “Changes in mechanical properties of vehicle components after strengthening under low-amplitude loads below the fatigue limit,” *Fatigue Fract. Eng. Mater. Struct.*, vol. 32, no. 10, pp. 847–855, Oct. 2009.

[316] K. Hectors and W. De Waele, “Cumulative damage and life prediction models for high-cycle fatigue of metals: A review,” *Metals*, vol. 11, no. 2. MDPI AG, pp. 1–32, 01-Feb-2021.

[317] A. Risitano and G. Risitano, “Cumulative damage evaluation of steel using infrared thermography,” *Theor. Appl. Fract. Mech.*, vol. 54, no. 2, pp. 82–90, Oct. 2010.

[318] B. A. Lerch, S. L. Draper, and J. M. Pereira, “Conducting high-cycle fatigue strength step tests on gamma TiAl,” *Metall. Mater. Trans. A Phys. Metall. Mater. Sci.*, vol. 33, no. 12, pp. 3871–3874, 2002.

[319] M. Bergant, T. Werner, M. Madia, A. Yawny, and U. Zerbst, “Short crack propagation analysis and fatigue strength assessment of additively manufactured materials: An application to AISI 316L,” *Int. J. Fatigue*, vol. 151, p. 106396, Oct. 2021.

[320] O. Andreau, E. Pessard, I. Koutiri, P. Peyre, and N. Saintier, “Influence of the position and size of various deterministic defects on the high cycle fatigue resistance of a 316L steel manufactured by laser powder bed fusion,” *Int. J. Fatigue*, vol. 143, p. 105930, Feb. 2021.

[321] O. Andreau *et al.*, “A competition between the contour and hatching zones on the high cycle fatigue behaviour of a 316L stainless steel: Analyzed using X-ray computed tomography,” *Mater. Sci. Eng. A*, vol. 757, pp. 146–159, May 2019.

[322] R. S. Bellows, S. Muju, and T. Nicholas, “Validation of the step test method for generating Haigh diagrams for Ti-6Al-4V,” *Int. J. Fatigue*, vol. 21, no. 7, pp. 687–697, Aug. 1999.

[323] Q. Song and C. Sun, “Mechanism of crack initiation and early growth of high strength steels in very high cycle fatigue regime,” *Mater. Sci. Eng. A*, vol. 771, p. 138648, Jan. 2020.

[324] M. Mehdizadeh and M. M. Khonsari, “On the application of fracture fatigue entropy to variable frequency and loading amplitude,” *Theor. Appl. Fract. Mech.*, vol. 98, pp. 30–37, Dec. 2018.

[325] C. Sun *et al.*, “The formation of discontinuous gradient regimes during crack initiation in high strength steels under very high cycle fatigue,” *Int. J. Fatigue*, vol. 124, pp. 483–492, Jul. 2019.

[326] R. Mackay and G. Byczynski, “An Evaluation of the Staircase and Over-Stress Probe Methods for Fatigue Life Characterization in Aluminum Sand Castings,” *Int. J. Met.*, pp. 1–18, Apr. 2021.

[327] M. Dallago, B. Winiarski, F. Zanini, S. Carmignato, and M. Benedetti, “On the effect of geometrical imperfections and defects on the fatigue strength of cellular lattice structures additively manufactured via Selective Laser Melting,” *Int. J. Fatigue*, vol. 124, pp. 348–360, Jul. 2019.

[328] J. W. Gao *et al.*, “Influence of artificial defects on fatigue strength of induction hardened S38C axles,” *Int. J. Fatigue*, vol. 139, p. 105746, Oct. 2020.

[329] C. Sun, Q. Song, L. Zhou, and X. Pan, “Characteristic of interior crack initiation and early growth for high cycle and very high cycle fatigue of a martensitic stainless steel,” *Mater. Sci. Eng. A*, vol. 758, pp. 112–120, Jun. 2019.

[330] Z. W. Xu, S. C. Wu, and X. S. Wang, “Fatigue evaluation for high-speed railway axles with surface scratch,” *Int. J. Fatigue*, vol. 123, pp. 79–86, Jun. 2019.

[331] D. C. D. Maxwell and T. Nicholas, “Rapid method for generation of a Haigh diagram for high cycle fatigue,” *ASTM Spec. Tech. Publ.*, no. 1332, pp. 626–641, 1999.

[332] F. Abroug, E. Pessard, G. Germain, and F. Morel, “HCF of AA7050 alloy containing surface defects: Study of the statistical size effect,” *Int. J. Fatigue*, vol. 110, pp. 81–94, May 2018.

[333] S. Baragetti, Božić, and E. V. Arcieri, “Stress and fracture surface analysis of uncoated and coated 7075-T6 specimens under the rotating bending fatigue loading,” *Eng. Fail. Anal.*, vol. 112, p. 104512, May 2020.

[334] X. Hu, X. Jia, Z. Bao, and Y. Song, “Effect of notch geometry on the fatigue strength and critical distance of TC4 titanium alloy †,” *J. Mech. Sci. Technol.*, vol. 31, no. 10, pp. 4727–4737, 2017.

[335] G. Edwards and L. A. Pacheco, “A Bayesian method for establishing fatigue design curves,” *Struct. Saf.*, vol. 2, no. 1, pp. 27–38, Jan. 1984.

[336] M. Guida and F. Penta, “A Bayesian analysis of fatigue data,” *Struct. Saf.*, vol. 32, no. 1, pp. 64–76, Jan. 2010.

[337] I. Babuška, Z. Sawlan, M. Scavino, B. Szabó, and R. Tempone, “Bayesian inference and model comparison for metallic fatigue data,” *Comput. Methods Appl. Mech. Eng.*, vol. 304, pp. 171–196, 2016.

[338] D. Leonetti, J. Maljaars, and H. H. (Bert. Snijder, “Fitting fatigue test data with a novel S-N

curve using frequentist and Bayesian inference," *Int. J. Fatigue*, vol. 105, pp. 128–143, Dec. 2017.

[339] X. W. Liu, D. G. Lu, and P. C. J. Hoogenboom, "Hierarchical Bayesian fatigue data analysis," *Int. J. Fatigue*, vol. 100, pp. 418–428, Jul. 2017.

[340] L. Smalakys and A. Melninkaitis, "Predicting lifetime of optical components with Bayesian inference," *Opt. Express*, vol. 29, no. 2, p. 903, Jan. 2021.

[341] B. T. Never, "A D-Optimality-Based Sensitivity Test," *Technometrics*, vol. 36, no. 1, pp. 61–70, 1994.

[342] F. G. Pascual, "Theory for optimal test plans for the random fatigue-limit model," *Technometrics*, 2003. [Online]. Available: https://www.jstor.org/stable/25047010?seq=1#metadata_info_tab_contents. [Accessed: 17-Sep-2021].

[343] A. Holst, "Optimal test planning for High Cycle Fatigue limit testing," *Ann. Oper. Res. 2010 2241*, vol. 224, no. 1, pp. 101–110, Nov. 2010.

[344] G. E. P. Box and G. C. Tiao, *Bayesian Inference in Statistical Analysis*. Hoboken, NJ, USA: John Wiley & Sons, Inc., 1992.

[345] Z. Wang and S. Jegelka, *Max-value Entropy Search for Efficient Bayesian Optimization*, vol. 7. 2017, pp. 5530–5543.

[346] D. S. Sivia and J. Skilling, "Data Analysis - A Bayesian Tutorial."

[347] A. R. Pearse *et al.*, "SSNdesign—An R package for pseudo-Bayesian optimal and adaptive sampling designs on stream networks," *PLoS One*, vol. 15, no. 9, p. e0238422, Sep. 2020.

[348] R. Marchant and F. Ramos, "Bayesian Optimisation for informative continuous path planning," in *Proceedings - IEEE International Conference on Robotics and Automation*, 2014, pp. 6136–6143.

[349] R. Fuentes *et al.*, "Autonomous ultrasonic inspection using Bayesian optimisation and robust outlier analysis," *Mech. Syst. Signal Process.*, vol. 145, p. 106897, Nov. 2020.

[350] D. V. Lindley, *Bayesian Statistics*. Society for Industrial and Applied Mathematics, 1972.

[351] D. V. Lindley, "The Choice of Variables in Multiple Regression," *J. R. Stat. Soc. Ser. B*, vol. 30, no. 1, pp. 31–53, Jan. 1968.

[352] D. V. Lindley, "On a Measure of the Information Provided by an Experiment," *Ann. Math. Stat.*, vol. 27, no. 4, pp. 986–1005, Dec. 1956.

[353] A. DasGupta, "Review of Optimal Bayes Designs (Technical Report #95-4)." 1995.

[354] K. Chaloner, I. Verdinelli, and I. V. K. Chaloner, "Bayesian experimental design: A review," *Stat. Sci.*, vol. 10, no. 3, pp. 273–304, 1995.

[355] E. G. Ryan, C. C. Drovandi, J. M. Mcgree, and A. N. Pettitt, "Fully Bayesian Optimal Experimental Design: A Review."

[356] E. G. Ryan, C. C. Drovandi, J. M. McGree, and A. N. Pettitt, "A Review of Modern Computational Algorithms for Bayesian Optimal Design," *Int. Stat. Rev.*, vol. 84, no. 1, pp. 128–154, Apr. 2016.

[357] A. Arutyunyan, "Microscale and ultrafast high cycle fatigue testing of titanium," University

of Oxford, 2019.

[358] ASM International, “ASM Volume 2 - Properties and Selection: Nonferrous Alloys and Special Purpose Materials,” in *ASM Handbook*, ASM International, 2020, p. 1101.

[359] N.-S. Peighambardoust and F. Nasirpouri, “Electropolishing behaviour of pure titanium in perchloric acid–methanol–ethylene glycol mixed solution,” *Trans. IMF*, vol. 92, no. 3, pp. 132–139, May 2014.

[360] F. Wood, *Principal Component Analysis*. 2009.

[361] I. T. Jollife and J. Cadima, “Principal component analysis: A review and recent developments,” *Philosophical Transactions of the Royal Society A: Mathematical, Physical and Engineering Sciences*, vol. 374, no. 2065. 2016.

[362] J. Shlens, “A tutorial on principal component analysis: derivation, discussion and singular value decomposition,” *Online Note httpwww snl salk edushlenspubnotespca pdf*, vol. 2, pp. 1–16, 2003.

[363] C. M. Magazzeni and R. Rose, “cmmagazz/BayesOptFatigue: Code for ‘Bayesian Optimised Collection Strategies for Fatigue Testing Constant Life Testing.’” [Online]. Available: https://github.com/cmmagazz/BayesOptFatigue. [Accessed: 17-Sep-2021].

[364] K. Wallin, “Statistical aspects of fatigue life and endurance limit,” *Fatigue Fract. Eng. Mater. Struct.*, vol. 33, no. 6, pp. 333–344, Feb. 2010.

[365] H. Li, D. Wen, Z. Lu, Y. Wang, and F. Deng, “Identifying the Probability Distribution of Fatigue Life Using the Maximum Entropy Principle,” *Entropy 2016, Vol. 18, Page 111*, vol. 18, no. 4, p. 111, Mar. 2016.

[366] Y. X. Zhao and B. Yang, “Probabilistic measurements of the fatigue limit data from a small sampling up-and-down test method,” *Int. J. Fatigue*, vol. 30, no. 12, pp. 2094–2103, Dec. 2008.

[367] C. R. A. Schneider and S. J. Maddox, “Commission XIII-WG1 BEST PRACTICE GUIDE ON STATISTICAL ANALYSIS OF FATIGUE DATA,” 2003.

[368] S. Chi-liu, “The Statistical analysis of fatigue data,” The University of Arizona, 1994.

[369] D. Grove and F. Campean, “A comparison of two methods of analysing staircase fatigue test data,” *Qual. Reliab. Eng. Int.*, vol. 24, no. 4, pp. 485–497, Jun. 2008.

[370] S.-K. Lin, Y.-L. Lee, and M.-W. Lu, “Evaluation of the staircase and the accelerated test methods for fatigue limit distributions,” *Int. J. Fatigue*, vol. 23, pp. 75–83, 2001.

[371] J. Zhang, D. B. Kececioglu, and I. S. of S. and A. Technologies, *New Approaches to Determine the Endurance Strength Distribution*. ISSAT, 1998.

[372] H. Choucair and B. Jawad, “Analyzing Field Failures of Engine Valve Springs in Presence of Non Metallic Inclusions by Applying Statistical and Fracture Mechanics Models,” *SAE Int. J. Mater. Manuf.*, vol. 2, no. 1, pp. 265–273, Apr. 2009.

[373] K. V. Anderson and S. R. Daniewicz, “Statistical analysis of the influence of defects on fatigue life using a Gumbel distribution,” *Int. J. Fatigue*, vol. 112, pp. 78–83, Jul. 2018.

[374] A. Hor, N. Saintier, C. Robert, T. Palin-Luc, and F. Morel, “Statistical assessment of multiaxial HCF criteria at the grain scale,” *Int. J. Fatigue*, vol. 67, pp. 151–158.

[375] A. Schönning, J. Neal, P. D. Eason, M. Tiryakioğlu, and Z. S. Logan, “On fatigue life

variability in bone cement," *https://doi.org/10.1080/02670836.2020.1821965*, vol. 36, no. 15, pp. 1695–1703, Oct. 2020.

[376] D. El Khoukhi *et al.*, "Experimental investigation of the size effect in high cycle fatigue: Role of the defect population in cast aluminium alloys," *Int. J. Fatigue*, vol. 129, p. 105222, Dec. 2019.

[377] J. Hoole, P. Sartor, J. Booker, J. Cooper, X. V. Gogouvitis, and R. K. Schmidt, "Systematic statistical characterisation of stress-life datasets using 3-Parameter distributions," *Int. J. Fatigue*, vol. 129, p. 105216, Dec. 2019.

[378] S. Chi-liu, "The Statistical analysis of fatigue data," 1994.

[379] W. Nelson, "Accelerated testing : statistical models, test plans and data analyses," p. 601, 2004.

[380] C. Han and K. Chaloner, "Bayesian Experimental Design for Nonlinear Mixed-Effects Models with Application to HIV Dynamics," vol. 60, no. 1, pp. 25–33, 2004.

[381] R. E. Kass and A. E. Raftery, "Bayes factors," *J. Am. Stat. Assoc.*, vol. 90, no. 430, pp. 773–795, 1995.

[382] H. P. Gänser, J. Maierhofer, and T. Christiner, "Statistical correction for reinserted runouts in fatigue testing," *Int. J. Fatigue*, vol. 80, pp. 76–80, Jun. 2015.

[383] D. B. Lanning, T. Nicholas, and G. K. Haritos, "Effect of plastic prestrain on high cycle fatigue of Ti-6Al-4V," *Mech. Mater.*, vol. 34, no. 2, pp. 127–134, Feb. 2002.

[384] G. Lutjering and A. Gysler, "Critical Review of Fatigue in Titanium ."

[385] M. Tiryakioğlu, "Relationship between defect size and fatigue life distributions in Al-7 Pct Si-Mg alloy castings," *Metall. Mater. Trans. A Phys. Metall. Mater. Sci.*, vol. 40, no. 7, pp. 1623–1630, Jul. 2009.

[386] A. Halfpenny, A. Chabod, P. Czapski, J. Aldred, K. Munson, and M. Bonato, "Probabilistic Fatigue and Reliability Simulation," *Procedia Struct. Integr.*, vol. 19, pp. 150–167, Jan. 2019.

[387] Q. G. Wang, D. Apelian, and D. A. Lados, "Fatigue behavior of A356/357 aluminum cast alloys. Part II - Effect of microstructural constituents," *J. Light Met.*, vol. 1, no. 1, pp. 85–97, Feb. 2001.

[388] J. Schijve, "Statistical distribution functions and fatigue of structures," *Int. J. Fatigue*, vol. 27, no. 9, pp. 1031–1039, Sep. 2005.

[389] W. Weibull, "Basic aspects of fatigue," *Colloq. Fatigue / Colloq. Fatigue / Kolloquium über Ermüdungsfestigkeit*, pp. 289–298, 1956.

[390] F. G. Pascual and W. Q. Meeker, "Estimating Fatigue Curves With the Random Fatigue-Limit Mode," *Technometrics*, vol. 41, pp. 277–302, 1999.

[391] *Fatigue and Scatter*. Springer Netherlands, 2008, pp. 373–394.

[392] M. L. Facchinetti, "Fatigue Tests for Automotive Design: Optimization of the Test Protocol and Improvement of the Fatigue Strength Parameters Estimation," in *Procedia Engineering*, 2015, vol. 133, pp. 21–30.

[393] Q. G. Wang, C. J. Davidson, J. R. Griffiths, and P. N. Crepeau, "Oxide Films, Pores and the Fatigue Lives of Cast Aluminum Alloys."

[394] D. Casellas, R. Pérez, and J. M. Prado, “Fatigue variability in Al–Si cast alloys,” *Mater. Sci. Eng. A*, vol. 398, no. 1–2, pp. 171–179, May 2005.

[395] C. Nyahumwa, N. R. Green, and J. Campbell, “Influence of Casting Technique and Hot Isostatic Pressing on the Fatigue of an Al-7Si-Mg Alloy.”

[396] N. D. Alexopoulos, “Fracture Related Mechanical Properties of Aircraft Cast Aluminum Alloy A357,” *Fract. Nano Eng. Mater. Struct. - Proc. 16th Eur. Conf. Fract.*, pp. 509–510, 2006.

[397] P. C. Gope, “Determination of sample size for estimation of fatigue life by using Weibull or log-normal distribution,” *Int. J. Fatigue*, vol. 21, no. 8, pp. 745–752, Sep. 1999.

[398] T. Svensson and J. De, “Random Features of the Fatigue Limit,” *Extremes*, vol. 2, no. 2, pp. 165–176, 1999.

[399] A. Wolfenden and N. Parida, “Reliability and Life Estimation from Component Fatigue Failures Below the Go-No-Go Fatigue Life Limit,” *J. Test. Eval.*, vol. 19, no. 6, p. 450, 1991.

[400] D. S. Paolino and M. P. Cavatorta, “On the application of the stochastic approach in predicting fatigue reliability using Miner’s damage rule,” *Fatigue Fract. Eng. Mater. Struct.*, vol. 37, no. 1, pp. 107–117, Jan. 2014.

[401] R. Dumonceaux and C. E. Antle, “Discrimination Between the Log-Normal and the Weibull Distributions .”

[402] ISE/101/5, “Metallic materials — Instrumented indentation test for hardness and materials parameters — Part 1: Test method,” *ISO*, vol. 3, no. 1, p. 27, 2002.

[403] Bathias and C. Bathias, “There is no infinite fatigue life in metallic materials,” *Fatigue Fract. Eng. Mater. Struct.*, vol. 22, no. 7, pp. 559–565, Jul. 1999.

# 5. Appendix

## 5.1. Metallographic Preparation

1) Mount the specimen in conductive Bakelite, if possible (geometry and process permitting).
2) Grind the specimen using SiC grinding papers at ca. 100 rpm by hand, beginning with 400 grit paper to ensure planarity.
3) Grind the specimen using progressively finer grit paper until 4000 grit. Occasionally rotating the specimen by 45-90 degrees can indicate when to change paper:
    a. Specimens are ground for the first pass for a few seconds, or until all visible scratches align with the direction of grinding.
    b. Rotating by 45-90 degrees, the specimens is ground for a few more seconds, or until all scratches align with this new direction.
    c. One more pass of the same step is repeated, and was found to be sufficient to prepare specimens.
    d. The specimen and grinding wheel are rinsed thoroughly with water before transitioning to a finer grit to ensure no contamination of abrasive material.
4) Colloidal silica with 5% by volume of Hydrogen Peroxide (70% solution) is used on the appropriate pad using a polishing machine with a motorised head.
    a. The motorised head is used to produce a rotating movement opposite in direction to the base plate. The base plate is rotated at 20 rpm in order to retain the abrasive solution, and the motorised rotates at 90 rpm. The centre of rotation of the motorised head is placed approximately halfway along the radius of the baseplate, so long as the sample remains within the area of the baseplate.
    b. It was found that best results are obtained when using a force of approximately 17 $Ncm^{-2}$ scaled by the area of the titanium sample.
    c. The sample is polished for 30 minutes to 1 hour, or until the microstructure can be clearly seen through a cross-polarised microscope.
5) Following this last step, the following process can avoid excessive residual colloidal silica particles on the surface:
    a. The sample is rapidly placed under a soft jet of running water
    b. Without allowing the sample to dry, it is sprayed gently with the following solvents:
        i. Acetone,
        ii. Ethanol,
        iii. and finally IPA.
    c. It is allowed to dry at an incline, followed by a further spray of IPA, and a final dry at an incline. Drying at an incline avoids any final residue from remaining on the area of interest.

## 5.2. Nanoindentation Mapping Supplementary Details

Tip calibration persistence is illustrated from the nanoindentation map performed on the fused silica reference material shown in Figure 115. The map, where each indent corresponds to one pixel, was constructed of 3x3 bundles, starting from the bottom-right of the image, and progressively moving up in a serpentine motion starting in the negative x-direction.

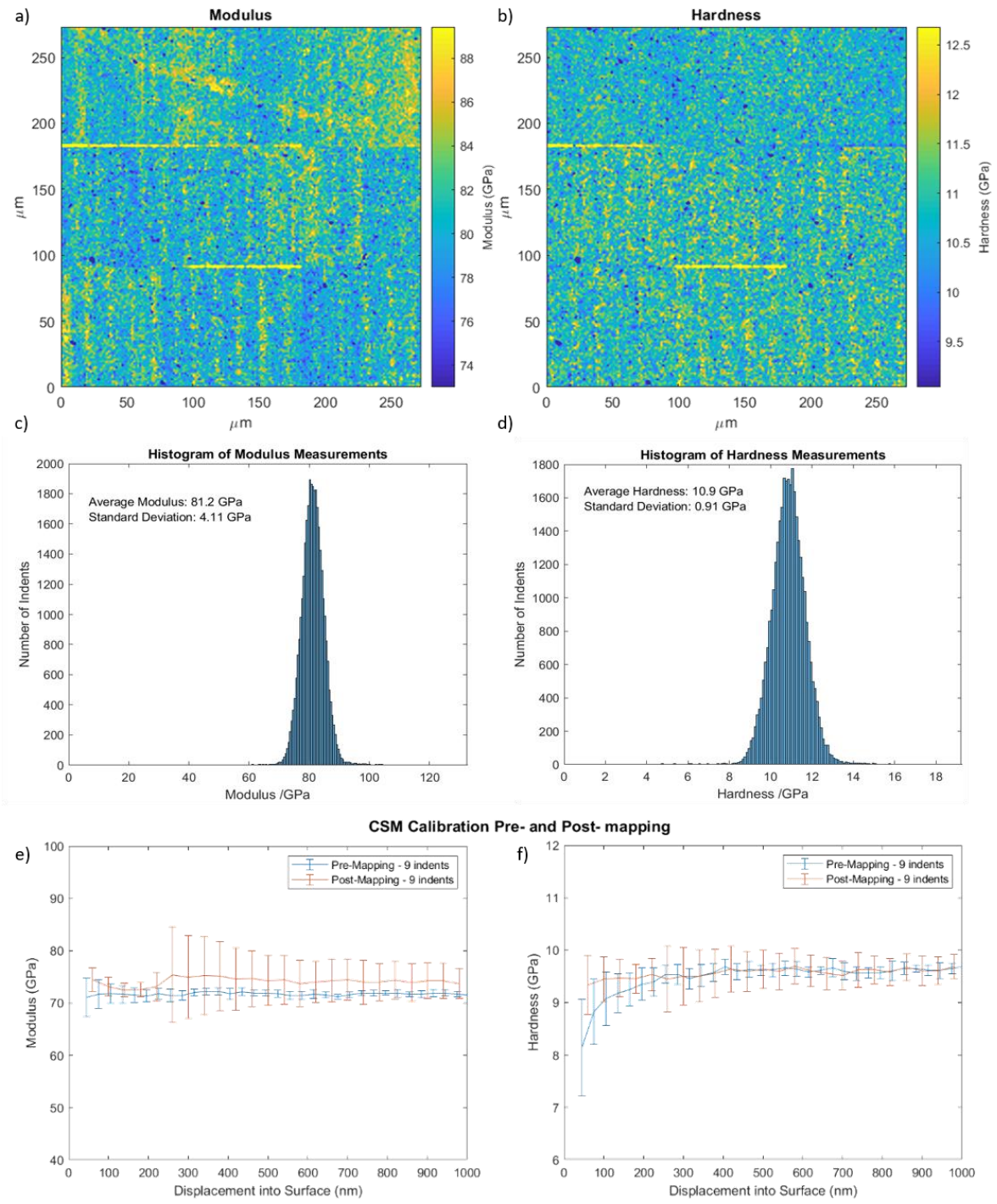



*Figure 115: Hardness (a) and modulus (b) figure of nanoindentation map on Fused Silica. Indents are performed at 3mN, spaced 1.5um apart. This corresponds to a depth/spacing ratio of 1:10, with indents approximately 150nm deep. Histograms of modulus (c) and hardness (d) maps obtained in (a) and (b). CSM nanoindentation data corresponding to modulus (e) and hardness (f) both before (blue) and after (red) performing the nanoindentation map. The large increase in error after ca. 200nm is likely due to a particle lodged in the tip during mapping at this depth: this increase was observed only in the first of the 9 indents, and corresponds to a depth slightly beyond that achieved during the mapping.*

This map corresponds to a depth/spacing ratio of ~1:10, with indents approximately ~150 nm deep. This was preceded and followed by two sets of nine CSM nanoindents to a target depth of 2000 nm. These were performed with an indentation strain rate of 0.05 $s^{-1}$, with a harmonic oscillation of 2 nm at 45 Hz, parameters used for all other CSM tests in this study. The first of

these sets was used for tip area function calibration, using the software's default analytical method with parameters as set out in Table XIV.

*Table XIV: Parameters used during software calibration of tip area function through CSM indents on fused silica.*

| **Parameter** | **Value / Range** |
|---|---|
| Range of depth for area calculation | 50-2000nm |
| Nominal modulus of tested material | Fixed at 72 GPa |
| Range of depth for load frame stiffness calculation | 1500-2000nm |
| Coefficient count | 9, allowing negative |
| Lead term for area function | Unfixed |
| Analytical model: Beta and Epsilon | 1.00, 0.75 (default)[402] |

In Figure 115 a) & b) it can be seen that there is an inaccuracy in the stage movement travelling between bundles: the horizontal lines of high modulus correspond to indents more closely spaced than programmed. The collection strategy within bundles can also be seen, with vertical stripes corresponding to slight systematic errors in x-stage positioning within bundles. These factors contribute to noise in the nanoindentation mapping, but do not prevent the extraction of trends from the full map.

Histograms of the modulus and hardness values for the entire map are shown in Figure 115 c) & d). The mean modulus is 12.5% higher than the value of 72 GPa established using slower standard CSM mode nanoindentation. However, it is reassuring that there is minimal increase in modulus or hardness across the bundles, indicating little tip wear within a map of this size.

The CSM data shown in Figure 115 e) & f) supports this conclusion. The first set of nine indents made before mapping were used for calibration, while the second set obtained after mapping show little to no change in modulus, ~2 GPa, at the 150 nm depth used for the indentation

mapping. This indicates there is no significant systematic change in tip calibration during the indentation mapping.

Further to discussions of tip calibration persistence, it is necessary to consider the spatial resolution of this mapping technique. We compare results obtained using conventional CSM nanoindentation measurements and nanoindentation mapping on the same material. Figure 117 and Figure 118 provide an example of the discrepancy between nanoindentation mapping and CSM nanoindentation results for a fused silica calibration specimen, and the CP titanium specimen studied. There is a persistent artificial increase in hardness and modulus recorded when performing nanoindentation mapping, which decreases as depth is increased. This may be related to the rate at which the indents were performed, or due to the difference in the way these values are calculated. Despite these systematic variations, nanoindentation mapping provides data in line with literature accepted values for fused silica.

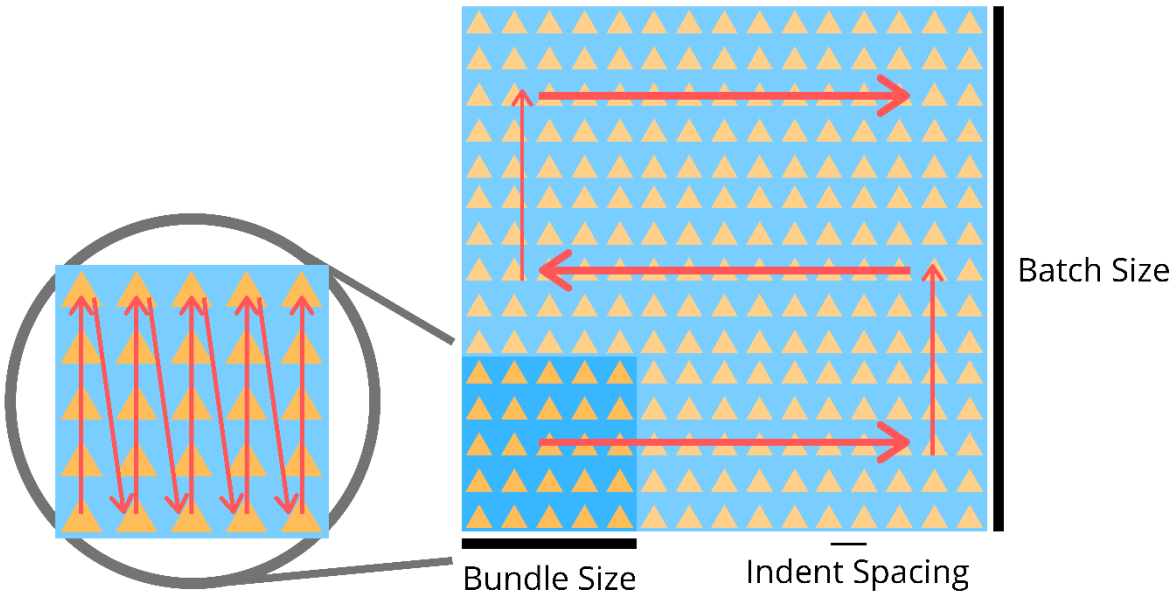



*Figure 116: Graphical representation of nanoindentation mapping strategy. Individual bundles, shown in the inset on the left, are populated line-by-line travelling along the y-axis. The map is populated with bundles in a serpentine motion, with the direction depending on the position of the starting point.*

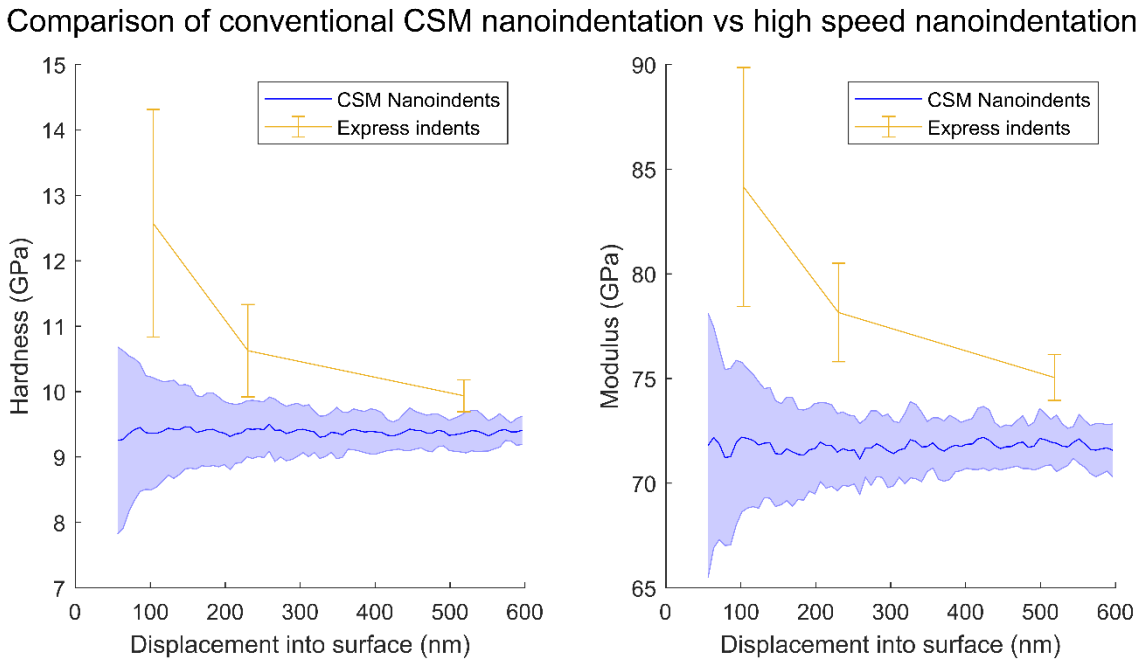



*Figure 117: Comparison of conventional CSM nanoindentation against high-speed nanoindentation mapping, performed in fused silica. Mapping nanoindents were performed at a depth : spacing ratio of 1:10.*

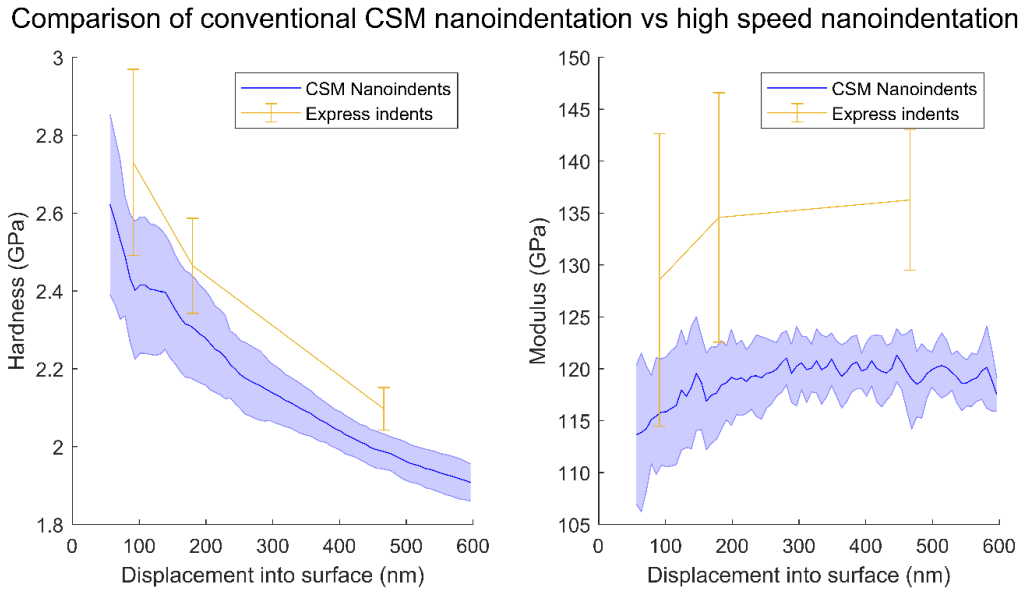



*Figure 118: Comparison of conventional CSM nanoindentation against high speed nanoindentation mapping, performed in Specimen 1 – CP titanium. Mapping nanoindents were performed at a depth : spacing ratio of 1:10.*

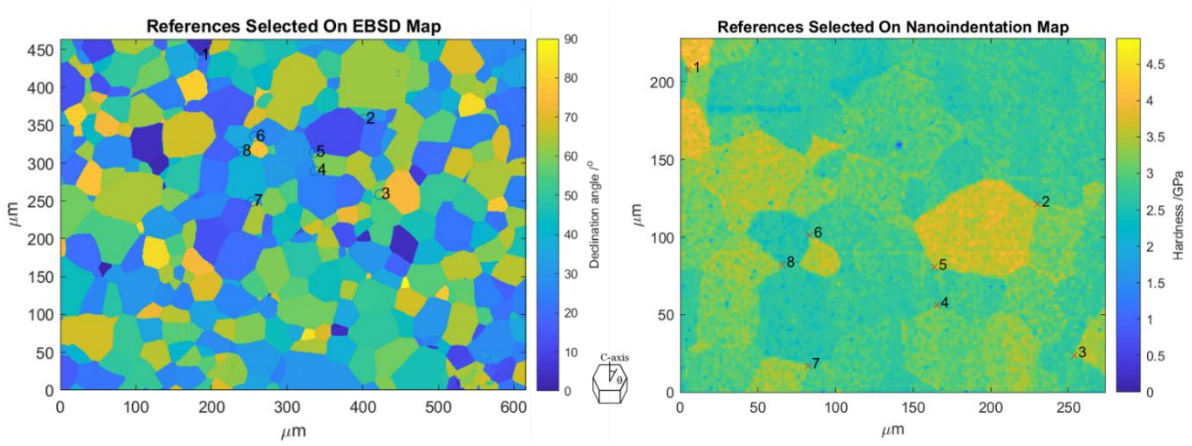



*Figure 119: EBSD (left) alongside the nanoindentation hardness map (right) highlighting the corresponding points in each map used for transforming the EBSD map.*

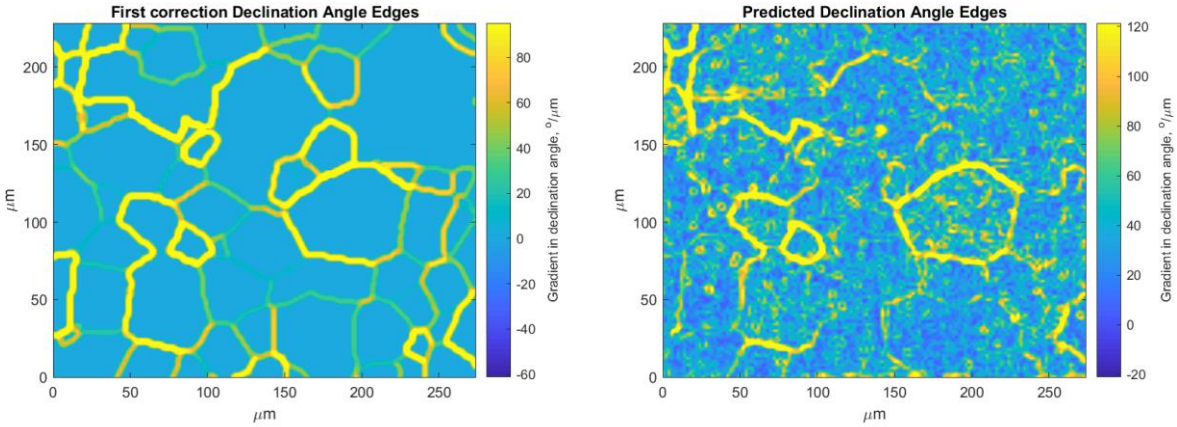



*Figure 120: EBSD declination angle edges, as aligned (left) compared with the simulated declination angle (right) calculated through the hardness relationship. These were obtained with a Sobel edge detection filter* [138].

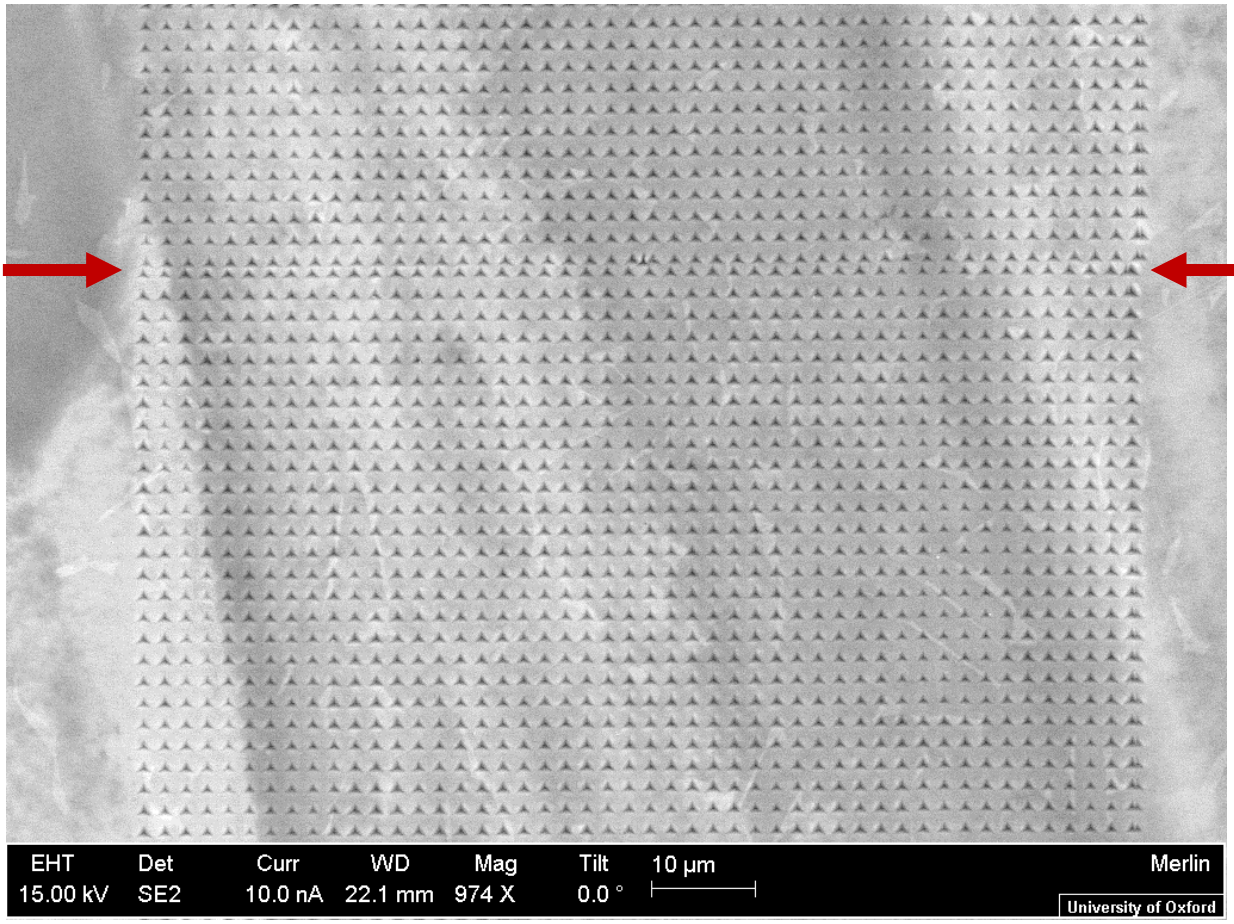



*Figure 121: SEM image of nanoindentation mapping. Image shows two bundles of 48x48 indents spaced 2 µm apart, with the border between them situated along the top of the image. A small offset between the bundles can be seen as a row of indents placed closer to each other than designed, highlighted with red arrows.*

## 5.3. Nanoindentation Stiffness Measurement

The exact experimental process is detailed below:

1. Mount the nanoindenter tip with the chevron cut facing the rear of the unit. This ensures that the flat face of the Berkovich tip is facing the neck of the cantilever, minimising plastic deformation. This can be verified with a quick Microscope to Indenter Calibration (MIC) test.
2. Mount the samples into the sample holder, ensuring that the cantilever “points” away from the highest point in the holder. If applicable, ensure that the incoming laser side is facing up. These two details ensure consistency across datasets.
3. Mount the sample holder into the “nano” piezo-electric stage. This ensures a snug fit, as well as providing a second slot for a Fused Silica calibration specimen.

4. Ensure that the height of the cantilever discs is as close to the surface height of the fused silica specimen. Alternatively, that the top of the sample holder is slightly above the height of the fused silica. This can be verified roughly by observing the focus level of both surfaces.
5. Ensure that the sample holder is rotated such that higher section of the sample holder is close to you to minimise the risk of the tip crashing into the holder.
6. Use the MIC procedure to calibrate the indenter.
7. On the first sample of every re-mount, carry out a MIC on the ring of one of the specimens, to ensure that the samples are not beyond the zero line +/- 100 µm.
8. Measure the coordinates of recognisable features on the cantilever hammer, using the camera and stage movement. Calculate the mid-point of this, and travel to this location.
9. Under scanning mode (right-click, Scanning handset under nanovision mode).
10. Right click on screen, "configure tip engage" settings make sure park height is 9 µm and offset is 0, 0 µm.
11. For scanning method, choose:
    a. old methods/methods/nanovision scanning/G-series nanovision interactive scan.msm
12. Engage the tip – the tip will fast approach, then it will park above the sample at 9 µm.
13. When the image of the sample displays, click on test mode and select the following method:
    a. Old methods folder/cantilever/Bending method offset displacement control for DCM CMM.msm
14. Complete the testing parameters as follows:

| Panel Inputs | Value | Units |
|---|---|---|
| Depth Limit | 2000 | nm |

| | | |
|---|---|---|
| Displacement Rate | 30 | nm/s |
| Frequency Target | 42 | Hz |
| Harmonic Displacement Target | 2 | nm |
| Poisson's Ratio | 0.28 | |
| Spacing in X | 0 | nm |
| Spacing in Y | 0 | nm |
| Strain Rate Target | 0.05 | 1/s |
| Surface Approach Detection Stiffness Criterion | 200 | N/m |
| Surface Approach Distance | 5000 | nm |
| Surface Approach Velocity | 30 | nm/s |

15. Start the indent. The tip will approach the surface and start recording when it reaches the surface (when stiffness reaches 200 N/m). The tip will continue to travel until the depth limit has been reached, and then retract. The method has been modified to continue collecting data until manually stopped.
16. In order to minimise the effect of the surface plastic deformation, a second indent is made in the same location. This method therefore only retracts the tip to the parking position near the surface, minimising any drift.
17. The second indent is made to 1500 nm to ensure minimal added plastic deformation. To remove the influence of frame stiffness, it is crucial to manually press the stop button **after** a few data points are collected in air.
18. The data is exported to excel, and the tip retracted to return to the microscope view. If applicable, return to step 8.

## 5.4. Fatigue Sample Holder Machining

The dimensions of the sample holder assembly are shown in Figure 122.

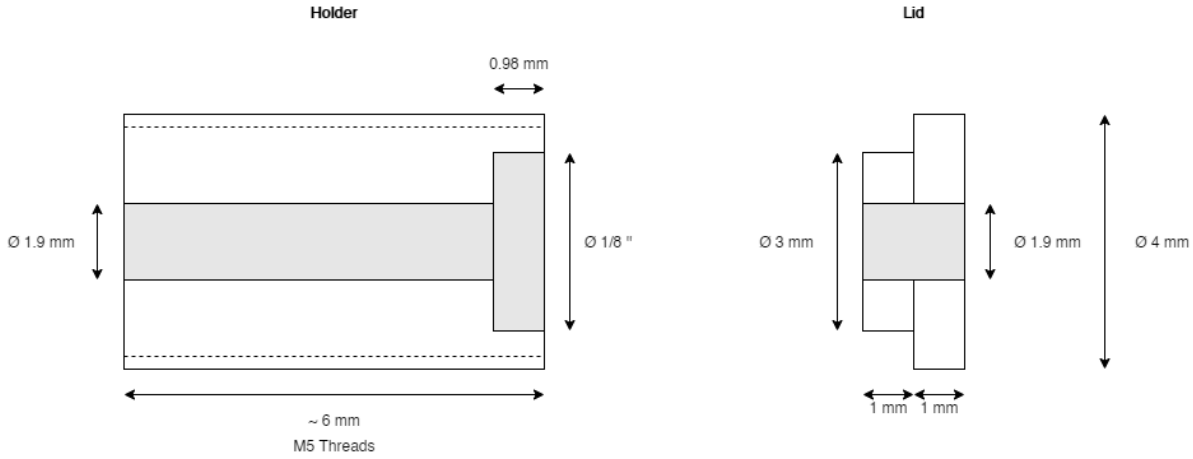



*Figure 122: Dimensions of Specimen Holder and Lid. Each component is machined out of a standard M5 grub screw on a lathe, and are axisymmetric. The depth of the sample hole in the holder is slightly less than 1 mm, such that the inner section of the lid presses against the sample rather than the top of the holder.*

The procedure for making these is outlined below, with the grub screws secured in the lathe with the holder shown in Figure 123. For holders:

1) Secure the grub screw in in the lathe with the end side to be machined, and face it off until it is approximately 6 mm long.
2) Drill a pilot hole in the centre.
3) Using a 1.9 mm bore drill, drill through-thickness.
4) Using a 1/8$^{th}$ inch flat tipped drill, carefully remove just under 1 mm of material.

The purpose of the last step is to create the surface on which the sample is held. This creates an inset that is slightly over 3 mm in diameter (1/8$^{th}$ of an inch being approximately 3.18 mm), with minimal burs.
To machine a lid:

1) Secure the grub screw to in the lathe in either orientation.
2) Machine the sides until the threads are no longer visible.
3) Machine the first few millimetres to 4 mm in diameter.
4) Machine the first 1 mm of length to a diameter of 3 mm. Ensure that this is safely at least 1 mm in length.

5) Drill a pilot hole in the centre.

6) Using a 1.9 mm bore drill, drill at least 3 mm into the piece.

7) Use a parting tool to cut off the first 2 mm.

    a. With care, it is advisable to de-burr the edges before fully parting off the piece.

8) De-burr the pieces remaining from the parting using grinding paper.

This simple methodology for designing sample holders was in part the motivation for a 3 mm wide disc design.




*Figure 123: Jig for mounting M5 grub screws in a lathe. The grub screw enters the threaded hole in the left hand side of the image, through the hole that is covered by the silver nut at the back.*